

UNIVERSITY OF NOTTINGHAM



The University of  
Nottingham

UNITED KINGDOM · CHINA · MALAYSIA

SCHOOL OF MATHEMATICAL SCIENCES

# One Dimensional Models for Slugging in Channel Flow

Josef A. Giddings, MMath.

A thesis submitted to the University of Nottingham for the  
degree of  
DOCTOR OF PHILOSOPHY

OCTOBER 2016

---

## ABSTRACT

Gas-liquid pipe flows are extremely important in many industries, one of which is the oil/gas industry which is where the motivation for this work comes from. In subsea natural gas pipelines the gas is compressed before being pumped through the pipe at high pressure. As it flows through the pipe some of the gas condenses into a low density mixture of hydrocarbon liquids. When gas and liquid flow together there are several possible flow regimes that can occur depending on the velocity of the gas and liquid, one of which is slug flow where the liquid forms a series of plugs (slugs) separated by relatively large gas pockets. The occurrence of slug flow is a major concern in the oil and gas industry due to the difficulty of dealing with large changes in the oil and gas flow rates at the exit of the pipe.

We develop a hydraulic theory to describe the occurrence and structure of slugging in two-layer-gas-liquid flow generated by prescribed, constant, upstream flow rates in each layer. We will investigate how small-amplitude disturbances affect the flow in order to study the stability of spatially uniform solutions. We will then consider the existence of periodic travelling wave solutions numerically in order to investigate the influencing factors that may lead to a transition from stratified flow to slug flow. We then solve the governing equations numerically as an initial value problem in order to improve our understanding of how and why slugs form and are able to compare our solutions to those predicted by the periodic travelling wave theory. Finally, we investigate the effects of non-horizontal channels with small, slowly varying inclination on the development of slug flow by re-writing our equations in terms of a curvilinear co-ordinate system. From this we find that the height of the layer of liquid increases with the angle of the channel and our solutions are significantly different to those in the horizontal case.

---

## ACKNOWLEDGEMENTS

I would like to thank my supervisors, John Billingham and Stephen Cox, for their help and guidance throughout my Ph.D. I would also like to thank them, along with the School of Mathematical Sciences administration staff, for their continued support and understanding in order for me to complete my Ph.D alongside my extracurricular commitments, in particular Helen Cunliffe whose help and consideration has been instrumental in achieving this.

I am grateful for access to the University of Nottingham High Performance Computing Facility, without which the depth of my simulations would not have been possible.

This work was funded by the Engineering and Physical Sciences Research Council, via a doctoral training award.

---

# CONTENTS

---

1	INTRODUCTION	1
1.1	Slugging in Natural Gas Pipelines . . . . .	1
1.2	Literature Review . . . . .	2
1.2.1	Semi-Mechanistic Models . . . . .	4
1.2.2	Kelvin-Helmholtz Instability . . . . .	6
1.2.3	Shear Stresses . . . . .	13
1.2.4	Roll Waves . . . . .	21
1.2.5	Computational Fluid Dynamics . . . . .	28
1.2.6	The Development of Slugging in Two-Layer Hydraulic Flows . . . . .	33
1.3	Thesis Outline . . . . .	35
2	THE HYDRAULIC MODEL	38
2.1	Conservation of Mass . . . . .	40
2.2	Conservation of Momentum . . . . .	41
2.3	Non-Dimensional Equations of Motion . . . . .	44
2.4	Parameter Values . . . . .	46
2.5	Conclusion . . . . .	49
3	LINEARISED STABILITY OF THE UNIFORM FLOW	50
3.1	Linear Stability Condition . . . . .	51
3.2	Instability Growth Rate Analysis . . . . .	53
3.3	Conclusion . . . . .	59
4	PERIODIC TRAVELLING WAVE THEORY	60
4.1	Analysis of Equilibrium Points . . . . .	67
4.2	Analysis for $h \sim \epsilon^{-1}$ . . . . .	70

4.3	Numerical Calculation of the Periodic Solutions . . . . .	72
4.4	Conclusion . . . . .	94
5	INITIAL VALUE PROBLEM	106
5.1	Formulation of Equations . . . . .	107
5.1.1	Spatial Step Size Analysis . . . . .	110
5.1.2	IVP Linear Stability . . . . .	111
5.2	Analysis of the Stability of Periodic Travelling Waves . . . . .	113
5.3	Channel Simulations . . . . .	122
5.3.1	Varying Parameters . . . . .	131
5.4	Effects of Varying the Parameters . . . . .	135
5.5	Conclusion . . . . .	153
6	THE EFFECT OF INCLINATION IN THE THIN LAYER LIMIT	157
6.1	Equation Derivation . . . . .	157
6.2	Periodic Travelling Wave Theory . . . . .	165
6.2.1	$\bar{\lambda} < -1$ (Strongly Uphill) . . . . .	170
6.2.2	$-1 < \bar{\lambda} < 0$ (Downhill) . . . . .	187
6.2.3	Summary of Periodic Travelling Wave Solutions . . . . .	202
6.3	Constant $\bar{\theta}$ - Initial Value Problem . . . . .	204
6.4	Varying $\bar{\theta}$ - Initial Value Problem . . . . .	209
6.5	Conclusion . . . . .	214
7	CONCLUSION	218
7.1	Thesis Results . . . . .	218
7.2	Future Work . . . . .	221
A	APPENDIX	224
A.1	Channel Simulations . . . . .	224
A.2	Effects of Varying the Parameters . . . . .	243
	Bibliography	250

---

## LIST OF FIGURES

---

Figure 1.1	The co-ordinate system. . . . .	6
Figure 1.2	The co-ordinate system. . . . .	23
Figure 2.1	The co-ordinate system. . . . .	39
Figure 2.2	A comparison of $\text{Re}_l$ against $c_l$ from (2.4.3). . . . .	48
Figure 3.1	The growth rate when varying the parameters. . . . .	55
Figure 3.2	The neutral curve and the maximum growth rate curve	58
Figure 4.1	A comparison of (4.0.13) against Needham et al. [132].	64
Figure 4.2	A typical bifurcation diagram for $B < 0$ . . . . .	65
Figure 4.3	A typical bifurcation diagram for $B > 0$ . . . . .	66
Figure 4.4	The phase portrait for $(\dot{H}, \dot{W})$ , from (4.2.11). . . . .	73
Figure 4.5	The periodic solutions for $\epsilon = 0.1$ and $U = 2.09$ . . . . .	75
Figure 4.6	The periodic solution of wavelength 1.0666 for $\epsilon = 0.1$ .	76
Figure 4.7	The bifurcation diagram for $\epsilon = 0.1$ and $F_0 = 4$ . . . . .	77
Figure 4.8	The bifurcation diagram from the steady state solution.	78
Figure 4.9	The periodic solution at $U = 2.095$ . . . . .	80
Figure 4.10	The bifurcation diagram for $\epsilon = 0.1$ and $F_0 = 6.7$ . . . . .	81
Figure 4.11	The bifurcation diagram for $\epsilon = 0.01$ . . . . .	82
Figure 4.12	The periodic solutions for $\epsilon = 0.1$ and $U = 2.3$ . . . . .	83
Figure 4.13	The periodic solution and phase plane for $U = 2.150$ .	86
Figure 4.14	The periodic solution and phase plane for $U = 2.199$ .	87
Figure 4.15	The periodic solution and phase plane for $U = 2.206$ .	88
Figure 4.16	The periodic solution and phase plane for $U = 2.350$ .	89
Figure 4.17	The periodic solution and phase plane for $U = 2.472$ .	90
Figure 4.18	The periodic solution and phase plane for $U = 2.480$ .	91
Figure 4.19	The periodic solution and phase plane for $U = 2.490$ .	92

List of Figures

Figure 4.20	The periodic solution and phase plane for $U = 2.730$ .	95
Figure 4.21	The periodic solution and phase plane for $U = 2.710$ .	96
Figure 4.22	The periodic solution and phase plane for $U = 4.250$ .	97
Figure 4.23	The periodic solution and phase plane for $U = 4.194$ .	98
Figure 4.24	The periodic solution and phase plane for $U = 4.100$ .	99
Figure 4.25	The periodic solution and phase plane for $U = 4.067$ .	100
Figure 4.26	The periodic solution and phase plane for $U = 4.033$ .	101
Figure 4.27	The periodic solution and phase plane for $U = 3.989$ .	102
Figure 4.28	The periodic solution and phase plane for $U = 3.950$ .	103
Figure 4.29	The periodic solution and phase plane for $U = 3.581$ .	104
Figure 5.1	The bvp5c and IVP solution when varying $\Delta x$ . . . . .	112
Figure 5.2	The solutions for $F_0 = 3.2$ at various times. . . . .	114
Figure 5.3	The solution at $t = 9$ for $F_0 = 10$ . . . . .	114
Figure 5.4	The bifurcation diagram for Parameter Set 1. . . . .	116
Figure 5.5	The bifurcation diagram for Parameter Set 2. . . . .	116
Figure 5.6	Legends for Figures 5.7 and 5.8. . . . .	118
Figure 5.7	$U$ from bvp5c and the IVP for Parameter Set 1. . . . .	118
Figure 5.8	$U$ from bvp5c and the IVP for Parameter Set 2. . . . .	118
Figure 5.9	The bvp5c and IVP solutions for Parameter Set 1. . . . .	119
Figure 5.10	The bvp5c and IVP solutions for Parameter Set 2. . . . .	120
Figure 5.11	The solution at $t = 900$ . . . . .	123
Figure 5.12	The slugs at $t = 900$ . . . . .	124
Figure 5.13	Slug 2 compared to the bvp5c solution. . . . .	125
Figure 5.14	The solutions as a slug is formed. . . . .	126
Figure 5.15	The solutions as the slug leaves liquid behind. . . . .	127
Figure 5.16	A slug at $t = 962$ compared to the bvp5c solution. . . . .	128
Figure 5.17	Legend for width figures. . . . .	129
Figure 5.18	The width and height against location. . . . .	130
Figure 5.19	The width and height against location compilation. . . . .	131
Figure 5.20a	The solution of Data Set 8 at $t = 3000$ . . . . .	136
Figure 5.20b	The solution of Data Set 14 at $t = 3000$ . . . . .	136

List of Figures

---

Figure 5.21a	The width and height against location for Data Set 8.	137
Figure 5.21b	The width and height against location for Data Set 14.	137
Figure 5.22	$\delta$ against $\lambda$ against average slugs per unit time. . . . .	140
Figure 5.23a	The solution and width against location for Data Set 32.	142
Figure 5.23b	The solution and width against location for Data Set 33.	142
Figure 5.23c	The solution and width against location for Data Set 34.	143
Figure 5.23d	The solution and width against location for Data Set 35.	143
Figure 5.24	The average number of slugs per unit time. . . . .	144
Figure 5.25	The wave peak height against $B$ . . . . .	145
Figure 5.26	The propagation speed, $U$ , against $B$ . . . . .	146
Figure 5.27	The propagation speed, $U$ , against wave peak height.	146
Figure 5.28a	The bifurcation diagram for $B = -0.2$ . . . . .	147
Figure 5.28b	The bifurcation diagram for $B = -0.3$ . . . . .	147
Figure 5.28c	The bifurcation diagram for $B = -0.4$ . . . . .	148
Figure 5.28d	The bifurcation diagram for $B = -0.5$ . . . . .	148
Figure 5.28e	The bifurcation diagram for $B = -0.6$ . . . . .	149
Figure 5.28f	The bifurcation diagram for $B = -0.7$ . . . . .	149
Figure 5.28g	The bifurcation diagram for $B = -0.8$ . . . . .	150
Figure 5.29	The average number of slugs compared to $F_0$ and $\delta$ . .	152
Figure 5.30	The average number of slugs compared to $F_0$ and $\epsilon$ . .	153
Figure 5.31	The average number of slugs compared to $R_l$ and $R_g$ .	154
Figure 6.1	The Cartesian co-ordinate system. . . . .	158
Figure 6.2	The curvilinear co-ordinate system. . . . .	159
Figure 6.3	Plot of $\bar{\lambda}$ against $\bar{\theta}$ . . . . .	164
Figure 6.4	The typical bifurcation diagram for $B < 0$ and $\bar{\lambda} < -1$ .	170
Figure 6.7	The typical bifurcation diagram for $B > 0$ and $\bar{\lambda} < -1$ .	172
Figure 6.5	The bifurcation diagram for $\bar{\lambda} = -2$ and $B = -0.1$ . .	173
Figure 6.6	The limit cycle solutions for $\bar{\lambda} = -2$ and $B = -0.1$ . .	174
Figure 6.8	The bifurcation diagram for $B = 0.04$ and $\bar{\lambda} = -5$ . . .	178
Figure 6.9	The bifurcation diagram for $B = 0.5$ and $\bar{\lambda} = -5$ . . .	178
Figure 6.10	The bifurcation diagram for $B = 0.95$ and $\bar{\lambda} = -5$ . . .	179

List of Figures

---

Figure 6.11	The bifurcation diagram for $B = 1.01$ and $\bar{\lambda} = -5$ . . .	180
Figure 6.12	The bifurcation diagram for $B = 1.04$ and $\bar{\lambda} = -5$ . . .	181
Figure 6.13	The bifurcation diagram for $B = 1.05$ and $\bar{\lambda} = -5$ . . .	182
Figure 6.14	The bifurcation diagram for $B = 1.055$ and $\bar{\lambda} = -5$ . . .	182
Figure 6.15	The bifurcation diagram for $B = 1.056$ and $\bar{\lambda} = -5$ . . .	183
Figure 6.16	The bifurcation diagram for $B = 1.06$ and $\bar{\lambda} = -5$ . . .	183
Figure 6.17	The bifurcation curves in the $(U, B)$ plane. . . . .	184
Figure 6.18	The bifurcation curves zoomed in around $U = U_{\min}$ . . .	185
Figure 6.19	The bifurcation diagram for $B = 0.5$ and $\bar{\lambda} = -5$ . . . . .	185
Figure 6.20	The limit cycle solutions from <code>bvp5c</code> and the IVP. . .	186
Figure 6.21	Typical bifurcation diagrams for $B > 0$ and $-1 < \bar{\lambda} < 0$ . . .	187
Figure 6.22	The bifurcation diagram for $B = 2$ and $\bar{\lambda} = -0.2$ . . . . .	190
Figure 6.23	The bifurcation diagram for $B = 2.5$ and $\bar{\lambda} = -0.8$ . . . . .	191
Figure 6.24	The limit cycle solutions for $-1 < \bar{\lambda} < 0$ and $B > 0$ . . .	191
Figure 6.25	Typical bifurcation diagrams for $B < 0$ and $-1 < \bar{\lambda} < 0$ . . .	192
Figure 6.26	The bifurcation diagram for $B = -0.1$ and $\bar{\lambda} = -0.2$ . . .	195
Figure 6.27	The bifurcation diagram for $B = -2$ , $\bar{\lambda} = -0.8$ & $F_0 = 0.5$ . . .	195
Figure 6.28	The bifurcation diagram for $B = -2$ , $\bar{\lambda} = -0.8$ & $F_0 = 0.4$ . . .	195
Figure 6.29	The limit cycle solutions for $B = -0.1$ and $\bar{\lambda} = -0.2$ . . .	196
Figure 6.30	The phase planes for $B = -0.1$ and $\bar{\lambda} = -0.2$ . . . . .	197
Figure 6.31	The solutions near the heteroclinic bifurcation. . . . .	198
Figure 6.32	The bifurcation diagram for $B = -0.5$ , $\bar{\lambda} = -0.2$ & $F_0 = 5$ . . .	200
Figure 6.33	The bifurcation diagram for $B = -0.5$ , $\bar{\lambda} = -0.2$ & $F_0 = 18$ . . .	200
Figure 6.34	The bifurcation diagram for $B = -2.47$ and $\bar{\lambda} = -0.8$ . . . . .	201
Figure 6.35	The limit cycle solutions for $B = -0.5$ and $\bar{\lambda} = -0.2$ . . .	202
Figure 6.36	The solutions at $t = 1000$ for $\bar{\lambda} > 0$ . . . . .	205
Figure 6.37	The solutions at $t = 1000$ for $-1 < \bar{\lambda} < 0$ . . . . .	206
Figure 6.38	The average peak height against $\bar{\lambda} > -1$ . . . . .	207
Figure 6.39	The solutions at $t = 1000$ for $\bar{\lambda} < -1$ . . . . .	208
Figure 6.40	The average peak height against $\bar{\lambda} < -1$ . . . . .	208
Figure 6.41	The solution at $t = 1000$ for $\bar{\lambda} = -5$ and $F_0 = 12$ . . . . .	210

List of Figures

---

Figure 6.42	The solutions as a larger roll wave is formed for $\bar{\lambda} = -5.210$	
Figure 6.43	The solution at $t = 1000$ for a 'bump' in the channel. .	211
Figure 6.44	The effects of varying $a$ and $b$ for $F_0 = 10$ . . . . .	213
Figure 6.45	The steady state solution for $K = 0.4$ , $a = 2$ and $b = 1$ .	214
Figure 6.46	The effect of varying $b$ with a flat channel end. . . . .	215
Figure A.1a	The solution of Data Set 1 at $t = 3000$ . . . . .	225
Figure A.1b	The solution of Data Set 2 at $t = 3000$ . . . . .	225
Figure A.1c	The solution of Data Set 3 at $t = 3000$ . . . . .	226
Figure A.1d	The solution of Data Set 4 at $t = 3000$ . . . . .	226
Figure A.1e	The solution of Data Set 5 at $t = 3000$ . . . . .	227
Figure A.1f	The solution of Data Set 6 at $t = 3000$ . . . . .	227
Figure A.1g	The solution of Data Set 7 at $t = 3000$ . . . . .	228
Figure A.1h	The solution of Data Set 8 at $t = 3000$ . . . . .	228
Figure A.1i	The solution of Data Set 9 at $t = 3000$ . . . . .	229
Figure A.1j	The solution of Data Set 13 at $t = 3000$ . . . . .	229
Figure A.1k	The solution of Data Set 14 at $t = 3000$ . . . . .	230
Figure A.1l	The solution of Data Set 16 at $t = 3000$ . . . . .	230
Figure A.1m	The solution of Data Set 17 at $t = 3000$ . . . . .	231
Figure A.1n	The solution of Data Set 18 at $t = 3000$ . . . . .	231
Figure A.1o	The solution of Data Set 23 at $t = 3000$ . . . . .	232
Figure A.1p	The solution of Data Set 25 at $t = 3000$ . . . . .	232
Figure A.1q	The solution of Data Set 26 at $t = 3000$ . . . . .	233
Figure A.1r	The solution of Data Set 27 at $t = 3000$ . . . . .	233
Figure A.2a	The width and height against location for Data Set 1.	234
Figure A.2b	The width and height against location for Data Set 2.	234
Figure A.2c	The width and height against location for Data Set 3.	235
Figure A.2d	The width and height against location for Data Set 4.	235
Figure A.2e	The width and height against location for Data Set 5.	236
Figure A.2f	The width and height against location for Data Set 6.	236
Figure A.2g	The width and height against location for Data Set 7.	237
Figure A.2h	The width and height against location for Data Set 8.	237

## List of Figures

---

Figure A.2i	The width and height against location for Data Set 9.	238
Figure A.2j	The width and height against location for Data Set 13.	238
Figure A.2k	The width and height against location for Data Set 14.	239
Figure A.2l	The width and height against location for Data Set 16.	239
Figure A.2m	The width and height against location for Data Set 17.	240
Figure A.2n	The width and height against location for Data Set 18.	240
Figure A.2o	The width and height against location for Data Set 23.	241
Figure A.2p	The width and height against location for Data Set 25.	241
Figure A.2q	The width and height against location for Data Set 26.	242
Figure A.2r	The width and height against location for Data Set 27.	242

---

## LIST OF TABLES

---

Table 2.1	The typical ranges of the dimensional parameters. . .	47
Table 2.2	The typical ranges of the non-dimensional parameters.	49
Table 5.1	A comparison of $U$ and $B$ for varying $\Delta x$ . . . . .	111
Table 5.2	$U$ and $B$ from bvp5c and the IVP for Parameter Set 1.	117
Table 5.3	$U$ and $B$ from bvp5c and the IVP for Parameter Set 2.	117
Table 5.4	Data for which slugs form. . . . .	133
Table 5.5	Data for which no slugs form. . . . .	134
Table 5.6	Other. . . . .	134
Table 5.7	Data for which slugs form when varying $\delta$ and $\lambda$ . . .	138
Table 5.8	Data for which no slugs form when varying $\delta$ and $\lambda$ .	139
Table 6.1	$U$ and $B$ from bvp5c compared to those from the IVP.	186
Table A.1	Data for which slugs form when varying $\delta$ , $\lambda$ & $F_0$ . .	245
Table A.2	Data for which no slugs form when varying $\delta$ , $\lambda$ & $F_0$ .	249

---

## INTRODUCTION

---

### 1.1 SLUGGING IN NATURAL GAS PIPELINES

Gas-liquid pipe flows are extremely important in many industries, one of which is the oil/gas industry which is where the motivation for this work comes from. In subsea natural gas pipelines the gas is compressed before being pumped through the pipe at high pressure, resulting in a highly turbulent flow. As it flows through the pipe some of the gas condenses into a low density mixture of hydrocarbon liquids. When gas and liquid flow together there are several possible flow regimes that can occur depending on the velocity of the gas and liquid. The three main types we are interested in are:

- stratified - where the liquid flows along the bottom of the pipe with the gas flowing separately above it;
- bubble flow - where the gas moves as small dispersed bubbles through the liquid;
- slug flow - where the gas is contained in large bubbles, separated by liquid slugs which locally fill the pipe.

A major concern in the oil and gas industry is the occurrence of slug flow due to the difficulty of dealing with large changes in the oil and gas flow rates at the exit of the pipe and the potential of this damaging the

processing plant facilities. In order to combat this, the pipelines are often designed in such a way that, although they may reduce slugging, results in a compromise of efficiency and/or size of the processing plant. Although there has been a lot of research on the occurrence of slug flow and the transition to it from stratified flow, there is still a lot that has not been explained.

Throughout this thesis we will refer to:

- roll waves – as defined by Dressler [50], as any wave formation, periodic in distance, that occurs when a liquid flows turbulently down an open inclined channel, where the wave profile progresses downstream at a constant speed without distortion and such that the velocity of the water particles is everywhere less than the wave velocity;
- slugs – as any wave which is significantly larger than the roll waves around it and which nears the top of the channel.

## 1.2 LITERATURE REVIEW

The study of the formation of slug flow regimes in two-layer hydraulic flow has mainly been aimed at investigating the point at which a stratified flow becomes unstable via linear stability theory, better known as the Kelvin-Helmholtz instability. This is done by linearising the non-linear equations and considering the effect of a small disturbance to the flow. The use of Kelvin-Helmholtz instability theory has shown that, in order for slugs to form, the pressure above a wave, caused by the Bernoulli principle, must be large enough to overcome the stabilising effect of gravity. However, Kelvin-Helmholtz instability theory assumes that the liquid is inviscid and neglects surface tension. As a result, the instability that arises grows exponentially as  $k \rightarrow \infty$ , where  $k$  is the wave number, known as the Hadamard instability (Joseph and Saut [95]).

Classical Kelvin-Helmholtz instability theory has been extended to include viscous terms using the theory of viscous potential, see Funada and Joseph [71], however this assumes that the shear induced by the gas flow is negligible. By including the liquid viscous and inertia terms in the equation, they can be evaluated using pseudo-steady state approximations relating them to the flow variables, see Lin and Hanratty [115]. A comparison of different linear stability methods against experimental results is given by Mata et al. [122].

Although linear stability methods can predict the instability of an interface, it is necessary to understand non-linear effects on the growth of interfacial waves to determine whether slug flow will develop. In order to investigate these non-linear effects it should be noted that the governing equations of a two-layer hydraulic flow, as seen in Needham et al. [132], have a structure similar to that of roll waves down inclined channels. Beginning with the equations from shallow water theory, using the Chézy formula for turbulent resistance, it can be shown that no continuous solution which is periodic in space exists. However one continuous solution does exist which can be used as a basis for constructing discontinuous periodic solutions joined by shocks, see Dressler [50].

Now consider the same starting equations as Dressler [50], but with energy dissipation expressed through tangential shear and a term expressing the effect of energy dissipation by shearing normal to the flow. By linearising the governing equations we can find a necessary and sufficient condition on the Froude number for which the uniform flow is temporally stable, but unstable otherwise. When the flow is temporally unstable and considering the effect of a small perturbation to the flow, by the Hopf bifurcation theorem, it can be shown that periodic solutions exist (Needham and Merkin [131]). Hence we may assume that periodic solutions will also exist for the governing equations of a two-layer hydraulic flow, see Needham et al. [132].

In order to gain a full understanding of the underlying causes of slug flow, we must consider the full non-linear equations. Previously this was not possible; however, due to advances in modern computing we are now able to solve the governing equations numerically. This area is dominated by two distinct methods; slug tracking and slug capturing, and has led to the development of commercial codes. In slug tracking models, such as that developed by Barnea and Taitel [18], slug statistics are used at the inlet and the slug fronts and tails are tracked in order to investigate the effects on the slugs as they propagate downstream. However, these models do not provide an insight on how the slugs are formed. This led to the development of slug capturing models, such as that by Issa and Kempf [87]. These models do not require any slug statistics data and instead the slugs develop automatically, allowing the user to investigate how the slugs form as well as investigating the slug characteristics.

### 1.2.1 *Semi-Mechanistic Models*

Due to the structure of slug flow being periodic in neither space nor time, an exact solution to the continuum equation is out of the question. Griffith and Wallis [75] and Nicklin et al. [134] were the first to identify the importance of the motion of the large gas pockets created in slug flow. This led some authors to use experimental data in order to design approximate methods for predicting slug flow characteristics, the most commonly used being those by Beggs and Brill [20] and Dukler et al. [55, 56]. This approach was successfully used for many years, however it did not explain how or why slug flow developed.

Early mechanistic models were designed using the "unit-cell" approach, developed by Wallis [182], where a control volume encompassing the liquid slug and gas pocket of a fully evolved slug flow regime was analysed. A moving frame of reference is then used which travels at the speed of the cell, in order for a steady-state analysis using mass and momentum balances to

be completed. This approach was developed for horizontal flow by Dukler and Hubbard [54] and Nicholson et al. [133]; inclined flow by Bonnecaze et al. [29]; vertical flow by Fernandes et al. [63], Orell and Rembrand [143] and Sylvester [169]; and unified models were developed by Gomez et al. [72, 73], Petalas and Aziz [144] and Taitel and Barnea [170].

Dukler and Hubbard [54] developed the first comprehensive unit-cell model for horizontal flows. They used extensive visualisation studies which included the use of fast shutter speed cameras to take both still photographs and videos of the flow. From these they formulated a description of the conditions for the initiation and dissipation of slug flow, for which they provided a qualitative explanation and derived their hydraulic model for predicting the structure of slug flow. Their model consisted of twelve independent equations and sixteen variables and, although it appeared complex to use, could be solved easily.

Taitel and Barnea [170] considered various options for modelling the hydrodynamic parameters and introduced a unified approach for the pressure drop in order to develop a model that was applicable for the horizontal, inclined and vertical cases. They present their approach in a way they view as being the best combination of engineering accuracy and ease of calculation, while reviewing previous work on the topic at each stage. The calculation procedure for their model contained several options for the user, to be chosen appropriately for the specific use required.

More recently, Gomez et al. [72] developed a unified model that was applicable to inclination angles from horizontal to upward vertical flow. Their model consisted of a unified flow pattern prediction model and unified individual models for each flow regime. Based on the work by Taitel and Barnea [170], Gomez et al. [72] developed a simpler slug flow model that avoided the need for numerical integration along the liquid film region. They compared predictions from their slug flow model to data sets from Felizola and Shoham [62], Nuland et al. [139] and Schmidt [156] and found them to be sufficiently accurate for practical applications.

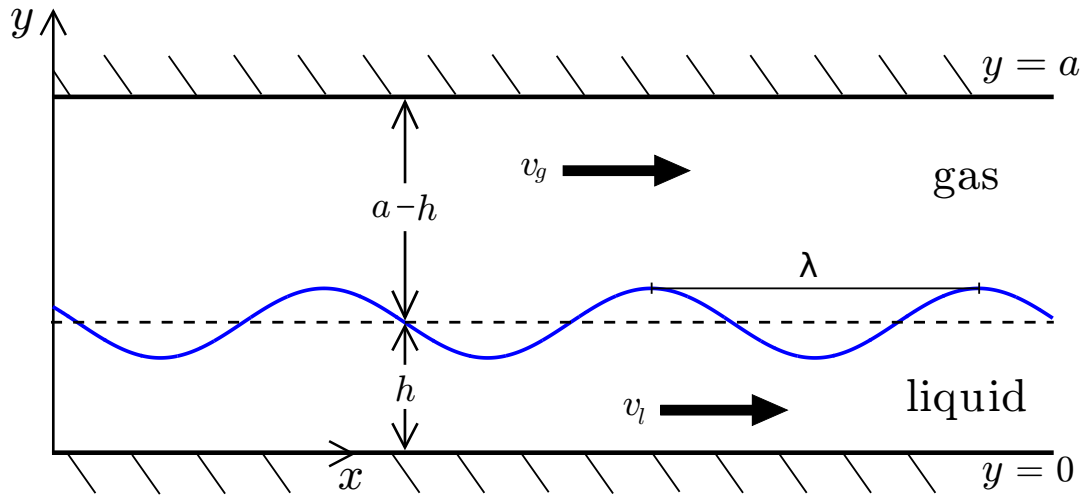


Figure 1.1.: The co-ordinate system.

An alternative approach, the "statistical cellular model", was developed by separating the flow into two flow patterns, the separated and the dispersed flow regions, then taking the statistical averages of the physical properties in each region. The dependent variables and the characteristics of the slugs can then be predicted using conditional averaging of the conservation equations, see Fabre and Liné [58], Fabre et al. [59, 60], Ferschneider [64].

The developments made through steady-state analysis improved the ability to predict some of the important flow parameters compared to the approximate methods developed empirically by authors such as Beggs and Brill [20] and Dukler et al. [55, 56]. However, they do not provide information on the formation of slugs, or on the statistics of slug lengths or propagation speeds. It has also been shown that they are not necessarily capable of capturing certain flow phenomenon, such as the dissipation of slugs in downhill flow, see Taitel et al. [174].

### 1.2.2 Kelvin-Helmholtz Instability

The classical Kelvin-Helmholtz instability is the instability of the uniform flow of inviscid and incompressible liquid and gas through a horizontal,

infinite channel. The interface may be wavy with wavelength  $\lambda$ , but has average liquid flow height  $h$  and average gas flow depth  $a - h$ , where  $a$  is the height of the channel, as shown in Figure 1.1. Using the long wavelength approximation and neglecting surface tension, Kelvin-Helmholtz instability occurs when

$$(v_g - v_l)^2 > g(\rho_l - \rho_g) \left( \frac{a - h}{\rho_g} + \frac{h}{\rho_l} \right), \quad (1.2.1)$$

for mean velocity  $v$ , density  $\rho$ , gravity  $g$  and subscripts  $l$  and  $g$  for the liquid and gas respectively. Assuming  $\rho_g \ll \rho_l$  and  $v_l \ll v_g$ , this simplifies to

$$v_g^2 > g(a - h) \frac{\rho_l - \rho_g}{\rho_g}. \quad (1.2.2)$$

By introducing, as suggested by Wallis [182],

$$j_g^* = v_g \frac{a - h}{a \sqrt{g a}} \sqrt{\frac{\rho_g}{\rho_l - \rho_g}}, \quad (1.2.3)$$

the dimensionless volumetric flux of the gas, and

$$\alpha = \frac{a - h}{a}, \quad (1.2.4)$$

the void fraction, (1.2.2) becomes

$$j_g^* > \alpha^{3/2}. \quad (1.2.5)$$

Many authors, as with the original Kelvin-Helmholtz instability analysis, assumed that viscosity and surface tension could be neglected, see Kordyban and Ranov [110], Mishima and Ishii [126], Taitel and Dukler [172]. Wallis and Dobson [183] explored experimentally when uniform flow transitions to a slug flow regime and found that the instabilities occur for

$$j_g^* > 0.5\alpha^{3/2}. \quad (1.2.6)$$

They concluded that the difference between (1.2.5) and (1.2.6) is probably due to (1.2.5) being essentially based on one-dimensional theory.

Kordyban and Ranov [110], based on the experiments of Baker [14] and previous theoretical work of Griffith and Lee [74] and Suo and Griffith [167], proposed that the transition to slug flow was due to the Kelvin-Helmholtz instability being magnified by the proximity of the upper wall of the channel, and hence is wave-amplitude dependent. As a result, they consider the pressure distribution over the wave to be dependent on the proximity of the upper wall and that slugs are an extension of growth of an already formed wave. They proposed that, at first order approximation, the pressure variations over the wave could be split into two components, one in phase with the wave profile and the other in phase with the wave slope. For simplicity, they neglected the component in phase with the wave slope and assume that the aerodynamic-pressure is proportional to the surface displacement and found the point of instability corresponded to the point the wave speed became imaginary, which they consider to be the point of initiation of slugs. By limiting their equation to deep water waves, assuming  $\rho_l \gg \rho_g$  and neglecting surface tension their stability criterion simplifies to

$$(v_g - v_l)^2 > \frac{\rho_l g}{\rho_g k \coth(k(a-h) - 0.9) + 0.45 \coth^2(k(a-h) - 0.9)}, \quad (1.2.7)$$

for wave number  $k = 2\pi/\lambda$ , for which a suitable value must be selected.

This led Kordyban [106] to investigate the inviscid Kelvin-Helmholtz stability for just the crest of an existing wave. He found the instability to be given by

$$K \frac{v_{gc}}{g(a-h_c)} \frac{\rho_g}{\rho_l - \rho_g} = 1, \quad (1.2.8)$$

where  $v_{gc}$  is the gas velocity at the crest of the wave,  $h_c$  is the height of the crest of the wave and  $K$  is defined as

$$K = 2 \frac{\Delta p}{\rho_g (v_{gc}^2 - v_{gt}^2)}, \quad (1.2.9)$$

for the difference between the maximum and minimum pressure over a wave,  $\Delta p$ , and gas velocity at the trough of the wave,  $v_{gt}$ . Through experi-

ments, Kordyban [109] found  $K = 1.35$  as an average, however noted that many individual waves have much larger values.

Mishima and Ishii [126] extended the work of Kordyban and Ranov [110] by introducing the wavelength of the "most dangerous wave" in order to determine the value of  $K$ . They considered the "most dangerous wave" to be the one with the largest growth rate as they proposed this would be the one that would develop into a slug. They concluded the slug criterion as

$$k(a - h) = 2.26, \quad (1.2.10)$$

and

$$v_g \geq v_l + 0.487 \sqrt{g(a - h)} \sqrt{\frac{\rho_l - \rho_g}{\rho_g}}. \quad (1.2.11)$$

However, Lin and Hanratty [115] noted that the analysis by Mishima and Ishii [126] shows that the "most dangerous wave" also requires the largest gas velocity in order for there to be an instability. Hence, wavelengths that do not grow fast may become unstable at lower gas velocities.

Taitel and Dukler [172] developed a fully predictive model for determining the flow regime transition based on physical concepts, rather than to use experimental data as has been done by many authors (see, for example, Kordyban and Ranov [110], Wallis and Dobson [183]). In order to use experimental data a decision about the coordinates to be used must be made, which Taitel and Dukler [172] considered to be a coordination of data rather than a correlation and may not hold true when applied to data outside of the data set being used. Instead, they developed a model based on realistic mechanisms for transitions between flow regimes by extending Kelvin-Helmholtz analysis to both horizontal rectangular channels and then inclined pipes, which allowed the instability limit to be calculated for pipes of any geometry. In order to evaluate their instability limit the liquid level in stratified equilibrium flow,  $h$ , must be calculated. To do this they used momentum balances in the gas and liquid phases in which the interfacial

shear,  $\tau_i$ , gas-wall shear,  $\tau_g$ , and liquid-wall shear,  $\tau_l$ , were evaluated using the pseudo-steady state approximations

$$\tau_i = \frac{1}{2}\rho_g f_i (v_g - v_i)^2, \quad (1.2.12)$$

$$\tau_g = \frac{1}{2}\rho_g f_g v_g^2, \quad (1.2.13)$$

$$\tau_l = \frac{1}{2}\rho_l f_l v_l^2, \quad (1.2.14)$$

where  $v_i$  is the interface velocity and  $f_i$ ,  $f_g$  and  $f_l$  are friction factors which must be estimated (this topic will be discussed in more detail later). According to Taitel and Dukler [172] a finite wave will grow in horizontal rectangular channels for

$$j_g^* > \left(1 - \frac{h}{a}\right) \alpha^{3/2}, \quad (1.2.15)$$

and in inclined pipes for

$$v_g > \left(1 - \frac{h}{a}\right) \sqrt{\frac{\rho_l - \rho_g}{\rho_g} \frac{A_g}{\frac{dA_l}{dh}} g \cos \theta}, \quad (1.2.16)$$

where  $A_g$  is the cross-sectional area of the gas,  $A_l$  is the cross-sectional area of the liquid and  $\theta$  is the angle of the incline.

Note that  $\alpha = (1 - h/a)$ , and if  $h/a = 0.5$  the result is consistent with Wallis and Dobson [183]. Taitel and Dukler [172] propose that  $h/a = 0.5$  is a critical value for which if  $h/a > 0.5$  a slug will form and if  $h/a < 0.5$  annular or dispersed annular flow will develop. Their reasoning behind this is that when suction over the crest of a finite amplitude wave causes it to grow, the liquid it draws in must come from around it, causing a trough to develop. If  $h/a > 0.5$  then the peak of the wave will reach the top of the pipe before the trough reaches the bottom, hence a slug is formed.

Although Taitel and Dukler [172] included viscous terms in order to evaluate  $h$  in their analysis, Lin and Hanratty [115] note that the derivation of the instability limit was done using inviscid fluid theory. Hence, in their work, Lin and Hanratty [115] included liquid viscous and inertia

terms and took into account shear stresses at the gas-liquid interface and the component of pressure out of phase with the wave height, using an approach similar to that of Andreussi et al. [6], Hanratty [79], Hanratty and Hershman [81]. By including these extra terms they found the wave velocity to be greater than the liquid velocity at neutral instability rather than equal to it as in the case for classical Kelvin-Helmholtz instability. As a result, the instabilities occur at a lower gas velocity than (1.2.5) predicts due to the destabilising effect of the inertia terms. They considered both turbulent gas-turbulent liquid and turbulent gas-laminar liquid for pipe flow and channel flow. They evaluated the gas-wall and liquid-wall shear using (1.2.13) and (1.2.14), respectively, however instead of using (1.2.12) they evaluated the interfacial shear using

$$\tau_i = \frac{1}{2} \rho_g f_i (v_g - C_R)^2, \quad (1.2.17)$$

where  $C_R$  is the real component of the wave velocity.

Their stability criterion for turbulent gas-laminar liquid in a channel is given by

$$j_g^* > K_l \alpha^{3/2}, \quad (1.2.18)$$

with

$$K_l = \left[ 1 - \frac{\Omega \Xi^2}{(1-\alpha)^3} \frac{\nu_g^4}{\nu_l g a^3} \left( \frac{a \alpha v_g}{\nu_g} \right)^{3.5} \right]^{1/2}, \quad (1.2.19)$$

where  $\Omega$  is a function of  $\alpha$ ,  $f_i$  and  $f_g$ ,  $\nu$  is the kinematic viscosity and

$$\Xi = \frac{1}{60.15} \left( \frac{1-\alpha}{\alpha} \right)^2 \left[ 1 + \frac{4}{3} \frac{1-\alpha}{\alpha} \right] \frac{\rho_g}{\rho_l}. \quad (1.2.20)$$

For large  $\nu_l$ ,  $K_l \cong 1$  and the stability criterion reduces to (1.2.5).

Motivated by the success of viscous potential flow analysis to the Rayleigh-Taylor instability by Joseph et al. [96], Funada and Joseph [71] used the theory of viscous potential flow in order to apply the Kelvin-Helmholtz instability to viscous flows where the shear from the gas is negligible. By

considering the neutral curve, the border between stability and instability, they found that the density and viscosity ratios

$$\hat{\rho} = \frac{\rho_l}{\rho_g}, \quad \hat{\mu} = \frac{\mu_l}{\mu_g}, \quad (1.2.21)$$

for viscosity  $\mu$ , have significant importance. They found that when  $\hat{\mu} = \hat{\rho}$  the marginal stability of their neutral curve is the same as the neutral stability of the inviscid case. Moreover, the maximum critical velocity is at  $\hat{\mu} = \hat{\rho}$ , hence the critical velocity for viscous fluids for which  $\hat{\mu} \neq \hat{\rho}$  is smaller than that of inviscid fluids. They found that for high viscosity liquids the stability limits can hardly be distinguished from each other, however for low viscous fluids there is a sharp decrease. For high-viscous fluids their work gives a much closer stability limit to that of (1.2.5), which has also been found by other authors (see Andritsos et al. [10], Barnea and Taitel [17]).

By taking the long-wavelength limit  $k \rightarrow 0$ , their stability criterion simplifies to

$$(v_g - v_l)^2 > g \frac{1 - \hat{\rho}}{\hat{\rho}} \frac{[a - (1 - \hat{\mu})h]^2}{a - (1 - \hat{\mu}^2/\hat{\rho})h} \left( 1 + \frac{\gamma k^2}{g(\rho_l - \rho_g)} \right), \quad (1.2.22)$$

where surface tension is denoted by  $\gamma$ . Hence, for long waves, surface tension does not have an effect on the stability, but the effects of viscosity are still important. By applying  $\hat{\mu} = \hat{\rho}$  this is identical to (1.2.1), the inviscid case.

Barnea and Taitel [17] noted that inviscid Kelvin-Helmholtz theory (such as studied by Kordyban [106], Kordyban and Ranov [110], Mishima and Ishii [126], Taitel and Dukler [172]) gave applicable results at high viscosities and only deviates from viscous Kelvin-Helmholtz theory (such as done by Andritsos and Hanratty [9], Andritsos et al. [10], Barnea [16], Crowley et al. [45], Lin and Hanratty [115], Wallis [182], Wu et al. [189]), which uses the full two-fluid model, at low viscosities. As a result, they considered not only the condition for which a disturbance becomes unstable, but also the rate of amplification of this disturbance. Through their analysis they found

that inviscid Kelvin-Helmholtz theory overpredicts the result found using viscous Kelvin-Helmholtz theory. However, in the region where the inviscid Kelvin-Helmholtz theory is stable, but the viscous Kelvin-Helmholtz theory is unstable, the rate of amplification of the viscous Kelvin-Helmholtz theory is very small until the point where the inviscid Kelvin-Helmholtz theory becomes unstable. Hence, although the inviscid and viscous cases predict the instability at different points, the rate of amplification for both is almost identical, which confirms the study by Barnea [16].

Mata et al. [122] compared analytical and experimental predictions by Jeffreys [91] and [93], Taitel and Dukler [172], Lin and Hanratty [115], Barnea and Taitel [17] and Funada and Joseph [71] with data found experimentally by themselves, Kordyban and Ranov [110] and Wallis and Dobson [183]. They concluded that none of the theories give good agreements to the experimental data as none of them are able to correctly account for the non-linear effects without empirical data on wall and interfacial friction.

### 1.2.3 *Shear Stresses*

In order to take into consideration the non-linear effects many authors, such as Dressler [50], Lin and Hanratty [115], Whitham [187], have expressed the shear stresses in terms of friction coefficients. The shear stresses caused by the friction between the moving gas/liquid and the pipe wall are directly related to the pressure drop through the pipe. We may describe the pressure gradient  $dp/dx$  using the dimensionless pipe friction factor

$$f = -\frac{D}{\frac{1}{2}\rho\bar{v}^2} \frac{dp}{dx}, \quad (1.2.23)$$

where  $D$  is the pipe diameter and  $\bar{v}^2$  is the mean horizontal velocity of the gas/liquid. By considering the force balance (see Schlichting and Gersten

[155]), the shear profile,  $\tau(y)$ , is found to be at its maximum at the wall and is given by

$$\tau_w = -\frac{D}{4} \frac{dp}{dx}, \quad (1.2.24)$$

for subscript  $w$  denoting the value at the wall. Combining this with (1.2.23) gives

$$f = \frac{\tau_w}{\frac{1}{8}\rho\bar{v}^2}, \quad (1.2.25)$$

which is known as the Darcy friction factor. Hence, by Newton's law of friction, the gas-wall shear,  $\tau_g$ , and liquid-wall shear,  $\tau_l$  may be expressed as

$$\tau_g = \mu_g \left( \frac{\partial v_g}{\partial y} \right)_{y=a} = \frac{1}{8} \rho_g f_g \bar{v}_g^2, \quad (1.2.26)$$

and

$$\tau_l = \mu_l \left( \frac{\partial v_l}{\partial y} \right)_{y=0} = \frac{1}{8} \rho_l f_l \bar{v}_l^2, \quad (1.2.27)$$

where  $f_g$  and  $f_l$  are the Darcy friction factors for the gas and liquid, respectively. Several other definitions of the friction factor are used, such as the Fanning friction factor

$$f_F = \frac{\tau_w}{\frac{1}{2}\rho\bar{v}^2}, \quad (1.2.28)$$

which is related to the Darcy friction factor by  $f_F = \frac{1}{4}f$ . In order to compare friction factor correlations more easily we shall present them in terms of the Darcy friction factor.

The relationship given in (1.2.23) is often called the Darcy-Weisbach equation (Rouse [153]) and is more commonly written as

$$-\frac{dp}{dx} = f \frac{\rho}{2} \frac{\bar{v}^2}{D}. \quad (1.2.29)$$

It was first presented by Darcy [47] based on his experiments on water flowing through pipes, before being further refined by Weisbach [185].

In order for (1.2.26) and (1.2.27) to be used, a value for  $f_g$  and  $f_l$  is needed. By using similarity theory, Blasius [27] established that  $f$  was a function of the Reynolds number,  $Re$ . From experimental data on smooth pipes he found that

$$f = \frac{0.316}{Re^{0.25}}, \quad (1.2.30)$$

which is known as the Blasius formula and has been shown to be valid for  $4000 < Re < 80000$ . Prandtl [145] took the ideas of Blasius [27] and applied it to data collected by Nikuradse [136] in order to find a better fit for all turbulent Reynolds number values for smooth pipes, which led to the relationship

$$\frac{1}{\sqrt{f}} = 2 \log_{10} (Re \sqrt{f}) - 0.8. \quad (1.2.31)$$

However, Zagarola and Smits [193] performed their own experiments on a much larger data set and found a much better fit for

$$\frac{1}{\sqrt{f}} = 1.88 \log_{10} (Re \sqrt{f}) - 0.131. \quad (1.2.32)$$

In engineering, however, most pipes cannot be considered as smooth at high Reynolds numbers (Schlichting and Gersten [155]). At high Reynolds numbers the friction coefficient becomes a function of only the relative roughness,  $\epsilon/D$ , where  $\epsilon$  is the height of the pipe wall roughness. Von Kármán [181] used the data collected by Nikuradse [137] and developed the relationship

$$\frac{1}{\sqrt{f}} = 1.14 - 2 \log_{10} \left( \frac{\epsilon}{D} \right). \quad (1.2.33)$$

In the experiments carried out by Nikuradse [137], he had coated the pipes with a uniform layer of sand covering the entire pipe interior,  $\epsilon/D$  was then varied by varying the diameter of the sand grains and pipes used. The data from these experiments showed a clear trend that could be explained by the interaction of the pipes roughness with the fluid boundary layer. However, subsea gas pipelines do not have a uniform relative roughness,

measurements by Colebrook and White [41] showed that in such a case (1.2.33) did not hold. For commercial pipes Colebrook et al. [42] proposed calculating  $f$  using

$$\frac{1}{\sqrt{f}} = -2 \log_{10} \left( \frac{\epsilon}{3.7D} + \frac{2.51}{\text{Re}\sqrt{f}} \right), \quad (1.2.34)$$

known as the Colebrook-White correlation, which must be solved using an iterative method which can be time consuming. Hence Moody [129] plotted a diagram known as the Moody Chart for which solutions to (1.2.34) could be read from.

The Colebrook-White correlation has been widely used in engineering since it was published (Katz and Lee [98], Massey and Ward-Smith [121]), along with the Moody Chart. However, White [186] has stated that the Moody Chart is only accurate to  $\pm 15\%$ . Hence, efforts have been made to approximate the Colebrook-White correlation using explicit formulas such as

$$f = \frac{0.25}{\left[ \log_{10} \left( \frac{\epsilon}{3.7D} + \frac{5.74}{\text{Re}^{0.9}} \right) \right]^2}, \quad (1.2.35)$$

which was developed by Swanee and Jain [168]. When approximations found using (1.2.35) were compared to values from the Colebrook-White correlation for  $10^{-6} < \epsilon/D < 10^{-2}$  and  $5000 < \text{Re} < 10^8$ , Swanee and Jain [168] found the error to be  $< 1\%$ .

However, when Haaland [77] compared approximations found from (1.2.35) to values from the Colebrook-White correlation he found the error to be up to 3%. He proposed the explicit formula

$$\frac{1}{\sqrt{f}} = -\frac{1.8}{n} \log_{10} \left[ \left( \frac{\epsilon}{3.75D} \right)^{1.11n} + \left( \frac{6.9}{\text{Re}} \right)^n \right], \quad (1.2.36)$$

for which with  $n = 1$  gives a close approximations to (1.2.34).

Smith et al. [162] performed experiments in very smooth pipes (similar to those used for natural gas pipelines) and found that the transition from the

smooth to the rough regime is much more abrupt than is indicated by the Colebrook-White correlation. In fact, they showed that choosing the friction factor to be the maximum of that by Prandlt for smooth pipes, given in (1.2.32), and von Kármán for rough pipes, given by (1.2.33), gives a better approximation than the Colebrook-White correlation. Hence, for natural gas pipelines, Haaland [77] proposed using  $n = 3$  in (1.2.36) in order to obtain a more abrupt transition as recommended by Uhl [177].

Similarly to (1.2.24), Taitel and Dukler [173] and many other authors used the approximations

$$\tau_i = \frac{1}{8}\rho_g f_i (v_g - v_i)^2, \quad (1.2.37)$$

for interfacial shear,  $\tau_i$ , friction co-efficient,  $f_i$  and velocity,  $v_i$ .

By treating the gas-liquid interface as a type of wall roughness, Wallis [182] fit four sets of liquid-film flow data using the ratio of mean film thickness  $\bar{h}$  to the pipe hydraulic diameter to get the relationship

$$f_i = 0.02 \left( 1 + 300 \frac{\bar{h}}{D} \right). \quad (1.2.38)$$

He noted that this gave a similar relationship to that of

$$f_w = 0.02 \left( 1 + 75 \frac{\epsilon}{D} \right), \quad (1.2.39)$$

an approximation of wall roughness for  $\epsilon/D < 0.03$ , implying that the wall roughness was four times greater than the mean film thickness. However, (1.2.38) does not accurately predict the behaviour of thicker films, for which the relationship corresponds to smaller gas flow rates and Reynolds numbers (Asali [12], Fore and Dukler [68], Fukano and Furukawa [70], Zabaras et al. [192]).

For a high velocity flow regime, Henstock and Hanratty [82] hypothesised that the liquid layer may have a wavy surface which will result in an increased drag of the gas on the liquid. Consequently, this would cause a larger frictional pressure loss than that caused by the drag on a smooth pipe

wall, hence the interfacial friction factor would be greater than the gas-wall friction factor. They used several data sets from which they presented a system of two equations based on a parameter  $F$ , which for horizontal flow are

$$\frac{f_i}{f_g} = 1 + 850F, \quad (1.2.40)$$

and

$$\frac{h}{D} = \frac{6.59F}{\sqrt{f_i/f_g}}. \quad (1.2.41)$$

By combining these two equations we have

$$f_i = f_g \left( 1 + 129 \sqrt{\frac{f_i}{f_g} \frac{h}{D}} \right), \quad (1.2.42)$$

from which we may write the explicit formula for  $f_i$  as

$$f_i = f_g \left[ 1 + \frac{129}{2} \frac{h}{D} \left( 129 \frac{h}{D} + \sqrt{4 + 129^2 \left( \frac{h}{D} \right)^2} \right) \right]. \quad (1.2.43)$$

When compared to experimental data, it was shown that although this correlation accurately predicts the interfacial friction factor for some flows at lower pressure, it severely overpredicts the value in higher pressure flows (Fore et al. [69]).

Taitel and Dukler [173] suggested that  $f_i \approx f_g$  and, evaluating the hydraulic diameter in the manner suggested by Agrawal et al. [1], gave the friction factors for turbulent flow as

$$f = \frac{0.184}{\text{Re}^{0.2}}, \quad (1.2.44)$$

and for laminar flow as

$$f = \frac{64}{\text{Re}}. \quad (1.2.45)$$

However, this model fails once waves have formed due to the approximation that  $f_i \approx f_g$ . It has also been shown that the predicted value of  $f_l$  from

this model underestimates it by as much as 100%, Kowalski [111]. Similar trends were found by Andreussi and Persen [5], Spedding and Hand [164] and Andritsos and Hanratty [8].

Cheremisinoff and Davis [39] used the interfacial friction factor relationships proposed by Cohen and Hanratty [40] in order to build a model for turbulent liquid-turbulent gas stratified pipe flow. For small amplitude waves they concluded that

$$f_i = 0.0568, \quad (1.2.46)$$

whereas for roll waves they gave it as

$$f_i = 0.032 + 8 \times 10^{-5} \text{Re}_l. \quad (1.2.47)$$

However Spedding and Hand [164] found these gave unsatisfactory results when compared to their experimental data.

Using additional data sets obtained from Asali [12] to those used by Henstock and Hanratty [82], Asali et al. [13] derived the relationship as

$$f_i = f_g \left[ 1 + 0.45 \text{Re}_g^{-0.2} \left( \text{Re}_g \sqrt{\frac{f_i}{8}} \frac{h}{D} - 4 \right) \right], \quad (1.2.48)$$

which, although similar to (1.2.42), attempts to take into account the effects of the laminar sublayer. They proposed that only films thicker than the laminar sublayer would increase the interfacial friction factor above the single-phase value, hence the subtraction of the constant 4 which is an approximation of the laminar sublayer. Using the relationship for the gas-wall friction factor given by Taitel and Dukler [173] in (1.2.44), i.e.

$$\text{Re}_g = \left( \frac{0.184}{f_g} \right)^5, \quad (1.2.49)$$

in (1.2.48) gives

$$f_i = f_g \left[ 1 + \frac{0.45 \times 0.184^4}{2\sqrt{2}f_g^{7/2}} \sqrt{\frac{f_i}{f_g}} \frac{h}{D} - \frac{1.8}{0.184} f_g \right], \quad (1.2.50)$$

which can be compared roughly to the relationship proposed by Henstock and Hanratty [82] by substituting a nominal value of  $f_g = 0.02$  to simplify (1.2.50) to approximately

$$f_i = f_g \left[ 0.8 + 161 \sqrt{\frac{f_i}{f_g}} \frac{h}{D} - \frac{1.8}{0.184} f_g \right]. \quad (1.2.51)$$

The correlation presented by Asali et al. [13] offers a good approximation at lower relative film thickness, which is typical of the data sets used in its derivation. However, as with the relationship proposed by Henstock and Hanratty [82], it overpredicts the interfacial friction factor for flows with a larger film thickness.

The effects that arise from the wavy gas-liquid interface acting like a rough surface over which the gas, being the faster fluid, flows are from multi-dimensional phenomenon, hence cannot be captured by a one-phase model (Issa et al. [88]). Andritsos and Hanratty [8] proposed a relationship based on an extensive set of experiments in horizontal pipes that accounted for the influence of waves on both  $f_l$  and  $f_i$ .  $f_g$  was calculated using (1.2.44) and (1.2.45).

They observed that the ratio of  $f_i$  to  $f_g$  remained relatively constant until a certain level of the superficial gas velocity,  $v_{sg} = v_{sg,t}$ , was reached, for which they found

$$v_{sg,t} = 5 \sqrt{\frac{\rho_{g0}}{\rho_g}}, \quad (1.2.52)$$

where  $\rho_{g0}$  is the density of the gas at atmospheric pressure. They then proposed the relationship

$$f_i = f_g, \quad \text{for } v_{sg} < v_{sg,t}, \quad (1.2.53)$$

$$f_i = f_g \left[ 1 + 15 \sqrt{\frac{h}{D}} \left( \frac{v_{sg}}{v_{sg,t}} - 1 \right) \right], \quad \text{for } v_{sg} \geq v_{sg,t}. \quad (1.2.54)$$

Spedding and Hand [164] and Shi and Kocamustafaogullari [159] showed that this correlation proved adequate at predicting the film height and pressure

drop even when the gas-liquid interface is far away from flat, regardless of the fluid properties and pipe diameter. However, it was found to underestimate the friction factors at high liquid flow rates and overestimate them at low liquid flow rates. Furthermore, since  $v_{sg,t}$  decreases significantly as the pressure is increased and the friction factor is inversely proportional to  $v_{sg,t}$ , for higher pressure flows (1.2.54) gives unreasonably high friction factors (Tzotzi and Andritsos [176]).

Foley and Vanoni [67] performed experiments from which the onset of the instability to the flow occurred much earlier than that predicted when using empirical formula. Hence, some authors (see, for example, Demekhin et al. [49], Tseluiko and Kalliadasis [175]) have proposed modelling the stresses using Reynolds stresses combined with the van Driest formula for the Prandtl's mixing length. Although this method may increase the accuracy of our model, it also adds an additional layer of complexity to our already very complex system. Therefore, in order to simplify our model and make our analysis easier, we will express the shear stresses in terms of friction coefficients as has been commonly used in previous work and shown to achieve accurate results (see, for example, Bonizzi et al. [28], Issa and Kempf [87], Kjølås et al. [105], Lin and Hanratty [115], Taitel and Dukler [172]).

It is common practise in multiphase pipe flow engineering to use the correlation proposed by Colebrook et al. [42] for the wall shear and the Taitel and Dukler [173] correlation for interfacial shear, hence these are the models we shall use in our work. As these correlations are for cylindrical pipes we will need to modify them for channel flow, which will be done in Section 2.4.

#### 1.2.4 *Roll Waves*

Roll waves, as defined by Dressler [50], are any wave formation, periodic in distance, that occurs when a liquid flows turbulently down an open inclined

channel, where the wave profile progresses downstream at a constant speed without distortion and such that the velocity of the water particles is everywhere less than the wave velocity. Photographs of roll waves in a long rectangular channel were first presented by Cornish [44], from which the periodic nature of roll waves was clear. Cornish [44] observed that the wave fronts were practically vertical surfaces of discontinuity and highly turbulent. Due to their common occurrence in man-made channels they have been reproduced and studied in experiments, such as those by Brock [31, 32]. He found that changes to the flow rates and flow depth greatly affected the formation of roll waves, which creates a large problem for engineers (Iverson et al. [90], Rouse [152]).

It has been shown that in multi-phase flow, roll waves are the main wave type that occurs under a wide range of conditions, as described by Hanratty and Engen [80]. The wavelengths are typically much longer than the film thickness and the roll waves maintain their form while travelling through the pipe. As roll waves carry fluid and mix liquid as they travel, they have been of interest in the determination of the characteristics of multi-phase flow and the formation of slugs (Kordyban [107]).

For the low Reynolds number case, some authors have used weakly non-linear and long wavelength theories in order to simplify the Navier-Stokes equation. This usually results in the governing equation being a single non-linear partial differential equation for the normal interfacial height as the local velocity profile can be approximated to leading order by the Nusselt profile, see Benjamin [25], Benney [26], Chang [38], Kawahara and Toh [99], Lin [116], Nakaya [130], Sivashinsky and Michelson [161], Yih [190]. They determined the critical Reynolds number that caused an instability and extended the theory into the non-linear regime. However, Pumir et al. [147] found that when the solutions to these equations were extended to the high Reynolds number case they diverged.

In order to investigate the high Reynolds number case, Jeffreys [92] used the St. Venants model combined with the Chézy formula for turbulent

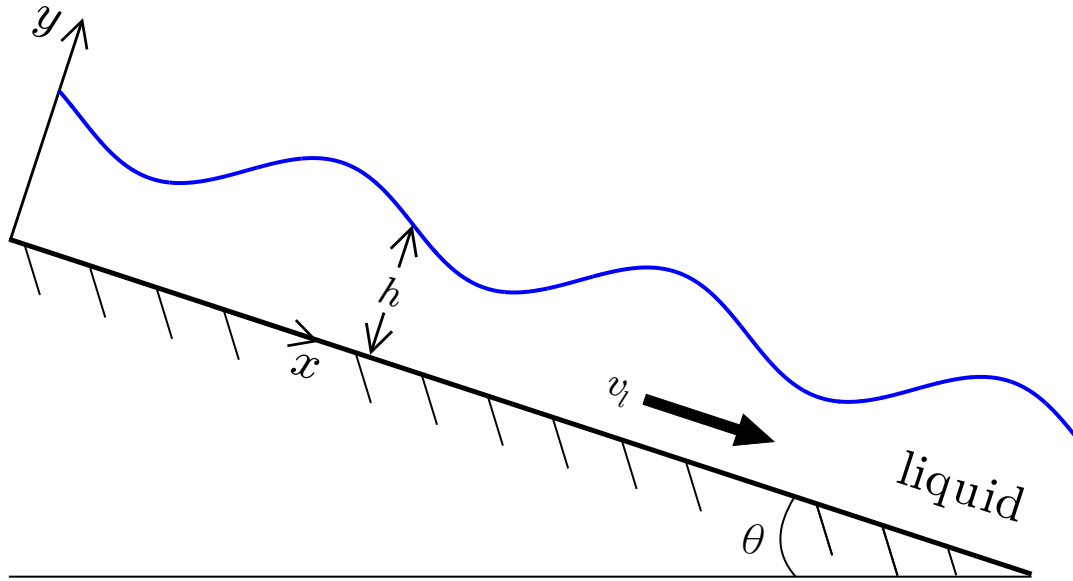


Figure 1.2.: The co-ordinate system.

resistance in order to include the effects of drag in his equation. He performed linear stability analysis in order to investigate the formation of roll waves and found the instability condition

$$F \leq 2, \quad (1.2.55)$$

where  $F$  is the Froude number given by

$$F = \frac{v_l}{\sqrt{gh \cos \theta}}, \quad (1.2.56)$$

and  $\theta$  is the angle from the horizontal, as shown in Figure 1.2.

Dressler [50] used the shallow water equations combined with the Chézy formula for turbulent resistance in order to find a necessary condition for the existence of a continuous solution that can be used as a basis for constructing discontinuous periodic solutions joined by shocks. For prescribed values of the slope,  $\theta$ , resistance and wave speed, he found there is a one-parameter family of roll-wave solutions, for which, if the wave length is also prescribed, the solution will then be unique. The need for shocks arises as Dressler [50], like Jeffreys [92], neglected the turbulent viscosity, which resulted in the equations being hyperbolic and shock forming. The condition found by

Dressler [50] was in fact the same as that by Jeffreys [92] for the instability of the uniform flow.

Yu and Kevorkian [191] concentrated on the weakly unstable case,  $0 < F - 2 \ll 1$ , in a broad, slightly inclined,  $\theta \ll 1$ , channel using the dimensionless shallow water equations given by Kevorkian [100]. They considered the initial conditions

$$h(x, 0; \epsilon) = 1 + \epsilon h_0(x), \quad (1.2.57)$$

$$u(x, 0; \epsilon) = 1 + \epsilon u_0(x), \quad (1.2.58)$$

where  $\epsilon$  was a small parameter which measured the amplitude of the initial disturbance and  $h_0(x)$  and  $u_0(x)$  were prescribed disturbance functions and restricted the Froude number to the one-parameter family

$$F = 2 + \alpha\epsilon, \quad (1.2.59)$$

for  $\alpha > 0$  and  $\alpha = O(1)$ . By performing a multiple scale asymptotic expansion, they derived the leading order governing equations which they found to be time dependent for  $0 < t < T(\epsilon)$ , where  $T = O(\epsilon^{-1})$ . However, for  $t = O(10T)$  the solution tends to the quasi-steady state as found by Dressler [50], for which they found that a given arbitrary periodic initial disturbance will tend to the roll wave having the same wavelength.

When Yu and Kevorkian [191] compared their results from the asymptotic analysis to results found from numerical integration, they found the transient behaviour of the solution including the characteristics of the discontinuities was accurately described. However, they conceded that this was in part due to them having only compared the limiting forms of both the asymptotic and exact equations and only having used one roll wave with periodic boundary conditions. In order to gain a more precise comparison they would have needed to integrate the full system sufficiently long enough

to ensure a well-developed quasi-steady solution, which they found to be impractical.

Some authors have built on the work of Dressler [50] by adding a diffusive term to the momentum equation, see Chang et al. [37], Huang and Lee [85], Kranenburg [112], Needham and Merkin [131], Prokopiou et al. [146], Whitham [187]. Needham and Merkin [131] included an energy dissipation expressed through tangential shear and a term expressing the effect of energy dissipation by shearing normal to the flow. By non-dimensionalising their governing equations and using linear stability analysis they found the same stability criteria as that by Dressler [50]. They then used the Hopf bifurcation theorem to examine the quasi-steady states of their governing equations and found that for  $F > 2$  there exists a critical value of the wave propagation speed  $U$  such that there is a Hopf bifurcation when

$$U = 1 + \frac{1}{F}. \quad (1.2.60)$$

By using an averaging method they generated uniformly valid expansions for the quasi-steady periodic solutions and showed that for each set of flow parameters there is a one-parameter family of roll wave solutions. Through further numerical integration, they discovered that these solutions do not exist indefinitely from the Hopf points, instead they appear to end abruptly. In two following papers (Merkin and Needham [124, 125]) they demonstrated that this end point corresponds to a homoclinic bifurcation for which they found analytical expressions for its location near the critical Froude number  $F = 2$  with  $U = 1.5$ .

Hwang and Chang [86] used dynamic singularity theory and numerical methods to analyse the model equations given by Dressler [50] and Needham and Merkin [131]. Their work was carried out independently to Merkin and Needham [124, 125] and used a different technique, which followed the methods used by Carr [35] and Guckenheimer and Holmes [76]. Their work confirmed the results found by Needham and Merkin [131] and Merkin and Needham [124, 125] and expanded it for  $U > 1.5$ , which resulted in them

finding roll waves within two very narrow bands either side of  $U = 1.5$ , which they found compared very well with the data of Brock [31, 32] and Brauner and Maron [30].

Huang and Lee [85] developed a diffusive shallow water equation model in order to study numerically the spatial evolution of roll waves which they compared to the experimental data of Brock [31, 32]. They found that undiffusive models largely overestimated the wave amplitude, whereas diffusive models gave good agreement to the experimental data as long as the proper turbulent viscosity value is selected. However, Hu et al. [84] found that Huang and Lee [85] evaluated their model incompletely and in fact their model was unable to resolve either natural roll waves or periodic permanent roll waves.

More recently, the shallow water equations have been combined with  $k - \epsilon$  turbulence closure in order to more accurately include the effects of turbulence. Richard and Gavrilyuk [150] proposed a model which included two types of enstrophies which represent the dispersion due to the non-uniform velocity distribution in the vertical. They found their model gave reasonable agreement when compared to the experimental data of Brock [31, 32], however it requires specified flow depth and velocity at a critical point. As a result, their model does not work in cases where there is no observed data nor is able to resolve sufficiently the formation process of roll waves (Cao et al. [34]).

Cao et al. [34] developed a physically enhanced model which, similarly to Richard and Gavrilyuk [150], combined the shallow water equations with  $k - \epsilon$  turbulence closure, along with a modification component. They compared their model numerically against a traditional shallow water equation model, a shallow water equation model incorporating the standard depth-averaged  $k - \epsilon$  turbulence closure, a shallow water equation model incorporating the standard depth-averaged  $k - \epsilon$  turbulence closure and dispersion and the Richard and Gavrilyuk [150] model. They found their model gave more accurate solutions when compared to the data of Brock [31, 32] and

conclude that this confirms the importance of turbulent Reynolds stress for roll waves.

Experimental evidence has shown that roll waves are not fully periodic, and in fact the faster roll waves tend to catch up with and absorb the slower ones, forming longer and higher roll waves, see Alavian [4] and Mayer [123]. Hence, Kranenburg [112] derived an amplitude evolution equation for small amplitude roll waves starting from equations similar to those used by Needham and Merkin [131], which to second order gave a modified Burgers equation. This equation had previously been studied by Novik [138], who had postulated it as a model equation without giving a derivation. Unlike the Burgers equation, Novik [138] found this model equation allowed steady, periodic solutions if  $F > 2$ .

Through analytical methods, Kranenburg [112] found that periodic roll waves are unstable to a sub-harmonic disturbance, which grow and annihilate the roll waves producing a roll wave of larger size. Using numerical computations, he showed his theoretical results agreed with the observed tendency of faster roll waves catching slower ones to form longer and higher roll waves, as observed by Alavian [4] and Mayer [123]. However, he was unable to give a quantitative comparison with experimental results due to the sensitivity to initial conditions.

Many authors have ignored bottom topography when studying turbulent roll waves. However, real channels are never perfectly flat and the effects of boundary roughness may affect the transition from a laminar to a turbulent regime. The instability of laminar film flow over a wavy surface has been studied both theoretically, see Cabal et al. [33], Floryan [66], Selvarajan et al. [158], and experimentally, see Vlachogiannis and Bontozoglou [180]. Following these authors, Balmforth and Mandre [15] studied the shallow-water equations with bottom drag and viscosity for turbulent flow over uneven surfaces. They performed linear stability analysis and found that low-amplitude topography destabilised the flow and allowed roll waves to form for lower Froude numbers, while higher-amplitude topography has

a stabilising effect on the flow, which is consistent with observations of hydraulic engineers, see Montes [128] and Rouse [152]. When Balmforth and Mandre [15] considered intermediate topography, they found a new form of instability that extended down to much smaller Froude numbers. In these unstable windows the growth rate increased dramatically, however, they were unable to precisely resolve the growth rate behaviour for this case. They found that this singular behaviour coincided with the point the inviscid equilibrium formed a hydraulic jump.

Andritsos and Hanratty [9] found experimentally that when a multiphase flow is above the Kelvin-Helmholtz instability limit, small disturbances will grow and form into roll waves. As roll waves may annihilate each other forming larger roll waves in an open channel, as found by Kranenburg [112], this may result in a transition into a slug flow regime in a closed channel. Hence, by using periodic travelling wave theory in order to develop an understanding of roll waves in multiphase flow, an understanding of the characteristics behind the transition to slug flow may be uncovered, see Needham et al. [132].

### 1.2.5 *Computational Fluid Dynamics*

Due to improvements in computing power and numerical techniques, many authors made attempts to use the multi-field model in order to create slug tracking models which capture flow regime transitions, see De Leebeek and Nydal [48], Kjølås [103], Renault [149], Ujang et al. [178]. These models track the position of each slug front and its tail using a Lagrangian approach as the slugs flow through the pipe. The data gathered from this was then used in the mass and momentum flux calculations, see Bendiksen et al. [22] and Straume et al. [166], and led to the development of one of the earliest commercial codes for oil and gas pipelines, OLGA, by Bendiksen et al. [21, 24].

Barnea and Taitel [18] proposed a kinematic model to predict the slug length distribution at any specified point with the pipe. They based their model on the bubble overtaking mechanism which occurs when the slugs are shorter than the stable developed slug length. At the inlet they assumed a random distribution of short slugs, where the gas pocket behind each slug was assumed to be associated with the slug length using a valid relation for fully developed slug flow. They used both a normal and uniform distribution for their slug length inlet distribution and found that this initial distribution had no bearing on the slug characteristics further down the pipe. From their calculations they showed that, for fully developed slug flow, the mean slug length is approximately 1.5 times the minimum stable slug length and the maximum length is approximately 3 times the minimum slug length. Cook and Behnia [43] compared this model to experimental data they had taken and found the calculated mean slug lengths and slug distribution to be quite accurate over a range of flow rates.

Zheng et al. [194] added the liquid-phase mass balance on the model developed by Barnea and Taitel [18] in order to track individual slugs. By considering the effects of a changing pipe angle for both the case where each slug maintains its identity and the case where new slugs are generated and disappear, Zheng et al. [194] proposed a model that is capable of simulating the slug behaviour over a hilly terrain. They compared the predicted slug characteristics from their model to experimental data from Zheng [195] and Zheng et al. [196] and found the model's predictions to be quite good. However, they admitted that due to their model assuming the film thickness is constant in the tail following the slug their model is flawed, although it does capture the main characteristics of the physical behaviour of slugs over a hilly terrain.

Nydal and Banerjee [141] presented a Lagrangian slug tracking model, where the slugs were tracked as sharp gas-liquid fronts. Using the Lagrangian description, they considered the slugs and gas pockets to be computational units moving with independent front and tail velocities. The gas-liquid

interface between the slug and gas pocket are evaluated using conservation of mass and conservation of momentum. They ran simulations for both horizontal and hilly terrain pipes and compared their results to experimental data by Nydal and Banerjee [140], Nydal et al. [142], Schmidt et al. [157] and Van Hout et al. [179] and concluded their model gave reasonably good comparisons between the computed and measured values.

Taitel and Barnea [171] use the approach in Barnea and Taitel [18] with an emphasis on incorporating the true effects of the gas compressibility. They simplify their model by neglecting the time derivatives in the momentum equation, hence their model assumed a local equilibrium force balance for each slug unit. At the pipe inlet they set the slugs and gas pockets to have constant size and found that this periodic fluctuation of mass entering the pipe caused a periodic fluctuation on the pressure and slug velocity. Their results showed that the gas compressibility causes an increase in slug unit length, but only has a minor effect on the growth of the slugs as they propagate through the pipe. Al-Safran et al. [3] included liquid hold-up and the gas pocket overtaking mechanism in the model proposed by Taitel and Barnea [171] and extended it to hilly terrain, based on the Zheng et al. [194] model. Their model was compared to two hilly terrain experimental cases, for which they found an accuracy of  $\pm 7.7\%$  for the maximum slug length. Following this, Wang et al. [184] extended the model to include the wake effect and the pressure drop term due to liquid film acceleration. They studied the experimental slug length distributions in a horizontal pipe and found the predicted mean and maximum slug lengths were in agreement with the measured data from half way along their pipe. However, due to assuming a short minimum stable slug length in the model, the mean slug length was underestimated when compared with the measured data from near the outlet of their pipe.

An analysis of slug tracking models is given by Rosa et al. [151] who develop a new model incorporating all terms introduced in previous slug tracking models and includes the advection term, which had previously

been neglected. They compare numerical solutions to their model to experimental data, focusing on the slug tracking models ability to capture the physical flow features of the intermittent slug regime. They found that the major limitation of their model, and hence slug tracking models in general, was due to the lack of reliable slug inlet models and wake law.

Due to the limitation of slug tracking models as a result of needing prescribed flow velocities, slug lengths, liquid hold-up and slug frequency at the inlet, some authors have developed slug capturing models, see Ansari and Shokri [11], Du and Nydal [53], Figueiredo et al. [65], Holmås et al. [83], Kadri et al. [97]. This has led to the development of commercial codes such as LedaFlow, by Danielson et al. [46], which has been shown to be very accurate when compared to experimental data, see Kjolaas and Johansen [104], Kjolaas et al. [105]. These models require considerable computational effort to solve a system of conservation equations using a sufficiently small grid in order to accurately capture the dynamics of the slug fronts. Hence, multi-grid methods have been developed which allow different grid spacing to be used such that computational cost is kept to a minimum whilst still fully resolving the system, see Akselsen and Nydal [2]. In these models slug generation and development happens automatically from the model itself, without the need for slug statistics or assumptions.

Bonizzi et al. [28] developed a model for slow transients in oil-gas pipes using four fields: continuous liquid, dispersed liquid, continuous gas and dispersed gas. By performing experiments and using the data of Andritsos et al. [10], Bendiksen [23], Lioumbas et al. [117] and Nydal et al. [142] they found their model to be valid for first order effects, such as flow structure evolution and transitions.

Issa and Kempf [87] developed a one-dimensional form of the two-fluid model by integrating the equations for conservation of mass and conservation of momentum for each phase over the cross-sectional area of the pipe. They computed numerous simulations and compared their predicted flow regime type against the flow regime maps of Taitel and Dukler [172]

for horizontal flow and Manolis [118] and Manolis et al. [119] for downward inclined flow, finding good agreement in both cases. They go on to compare their predicted slug frequencies against the experimental data of Manolis [118] and Manolis et al. [120], for which they are within the typical bound of experimental scatter. Finally, they compare their predicted slug body lengths against the data of Dukler and Hubbard [54], Dukler et al. [57] and Nydal et al. [142] and found their numerical calculations were well within the scattered data. Further, Issa et al. [89] compared solutions from the model to experiments for both hydrodynamic and severe slugging including terrain undulations and found excellent agreement.

Kjeldby et al. [102] developed a hybrid slug capturing and tracking scheme such that slug initiation can be captured from unstable stratified flow using a sufficiently fine grid and directly solving a two-fluid model, from a stratified flow stability criterion or from slug existence criterion. Previous slug capturing models, such as those by Issa and Kempf [87] and Bonizzi et al. [28], rely on a fine grid spacing in order to resolve sharp discontinuities in hold-up at bubble noses and slug fronts. However, Kjeldby et al. [102] used a Lagrangian model which allows them to track slug fronts using a moving grid and eliminates numerical diffusion at discontinuities. They compare their model to four experimental cases and found good correspondence with their numerical simulations.

In order to develop models which are computationally cost effective, many authors use a one-dimensional formulation. However, by doing so they lose information of cross-sectional variations and transfer of mass, momentum and energy are filtered out, which means that important interactions are lost in this process. This has led to the development of quasi three-dimensional models, see Danielson et al. [46], Johansen et al. [94], Mo et al. [127], Razavi and Namin [148], Simões et al. [160], whereby a three-dimensional method is averaged down to two-dimensions. These models have been shown to be in good agreement with experiments and give details on flow regimes and regime transitions missed by one-dimensional models.

In the Issa and Kempf [87] model, the only empirical information required is for the shear stresses, which are evaluated using friction factor correlations. They, similarly to other authors who have developed slug capturing models, investigated the effects on their numerical results for several correlations. They found that the correlation used had a large effect on the accuracy of their results when compared to the experimental data and chose the correlation which gave them the closest match. As a result, it is unknown whether it will still provide a close match if compared to different data sets than those used, or if it will require a different friction factor correlation to be selected. Hence, for our model, we will use the correlations proposed by Colebrook et al. [42] and Taitel and Dukler [173] for the wall and interfacial shear, respectively, as these are the industry standard in multiphase pipe flow engineering.

Further, due to the complexity of the model proposed by Issa and Kempf [87], they are unable to perform an analytic analysis of the system and only provide numerical results. We will use a simpler model, such as using a channel rather than a cylindrical pipe, such that we are able to investigate the system analytically to gain an understanding of the influencing factors that cause the transition to a slug flow regime.

### ***1.2.6 The Development of Slugging in Two-Layer Hydraulic Flows***

Needham et al. [132] derived the one-dimensional governing equations for hydraulic flow of a gas over a liquid inside a closed, rectangular, infinitely wide channel. They began with the depth-averaged hydraulic equations of motion (see Dressler [50], Dressler and Pohle [52], Needham and Merkin [131], Stoker [165], Whitham [187]) combined with the Chézy formula for turbulent friction and an appropriate eddy viscosity term in each layer to account for the streamwise turbulent viscosity. They also neglected the inertia terms in the gas layer relative to the inertia terms in the liquid layer since the density ratio of the gas to the liquid is small. By combining

and non-dimensionalising these equations and taking the small liquid layer limit, they arrived at the non-dimensional equations of motion

$$h_t + (hv)_x = 0, \quad (1.2.61)$$

$$v_t + vv_x + \frac{1-\rho}{F_0^2} h_x = \frac{1}{1+\lambda} + \frac{\lambda}{(1+\lambda)h} - \frac{v^2}{h} + \frac{1}{R_l h} [hv_x]_x, \quad (1.2.62)$$

subject to the steady-state solution

$$h = 1, \quad v = 1, \quad (1.2.63)$$

where  $\rho$  is the ratio of gas-to-liquid density,  $F_0$  is the Froude number,  $\lambda$  is a measure of the interfacial to flow resistance and  $R_l$  is the effective Reynolds number for the liquid.

They linearised their equations by considering

$$h(x, t) = 1 + \bar{h}(x, t), \quad v(x, t) = 1 + \bar{v}(x, t), \quad (1.2.64)$$

where  $\bar{h}, \bar{v} \ll 1$ , and investigated the evolution of a small-amplitude disturbance to the uniform flow. Using the stability criterion on the wave speeds, given by Whitham [187], they found their stability criterion

$$F_0 < 2(1+\lambda)\sqrt{1-\rho} \equiv F_c. \quad (1.2.65)$$

From which they concluded that small disturbances to the uniform flow will decay for  $F_0 < F_c$ , but grow for  $F_0 > F_c$ , in which case the flow may evolve into a slug flow regime.

They conjectured that, when  $F_0 > F_c$ , the flow would develop into a temporally periodic state, hence investigated the existence of periodic travelling wave solutions. By introducing a travelling co-ordinate they found three equilibrium points,  $H_1, H_2$  and  $H_3$ , where  $H_1 < H_2 < H_3$ , which are a stable node/spiral, a saddle and a node/spiral, respectively. They concluded, using bifurcation theory, that for each  $F_0 > F_c$  there exists a two-parameter

family of periodic travelling wave solutions which began at small amplitude from a Hopf bifurcation on  $H_3$  and grew in size as the propagation speed was increased, until they ended in a homoclinic bifurcation with  $H_2$ .

Finally, they investigated numerically how small disturbances to the uniform flow grew when  $F_0 > F_c$  using periodic boundary conditions. They found that for values of  $F_0$  close to  $F_c$ , the wavelength of the state that develops is close to the predicted linearly most unstable wavelength. However, after a long enough time, the growth, which is driven by non-linear processes, led the solution whose wavelength is considerably larger than the linearly most unstable wavelength. By varying their parameters, they found that the further  $F_0$  is away from  $F_c$  the quicker these non-linear processes dominate the growth.

Needham et al. [132] used the assumption that the layer of liquid is small. In this thesis we extend the work studied by Needham et al. [132] to liquid layers of arbitrary thickness which results in significantly different results, particularly when considering solutions for which the surface of the liquid is near the top of the channel.

### 1.3 THESIS OUTLINE

The aim of this thesis is to investigate the causes of the transition from a stratified flow regime to a slug flow regime and to examine the characteristics of these slugs when they have formed. Although subsea natural gas pipelines consist of cylindrical pipes, for simplicity, we will consider the flow through a semi-infinite closed rectangular channel. In order to do this, we will derive a tractable one dimensional system of equations governing the flow in the gas and liquid layers for multiphase flow. These will be simplified using the long wavelength approximation, depth-averaged velocity and Chézy coefficients for the wall and interfacial shear. By combining and non-dimensionalising these equations, we will be left with a system of two equations governing the flow, driven by prescribed, constant, upstream

flow rates in each layer. By considering the values of the dimensional parameters in subsea natural gas pipelines, we will provide the typical ranges for our non-dimensional parameters.

In Chapter 3, we will use linear stability theory to investigate how small-amplitude disturbances affect the uniform flow. This leads to a stability condition, for which small-amplitude disturbances to the uniform flow decay, and a non-hyperbolic condition, for which the model is ill-posed. We will then investigate the solution of our linearised equations for a single mode of spatial wave number in order to investigate how fast different wavelengths grow. From this we will find the neutral curve, for which small disturbances will neither grow nor decay and a maximum growth rate curve.

Once these disturbances begin to grow, they become dominated by non-linear effects and we expect them to form into roll waves, hence in Chapter 4 we investigate the existence of periodic travelling wave solutions. This will be done by introducing a travelling co-ordinate which simplifies our governing equations into one equation for one variable. By considering the equilibrium points of this equation we will find two equilibrium points that vanish in the previously studied limit,  $\epsilon \rightarrow 0$ , which come into existence near the top of the channel. Using asymptotic analysis, we deduce that one is a saddle and the other is a node or spiral where Hopf bifurcations may occur.

Using MATLAB routines `ode45` and `bvp5c` to solve our equations numerically, we will find high amplitude periodic solutions. By investigating the phase portraits of these solutions we find the possibility of multiple Hopf, homoclinic and periodic saddle-node bifurcations occurring, resulting in several regions in which periodic solutions can exist and which contain both stable and unstable limit cycle solutions. Due to the number of parameters and the extremely complicated nature of the phase planes, we find it infeasible to provide an exhaustive catalogue of possibilities. However, our investigation of periodic travelling wave solutions will give us some insight into how the parameters affect the system and show that slugs can exist.

In Chapter 5, we use a finite-difference method derived by Kurganov and Tadmor [114] which we combine with a second-order Runge-Kutta method to solve our governing equations as an initial value problem. We will set the initial condition to be the uniform flow and use some small amplitude random noise at the inlet and an outlet in order to simulate flow through a channel. By running simulations we will find parameter sets that result in slug flow regimes, from which we can observe how slugs form and the affects of the parameters on their growth.

Finally, in Chapter 6, we will consider the effects of bottom topography in the thin layer limit. We first consider the existence of periodic travelling wave solutions for constant channel inclination,  $\theta$ , and find that Hopf bifurcations can exist for  $B < 0$  and  $B > 0$ , whereas for the horizontal case it had only been possible for  $B < 0$ . We will then solve this system as an initial value problem and compare our solutions with those from the horizontal case in order to evaluate the effects of the channel inclination.

We will conclude this chapter by solving the governing equations as an initial value problem for an undulating topography. By considering the steady state solution of the system, we will examine how the height of the layer of liquid changes with the angle of the channel. We will then consider the effects of having either a downhill or uphill section of channel before a flat section, which we will compare to the horizontal case.

---

## THE HYDRAULIC MODEL

---

We will describe the flow of the liquid and gas through the channel in terms of a two-dimensional Cartesian co-ordinate system  $(x, y)$  with  $y$  pointing vertically upwards, perpendicular to the channel walls located at  $y = 0$  and  $y = a > 0$ , and with  $x$  measuring the distance along the channel in the streamwise direction. A layer of liquid will flow along the bottom of the channel whose free surface will be at  $y = h(x, t)$ , with  $t$  being time, as shown in Figure 2.1.

In the liquid we will denote the horizontal velocity as  $u_l(x, y, t)$ , the vertical velocity as  $v_l(x, y, t)$ , the pressure as  $p_l(x, y, t)$ , the constant density as  $\rho_l$  and the constant eddy viscosity as  $\mu_l$ . Similarly, in the gas for  $u_g(x, y, t)$ ,  $v_g(x, y, t)$ ,  $p_g(x, y, t)$ ,  $\rho_g$  and  $\mu_g$ . The acceleration due to gravity will be denoted by  $g$ .

Short wavelength instabilities have been investigated by Andritsos et al. [10] who found they play a crucial role in the development of slugs forming in flow with very high viscosity. Further, Fan et al. [61] observed in experiments that short wavelength instabilities lead to a transition to a slug flow regime for low superficial gas velocities. However, in subsea natural gas pipelines, the flow has neither very high viscosities nor low superficial gas velocity, hence we expect slugs to form due to long wavelength instabilities (see, for example, Andritsos [7], Barnea and Taitel [19], Kordyban [108], Mishima and Ishii [126], Taitel and Dukler [172]) as observed in the experiments by Fan et al. [61]. Further, viscous long wavelength theory, as

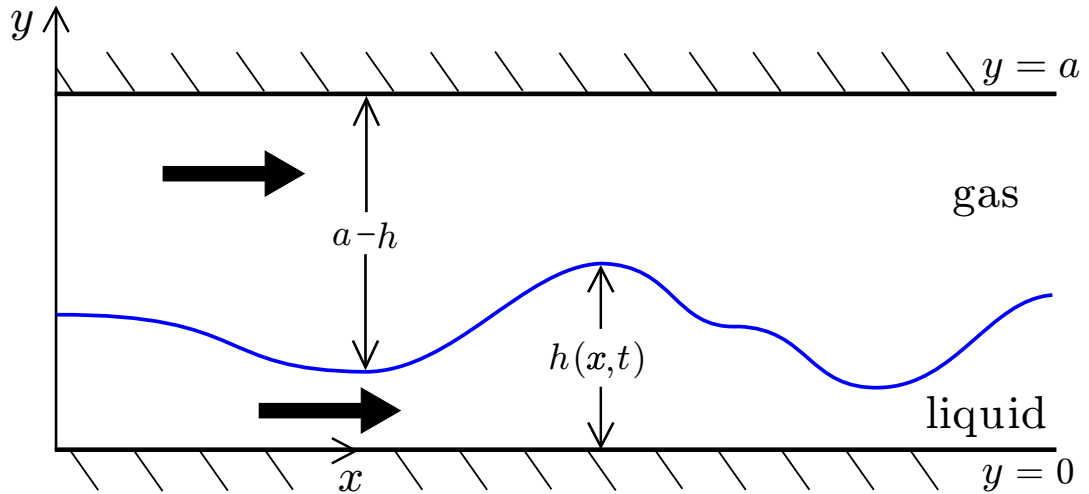


Figure 2.1.: The co-ordinate system.

studied by authors such as Lin and Hanratty [115] and Wu et al. [189], has been shown to accurately predict the transition from stratified flow to roll waves and the formation of slugs (see, for example, Soleimani and Hanratty [163], Woods et al. [188]). Hence, it is generally accepted that long wavelength instabilities cause the onset of slugging in horizontal and near horizontal pipes (Nieckele et al. [135]) and the use of a long wavelength assumption in the modelling of multiphase flow in order to investigate the transition to slug flow is both widely accepted and commonly used (see, for example, Kadri et al. [97], Nieckele et al. [135], Sanchis et al. [154]).

When a long wavelength assumption is used the model still retains some elements of the original system and solutions may eventually try to escape the long wavelength expansion. This may lead to the IVP being ill-posed due to short wavelength instabilities whereby the long wavelength assumption is invalid. However, in this case it is expected that the flow regime would change to bubble flow and hence does not detract from the models ability to investigate the development of slugging.

We will use a long wavelength assumption, conservation of mass, conservation of momentum, depth-averaged velocity and Chézy coefficients for the wall and interfacial shear to derive the governing equations of motion

for two-layer hydraulic flow through a semi-infinite channel, which we will then non-dimensionalise. Finally, we will discuss typical values for the parameters and what they mean in terms of our non-dimensional parameters.

## 2.1 CONSERVATION OF MASS

Starting from the two-dimensional continuity equation for incompressible fluid

$$\frac{\partial u_l}{\partial x} + \frac{\partial v_l}{\partial y} = 0, \quad (2.1.1)$$

and integrating with respect to  $y$  using Leibniz' integration rule and  $v_l|_{y=0} = 0$ , we have

$$\frac{\partial}{\partial x} \left( \int_0^h u_l \, dy \right) + v_l|_{y=h} - u_l|_{y=h} \frac{\partial h}{\partial x} = 0. \quad (2.1.2)$$

At the interface  $F \equiv h(x, t) - y = 0$ , hence

$$\frac{DF}{Dt} \equiv \frac{\partial h}{\partial t} + u_l|_{y=h} \frac{\partial h}{\partial x} - v_l|_{y=h} = 0. \quad (2.1.3)$$

Finally, combining (2.1.2) and (2.1.3) along with the definition

$$\bar{u}_l = \frac{1}{h} \int_0^h u_l \, dy, \quad (2.1.4)$$

of the horizontal depth averaged velocity in the liquid, results in

$$h_t + [h\bar{u}_l]_x = 0. \quad (2.1.5)$$

Similarly, in the gas

$$[a - h]_t + [(a - h)\bar{u}_g]_x = 0, \quad (2.1.6)$$

where  $\bar{u}_g$  is the horizontal depth averaged velocity in the gas defined as

$$\bar{u}_g = \frac{1}{a - h} \int_h^a u_g \, dy. \quad (2.1.7)$$

Adding (2.1.5) and (2.1.6), and integrating with respect to  $x$  gives us

$$(a - h)\bar{u}_g + h\bar{u}_l = A(t). \quad (2.1.8)$$

By letting  $A(t) = au_h$ , where  $u_h = u_h(t)$  is the homogeneous velocity, (2.1.8) becomes

$$(a - h)\bar{u}_g + h\bar{u}_l = au_h, \quad (2.1.9)$$

which re-arranges to

$$\bar{u}_g = \frac{au_h - h\bar{u}_l}{a - h}. \quad (2.1.10)$$

## 2.2 CONSERVATION OF MOMENTUM

We begin with the Navier-Stokes equation

$$\rho \left( \frac{\partial \mathbf{v}}{\partial t} + \mathbf{v} \cdot \nabla \mathbf{v} \right) = \mathbf{f} - \nabla p + \mu \nabla^2 \mathbf{v}. \quad (2.2.1)$$

We assume that  $y$  scales with  $a$  and  $x$  scales with  $L_x$ , where  $L_x$  is a typical wavelength, and  $L_x \gg a$ . Order of magnitude estimates from the continuity equation imply that  $v \sim \frac{a}{L_x}u$ , and so

$$v \ll u. \quad (2.2.2)$$

Since  $v$  is small, the vertical momentum equation is dominated by the pressure and gravity terms, hence the vertical momentum equation in the liquid is simply

$$\frac{\partial p_l}{\partial y} = -\rho_l g, \quad (2.2.3)$$

which integrates to

$$p_l = -\rho_l g y + \bar{p}_l(x, t). \quad (2.2.4)$$

Similarly, in the gas

$$p_g = -\rho_g g y + \bar{p}_g(x, t). \quad (2.2.5)$$

Due to continuity of pressure at  $y = h$ , we must have

$$p_l|_{y=h} = p_g|_{y=h}, \quad (2.2.6)$$

hence

$$\bar{p}_l - \bar{p}_g = gh(\rho_l - \rho_g). \quad (2.2.7)$$

We have the horizontal momentum equation in conservative form in the liquid as

$$\rho_l \left( \frac{\partial u_l}{\partial t} + \frac{\partial}{\partial x}(u_l^2) + \frac{\partial}{\partial y}(u_l v_l) \right) = -\frac{\partial p}{\partial x} + \mu_l \left( \frac{\partial^2 u_l}{\partial x^2} + \frac{\partial^2 u_l}{\partial y^2} \right). \quad (2.2.8)$$

By integrating with respect to  $y$  and using Leibniz' integration rule, (2.2.8) becomes

$$\begin{aligned} & \rho_l \left( \frac{\partial}{\partial t} \int_0^h u_l \, dy - u_l|_{y=h} \frac{\partial h}{\partial t} + \frac{\partial}{\partial x} \int_0^h u_l^2 \, dy - u_l^2|_{y=h} \frac{\partial h}{\partial x} + u_l|_{y=h} v_l|_{y=h} \right) \\ &= -\frac{\partial}{\partial x} \int_0^h p_l \, dy + p_l|_{y=h} \frac{\partial h}{\partial x} + \mu_l \left( \frac{\partial}{\partial x} \int_0^h \frac{\partial u_l}{\partial x} \, dy - \frac{\partial u_l}{\partial x} \Big|_{y=h} \frac{\partial h}{\partial x} + \left[ \frac{\partial u_l}{\partial y} \right]_0^h \right), \end{aligned} \quad (2.2.9)$$

which, by (2.1.3), (2.1.4), (2.2.4) and (2.2.6) and by assuming a close to uniform velocity profile, hence we let  $u_l^2 = \bar{u}_l^2$ , gives us

$$\begin{aligned} & \rho_l \left( [h\bar{u}_l]_t + [h\bar{u}_l^2]_x \right) \\ &= \rho_l g h h_x - [\bar{p}_l h]_x + h_x p_g|_{y=h} + \mu_l [h\bar{u}_l]_x + \mu_l \left( \left[ \frac{\partial u_l}{\partial y} \right]_0^h - h_x \frac{\partial u_l}{\partial x} \Big|_{y=h} \right). \end{aligned} \quad (2.2.10)$$

The effective stresses are dominated by the shear stresses

$$\tau_i = \mu_l \left. \frac{\partial u_l}{\partial y} \right|_{y=h}, \quad (2.2.11)$$

$$\tau_l = \mu_l \left. \frac{\partial u_l}{\partial y} \right|_{y=0}, \quad (2.2.12)$$

which, as discussed in Subsection 1.2.3, may be modelled using empirical correlations in order to simplify our model and make our analysis easier. Therefore, we will express the shear stresses in terms of the well-established Chézy formula for turbulent flow resistance (see Stoker [165]). Hence, (2.2.10) becomes

$$\begin{aligned} & \rho_l \left( [h\bar{u}_l]_t + [h\bar{u}_l^2]_x \right) \\ &= \rho_l g h h_x - [\bar{p}_l h]_x + h_x p_g|_{y=h} + [\mu_l h \bar{u}_{lx}]_x - \rho_l c_l \bar{u}_l^2 - \rho_l c_l^l (\bar{u}_l - \bar{u}_g) |\bar{u}_l - \bar{u}_g|, \end{aligned} \quad (2.2.13)$$

where  $c_l$  is the dimensionless Chézy coefficient associated with wall roughness between the channel wall and the liquid, while  $c_l^l$  is the dimensionless Chézy coefficient associated with the shear roughness between the gas and liquid at the interface. Similarly for  $c_g$  and  $c_l^g$  for the gas layer.

By (2.2.5) and (2.2.7) we see that

$$\rho_l g h h_x - [\bar{p}_l h]_x + h_x p_g|_{y=h} = -h \bar{p}_{lx}, \quad (2.2.14)$$

hence (2.2.13) reduces to

$$\rho_l \left( [h\bar{u}_l]_t + [h\bar{u}_l^2]_x \right) = -h \bar{p}_{lx} - \rho_l c_l \bar{u}_l^2 - \rho_l c_l^l (\bar{u}_l - \bar{u}_g) |\bar{u}_l - \bar{u}_g| + [\mu_l h \bar{u}_{lx}]_x, \quad (2.2.15)$$

and, similarly, in the gas we have

$$\rho_g \left( [(a-h)\bar{u}_g]_t + [(a-h)\bar{u}_g^2]_x \right)$$

$$= -(a-h)\bar{p}_{gx} - \rho_g c_g \bar{u}_g^2 - \rho_g c_l^g (\bar{u}_g - \bar{u}_l) |\bar{u}_g - \bar{u}_l| + [\mu_g(a-h)\bar{u}_{gx}]_x. \quad (2.2.16)$$

Continuity of interfacial shear requires that

$$\rho_l c_l^l = \rho_g c_l^g. \quad (2.2.17)$$

Hence by combining (2.2.15) and (2.2.16) and using (2.1.10) and (2.2.17) and dropping the bars from  $\bar{u}$  for convenience, we have the equations of motion as

$$h_t + [hu_l]_x = 0, \quad (2.2.18)$$

$$\begin{aligned} & \left( \rho_l + \frac{\rho_g h}{a-h} \right) u_{lt} + \left( \rho_l u_l + \frac{\rho_g h [2au_h - (a+h)u_l]}{(a-h)^2} \right) u_{lx} \\ & + \left( (\rho_l - \rho_g)g - \rho_g \frac{a^2(u_h - u_l)^2}{(a-h)^3} \right) h_x = -\frac{\rho_l c_l u_l^2}{h} + \frac{\rho_g c_g (au_h - hu_l)^2}{(a-h)^3} \\ & + \frac{a^3 \rho_g c_l^g}{h(a-h)^3} (u_h - u_l) |u_h - u_l| + \frac{\mu_l}{h} [hu_{lx}]_x - \frac{\mu_g}{a-h} \left[ \frac{a(u_h - u_l)}{a-h} h_x - hu_{lx} \right]_x. \end{aligned} \quad (2.2.19)$$

### 2.3 NON-DIMENSIONAL EQUATIONS OF MOTION

We will assume there exists an equilibrium at  $h = h_0$ ,  $u_l = u_l^0$  and  $u_g = u_g^0$  where  $h_0$ ,  $u_l^0$  and  $u_g^0$  are positive constants and hence, from (2.1.9),  $u_h$  is a positive constant. We will now use the scales

$$h = h_0 h', \quad u_l = u_l^0 v, \quad x = \frac{h_0}{c_l} x', \quad t = \frac{h_0}{c_l u_l^0} t', \quad (2.3.1)$$

and dimensionless parameters

$$\delta = \frac{u_l^0}{u_h}, \quad \rho = \frac{\rho_g}{\rho_l}, \quad \epsilon = \frac{h_0}{a}, \quad F_0 = \frac{u_l^0}{\sqrt{g h_0}},$$

$$R_l = \frac{h_0 p_l u_l^0}{\mu_l c_l}, \quad R_g = \frac{h_0 \rho_g u_l^0}{\mu_g c_l}, \quad \lambda = \frac{c_l^g}{c_g} \frac{a}{h_0}. \quad (2.3.2)$$

Note that as the flow is driven by imposed pressure in the gas we expect the velocity of the gas to be greater than that of the liquid, so we shall assume  $u_g^0 \geq u_h \geq u_l^0$ . Combining this with  $0 \leq h_0 \leq a$  we have  $0 \leq \epsilon, \delta \leq 1$  and recall that we must have  $L_x = \frac{h_0}{c_l} \gg a$ , which re-arranges to  $\epsilon \gg c_l$ . We will see in Subsection 2.4 that  $c_l$  is of order  $10^{-3}$ , hence  $L_x \gg a$  for  $\epsilon \gg 10^{-3}$ .

Substituting (2.3.1) and (2.3.2) into (2.2.18) and (2.2.19) (and dropping primes for convenience) gives

$$h_t + [hv]_x = 0, \quad (2.3.3)$$

$$\begin{aligned} & \left(1 + \frac{\rho \epsilon h}{1 - \epsilon h}\right) v_t + \left(v + \frac{\rho \epsilon h [2 - (1 + \epsilon h) \delta v]}{\delta (1 - \epsilon h)^2}\right) v_x \\ & \quad + \left(\frac{1 - \rho}{F_0^2} - \frac{\rho \epsilon (1 - \delta v)^2}{\delta^2 (1 - \epsilon h)^3}\right) h_x \\ & = -\frac{v^2}{h} + \frac{\rho c_l^g}{\delta^2 c_l} \left(\frac{(1 - \epsilon \delta h v)^2}{\lambda (1 - \epsilon h)^3} + \frac{(1 - \delta v) |1 - \delta v|}{h (1 - \epsilon h)^3}\right) \\ & \quad + \left(\frac{1}{h R_l} + \frac{\rho \epsilon}{(1 - \epsilon h) R_g}\right) [hv_x]_x - \frac{\rho \epsilon}{\delta (1 - \epsilon h) R_g} \left[\frac{1 - \delta v}{1 - \epsilon h} h_x\right]_x, \end{aligned} \quad (2.3.4)$$

subject to a steady state solution at

$$h = 1, \quad v = 1. \quad (2.3.5)$$

Substituting (2.3.5) into (2.3.4) and rearranging gives

$$\frac{\rho c_l^g}{\delta^2 c_l} = \frac{\lambda (1 - \epsilon)^3}{(1 - \epsilon \delta)^2 + \lambda (1 - \delta)^2}, \quad (2.3.6)$$

which when substituted back into (2.3.4) gives the dimensionless equations of motion as

$$h_t + [hv]_x = 0, \quad (2.3.7)$$

$$\begin{aligned}
 & \left(1 + \frac{\rho\epsilon h}{1 - \epsilon h}\right) v_t + \left(v + \frac{\rho\epsilon h[2 - (1 + \epsilon h)\delta v]}{\delta(1 - \epsilon h)^2}\right) v_x \\
 & \quad + \left(\frac{1 - \rho}{F_0^2} - \frac{\rho\epsilon(1 - \delta v)^2}{\delta^2(1 - \epsilon h)^3}\right) h_x \\
 = & -\frac{v^2}{h} + \frac{(1 - \epsilon)^3}{(1 - \epsilon\delta)^2 + \lambda(1 - \delta)^2} \left(\frac{(1 - \epsilon\delta h v)^2}{(1 - \epsilon h)^3} + \frac{\lambda(1 - \delta v)|1 - \delta v|}{h(1 - \epsilon h)^3}\right) \\
 & + \left(\frac{1}{hR_l} + \frac{\rho\epsilon}{(1 - \epsilon h)R_g}\right) [hv_x]_x - \frac{\rho\epsilon}{\delta(1 - \epsilon h)R_g} \left[\frac{1 - \delta v}{1 - \epsilon h} h_x\right]_x. \quad (2.3.8)
 \end{aligned}$$

If we assume the height of the liquid at the inlet is much less than the channel height and its velocity is much less than that of the gas, hence let  $\epsilon \rightarrow 0$  and  $\delta \rightarrow 0$  in (2.3.8), and assume  $\epsilon \ll \delta^2$ , then (2.3.8) becomes

$$v_t + v v_x + \frac{1 - \rho}{F_0^2} h_x = -\frac{v^2}{h} + \frac{1}{1 + \lambda} \left(1 + \frac{\lambda}{h}\right) + \frac{1}{hR_l} [hv_x]_x, \quad (2.3.9)$$

which was derived and analysed by Needham et al. [132].

## 2.4 PARAMETER VALUES

Table 2.1 shows the typical ranges of the real parameters, where  $\bar{\mu}_l$  and  $\bar{\mu}_g$  are the dynamic viscosities of the liquid and gas respectively, for natural gas pipelines.

In order to express these in terms of our non-dimensional parameters we need to calculate the values of our non-dimensional Chézy coefficients. The dimensional Chézy coefficient for the liquid,  $C_l$ , is related to the Darcy friction coefficient associated with wall roughness between the channel wall and the liquid,  $f_l$ , by

$$C_l = \sqrt{8g/f_l}, \quad (2.4.1)$$

(see, for example, Hanif Chaudhry [78]). It is common practise in multiphase pipe flow engineering to use the correlation proposed by Colebrook et al. [42] for the wall shear and the Taitel and Dukler [173] correlation for inter-

Parameter	Range			Units
$a$	0.5	→	1.2	m
$u_l^0$	0	→	10	m/s
$u_g^0$	4	→	20	m/s
$\rho_l$	700	→	800	kg/m <sup>3</sup>
$\rho_g$	60	→	185	kg/m <sup>3</sup>
$\bar{\mu}_l$	$5.5 \times 10^{-4}$	→	$6.5 \times 10^{-4}$	Pa·s
$\bar{\mu}_g$	$1 \times 10^{-5}$	→	$2 \times 10^{-5}$	Pa·s
Pipe Length	1	→	1,200	km

**Table 2.1.:** The typical ranges of the dimensional parameters.

facial shear, hence these are the models we shall use in our work. The Colebrook equation for the Darcy friction factor is found by solving

$$\frac{1}{\sqrt{f_l}} = -2 \log_{10} \left( \frac{\epsilon/D}{3.7} + \frac{2.51}{\text{Re}_l \sqrt{f_l}} \right), \quad (2.4.2)$$

where  $\text{Re}_l$  is the Reynolds number of the liquid and  $\text{Re}_l = \rho_l h u_l / \bar{\mu}_l$  for dynamic viscosity  $\bar{\mu}_l$ . Noting that  $C_l = \sqrt{g/c_l}$ , it is clear from (2.4.1) that  $c_l = f_l/8$ , hence (2.4.2) becomes

$$\frac{1}{\sqrt{c_l}} = -4\sqrt{2} \log_{10} \left( \frac{\epsilon/D}{3.7} + \frac{0.6275\sqrt{2}}{\text{Re}_l \sqrt{c_l}} \right). \quad (2.4.3)$$

$c_l$  does not vary much for changes to  $\text{Re}_l$  or  $\epsilon/D$ , shown in Figure 2.2, hence we will take it to be constant through the channel and it will be calculated from the uniform flow by solving

$$\frac{1}{\sqrt{c_l}} = -4\sqrt{2} \log_{10} \left( \frac{\epsilon/D}{3.7} + \frac{0.6275\sqrt{2}\bar{\mu}_l}{\rho_l h_0 u_l^0 \sqrt{c_l}} \right). \quad (2.4.4)$$

Similarly,  $c_g$  is found by solving

$$\frac{1}{\sqrt{c_g}} = -4\sqrt{2} \log_{10} \left( \frac{\epsilon/D}{3.7} + \frac{0.6275\sqrt{2}\bar{\mu}_g}{\rho_g(a-h_0)u_g^0 \sqrt{c_g}} \right). \quad (2.4.5)$$

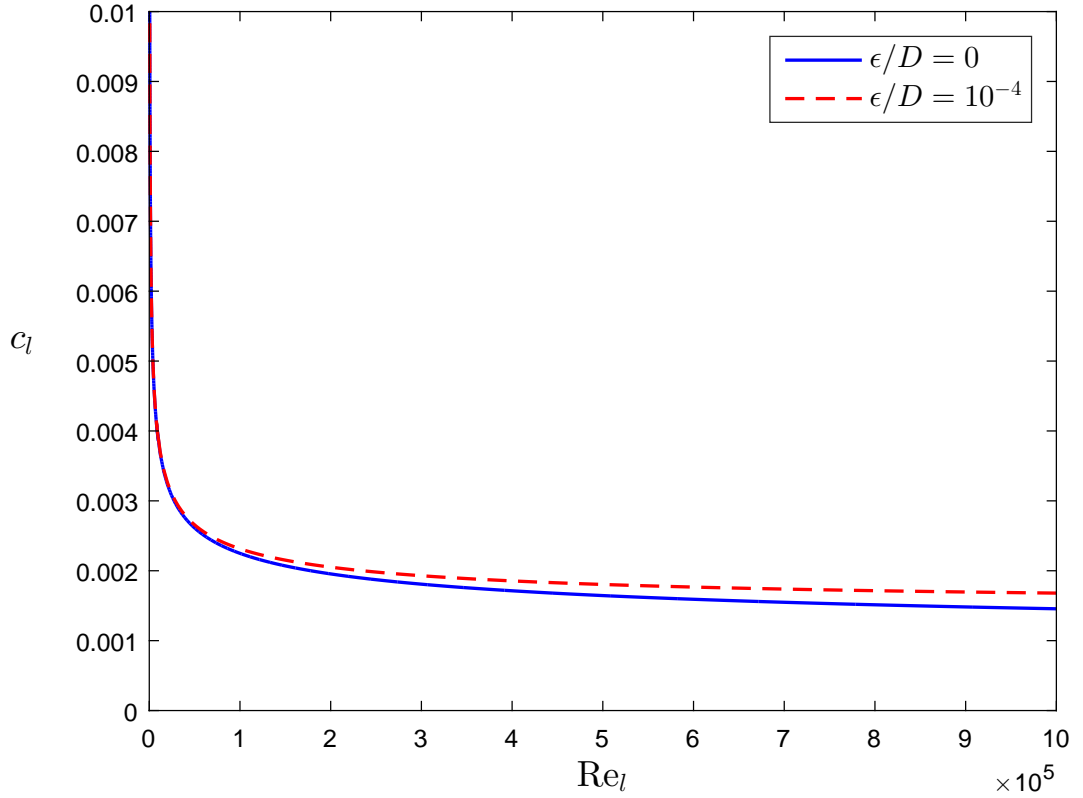


**Figure 2.2.:** A comparison of  $Re_l$  against  $c_l$  from (2.4.3).

The Taitel and Dukler [173] interfacial friction factor correlation is given by

$$f_i = \frac{0.184}{Re_i^{0.2}}, \quad (2.4.6)$$

where  $Re_i = \rho_g(a - h)(u_g - u_l) / \bar{\mu}_g$ . Again we will calculate this from the uniform flow, hence the equation for the non-dimensional interfacial Chézy coefficient is given by

$$c_l^g = 0.023 \left( \frac{\rho_g(a - h_0)(u_g^0 - u_l^0)}{\bar{\mu}_g} \right)^{-0.2}. \quad (2.4.7)$$

Using the values from Table 2.1 and varying  $\epsilon/D$  we find that  $1 \times 10^{-3} < c_l < 5 \times 10^{-3}$ ,  $0.7 \times 10^{-3} < c_g < 1.8 \times 10^{-3}$  and  $0.1 \times 10^{-3} < c_l^g < 1.1 \times 10^{-3}$ . We can now calculate the ranges of our non-dimensional parameters, which are shown in Table 2.2. Note that although we are concerned with highly

Parameter	Range		
$\epsilon$	0.01	→	0.2
$\delta$	0.1	→	1
$F_0$	1	→	50
$\rho$	0.075	→	0.125
$\lambda$	0.1	→	100
$R_l$	1	→	100
$R_g$	1	→	100

**Table 2.2.:** The typical ranges of the non-dimensional parameters.

turbulent flow ( $Re_l \approx 10^5$  and  $Re_g \approx 10^7$ ), our effective Reynolds numbers,  $R_l$  and  $R_g$ , are considerably smaller.

## 2.5 CONCLUSION

By using conservation of mass, conservation of momentum we have derived the governing equations of motion for two layer hydraulic flow through a semi-infinite channel, which we then non-dimensionalised. In order to do this we used the long wavelength assumption, depth-averaged velocity and expressed shear stresses through non-dimensional Chézy coefficients. Finally, we discussed typical values for the parameters and a method for calculating our Chézy coefficients which allowed us to express what our parameters mean in terms of our non-dimensional parameters.

# 3

---

## LINEARISED STABILITY OF THE UNIFORM FLOW

---

We wish to investigate how small-amplitude disturbances affect the uniform equilibrium flow in order to examine the possibility of slug flow developing. Thus, we write

$$h = 1 + \bar{h}, \quad v = 1 + \bar{v}, \quad (3.0.1)$$

where  $\bar{h}, \bar{v} \ll 1$ . On substituting (3.0.1) into (2.3.7) and (2.3.8) we obtain, at leading order, the linearised evolution equations

$$\bar{h}_t + [\bar{h} + \bar{v}]_x = 0, \quad (3.0.2)$$

$$\begin{aligned} & \left(1 + \frac{\rho\epsilon}{1-\epsilon}\right) \bar{v}_t + \left(1 + \frac{\rho\epsilon[2 - (1+\epsilon)\delta]}{\delta(1-\epsilon)^2}\right) \bar{v}_x + \left(\frac{1-\rho}{F_0^2} - \frac{\rho\epsilon(1-\delta)^2}{\delta^2(1-\epsilon)^3}\right) \bar{h}_x \\ &= -2\bar{v} + \bar{h} + \frac{(1-\epsilon)^3}{(1-\epsilon\delta)^2 + \lambda(1-\delta)^2} \left(\frac{3\epsilon(1-\epsilon\delta)^2}{(1-\epsilon)^4} \bar{h} - \frac{2\epsilon\delta(1-\epsilon\delta)}{(1-\epsilon)^3} (\bar{h} + \bar{v})\right) \\ & \quad - \frac{2\lambda\delta(1-\delta)}{(1-\epsilon)^3} \bar{v} + \frac{3\epsilon\lambda(1-\delta)^2}{(1-\epsilon)^4} \bar{h} - \frac{\lambda(1-\delta)^2}{(1-\epsilon)^3} \bar{h} + \left(\frac{1}{R_l} + \frac{\rho\epsilon}{(1-\epsilon)R_g}\right) \bar{v}_{xx} \\ & \quad - \frac{\rho\epsilon(1-\delta)}{\delta(1-\epsilon)^2 R_g} \bar{h}_{xx}. \quad (3.0.3) \end{aligned}$$

It is straightforward to eliminate  $\bar{v}$  from (3.0.3) using (3.0.2) to arrive at the single linear partial differential equation governing  $\bar{h}$  as

$$\begin{aligned}
 & \left(1 + \frac{\rho\epsilon}{1-\epsilon}\right) \bar{h}_{tt} + 2 \left(1 + \frac{\rho\epsilon(1-\epsilon\delta)}{\delta(1-\epsilon)^2}\right) \bar{h}_{xt} + \left(1 + \frac{\rho\epsilon(1-\epsilon\delta)^2}{\delta^2(1-\epsilon)^3} - \frac{1-\rho}{F_0^2}\right) \bar{h}_{xx} \\
 & \quad + 2 \left(1 + \frac{\delta[\epsilon(1-\epsilon\delta) + \lambda(1-\delta)]}{(1-\epsilon\delta)^2 + \lambda(1-\delta)^2}\right) \bar{h}_t \\
 & \quad + \left(3 - \frac{\lambda(1-\delta)(1-4\epsilon + 6\epsilon\delta - 3\delta) - 3\epsilon(1-\epsilon\delta)^2}{(1-\epsilon)[(1-\epsilon\delta)^2 + \lambda(1-\delta)^2]}\right) \bar{h}_x \\
 & = \left(\frac{1}{R_l} + \frac{\rho\epsilon}{(1-\epsilon)R_g}\right) \bar{h}_{xxt} + \left(\frac{1}{R_l} + \frac{\rho\epsilon(1-\epsilon\delta)}{\delta(1-\epsilon)^2 R_g}\right) \bar{h}_{xxx}. \quad (3.0.4)
 \end{aligned}$$

### 3.1 LINEAR STABILITY CONDITION

We can re-write (3.0.4) as

$$\left(\frac{\partial}{\partial t} + c_+ \frac{\partial}{\partial x}\right) \left(\frac{\partial}{\partial t} + c_- \frac{\partial}{\partial x}\right) \bar{h} + f_1 \left(\frac{\partial}{\partial t} + c_0 \frac{\partial}{\partial x}\right) \bar{h} = f_2 \bar{h}_{xxt} + f_3 \bar{h}_{xxx}, \quad (3.1.1)$$

where

$$c_{\pm} = c_1 \pm \sqrt{\frac{c_2}{F_0^2} - c_3}, \quad (3.1.2)$$

and

$$f_1 = 2 \frac{1-\epsilon}{1-\epsilon + \rho\epsilon} \frac{1-\epsilon\delta + \lambda(1-\delta)}{(1-\epsilon\delta)^2 + \lambda(1-\delta)^2} > 0, \quad (3.1.3)$$

$$f_2 = \frac{(1-\epsilon)R_g + \rho\epsilon R_l}{(1-\epsilon + \rho\epsilon)R_g R_l} > 0, \quad (3.1.4)$$

$$f_3 = \frac{\delta(1-\epsilon)^2 R_g + \rho\epsilon(1-\epsilon\delta)R_l}{\delta(1-\epsilon)(1-\epsilon + \rho\epsilon)R_g R_l} > 0, \quad (3.1.5)$$

$$c_0 = \frac{3(1-\epsilon\delta)^2 + \lambda(1-\delta)(2 + \epsilon - 3\epsilon\delta)}{2(1-\epsilon)[1-\epsilon\delta + \lambda(1-\delta)]}, \quad (3.1.6)$$

$$c_1 = \frac{\delta(1-\epsilon)^2 + \rho\epsilon(1-\epsilon\delta)}{\delta(1-\epsilon)(1-\epsilon + \rho\epsilon)} > 0, \quad (3.1.7)$$

$$c_2 = \frac{(1-\rho)(1-\epsilon)}{1-\epsilon + \rho\epsilon} > 0, \quad (3.1.8)$$

$$c_3 = \frac{\rho\epsilon(1-\delta)^2}{\delta^2(1-\epsilon)(1-\epsilon + \rho\epsilon)^2} > 0. \quad (3.1.9)$$

Equation (3.0.4) is non-hyperbolic for complex values of  $c_{\pm}$ , which happens when

$$F_0 > \frac{\delta \sqrt{1-\rho}(1-\epsilon) \sqrt{1-\epsilon+\rho\epsilon}}{\sqrt{\rho\epsilon}(1-\delta)} \equiv F_{NH}, \quad (3.1.10)$$

for which, if  $f_2, f_3 = 0$ , the IVP is ill-posed due to a short wavelength instability, hence the long wavelength assumption is invalid and suggests the flow regime would change to bubble flow, as discussed in Chapter 2. In general  $f_2, f_3 \neq 0$  and the higher derivative terms may regularise the system which will be discussed later in this chapter.

As shown by Whitham [187], the uniform flow is stable for

$$c_0 < c_+, \quad (3.1.11)$$

which can be re-arranged to give the stability condition

$$F_0 < \frac{\delta \sqrt{1-\rho} \sqrt[3]{1-\epsilon}}{\sqrt{(c_0-1)^2 \delta^2 (1-\epsilon)^3 + \rho\epsilon [\delta c_0 (1-\epsilon) - (1-\delta\epsilon)]^2}} \equiv F_c. \quad (3.1.12)$$

For  $\epsilon, \delta \ll 1$  we have

$$F_{NH} \sim \frac{\delta \sqrt{1-\rho}}{\sqrt{\rho\epsilon}}, \quad F_c \sim \frac{2\delta(1+\lambda) \sqrt{1-\rho}}{\sqrt{\delta^2 + 4\rho\epsilon(1+\lambda)^2}}, \quad (3.1.13)$$

hence

$$F_c < F_{NH}. \quad (3.1.14)$$

As  $\epsilon \rightarrow 0$  and  $\delta \rightarrow 0$ , and assuming  $\epsilon \ll \delta^2$ ,

$$F_c \rightarrow 2(1+\lambda) \sqrt{1-\rho}, \quad (3.1.15)$$

which was derived by Needham et al. [132], and

$$F_{NH} \rightarrow \infty, \quad (3.1.16)$$

and hence Needham et al. [132] do not require any non-hyperbolicity condition. Small disturbances to the uniform flow will decay when  $F_0 < F_c$ , but grow

when  $F_c < F_0 < F_{NH}$ . The dynamics of the flow when  $F_0 > F_c$  will be discussed in Chapter 4.

### 3.2 INSTABILITY GROWTH RATE ANALYSIS

Since the fastest growing wavelength will dominate the initial growth of the disturbance, let us consider the solution of (3.1.1) for a single mode of spatial wave number  $k$  in order to investigate how fast different wavelengths grow. We look for a solution of the form

$$\bar{h}(x, t) = Ae^{ikx + \omega t}, \quad (3.2.1)$$

for the complex constants  $A$  and  $\omega$ , and real constant  $k$ . Substituting (3.2.1) into (3.1.1) gives us the dispersion relation

$$\omega^2 + \alpha(k)\omega + \beta(k) = 0, \quad (3.2.2)$$

with

$$\alpha(k) = f_1 + f_2k^2 + i(c_+ + c_-)k, \quad (3.2.3)$$

$$\beta(k) = -c_+c_-k^2 + i[c_0f_1k + f_3k^3]. \quad (3.2.4)$$

It follows from (3.2.2) that

$$\omega^\pm(k) = \frac{1}{2} \left( -\alpha(k) \pm \sqrt{\alpha(k)^2 - 4\beta(k)} \right), \quad (3.2.5)$$

hence, denoting real and imaginary parts using a subscript  $\mathbb{R}$  and  $\mathbb{I}$  respectively, we can see that

$$\begin{aligned} \omega_{\mathbb{R}}^- &< -\frac{1}{2}\alpha_{\mathbb{R}}, \\ &< -\frac{f_1 + f_2k^2}{2}, \end{aligned} \quad (3.2.6)$$

which, from (3.1.3) and (3.1.4), is less than zero for all  $k$ . Hence the temporal mode corresponding to  $\omega^-$  is always stable and so any instability must be associated with the temporal mode corresponding to  $\omega^+$ , with growth rate  $\omega_{\mathbb{R}}^+$ .

As can be seen in Figure 3.1, increasing  $\delta$  or  $\lambda$  or decreasing  $\epsilon$ ,  $F_0$ ,  $\rho$  or  $R_l$  decreases the growth rate of the instabilities and decreases the range of wave numbers for which the instabilities will grow. We can also see that changes to  $R_g$  have very little effect on the growth rate. By considering the limit as  $k \rightarrow 0$  we find, at leading order, the equation for the growth rate reduces to

$$(\omega_{\mathbb{R}}^+)_{k \rightarrow 0} = \frac{(c_0 - c_-)(c_0 - c_+)}{f_1} k^2. \quad (3.2.7)$$

Due to the growth rate not being based on the direction a wave travels, but only on its wave number, there must be a reflection symmetry around  $k = 0$  and hence the leading order term is  $O(k^2)$ .

The asymptote of  $\omega^+$  as  $k \rightarrow \infty$  is given by

$$(\omega_{\mathbb{R}}^+)^{asympt} = \frac{(c_+ f_2 - f_3)(c_- f_2 - f_3)}{f_2^3}, \quad (3.2.8)$$

where  $(\omega_{\mathbb{R}}^+)^{asympt} < 0$  for

$$F_0 < F_{NH} \sqrt{\frac{R_g R_l^2}{(1 - \epsilon)(R_l - R_g) + R_g R_l^2}}, \quad (3.2.9)$$

which is greater than  $F_{NH}$  for  $R_g > R_l$ . We can see from (3.2.8) that  $\omega_{\mathbb{R}}^+ \rightarrow \infty$  as  $k \rightarrow \infty$  if  $f_2 = 0$ , for which, as stated earlier, the IVP is ill posed and the long wavelength assumption is invalid. Since  $f_2 > 0$ , from (3.1.4), even for  $F_0 > F_{NH}$  the higher derivative terms are stabilising the system. As we have used  $R_l = R_g = 50$  in Figure 3.1, (3.2.9) simplifies to  $F_0 < F_{NH}$  which is true for all the parameter sets we have used in Figure 3.1 except for when  $\delta = 0.25$ . For this parameter set  $(\omega_{\mathbb{R}}^+)^{asympt} = 0.0133$ , hence the system is non-hyperbolic and unstable for all values of  $k$ .

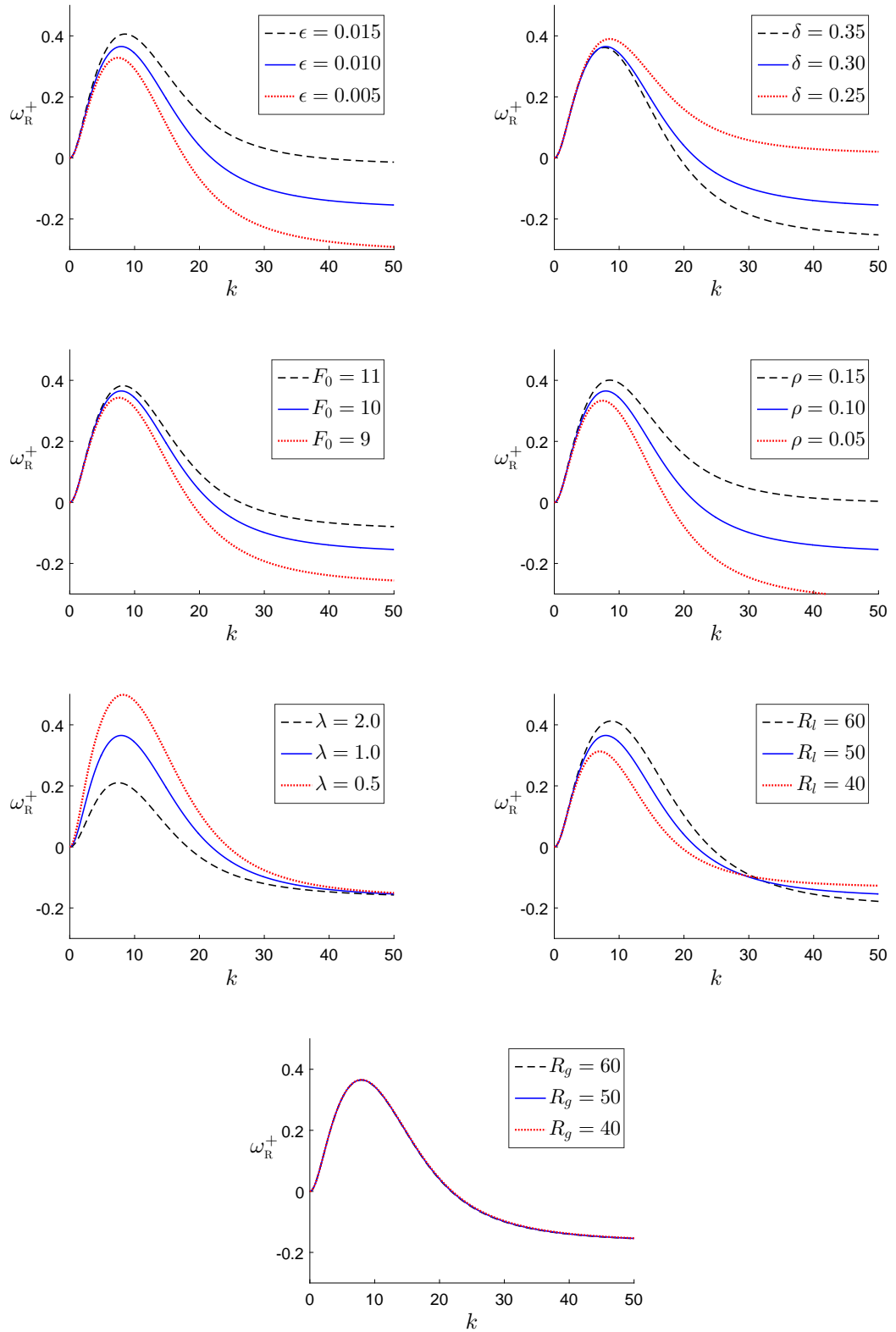


**Figure 3.1.:** The growth rate for the case  $\epsilon = 0.01$ ,  $\delta = 0.3$ ,  $F_0 = 10$ ,  $R_l = 50$ ,  $R_g = 50$ ,  $\lambda = 1$  and  $\rho = 0.1$  and the effect of varying the parameters.

To investigate  $\omega_{\mathbb{R}}^+$  further, let us consider the neutral curve of (3.2.2) which happens when  $\omega(k)$  is purely imaginary, i.e.  $\omega = iy$  where  $y$  is real. In this case, (3.2.2) becomes

$$-y^2 + i\alpha(k)y + \beta(k) = 0, \quad (3.2.10)$$

which has real and imaginary parts

$$(c_+k + y)(c_-k + y) = 0, \quad (3.2.11)$$

$$(f_1 + f_2k^2)y + c_0f_1k + f_3k^3 = 0. \quad (3.2.12)$$

Rearranging (3.2.12) gives

$$y = -\frac{(c_0f_1 + f_3k^2)k}{f_1 + f_2k^2}, \quad (3.2.13)$$

and substituting this into (3.2.11) and rearranging gives

$$\left(k^2 - \frac{(c_0 - c_+)f_1}{c_+f_2 - f_3}\right) \left(k^2 - \frac{(c_0 - c_-)f_1}{c_-f_2 - f_3}\right) = 0. \quad (3.2.14)$$

Hence,  $\omega = iy$  when

$$k_+ = \pm \sqrt{\frac{(c_0 - c_+)f_1}{c_+f_2 - f_3}} = \pm k_{N+}, \quad k_- = \pm \sqrt{\frac{(c_0 - c_-)f_1}{c_-f_2 - f_3}} = \pm k_{N-}, \quad (3.2.15)$$

which correspond to the values of  $k$  for which  $\omega_{\mathbb{R}}^+ = 0$  in Figure 3.1. By rearranging (3.2.15) for  $F_0$  we obtain

$$F_0 = \sqrt{\frac{c_2(f_1 + f_2k^2)^2}{[c_0f_1 + f_3k^2 - c_1(f_1 + f_2k^2)]^2 + c_3(f_1 + f_2k^2)^2}} \equiv F_n, \quad (3.2.16)$$

the equation for the neutral curve,  $F_n(k)$ . The asymptote of the neutral curve as  $k \rightarrow \infty$  is given by

$$F_n^{asympt} = \sqrt{\frac{c_2f_2^2}{(f_3 - c_1f_2)^2 + c_3f_2^2}}. \quad (3.2.17)$$

We can also find the maximum growth rate curve,  $F_m(k)$ , where  $k$  is found by solving

$$\frac{d}{dk}\omega_{\mathbb{R}}^+ = 0, \quad (3.2.18)$$

for each value of  $F_0 < F_{NH}$ . An example of the neutral curve and the maximum growth rate curve can be seen in Figure 3.2 for  $\lambda = 0.37$ ,  $\rho = 0.1$ ,  $R_l = 50$ ,  $R_g = 10$ ,  $\delta = 0.3$  and varying  $\epsilon$ .

In the region under  $F_n$ ,  $\omega_{\mathbb{R}}^+ < 0$  hence small disturbances to the uniform flow will decay. Whereas in the region above  $F_n$ ,  $\omega_{\mathbb{R}}^+ > 0$  hence small disturbances to the uniform flow will grow with the maximum growth rate at  $F_m$ . For large values of  $k$  we can see there is only a very small region for  $F_0$  in which  $\omega_{\mathbb{R}}^+ > 0$  and  $F_0 < F_{NH}$ , this means short wavelengths are stable except for a very small region near to  $F_{NH}$ .

For  $\epsilon = 0.1$ ,  $\lambda = 0.37$ ,  $\rho = 0.1$ ,  $R_l = 50$ ,  $R_g = 10$  and  $\delta = 0.3$ , shown in Figure 3.2a, (3.2.8) gives

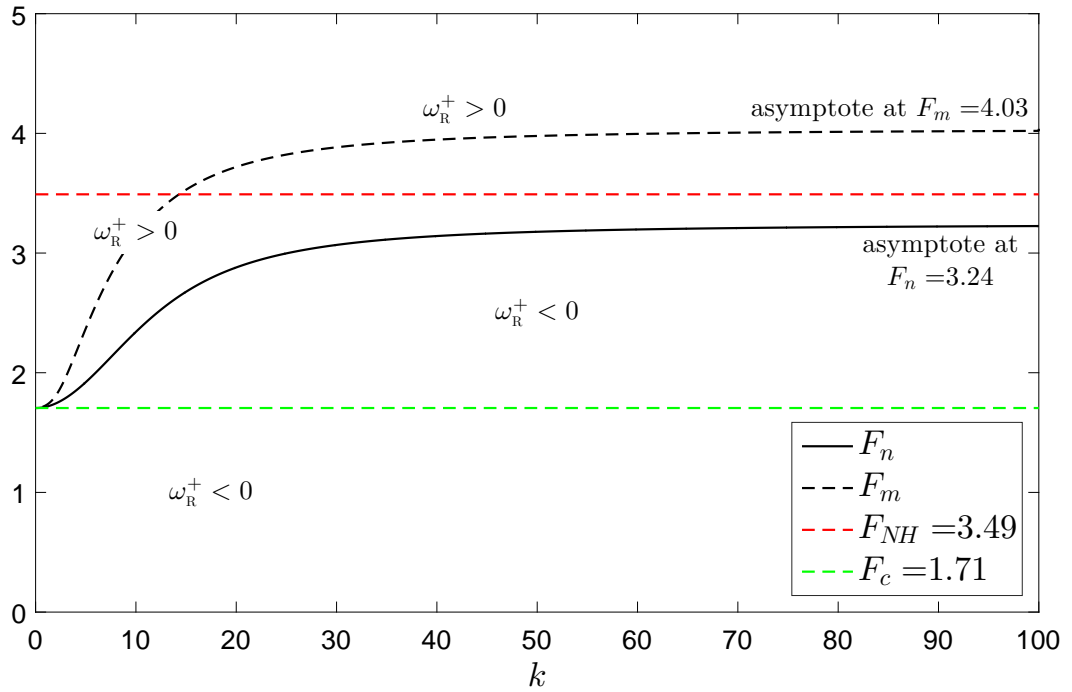
$$(\omega_{\mathbb{R}}^+)^{asympt} = \frac{4.057F_0^2 - 42.631}{F_0^2}, \quad (3.2.19)$$

hence small disturbances to the uniform flow will grow for all values of  $k$  for  $F_0 > 3.24$ . As  $F_0$  is increased above 3.24, the value of the maximum growth rate increases until  $F_0 = 4.03$ , the asymptote of  $F_m$ . At this point there is no turning point in the growth rate and instead the growth rate becomes monotone decreasing for  $k$ , hence in the region above  $F_m$  the maximum growth rate is found for  $k = \infty$ .

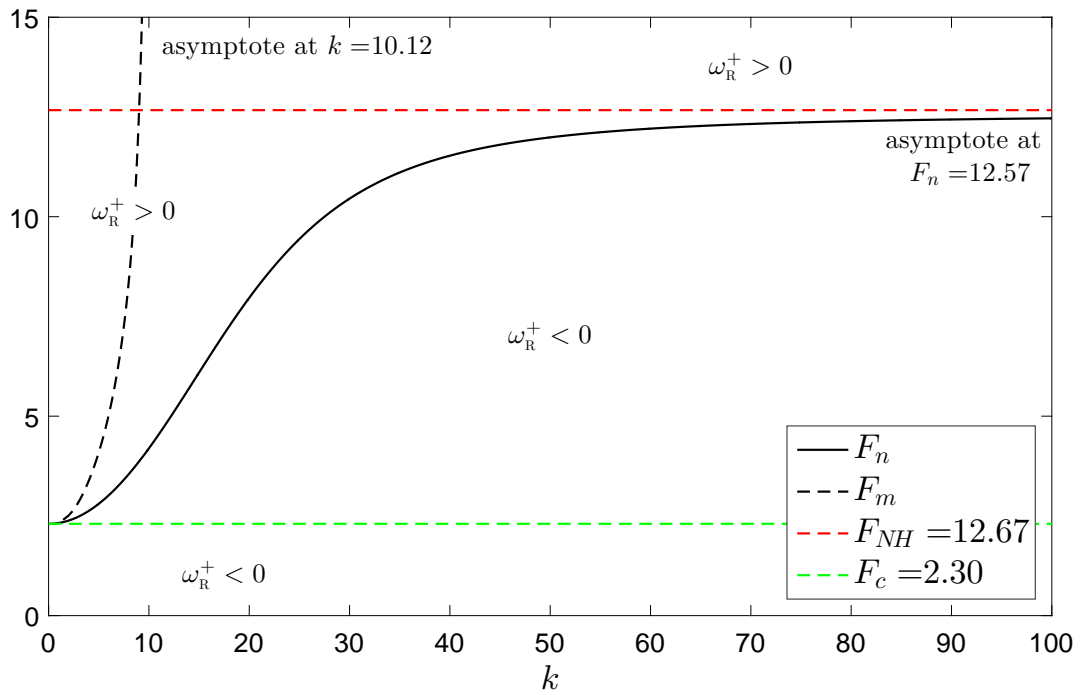
For  $\epsilon = 0.01$ ,  $\lambda = 0.37$ ,  $\rho = 0.1$ ,  $R_l = 50$ ,  $R_g = 10$  and  $\delta = 0.3$ , shown in Figure 3.2b, (3.2.8) gives

$$(\omega_{\mathbb{R}}^+)^{asympt} = \frac{0.283F_0^2 - 44.774}{F_0^2}, \quad (3.2.20)$$

hence small disturbances to the uniform flow will grow for all values of  $k$  for  $F_0 > 12.57$ . Unlike the previous example, we now find the asymptote of  $F_m$  at  $k = 10.12$  and the growth rate is monotone decreasing for  $k >$



(a)  $\epsilon = 0.1$ .



(b)  $\epsilon = 0.01$ .

**Figure 3.2.:** The neutral curve and the maximum growth rate curve for  $\lambda = 0.37, \rho = 0.1, R_l = 50, R_g = 10$  and  $\delta = 0.3$ .

10.12, hence small disturbances to the uniform flow will grow for short wavelengths, but their growth will be very slow.

In the work done by Needham et al. [132] they showed that as  $k \rightarrow \infty$ ,  $F_n \rightarrow \infty$ , whereas we have found an asymptote for  $F_n$  as  $k \rightarrow \infty$ . However, if we let  $\epsilon \rightarrow 0$  and  $\delta \rightarrow 0$  in (3.2.17), and assume  $\epsilon \ll \delta^2$ , we are left with  $F_n^{asympt} \rightarrow \infty$ .

### 3.3 CONCLUSION

We have investigated how small-amplitude disturbances affect the uniform equilibrium flow in order to examine the possibility of slug flow developing. By doing so, we have found a stability criterion,  $F_c$ , for which when  $F_0 > F_c$ , small disturbances in the uniform flow will grow and when  $F_0 < F_c$ , they will decay. We also found a non-hyperbolic criterion,  $F_{NH}$ , for which when  $F_0 > F_{NH}$  the IVP is ill-posed due to a short wavelength instability, hence the long wavelength assumption is invalid and suggests the flow regime would change to bubble flow. We then considered the solution of (3.1.1) for a single mode of spatial wave number  $k$  in order to investigate how fast different wavelengths grow. This allowed us to find the neutral curve,  $F_n$ , for which small disturbances will neither grow nor decay and the maximum growth rate curve,  $F_m$ . When the flow is unstable, i.e.  $F_0 > F_c$ , disturbances in the uniform flow will grow and eventually the linearised theory will break down. At this point the governing equations will be dominated by non-linear effects and the flow may evolve into a slugging state. In order to investigate this further we will consider, in the next chapter, the existence of periodic travelling wave solutions of (2.3.7) and (2.3.8) when  $F_0 > F_c$ .

# 4

---

## PERIODIC TRAVELLING WAVE THEORY

---

When the uniform flow is unstable we expect the flow to develop into roll waves, as observed by many authors (see, for example, Mayer [123], Alavian [4]), which take the form of periodic travelling waves far downstream. Hence we expect the existence of periodic travelling wave solutions of (2.3.7) and (2.3.8). We will restrict attention to those solutions with positive propagation speed  $U$  since we are expecting disturbances to propagate downstream. We therefore introduce the travelling coordinate  $z = x - Ut$  and consider solutions of the form

$$h = h(z), \quad v = v(z), \quad (4.0.1)$$

for

$$0 \leq h(z) \leq \frac{1}{\epsilon}, \quad (4.0.2)$$

where  $1/\epsilon$  is the top of the channel and both  $h(z)$  and  $v(z)$  are periodic in  $z$ . On substitution of (4.0.1) into (2.3.7) and (2.3.8), we get

$$[h(v - U)]_z = 0, \quad (4.0.3)$$

$$\begin{aligned} -U \left( 1 + \frac{\rho \epsilon h}{1 - \epsilon h} \right) v_z + \left( v + \frac{\rho \epsilon h [2 - (1 + \epsilon h) \delta v]}{\delta (1 - \epsilon h)^2} \right) v_z \\ + \left( \frac{1 - \rho}{F_0^2} - \frac{\rho \epsilon (1 - \delta v)^2}{\delta^2 (1 - \epsilon h)} \right) h_z \end{aligned}$$

$$\begin{aligned}
 &= -\frac{v^2}{h} + \frac{(1-\epsilon)^3}{(1-\epsilon\delta)^2 + \lambda(1-\delta)^2} \left( \frac{(1-\epsilon\delta hv)^2}{(1-\epsilon h)^3} + \frac{\lambda(1-\delta v)|1-\delta v|}{h(1-\epsilon h)^3} \right) \\
 &\quad + \left( \frac{1}{hR_l} + \frac{\rho\epsilon}{(1-\epsilon h)R_g} \right) [hv_z]_z - \frac{\rho\epsilon}{\delta(1-\epsilon h)R_g} \left[ \frac{1-\delta v}{1-\epsilon h} h_z \right]_z. \quad (4.0.4)
 \end{aligned}$$

Integrating (4.0.3) leads us to

$$h(v - U) = B, \quad (4.0.5)$$

where  $B$  is a real constant. On rearranging (4.0.5), we obtain

$$v(z) = U + \frac{B}{h(z)}, \quad (4.0.6)$$

which, after substitution into (4.0.4), leads to

$$\begin{aligned}
 &\left( \frac{B}{R_l} + \frac{B\rho\epsilon h}{(1-\epsilon h)R_g} + \frac{\rho\epsilon h [h(1-\delta U) - \delta B]}{\delta(1-\epsilon h)^2 R_g} \right) h_{zz} \\
 &= \left( \frac{B}{hR_l} + \frac{B\rho\epsilon}{(1-\epsilon h)R_g} - \frac{\rho\epsilon [\epsilon(1-\delta U)h^2 + \delta B(1-2\epsilon h)]}{\delta(1-\epsilon h)^3 R_g} \right) h_z^2 \\
 &- \left( UB \frac{\rho\epsilon h}{1-\epsilon h} - \frac{B^2}{h} - \frac{B\rho\epsilon [2h - \delta(1+\epsilon h)(Uh + B)]}{\delta(1-\epsilon h)^2} + \frac{(1-\rho)h^2}{F_0^2} \right. \\
 &\quad \left. - \frac{\rho\epsilon [h - \delta(Uh + B)]^2}{\delta^2(1-\epsilon h)} \right) h_z - \frac{(Uh + B)^2}{h} \\
 &+ \frac{(1-\epsilon)^3}{(1-\epsilon\delta)^2 + \lambda(1-\delta)^2} \left( \frac{[h - \epsilon\delta h(Uh + B)]^2}{(1-\epsilon h)^3} \right. \\
 &\quad \left. + \frac{\lambda [h - \delta(Uh + B)] |h - \delta(Uh + B)|}{h(1-\epsilon h)^3} \right). \quad (4.0.7)
 \end{aligned}$$

For analysis, it is convenient to rewrite (4.0.7) as the equivalent 2D autonomous dynamical system

$$h' = w, \quad (4.0.8)$$

$$\left( \frac{B}{R_l} + \frac{B\rho\epsilon h}{(1-\epsilon h)R_g} + \frac{\rho\epsilon h [h(1-\delta U) - \delta B]}{\delta(1-\epsilon h)^2 R_g} \right) w'$$

$$\begin{aligned}
 &= \left( \frac{B}{hR_l} + \frac{B\rho\epsilon}{(1-\epsilon h)R_g} - \frac{\rho\epsilon [\epsilon(1-\delta U)h^2 + \delta B(1-2\epsilon h)]}{\delta(1-\epsilon h)^3 R_g} \right) w^2 \\
 &- \left( UB \frac{\rho\epsilon h}{1-\epsilon h} - \frac{B^2}{h} - \frac{B\rho\epsilon [2h - \delta(1+\epsilon h)(Uh+B)]}{\delta(1-\epsilon h)^2} + \frac{(1-\rho)h^2}{F_0^2} \right. \\
 &\quad \left. - \frac{\rho\epsilon [h - \delta(Uh+B)]^2}{\delta^2(1-\epsilon h)} \right) w - \frac{(Uh+B)^2}{h} \\
 &+ \frac{(1-\epsilon)^3}{(1-\epsilon\delta)^2 + \lambda(1-\delta)^2} \left( \frac{[h - \epsilon\delta h(Uh+B)]^2}{(1-\epsilon h)^3} \right. \\
 &\quad \left. + \frac{\lambda [h - \delta(Uh+B)] |h - \delta(Uh+B)|}{h(1-\epsilon h)^3} \right), \quad (4.0.9)
 \end{aligned}$$

where a prime denotes  $d/dz$ . We are interested in the existence of periodic travelling wave solutions for this system of equations, hence (recalling our definitions of roll waves and slugs from Chapter 1) we look for limit cycle solutions which correspond to roll waves and, by varying our parameters, investigate whether we can find slug solutions. In order to find values of  $U$  and  $B$  for which these limit cycles can exist, we must understand the structure of the phase plane and its bifurcations. This will be done in Sections 4.2 and 4.3.

By setting the coefficient of  $w'$  equal to zero in (4.0.9), we find a line of singularities at

$$U_s = \frac{B(1-\epsilon h)^2 R_g}{\rho\epsilon h^2 R_l} + \frac{1}{\delta} - B\epsilon, \quad (4.0.10)$$

which, for  $B < 0$ , increases as  $h$  increases hence  $U_s$  is maximal at

$$U_s(h = 1/\epsilon) = \frac{1}{\delta} - B\epsilon \equiv U_{st}. \quad (4.0.11)$$

As limit cycle solutions approach this line of singularities their peaks become sharper until, just before they reach the line of singularities, the peaks become a free surface corner and resemble a sawtooth wave. An example of this will be seen in Section 4.3.

If we now let  $\epsilon \rightarrow 0$  and  $\delta \rightarrow 0$  in (4.0.9), and assume  $\epsilon \ll \delta^2$ , equation (4.0.9) becomes

$$\frac{B}{R_l} w' = \frac{B}{hR_l} w^2 - \left( \frac{(1-\rho)h^2}{F_0^2} - \frac{B^2}{h} \right) w - \frac{(Uh+B)^2}{h} + \frac{h^2 + \lambda h}{1+\lambda}, \quad (4.0.12)$$

which is consistent with the result of Needham et al. [132].

Equilibrium points of (4.0.9) have  $w = 0$ ,  $h = H$ , where  $H$  satisfies

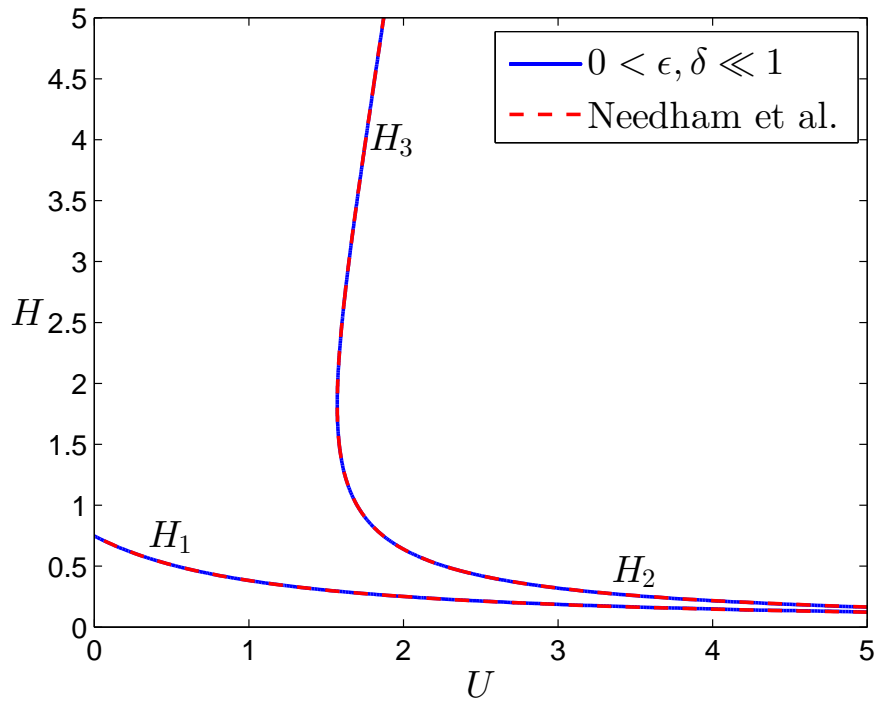
$$\begin{aligned} & \left[ (1-\epsilon\delta)^2 + \lambda(1-\delta)^2 \right] (UH+B)^2 (1-\epsilon H)^3 \\ & = (1-\epsilon)^3 \left( H^3 [1-\epsilon\delta(UH+B)]^2 + \lambda [H-\delta(UH+B)] |H-\delta(UH+B)| \right), \end{aligned} \quad (4.0.13)$$

which is a fifth order polynomial and hence has up to five real solutions. A plot of  $H$  against  $U$  is shown in Figure 4.1 for  $\lambda = 1$ ,  $B = -1$ ,  $\epsilon = 1 \times 10^{-10}$  and  $\delta = 1 \times 10^{-3}$ ,  $\rho = 0.1$ ,  $R_l = 50$  and  $R_g = 50$ . For  $H \ll 1/\epsilon$  we see that we reproduce the results of Needham et al. [132] (discussed in Subsection 1.2.6), as shown in Figure 4.1a. However, when we compare the two models on a scale of  $O(\epsilon^{-1})$ , we see a significant difference, as shown in Figure 4.1b. In particular, when  $\delta U = O(1)$  there are two more equilibrium points for  $H = O(\epsilon^{-1})$  which appear to join at  $H = \epsilon^{-1}$ ,  $U = U_{st}$ . We can investigate this by setting  $U = U_{st}$  in (4.0.13), which can then be re-arranged to give

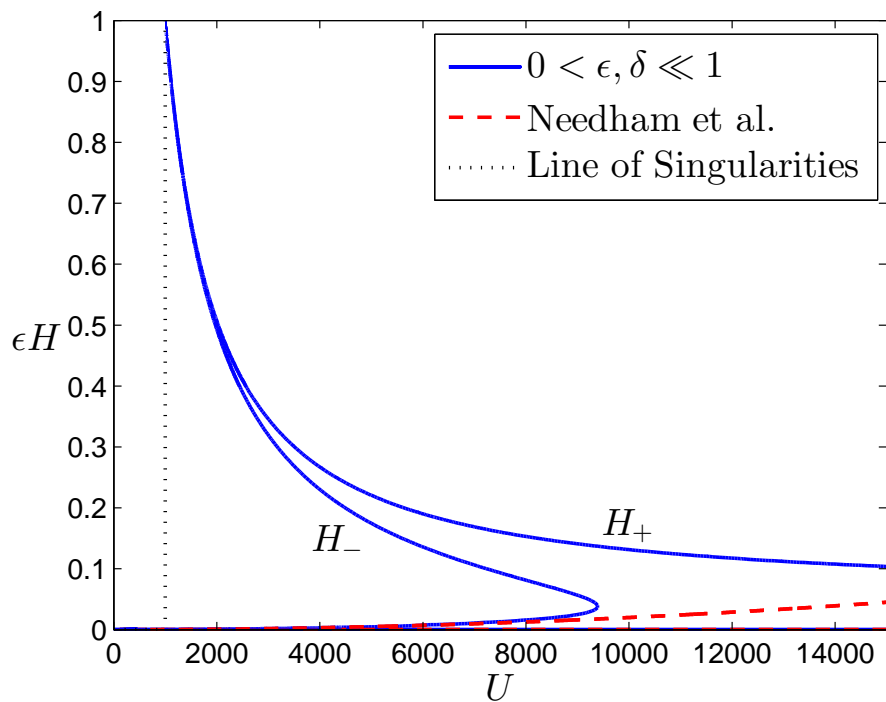
$$\begin{aligned} & \left[ (1-\epsilon\delta)^2 + \lambda(1-\delta)^2 \right] \left[ \frac{H}{\delta} + B(1-\epsilon H) \right]^2 (1-\epsilon H)^3 \\ & = H^3 (1-B\epsilon\delta)^2 (1-\epsilon H)^2 - \lambda\delta^2 B|B| (1-\epsilon H)^2, \end{aligned} \quad (4.0.14)$$

hence  $H = \epsilon^{-1}$  is a double root for  $U = U_{st}$ . (Note that for dimensional propagation speed  $V$ , where  $V = u_l^0 U$ ,  $U \approx 1/\delta$  implies that  $V \approx u_h$ .)

These new equilibrium points represent uniform states in which the liquid almost fills the channel. From this we can conclude that the bifurcation



(a) A comparison of the equilibrium points for  $H \ll \epsilon^{-1}$ .



(b) A comparison of the equilibrium points on a scale of  $O(\epsilon^{-1})$ .

**Figure 4.1.:** A comparison of the equilibrium points of those obtained using (4.0.13) against those by Needham et al. [132] for  $\lambda = 1$ ,  $B = -1$ ,  $\epsilon = 1 \times 10^{-10}$  and  $\delta = 1 \times 10^{-3}$ ,  $\rho = 0.1$ ,  $R_l = 50$  and  $R_g = 50$ .

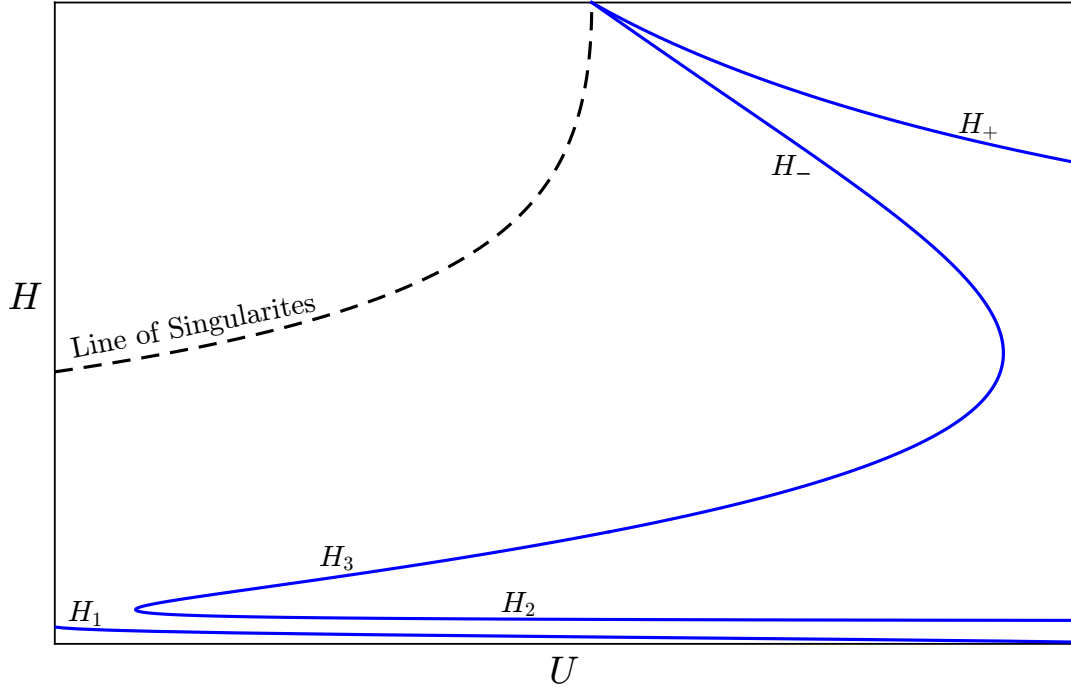


**Figure 4.2.:** A typical bifurcation diagram comparing  $U$  against equilibrium points for fixed  $\epsilon, \delta, F_0, R_l, R_g, \lambda, \rho$  and  $B < 0$ .

structure is the same as found by Needham et al. [132] for  $h \ll \epsilon^{-1}$ , however as  $U$  increases we see two equilibrium points that vanish in the previously studied limit,  $\epsilon \rightarrow 0$ , at  $h = H_+$  and  $h = H_-$  which come into existence near the top of the channel for  $\delta U \approx 1$ . For simplicity we will label the original three equilibrium points  $H_1, H_2$  and  $H_3$  where  $H_1 < H_2 < H_3 < H_- < H_+$  for which  $H_1$  is a stable node/spiral,  $H_2$  is a saddle and  $H_3$  is a spiral/node with the possibility of Hopf bifurcations occurring (as discussed in Subsection 1.2.6). As  $U$  increases further,  $H_+$  and  $H_-$  decrease until  $H_3$  and  $H_-$  disappear in a saddle-node bifurcation and we are left with  $H_1, H_2$  and  $H_+$ . Figures 4.2 and 4.3 show a typical diagram comparing  $U$  against equilibrium points for fixed  $B < 0$  and  $B > 0$ , respectively, for fixed  $\epsilon, \delta, F_0, R_l, R_g, \lambda$  and  $\rho$ .

For  $B > 0$  Needham et al. [132] found  $H_1$  to be a saddle point hence there could be no limit cycle solutions. However, due to our line of singularities possibly intersecting  $H_1$ , it is possible for it to become a node or spiral which would allow the possibility of a Hopf Bifurcation occurring, or a

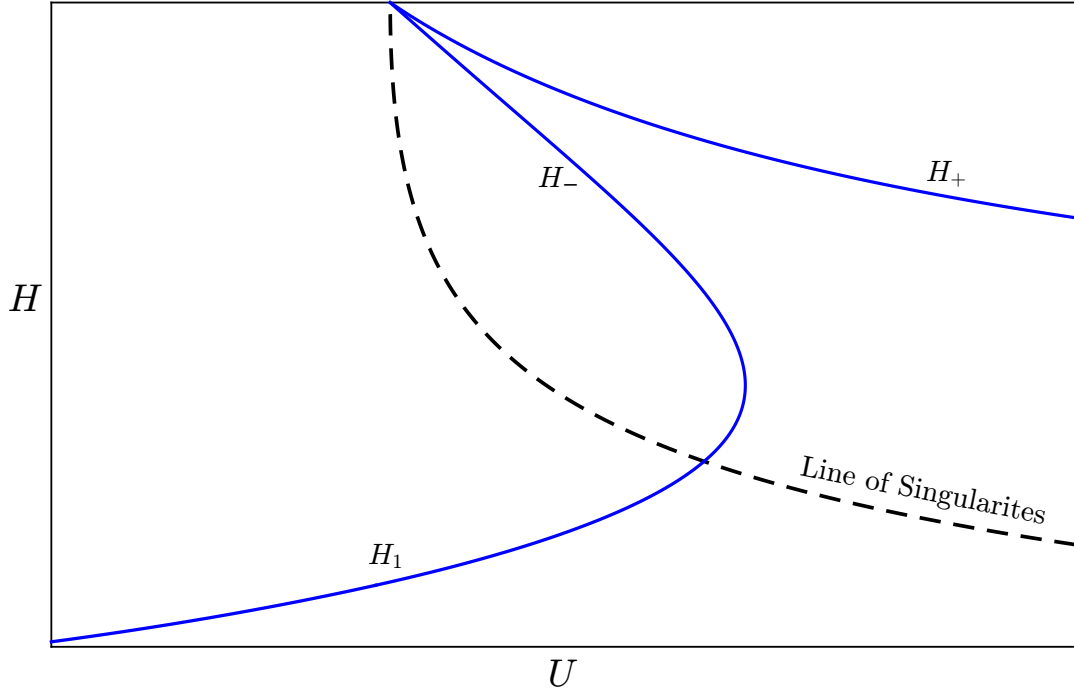


**Figure 4.3.:** A typical bifurcation diagram comparing  $U$  against equilibrium points for fixed  $\epsilon, \delta, F_0, R_l, R_g, \lambda, \rho$  and  $B > 0$ .

Hopf Bifurcation could occur on  $H_-$  or  $H_+$ . In either of these cases we will not be able to find Hopf Bifurcations occurring for small  $h$ , so will not be able to find limit cycle solutions that represent roll waves forming on a thin layer of liquid. As it is these cases we wish to find in order to investigate how they grow and potentially form slugs, we will continue our work considering  $B < 0$  only.

We can find an asymptotic approximation to the point at which the saddle-node bifurcation between  $H_3$  and  $H_-$  occurs by noting that  $\delta U = O(1)$  and  $\epsilon H = O(1)$ , hence we let

$$\delta U = \check{U}, \quad \epsilon H = \check{H}, \quad (4.0.15)$$

in (4.0.13), which at leading order gives

$$(1 + \lambda)\epsilon\delta^{-2}(1 - \check{H})^3\check{U}^2 \sim \check{H}(1 - \check{H}\check{U})^2. \quad (4.0.16)$$

To get a leading order balance we let

$$\delta = d_0 \epsilon^{\frac{1}{2}}, \quad (4.0.17)$$

where  $d_0 = O(1)$  is a positive constant, in (4.0.16), which gives

$$\check{U}_{\pm} = \frac{\check{H}^2 \pm \sqrt{(1 + \lambda)d_0^{-2}(1 - \check{H})^3 \check{H}}}{\check{H}^3 - (1 + \lambda)d_0^{-2}(1 - \check{H})^3}. \quad (4.0.18)$$

From Figures 4.2 and 4.3 we can see that, for a given value of  $H = H_- = H_+$ ,  $U(H_+) > U(H_-)$  hence as we are interested in  $H_-$  we use  $\check{U}_-$  and solve

$$\frac{d\check{U}_-}{d\check{H}} = 0, \quad (4.0.19)$$

to get

$$\check{H} = \frac{1}{2} \frac{(1 + \lambda)^{\frac{1}{3}} \left( \sqrt{d_0^2 + 1 + \lambda + d_0} \right)^{\frac{2}{3}} + (1 + \lambda)^{\frac{2}{3}}}{\sqrt{d_0^2 + 1 + \lambda} \left( \sqrt{d_0^2 + 1 + \lambda + d_0} \right)^{\frac{1}{3}}}. \quad (4.0.20)$$

We can then substitute (4.0.17), (4.0.18) and (4.0.20) into (4.0.15) to get the explicit result. For  $\lambda = 1$ ,  $\delta = 1 \times 10^{-3}$  and  $\epsilon = 1 \times 10^{-10}$  we have the turning point at  $(U, H) = (9394, 0.0382 \times 10^{10})$  which corresponds with Figure 4.1b.

## 4.1 ANALYSIS OF EQUILIBRIUM POINTS

In order to investigate  $H_-$  and  $H_+$  we will try to find an asymptotic expansion for  $H$  as  $H \rightarrow \epsilon^{-1}$ . Since  $H \leq \epsilon^{-1}$  and  $U(H = 1/\epsilon) = U_{st} \equiv \frac{1}{\delta} - B\epsilon$ , from (4.0.11), we define

$$H = \epsilon^{-1} - \hat{H}\epsilon^{\alpha-1}, \quad \hat{H} \geq 0, \quad 0 < \alpha < 1, \quad (4.1.1)$$

$$\delta U = 1 - B\epsilon\delta + A\epsilon^{\beta}, \quad 0 < \beta < 1, \quad (4.1.2)$$

and

$$\delta = d_1 \epsilon^{\frac{\beta}{2}}, \quad (4.1.3)$$

where  $A, d_1 = O(1)$  are constants to be determined. Substituting (4.1.1), (4.1.2) and (4.1.3) into (4.0.13) at leading order gives

$$(1 + \lambda)d_1^{-2}\hat{H}^3\epsilon^{3\alpha-\beta} \sim \epsilon^{-1} \left( \hat{H}\epsilon^\alpha - A\epsilon^\beta \right)^2 - \lambda A|A|\epsilon^{2\beta}. \quad (4.1.4)$$

Since  $0 < \alpha, \beta < 1$  the first term on the right hand side must be zero for a leading order balance, so we must have

$$\alpha = \beta, \quad \hat{H} = A. \quad (4.1.5)$$

Hence (4.1.1) becomes

$$\begin{aligned} H &= \epsilon^{-1} - A\epsilon^{\beta-1}, \\ &\sim \frac{1}{\epsilon\delta U'} \end{aligned} \quad (4.1.6)$$

and  $\hat{H} \geq 0$  implies that  $A \geq 0$ , hence equilibrium points close to  $H = \epsilon^{-1}$  exist only for  $U > U_{st}$ . Since we have not found a value for  $\beta$  we must look for another term in the asymptotic expansion. It is convenient to define

$$H = \frac{1}{\epsilon\delta U} + \tilde{H}\epsilon^{\gamma-1}, \quad \gamma > \beta. \quad (4.1.7)$$

Substituting (4.1.2), (4.1.3) and (4.1.7) into (4.0.13) and again looking for a leading order balance gives

$$(1 + \lambda)d_1^{-2}A^3\epsilon^{2\beta} \sim \tilde{H}^2\epsilon^{2\gamma-1} - \lambda A^2\epsilon^{2\beta}. \quad (4.1.8)$$

Equating powers of  $\epsilon$  gives

$$\gamma = \beta + \frac{1}{2}, \quad (4.1.9)$$

and

$$\tilde{H} = \pm \frac{A\sqrt{(1+\lambda)A + \lambda d_1^2}}{d_1}. \quad (4.1.10)$$

By combining (4.1.2),(4.1.3), (4.1.7), (4.1.9) and (4.1.10) we have our asymptotic expansion of the two equilibrium points as

$$H_{\pm} = \frac{1}{\delta U} \epsilon^{-1} \pm (\delta U - 1 + B\epsilon\delta) \sqrt{(1+\lambda)(\delta U - 1 + B\epsilon\delta)\delta^{-2} + \lambda} \epsilon^{-\frac{1}{2}}. \quad (4.1.11)$$

In order to investigate what type of equilibrium points  $H_{\pm}$  are, let us consider (4.0.9) in the form

$$w' = g_1(h)w^2 + g_2(h)w + g_3(h). \quad (4.1.12)$$

We can now express the Jacobian,  $J$ , of (4.0.8) and (4.0.9) as

$$J = \begin{pmatrix} 0 & 1 \\ \frac{dg_3}{dh}(H), & g_2(H) \end{pmatrix}. \quad (4.1.13)$$

Hence, the eigenvalues of (4.0.8) and (4.0.9) are

$$\lambda_{\pm} = \frac{1}{2} \left( g_2(H) \pm \sqrt{g_2(H)^2 + 4 \frac{dg_3}{dh}(H)} \right). \quad (4.1.14)$$

By defining  $F_0 = F_1 \epsilon^{-\bar{\gamma}}$  where  $F_1$  is a positive constant and  $0 < \bar{\gamma} < 1$ , (4.1.14) becomes

$$\lambda_{\pm} = -\frac{R_g A d_1}{2\rho} \left[ \frac{-2B\rho d_1 F_1^2 \epsilon^{-\frac{3}{2}\beta} + \rho A^2 F_1^2 \epsilon^{-1} - (1-\rho) A d_1^2 \epsilon^{-2+2\bar{\gamma}}}{A d_1^2 F_1^2} \right. \\ \left. \pm \left( \left( \frac{-2B\rho d_1 F_1^2 \epsilon^{-\frac{3}{2}\beta} + \rho A^2 F_1^2 \epsilon^{-1} - (1-\rho) A d_1^2 \epsilon^{-2+2\bar{\gamma}}}{A d_1^2 F_1^2} \right)^2 \right. \right. \\ \left. \left. - 8 \frac{\rho \tilde{H}}{R_g (1+\lambda) A^4 d_1} \epsilon^{-\frac{3}{2} - \frac{7}{2}\beta} \right)^{\frac{1}{2}} \right] \epsilon^{1+\frac{3}{2}\beta}, \quad (4.1.15)$$

at leading order. Since, from (4.1.10),  $\tilde{H}$  is negative for  $H_-$  and positive for  $H_+$ , we can deduce from (4.1.15) that, in general,  $H_-$  is a saddle point and  $H_+$  is a node or spiral. A Hopf bifurcation will occur on  $H^+$  for  $g_2(H) = 0$  which happens when

$$U = \frac{1}{\delta} - B\epsilon + \frac{(1-\rho)\delta^2 \pm \sqrt{(1-\rho)^2\delta^4 + 8B\rho^2\delta\epsilon^3 F_0^4}}{2\rho F_0^2 \epsilon \delta} \equiv U_{\pm}^{Hopf}, \quad (4.1.16)$$

which, for  $B < 0$ , is a real quantity when

$$F_0 < \left( -\frac{(1-\rho)^2\delta^3}{8B\rho^2\epsilon^3} \right)^{1/4} \equiv F_{max+}^{Hopf}. \quad (4.1.17)$$

As  $F_0 \rightarrow 0$ ,  $U_{Hopf-}^+ \rightarrow U_{st}$  from (4.0.11), hence for  $0 < F_0 < F_{max+}^{Hopf}$  there will be two Hopf bifurcations on  $H_+$ . (Note that for  $B > 0$ ,  $F_{max+}^{Hopf} < 0$ , hence we do not get Hopf bifurcations on  $H_+$ .)

## 4.2 ANALYSIS FOR $h \sim \epsilon^{-1}$

We will see in Section 4.3 that when  $\delta U \approx 1$  we obtain limit cycle solutions where the liquid almost fills the channel. We will now consider the case where  $\delta U \approx 1$  and consider the phase plane for  $|h - \epsilon^{-1}| \ll 1$  in order to see if it is possible for limit cycles to pass through this region without the existence of  $H_-$  and  $H_+$ . To do this let

$$h = \epsilon^{-1}(1 - \phi(\epsilon)\dot{H}), \quad \phi(\epsilon) \ll 1, \quad \dot{H} > 0, \quad (4.2.1)$$

$$w = \psi(\epsilon)W, \quad W > 0, \quad (4.2.2)$$

and

$$\delta = \chi(\epsilon), \quad 0 \leq \chi(\epsilon) \leq 1. \quad (4.2.3)$$

Substituting (4.2.1) and (4.2.3) into (4.0.9) and looking for a leading order balance for  $\epsilon$  and  $\phi(\epsilon)$  gives

$$\begin{aligned} \frac{\rho(1-U\chi(\epsilon))}{R_g\chi(\epsilon)\epsilon\phi(\epsilon)^2\dot{H}^2}\psi(\epsilon)W' &= \frac{-\rho(1-U\chi(\epsilon))}{R_g\chi(\epsilon)\phi(\epsilon)^3\dot{H}^3}\psi(\epsilon)^2W^2 \\ &+ \left( \frac{2\rho B(1-U\chi(\epsilon))}{\chi(\epsilon)\phi(\epsilon)^2\dot{H}^2} + \frac{\rho(1-U\chi(\epsilon))}{\chi(\epsilon)^2\epsilon\phi(\epsilon)\dot{H}} \right) \psi(\epsilon)W \\ &+ \frac{1-U\chi(\epsilon)}{(1+\lambda)\epsilon^2\phi(\epsilon)^3\dot{H}^3}, \end{aligned} \quad (4.2.4)$$

which rearranges to

$$\frac{dW}{d\dot{H}} = \frac{W}{\dot{H}} - 2R_gB\frac{\phi(\epsilon)}{\psi(\epsilon)} - \frac{R_g\dot{H}\phi(\epsilon)^2}{\chi(\epsilon)\epsilon\psi(\epsilon)} - \frac{R_g\chi(\epsilon)}{\rho(1+\lambda)\dot{H}W\epsilon^2\psi(\epsilon)^2}. \quad (4.2.5)$$

In order to find a leading order balance, let

$$\chi(\epsilon) = d_2\epsilon^{\frac{1}{2}}, \quad 0 \leq d_2 \leq \epsilon^{-\frac{1}{2}}, \quad (4.2.6)$$

which leads us to

$$\phi(\epsilon) = \epsilon^{\frac{3}{8}}, \quad \psi(\epsilon) = \epsilon^{-\frac{3}{4}}. \quad (4.2.7)$$

The leading order equation is therefore

$$\frac{dW}{d\dot{H}} = \frac{W}{\dot{H}} - \frac{R_g}{d_2}\dot{H} - \frac{R_gd_2}{\rho(1+\lambda)}\frac{1}{\dot{H}W}. \quad (4.2.8)$$

By making the substitutions

$$\dot{H} = \sqrt[4]{\frac{d_2^3}{R_g\rho(1+\lambda)}}\dot{H}, \quad W = \sqrt{\frac{R_gd_2}{\rho(1+\lambda)}}\dot{W}, \quad (4.2.9)$$

our approximations for  $h$  and  $w$  ((4.2.1) and (4.2.2), respectively) become

$$h = \epsilon^{-1} - \sqrt[4]{\frac{d^3}{R_g\rho(1+\lambda)}}\epsilon^{-\frac{5}{8}}\dot{H}, \quad w = \sqrt{\frac{R_gd}{\rho(1+\lambda)}}\epsilon^{-\frac{3}{4}}\dot{W}, \quad (4.2.10)$$

and (4.2.8) reduces to the parameterless equation

$$\frac{d\dot{W}}{d\dot{H}} = \frac{\dot{W}^2 - \dot{W}\dot{H}^2 - 1}{\dot{W}\dot{H}}. \quad (4.2.11)$$

By solving  $\frac{d\dot{W}}{d\dot{H}} = 0$  we find the nullclines at

$$\dot{W} = \frac{\dot{H}^2 \pm \sqrt{\dot{H}^4 + 4}}{2}, \quad (4.2.12)$$

and can see from (4.2.11) that for

$$\dot{W} \rightarrow 0^+, \quad \frac{d\dot{W}}{d\dot{H}} \rightarrow -\infty, \quad (4.2.13)$$

$$\dot{W} \rightarrow 0^-, \quad \frac{d\dot{W}}{d\dot{H}} \rightarrow +\infty, \quad (4.2.14)$$

$$\dot{H} \rightarrow 0, \quad \frac{d\dot{W}}{d\dot{H}} \rightarrow \begin{cases} +\infty & \text{if } \dot{W} > 1 \text{ or } -1 < \dot{W} < 0 \\ 0 & \text{if } \dot{W} = 1 \text{ or } \dot{W} = -1 \\ -\infty & \text{if } \dot{W} < -1 \text{ or } 0 < \dot{W} < 1 \end{cases}. \quad (4.2.15)$$

Using (4.2.12) - (4.2.15) we can plot the phase portrait of equation (4.2.11), shown in Figure 4.4, which shows that it is not possible for limit cycles to pass through the region when  $|h - \epsilon^{-1}| = O(\epsilon^{-\frac{5}{8}})$ . Hence when  $\delta U \not\approx 1$ , there is an upper bound on the amplitude of the periodic solutions and they cannot reach the top of the channel.

### 4.3 NUMERICAL CALCULATION OF THE PERIODIC SOLUTIONS

In order to investigate numerical solutions to (4.0.8) and (4.0.9) it is possible to use software such as Auto which offers a systematic and efficient way of tracing all travelling wave solutions and their bifurcations. However, due to the complexity of the system and the number of parameters, it would be difficult to gain an in depth understanding of the system this way. Hence, we will use a combination of MATLAB routines ode45 and bvp5c as discussed below. This method requires a more 'hands-on' approach allowing us to understand the effects of the parameters on the solutions and their phase planes. It must be noted that, by using this approach, it is

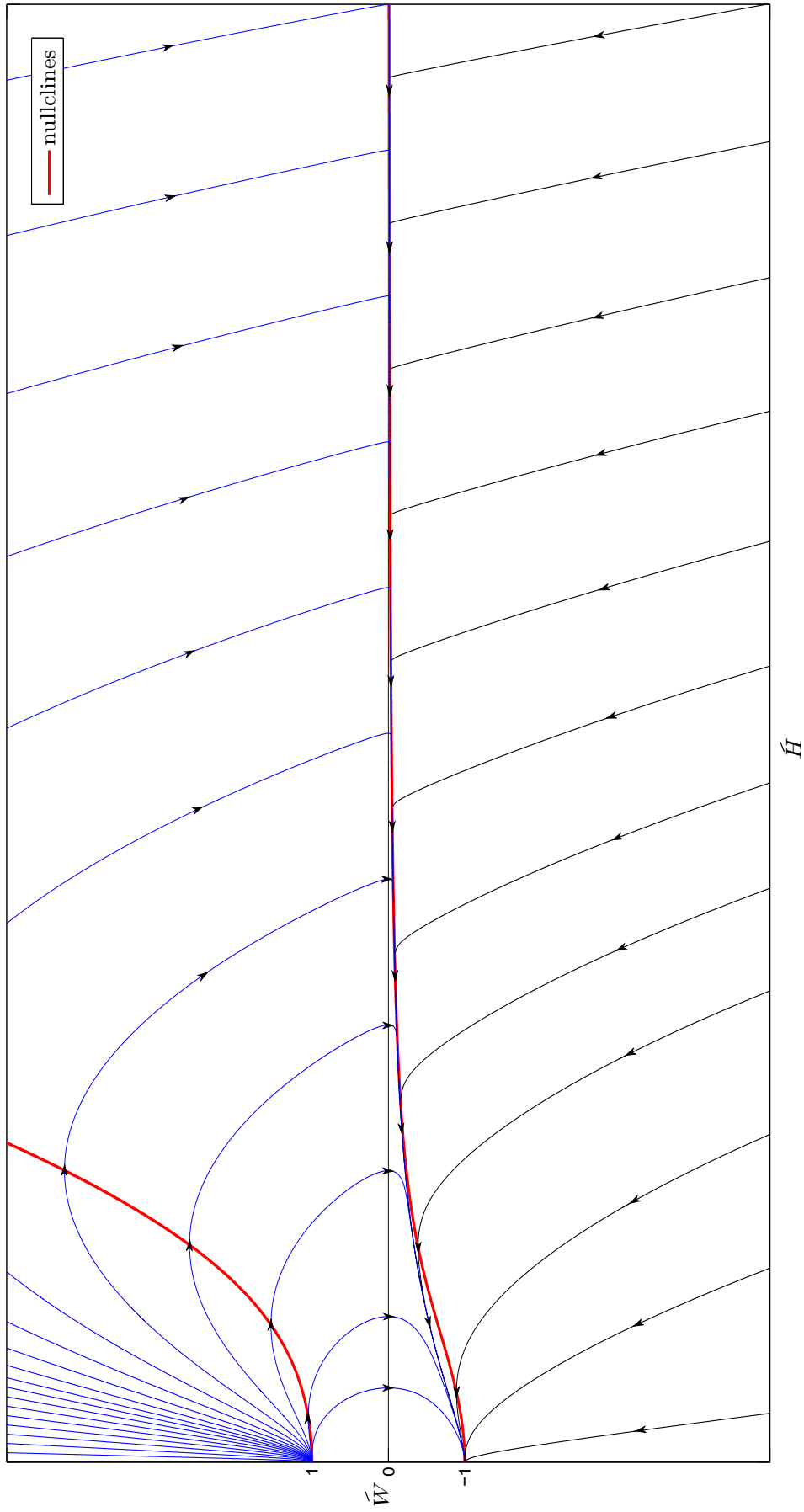


Figure 4.4.: The phase portrait for  $(\hat{H}, \hat{W})$ , from (4.2.11).

possible we have missed some solution branches. Though, as will be seen in this Section, we are able to successfully use this approach in finding solution branches and are able to explain the structure of their respective bifurcation diagrams.

We begin by taking  $\epsilon$  and  $\delta$  to be small ( $\epsilon = 1 \times 10^{-10}$ ,  $\delta = 1 \times 10^{-3}$ ), using the same parameters as Needham et al. [132] in their Figure 13 ( $U = 1.73276$ ,  $B = -0.7$ ,  $F_0 = 10$ ,  $R_l = 50$ ,  $\lambda = 1$  and  $\rho = 0.1$ ) and using  $R_g = 50$ . We then integrate (4.0.8) and (4.0.9) numerically in MATLAB using routine ode45 allowing it to run until the solution has become periodic (and we get the same solution as Figure 13 by Needham et al. [132]).

Let us now define  $\hat{z} = z/L$ , where  $L$  is the period, or wavelength, of the solution so that, (4.0.8) and (4.0.9) become

$$h' = Lw, \quad (4.3.1)$$

$$\begin{aligned} & \left( \frac{B}{R_l} + \frac{B\rho\epsilon h}{(1-\epsilon h)R_g} + \frac{\rho\epsilon h [h(1-\delta U) - \delta B]}{\delta(1-\epsilon h)^2 R_g} \right) w' \\ &= L \left[ \left( \frac{B}{hR_l} + \frac{B\rho\epsilon}{(1-\epsilon h)R_g} - \frac{\rho\epsilon [\epsilon(1-\delta U)h^2 + \delta B(1-2\epsilon h)]}{\delta(1-\epsilon h)^3 R_g} \right) w^2 \right. \\ & \quad - \left( UB \frac{\rho\epsilon h}{1-\epsilon h} - \frac{B^2}{h} - \frac{B\rho\epsilon [2h - \delta(1+\epsilon h)(Uh+B)]}{\delta(1-\epsilon h)^2} + \frac{(1-\rho)h^2}{F_0^2} \right. \\ & \quad \quad \quad \left. \left. - \frac{\rho\epsilon [h - \delta(Uh+B)]^2}{\delta^2(1-\epsilon h)} \right) w - \frac{(Uh+B)^2}{h} \right. \\ & \quad \left. + \frac{(1-\epsilon)^3}{(1-\epsilon\delta)^2 + \lambda(1-\delta)^2} \left( \frac{[h - \epsilon\delta h(Uh+B)]^2}{(1-\epsilon h)^3} \right. \right. \\ & \quad \quad \left. \left. + \frac{\lambda [h - \delta(Uh+B)] |h - \delta(Uh+B)|}{h(1-\epsilon h)^3} \right) \right], \quad (4.3.2) \end{aligned}$$

for  $0 \leq \hat{z} \leq 1$ , where a prime denotes  $d/d\hat{z}$ , to be solved subject to the periodic boundary conditions

$$h(0) = h(1), \quad w(0) = w(1) = 0. \quad (4.3.3)$$

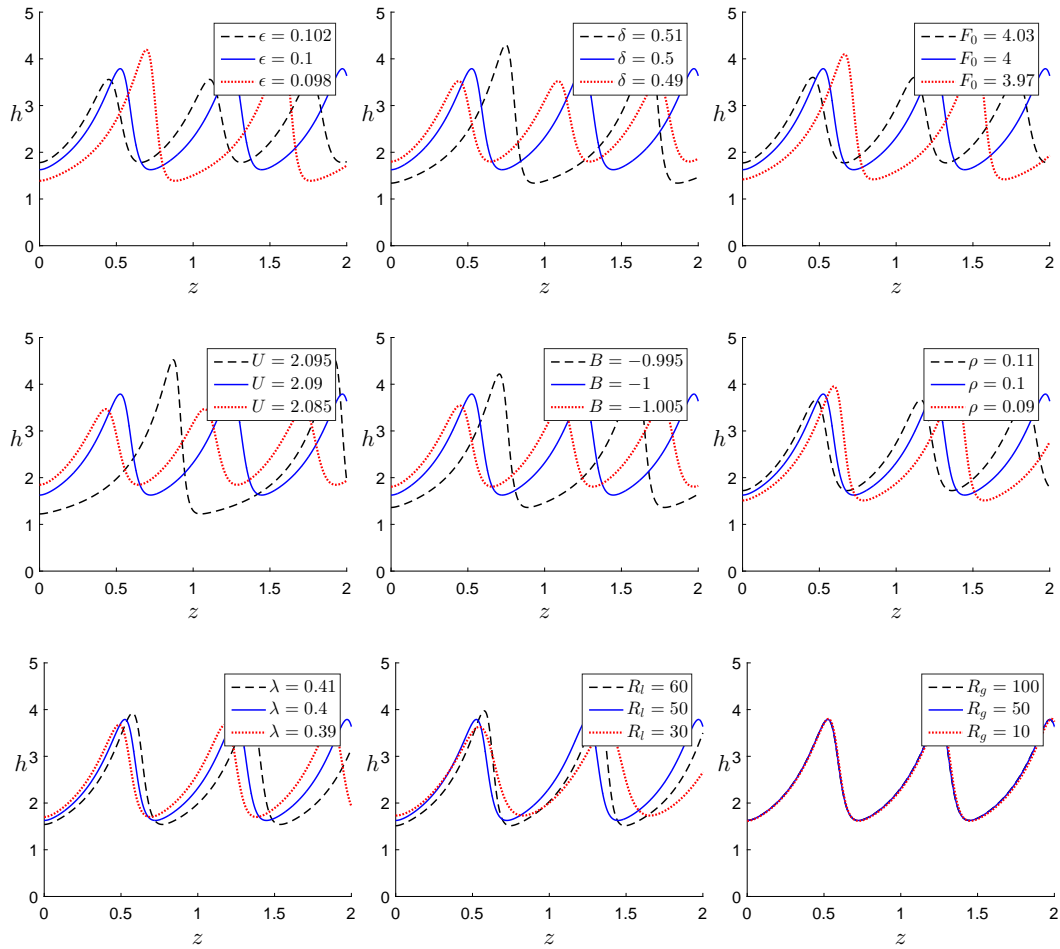


**Figure 4.5.:** The periodic solutions for the case  $\epsilon = 0.1$ ,  $\delta = 0.5$ ,  $U = 2.09$ ,  $B = -1$ ,  $F_0 = 4$ ,  $R_l = 50$ ,  $R_g = 50$ ,  $\lambda = 0.4$  and  $\rho = 0.1$  and the effect of varying the parameters.

We are now able to use routine `bvp5c` to solve (4.3.1) and (4.3.2) with  $L$  as an eigenvalue and using the solution generated by routine `ode45` previously as our initial guess. The effects of varying  $\epsilon$ ,  $\delta$ ,  $U$ ,  $B$ ,  $F_0$ ,  $R_l$ ,  $R_g$ ,  $\lambda$  and  $\rho$  are shown in Figure 4.5. By increasing  $B$ ,  $F_0$  and  $U$  we see the amplitude of the periodic solution increases towards the top of the channel (at  $h = 10$ ), as can be seen in Figure 4.6.

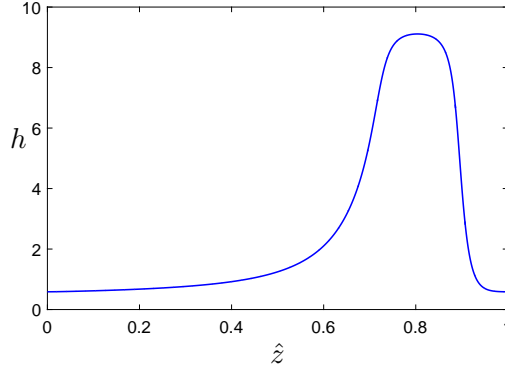


**Figure 4.6.:** The periodic solution of wavelength 1.0666 for the case  $\epsilon = 0.1$ ,  $\delta = 0.5$ ,  $U = 2.199$ ,  $B = -0.7$ ,  $F_0 = 6.7$ ,  $R_l = 50$ ,  $R_g = 50$ ,  $\lambda = 0.4$  and  $\rho = 0.1$ .

In order to understand the periodic solutions, it is necessary to examine the phase portrait. To do this we must first note that we have a line of singularities at  $h = 0$ , for which (4.0.9) becomes

$$\frac{B}{R_l}w^2 + B^2w - B^2 - \frac{(1 - \epsilon)^3}{(1 - \epsilon\delta)^2 + \lambda(1 - \delta)^2}\lambda\delta^2|B| = 0, \quad (4.3.4)$$

at leading order, hence either  $B = 0$ , or

$$w_{\pm} = \frac{R_l}{2} \left[ -B \pm \sqrt{B^2 + \frac{4B}{R_l} + \frac{\lambda\delta^2(1 - \epsilon)^3|B|}{R_l[(1 - \epsilon\delta)^2 + \lambda(1 - \delta)^2]}} \right]. \quad (4.3.5)$$

An example of a typical bifurcation diagram can be seen in Figure 4.7 for  $\epsilon = 0.1$ ,  $\delta = 0.5$ ,  $B = -1$ ,  $F_0 = 4$ ,  $R_l = 50$ ,  $R_g = 50$ ,  $\lambda = 0.4$  and  $\rho = 0.1$ , these are the same parameters we used in Figure 4.5. The equilibrium points are shown in blue and are represented by solid lines if they are stable and dashed lines if they are unstable. In this case there is a Hopf bifurcation at  $H_3$  when  $U \approx 2.074$ . As  $U$  increases there are periodic solutions passing around  $H_3$  and in between  $H_2$  and  $H_-$ , represented by the shaded region with the maximum and minimum values of the solutions shown in red to represent stable solutions (we will represent unstable solutions with pink). The solutions increase in amplitude until  $U \approx 2.095$ , at which point there is a homoclinic bifurcation at  $H_2$ , marked by the green line.

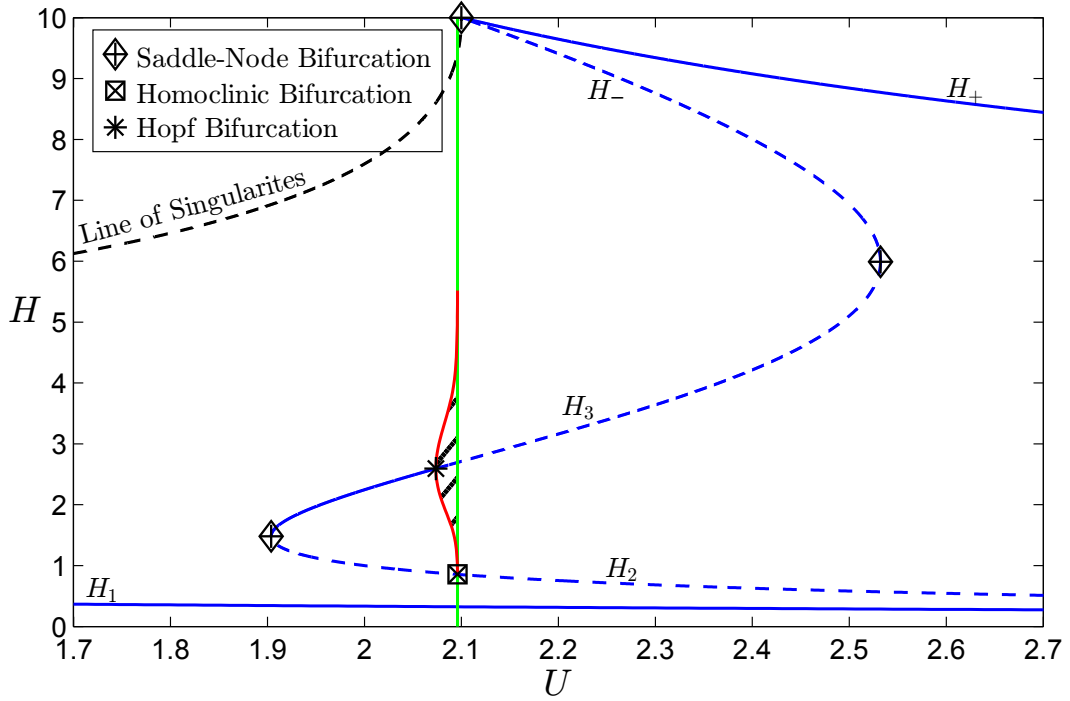


**Figure 4.7.:** The bifurcation diagram for  $\epsilon = 0.1$ ,  $\delta = 0.5$ ,  $B = -1$ ,  $F_0 = 4$ ,  
 $R_l = 50$ ,  $R_g = 50$ ,  $\lambda = 0.4$  and  $\rho = 0.1$ .

For a given set of parameters, such as those used in Figure 4.7, we can find the value of  $B$  for which a Hopf bifurcation occurs at the trivial steady state. This value is found by setting  $h = 1$  and  $U = 1 - B$ , which from (4.0.5) corresponds to  $v = 1$ , and using the Hopf bifurcation theorem solving for  $B$ . For the parameters used in Figure 4.7 this gives a supercritical Hopf bifurcation for  $h = v = 1$  when  $B = -0.22385$  and  $U = 1.22385$  from which a unique limit cycle solution bifurcates in  $U > 1.22385$ . The solutions increase in amplitude as  $U$  is increased until  $U \approx 1.24439$ , at which point there is a homoclinic bifurcation at  $H_2$ , as shown in Figure 4.8. By considering the limit cycle solution just after the Hopf bifurcation we find it has wavelength 0.51985 and hence wave number  $k = 12.18654$ . Using our analysis in Section 3.2, we can calculate the predicted propagation speed, given by

$$U = \frac{\omega_{\mathbf{I}}^+}{k}. \quad (4.3.6)$$

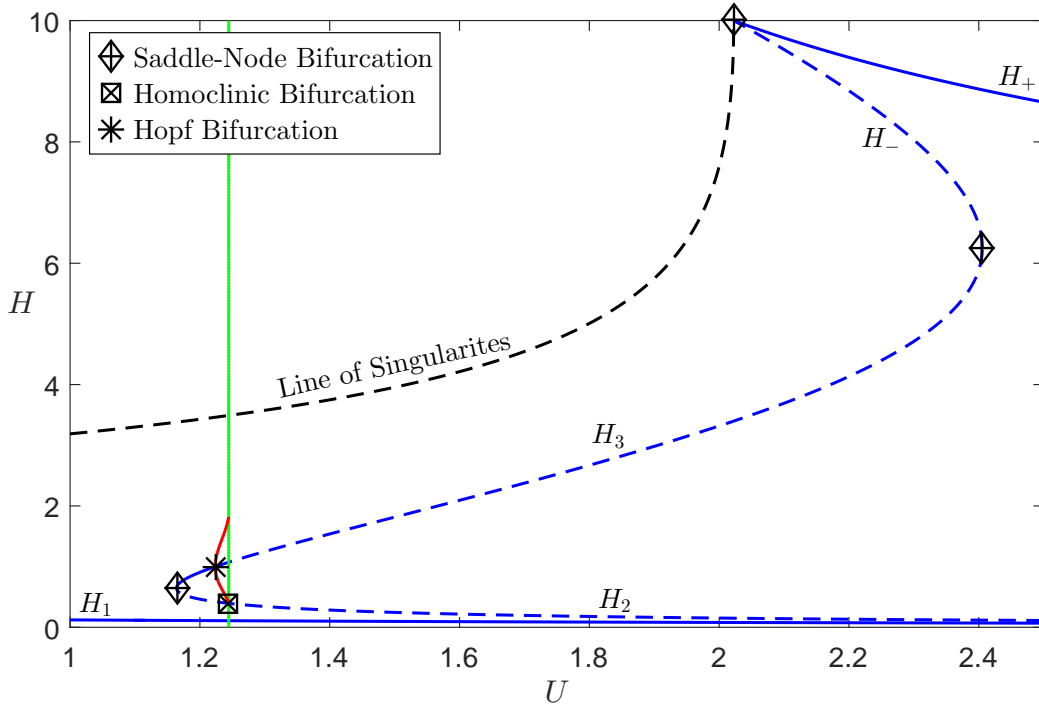


**Figure 4.8.:** The bifurcation diagram from the steady state solution where  $\epsilon = 0.1$ ,  $\delta = 0.5$ ,  $B = -0.224$ ,  $F_0 = 4$ ,  $R_l = 50$ ,  $R_g = 50$ ,  $\lambda = 0.4$  and  $\rho = 0.1$ .

In this case our linear stability analysis predicts  $U = 1.22087$ , hence gives a close match to the actual propagation speed.

We have shown it is possible for limit cycle solutions to bifurcate from the steady state, which grow in size as their propagation speed increases. As can be seen in Figure 4.8, there is a maximum amplitude and propagation speed for which the solutions exist. However, as can be seen by comparing Figures 4.7 and 4.8, if the value of  $B$  is decreased we increase the values of  $U$  for which the limit cycles exist and are able to produce larger amplitude solutions. Hence, solutions in the IVP will originate from the steady state with larger values of  $B$  and as they grow in amplitude will correspond to smaller values of  $B$ . This will be discussed in more detail in Section 5.4.

By varying the values of  $\epsilon$ ,  $\delta$ ,  $B$ ,  $F_0$ ,  $R_l$ ,  $R_g$ ,  $\lambda$  and  $\rho$ , we alter the positions of the equilibrium points and the Hopf and homoclinic bifurcations. Hence, as we kept a constant value of  $U$  in Figure 4.5 as we varied the other

parameters, we changed the point within the region where limit cycle solutions exist we were generating our solutions. As a result of this our comparisons in Figure 4.5 do not reflect the effects of varying the parameters on the system as a whole. For example, in Figure 4.5 where we have increased  $F_0$  and produced smaller solutions, this is a result of the Hopf bifurcation occurring at a larger value of  $U$  hence the solution at  $U = 2.09$  is closer to the Hopf bifurcation and hence smaller.

The periodic solution at  $U = 2.095$ , just before the homoclinic bifurcation, is shown in Figure 4.9. We can see that, although the periodic solution represents large waves, it has not produced slugs. From our work in Section 4.2 we know that we are only able to get periodic solutions that near the top of the channel for  $U \approx 1/\delta$  and due to the line of singularities we must also have  $U > 1/\delta - B\epsilon$ . Hence it is only possible to get slugs for

$$U = 1/\delta - B\epsilon + A, \quad 0 < A \ll 1. \quad (4.3.7)$$

In order for limit cycle solutions that are produced from a Hopf bifurcation on  $H_3$  to reach the top of the channel this means they must pass around both  $H_-$  and  $H_+$ . For the parameter set used in Figure 4.7 we would need  $U = 2.1 + A$  for there to be a possibility of slug solutions existing, however the limit cycle solutions only exist for  $2.074 < U < 2.095$ . In order for the limit cycles to exist where  $U = 1/\delta - B\epsilon + A$ , where we may produce slug solutions, we must increase the value of  $B$ .

Two examples of bifurcation diagrams with larger values of  $B$  can be seen in Figure 4.10 and Figure 4.11. In Figure 4.10 the parameters are the same as in Figure 4.7 except now  $B = -0.7$  and  $F_0 = 6.7$ . By comparing these figures we can see we now have a significantly larger region for which periodic solutions exist and we have periodic solutions that exist which go around  $H_-$  and  $H_+$  which near the top of the channel. Figure 4.12 shows the effect of varying effects of varying  $\epsilon$ ,  $\delta$ ,  $U$ ,  $B$ ,  $F_0$ ,  $R_l$ ,  $R_g$ ,  $\lambda$  and  $\rho$  on these solutions. In Figure 4.5 the amplitude of the waves increased as we increased  $U$  and

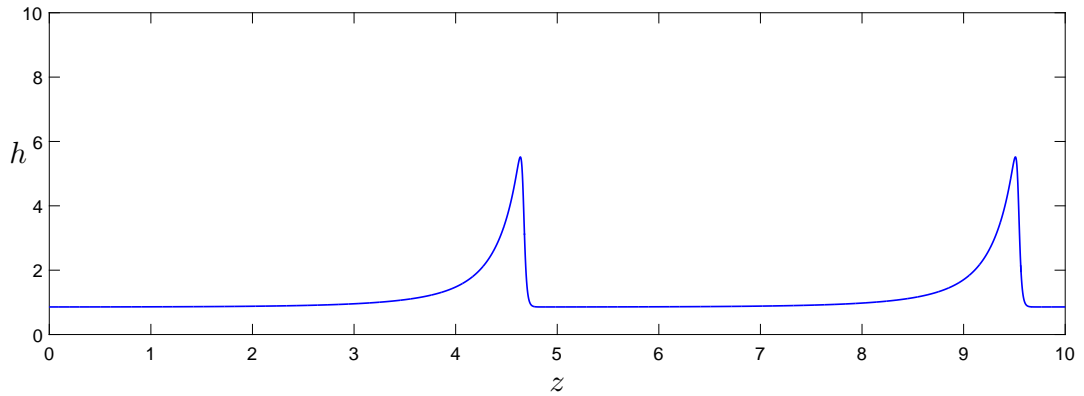


**Figure 4.9.:** The periodic solution at  $U = 2.095$ , just before the homoclinic bifurcation.

$B$ , however in Figure 4.12 the amplitude decreases as we do this as now increasing  $U$  and  $B$  moves us further from the point  $U = 1/\delta - B\epsilon$ .

Note that for Figures 4.13b - 4.29b we have used:

- yellow for stable limit cycles,
- brown for unstable limit cycles,
- red for the top right of the saddle at  $H_2$ ,
- dark blue for the bottom right of the saddle at  $H_2$ ,
- pink for the bottom right of the saddle at  $H^-$ ,
- light blue for the bottom left of the saddle at  $H^-$ ,
- green for the top left of the saddle at  $H^-$ ,

and all points outside the lines shown go to  $H_1$ .

Figure 4.10 shows the bifurcation diagram for  $\epsilon = 0.1$ ,  $\delta = 0.5$ ,  $B = -0.7$ ,  $F_0 = 6.7$ ,  $R_l = 50$ ,  $R_g = 50$ ,  $\lambda = 0.4$  and  $\rho = 0.1$  and Figures 4.13-4.19 show the corresponding periodic solutions and phase planes. For this parameter set  $w_+ = 34.047$  and  $w_- = 0.953$  which is not shown in the phase plane diagrams as it has no effect on the phase plane structure. In this case there is a Hopf bifurcation at  $H_3$  when  $U \approx 2.032$ , as  $U$  increases there are

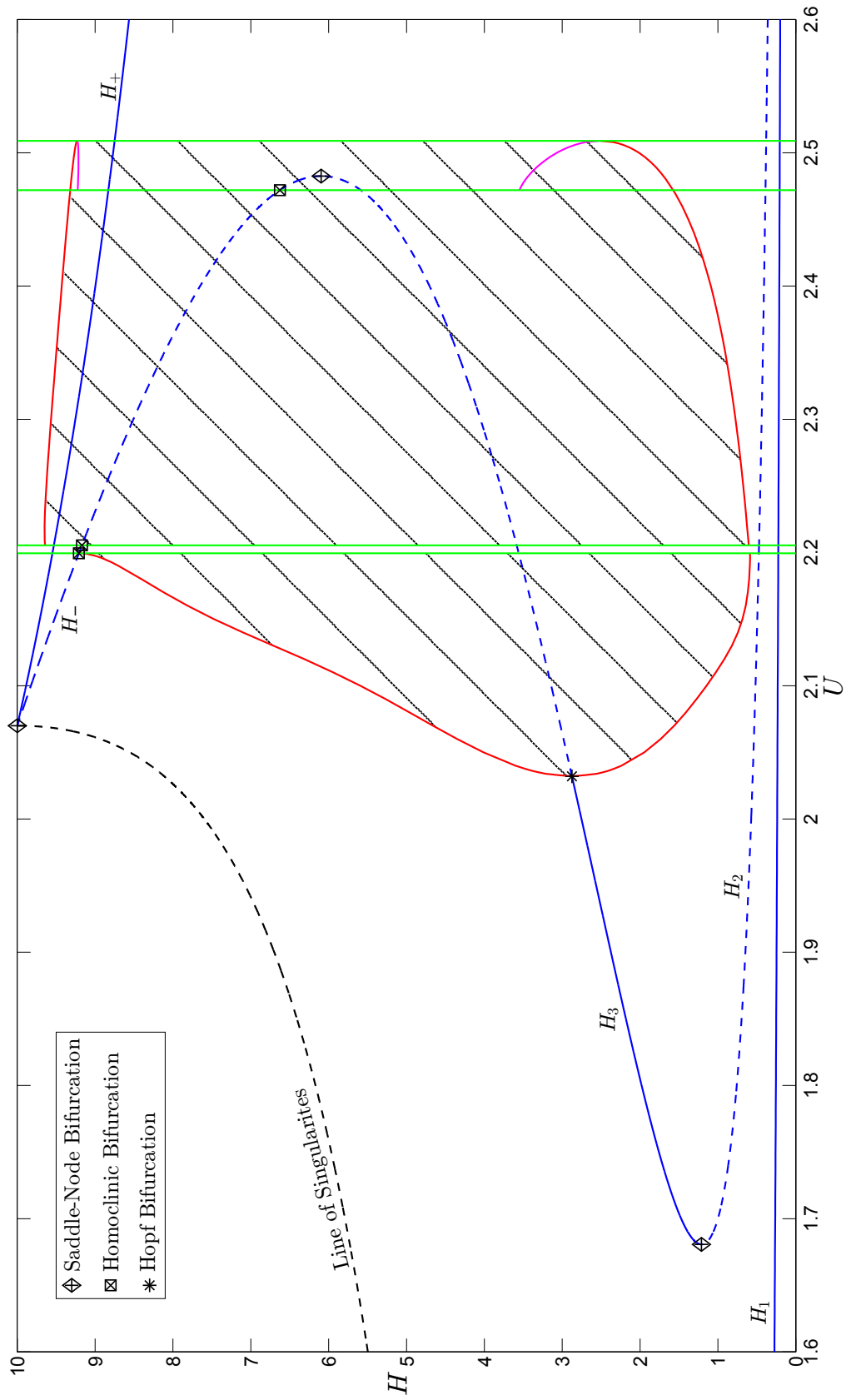


Figure 4.10.: The bifurcation diagram for  $\epsilon = 0.1, \delta = 0.5, B = -0.7, F_0 = 6.7, R_l = 50, R_g = 50, \lambda = 0.4$  and  $\rho = 0.1$ .

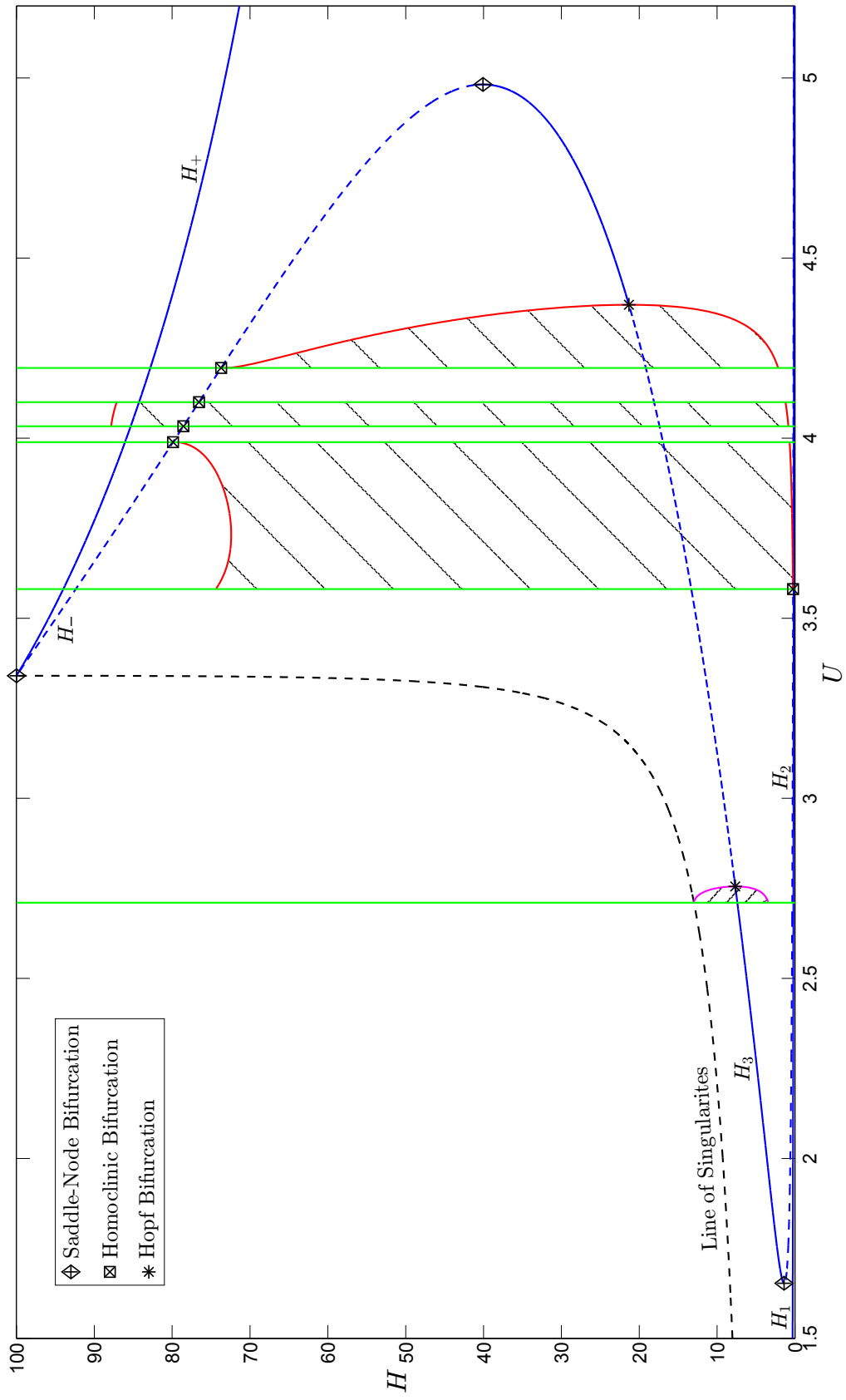
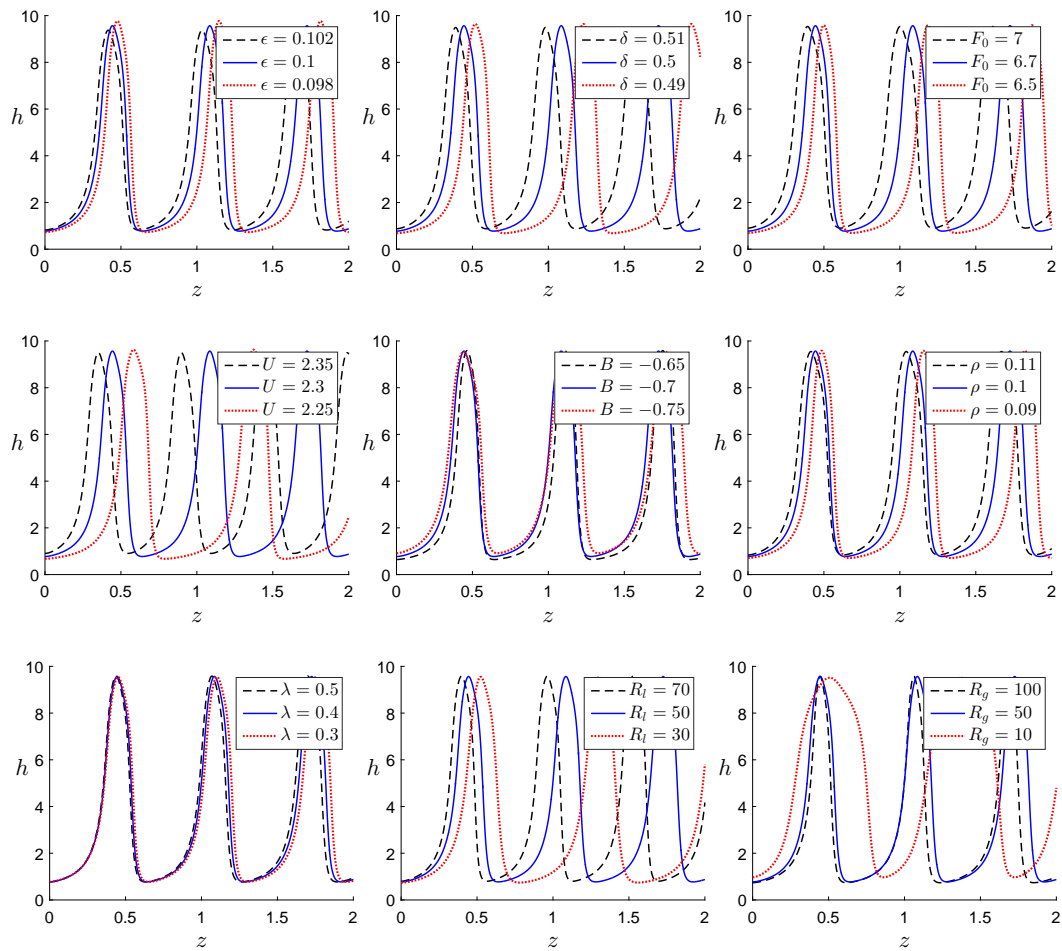


Figure 4.11.: The bifurcation diagram for  $\epsilon = 0.01$ ,  $\delta = 0.3$ ,  $B = -0.7$ ,  $F_0 = 25$ ,  $R_l = 50$ ,  $R_g = 10$ ,  $\lambda = 0.37$  and  $\rho = 0.1$ .

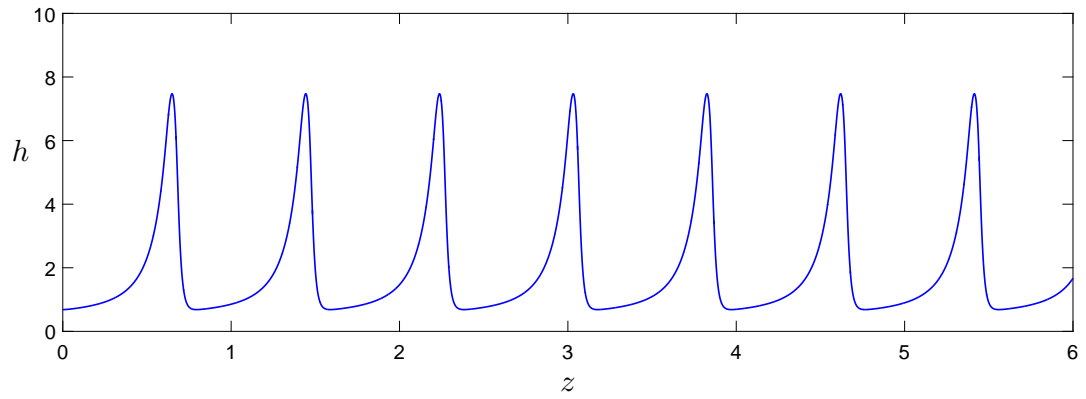


**Figure 4.12.:** The periodic solutions for the case  $\epsilon = 0.1$ ,  $\delta = 0.5$ ,  $U = 2.3$ ,  $B = -0.7$ ,  $F_0 = 6.7$ ,  $R_l = 50$ ,  $R_g = 50$ ,  $\lambda = 0.4$  and  $\rho = 0.1$  and the effect of varying the parameters.

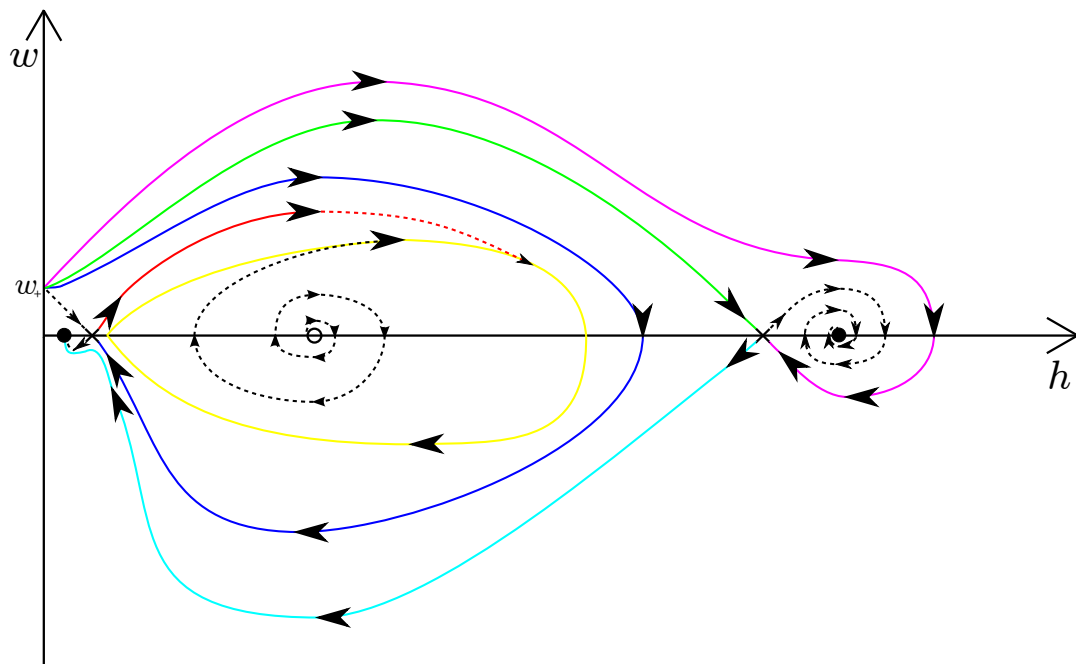
periodic solutions passing around  $H_3$  and in between  $H_2$  and  $H_-$  (shown in Figure 4.13 where the limit cycle is shown in yellow) which increase in amplitude until  $U \approx 2.199$  at which point there is a homoclinic bifurcation (hom<sub>1</sub>) at  $H_-$  (shown in Figure 4.14). As  $U$  is increased past this point there are no periodic solutions until  $U \approx 2.206$  where there is another homoclinic bifurcation at  $H_-$  (shown in Figure 4.15). By comparing Figures 4.14b and 4.15b we can see that, as  $U$  has increased, the limit cycle now passes around  $H_-$  and  $H_+$  in the phase plane, before coming back in towards  $H_-$ . This results in the periodic solutions having a 'bump'-like shape at their peak, as can be seen in Figure 4.15a. After this second homoclinic bifurcation there are periodic solutions again which decrease in amplitude as  $U$  increases and no longer pass near  $H_-$  in the phase plane, removing the 'bump'-like peak (shown in Figure 4.16). This continues until  $U \approx 2.472$ , at which point there is a third homoclinic bifurcation (hom<sub>3</sub>) at  $H_-$  inside the limit cycle which results in an unstable limit cycle (shown in Figure 4.17 where the stable and unstable periodic solutions are shown in blue and red, respectively, and the stable and unstable limit cycles are shown in yellow and dark green, respectively). Similarly to earlier, in the phase plane at hom<sub>3</sub>, the unstable limit cycle passes around  $H_3$ ,  $H_-$  and  $H_+$ , before coming back in towards  $H_-$  resulting in the unstable periodic solutions having a 'bump'-like shape at their peak. After this third homoclinic bifurcation there are both stable and unstable limit cycles (shown in Figure 4.18) where the stable periodic solution decreases in amplitude and the unstable periodic solution increases in amplitude as  $U$  increases. At  $U \approx 2.483$  there is a saddle-node bifurcation between  $H_3$  and  $H_-$  after which we continue to get both stable and unstable periodic solutions (shown in Figure 4.18) until  $U \approx 2.509$  at which point there is a periodic saddle-node bifurcation and they annihilate each other.

Recalling our definitions of roll waves and slugs from Chapter 1 we can see examples of these in Figures 4.13a-4.19a. After the Hopf bifurcation the periodic solutions resemble roll waves which increase in amplitude as  $U$  is increased, such as in Figure 4.13a. The roll waves continue to increase in

amplitude until  $U \approx 2.199$ , just before  $\text{hom}_1$ , at which point they begin to grow in width and form slugs, such as in Figure 4.14a. The largest slugs for this parameter set occur just after  $\text{hom}_2$  where  $U \approx 2.206$ , such as in Figure 4.15a, which begin to decrease in size as  $U$  is increased, such as in Figure 4.16a.

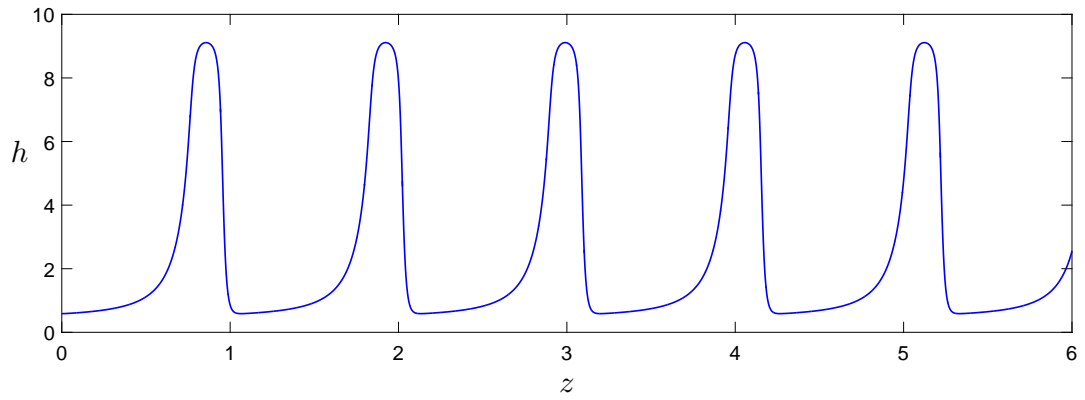


(a) The periodic solution between the Hopf bifurcation and  $\text{hom}_1$ .

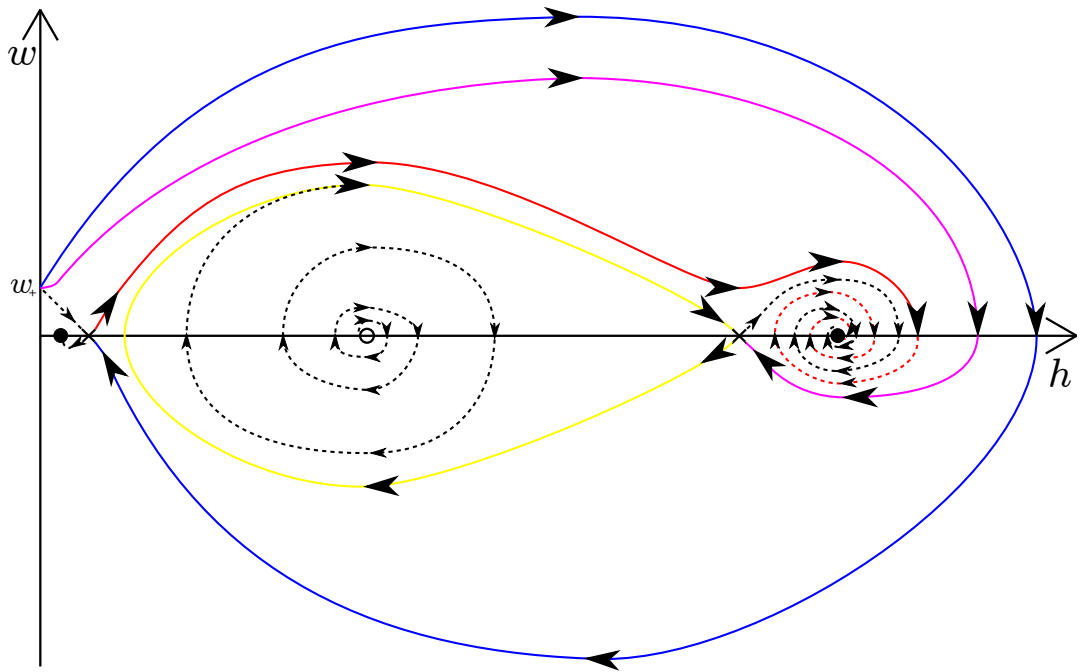


(b) The phase plane between the Hopf bifurcation and  $\text{hom}_1$ .

Figure 4.13.:  $U = 2.150$ .

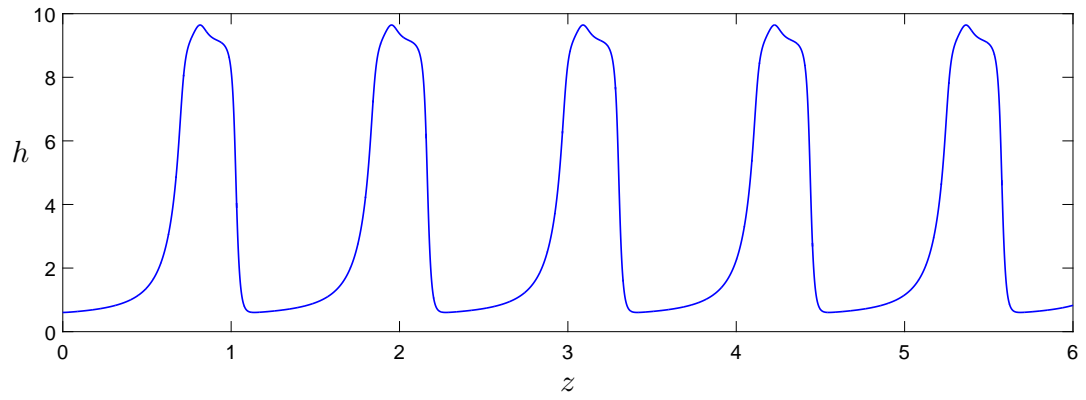


(a) The periodic solution just before  $\text{hom}_1$ .

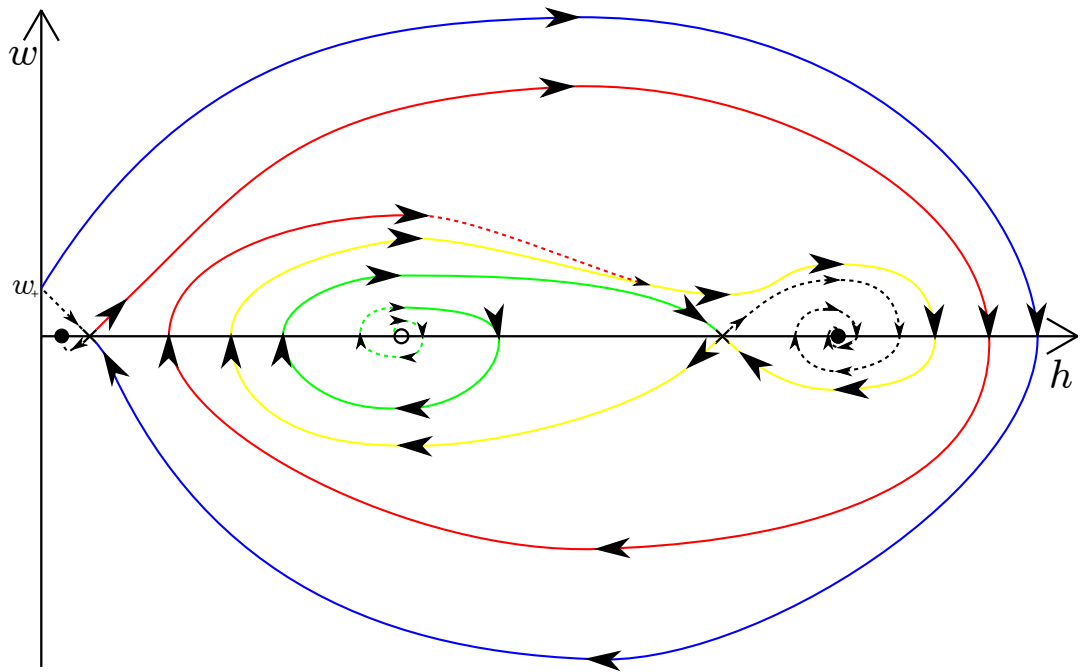


(b) The phase plane at  $\text{hom}_1$ .

Figure 4.14.:  $U = 2.199$ .

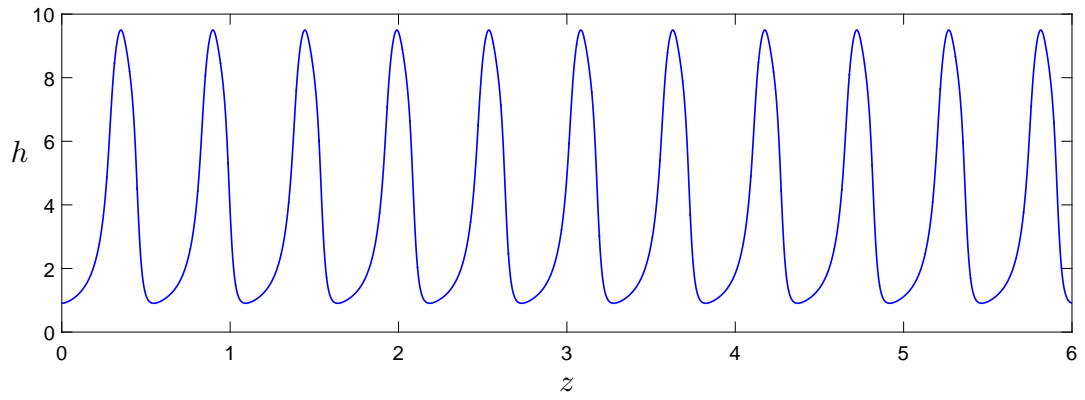


(a) The periodic solution just after  $\text{hom}2$ .

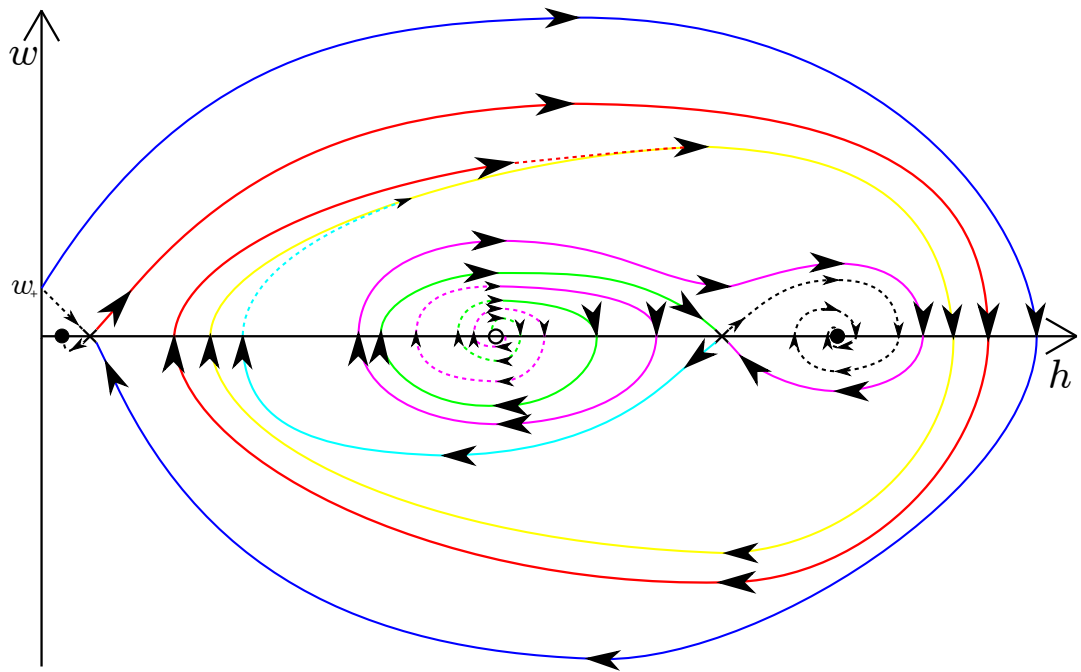


(b) The phase plane between at  $\text{hom}2$ .

Figure 4.15.:  $U = 2.206$ .

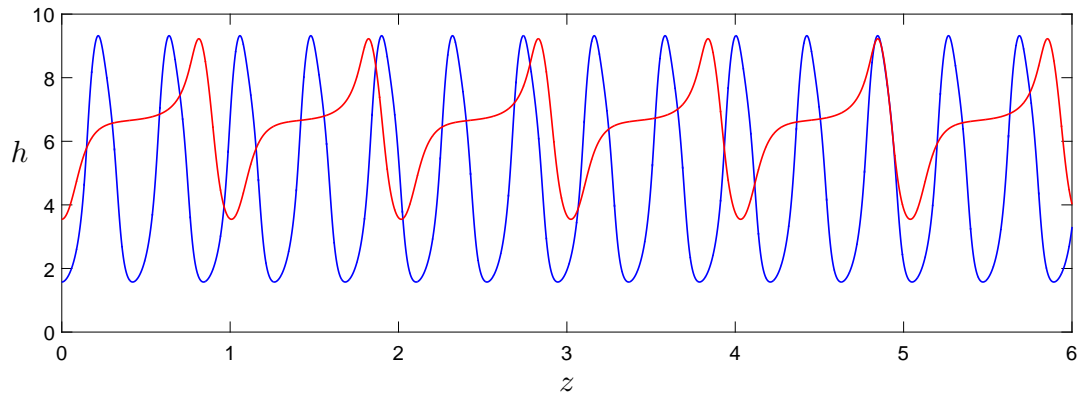


(a) The periodic solution between hom2 and hom3.

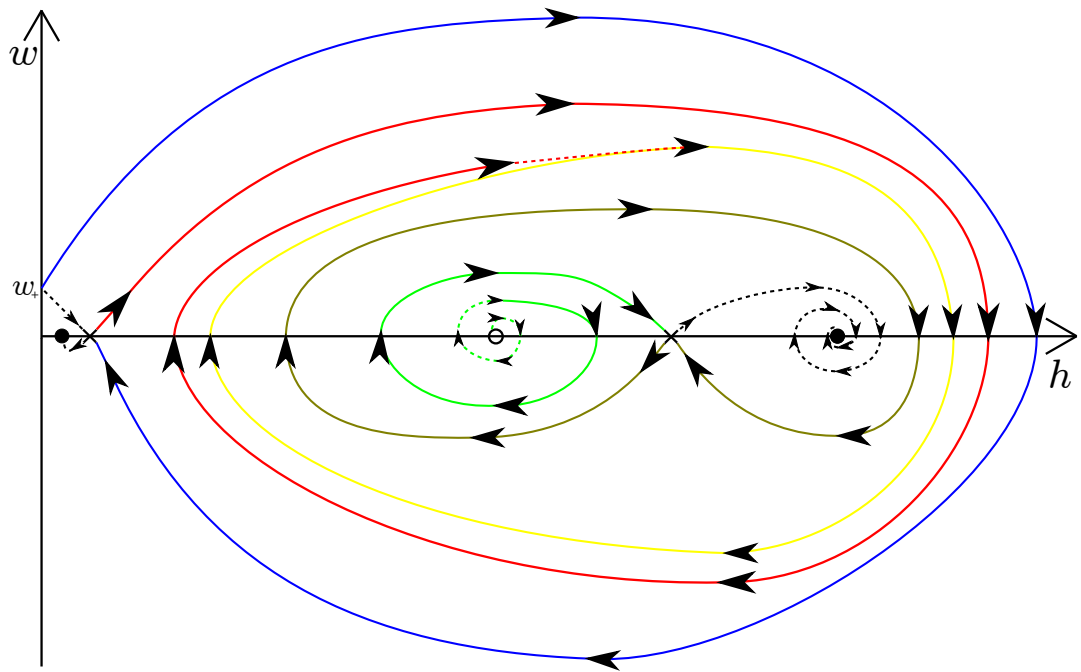


(b) The phase plane between hom2 and hom3.

Figure 4.16.:  $U = 2.350$ .

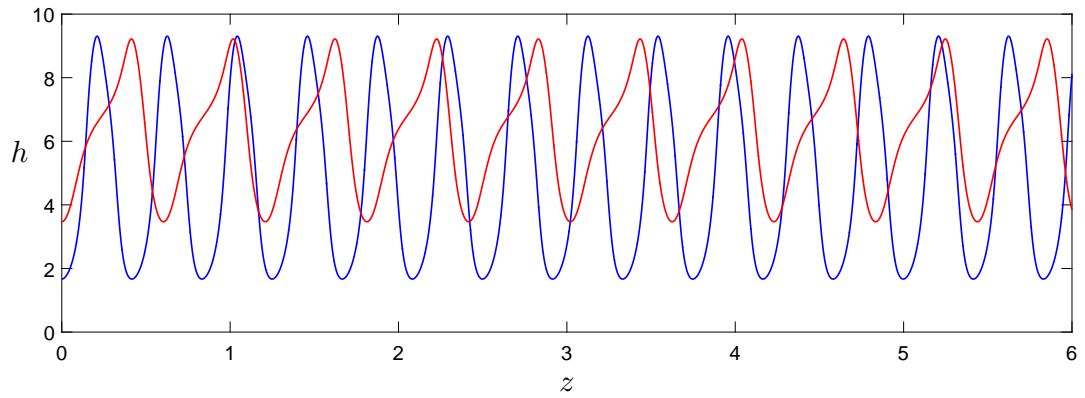


(a) The periodic solution just after  $\text{hom}_3$ .

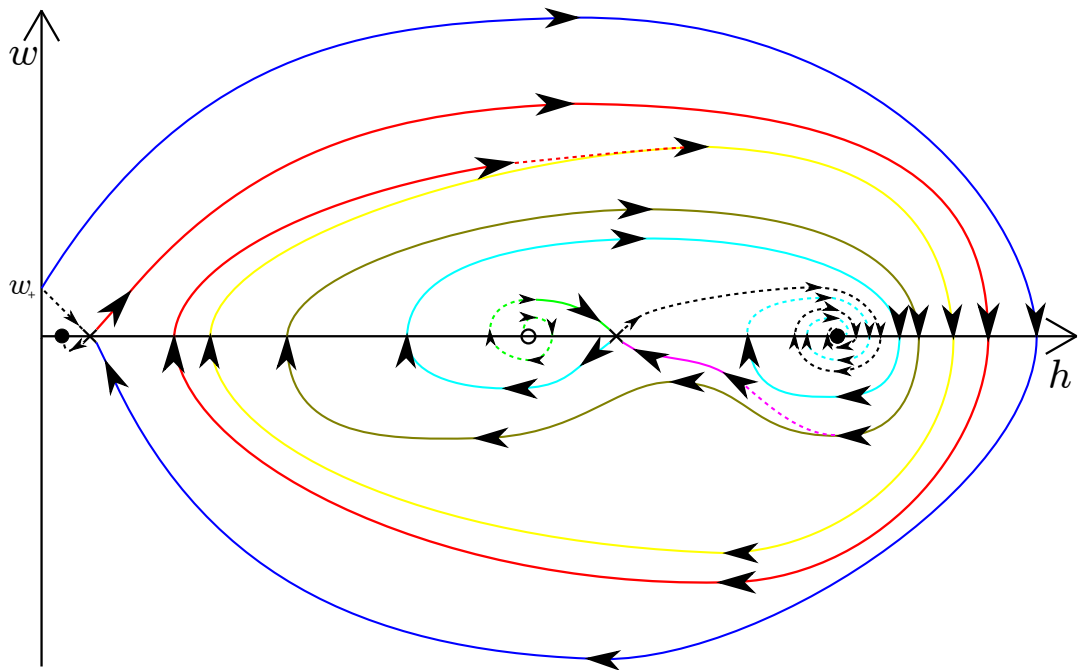


(b) The phase plane at  $\text{hom}_3$ .

Figure 4.17.:  $U = 2.472$ .

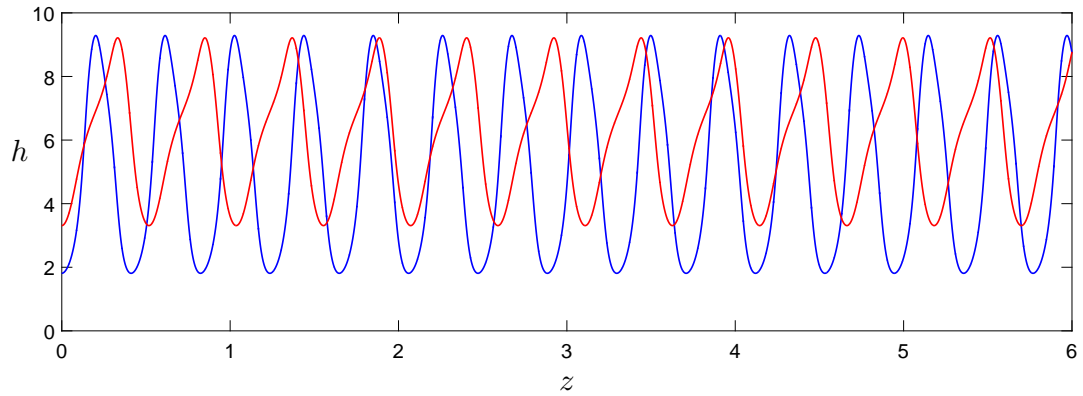


(a) The periodic solution between  $\text{hom}_3$  and the saddle-node bifurcation.

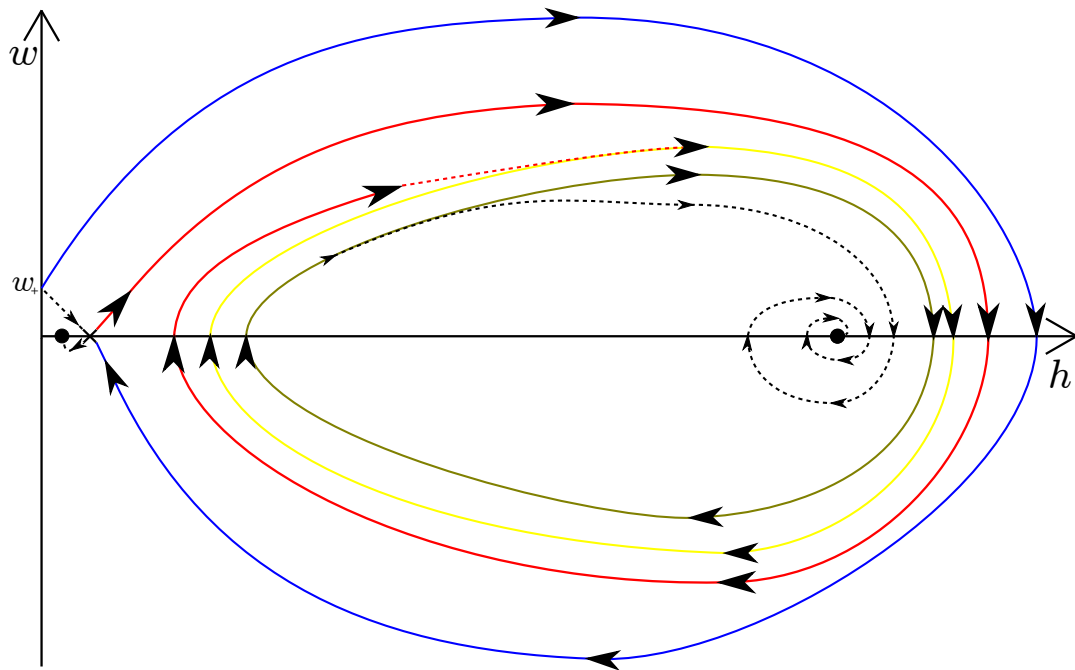


(b) The phase plane between  $\text{hom}_3$  and the saddle-node bifurcation.

**Figure 4.18.:**  $U = 2.480$ .



(a) The periodic solution between the saddle-node bifurcation and the stable-unstable limit cycle annihilation.



(b) The phase plane between the saddle-node bifurcation and the stable-unstable limit cycle annihilation.

Figure 4.19.:  $U = 2.490$ .

Figure 4.11 shows the bifurcation diagram for  $\epsilon = 0.01$ ,  $\delta = 0.3$ ,  $B = -0.7$ ,  $F_0 = 25$ ,  $R_l = 50$ ,  $R_g = 10$ ,  $\lambda = 0.37$  and  $\rho = 0.1$  and Figures 4.20-4.29 show the corresponding periodic travelling waves and phase planes. For this parameter set  $w_+ = 33.999$  and  $w_- = 1.0013$  again is not shown in the phase plane diagrams as it has no effect on the phase plane structure. In this case there are two Hopf bifurcations, the first (Hopf1) is at  $H_3$  when  $U \approx 2.755$  and is subcritical. As  $U$  decreases there are periodic solutions passing around  $H_3$  and in between the line of singularities and  $H_2$  (shown in Figure 4.20) which increase in amplitude until  $U \approx 2.710$  at which point the limit cycles reach the line of singularities (shown in Figure 4.21). From Figures 4.20 and 4.21 we can see the amplitude of the periodic travelling wave has increased as  $U$  is decreased and its peak has become a free surface corner and similar to a sawtooth wave as it reaches the line of singularities.

The second Hopf bifurcation (Hopf2) is also at  $H_3$  when  $U \approx 4.371$  and is supercritical. As  $U$  decreases there are periodic solutions passing around  $H_3$  and in between  $H_2$  and  $H_-$  (shown in Figures 4.22) which increase in amplitude until  $U \approx 4.194$  at which point there is a homoclinic bifurcation (hom1) at  $H_-$  (shown in Figure 4.23). When  $U$  is decreased past this point there are no periodic solutions until  $U \approx 4.100$  where there is a second homoclinic bifurcation (hom2) at  $H_-$  and the periodic solution also passes around  $H_-$  and  $H_+$  (shown in Figure 4.24). As  $U$  is decreased further, the amplitude of the periodic solution continues to increase until  $U \approx 4.033$ , at which point there is a third homoclinic bifurcation (hom3) at  $H_-$  (shown in Figure 4.26). As  $U$  is decreased there are no periodic solutions again until there is a fourth homoclinic bifurcation (hom4) at  $H_-$  for  $U \approx 3.989$  (shown in Figure 4.27). As  $U$  is decreased past this point there are periodic solutions again only passing around  $H_3$  and in between  $H_2$  and  $H_-$  (shown in Figures 4.28) which decrease in amplitude to a local minimum before increasing again. Finally, as  $U$  is decreased further, there is a homoclinic bifurcation (hom5) at  $H_2$  for  $U \approx 3.581$  (shown in Figure 4.29).

In the region  $4.033 < U < 4.100$ , where limit cycles exist between  $\text{hom}_2$  and  $\text{hom}_3$ , we find that although the amplitude continues to increase as  $U$  is decreased, the wavelength decreases to a local minimum at  $U \approx 4.067$  (shown in Figure 4.25) before increasing again.

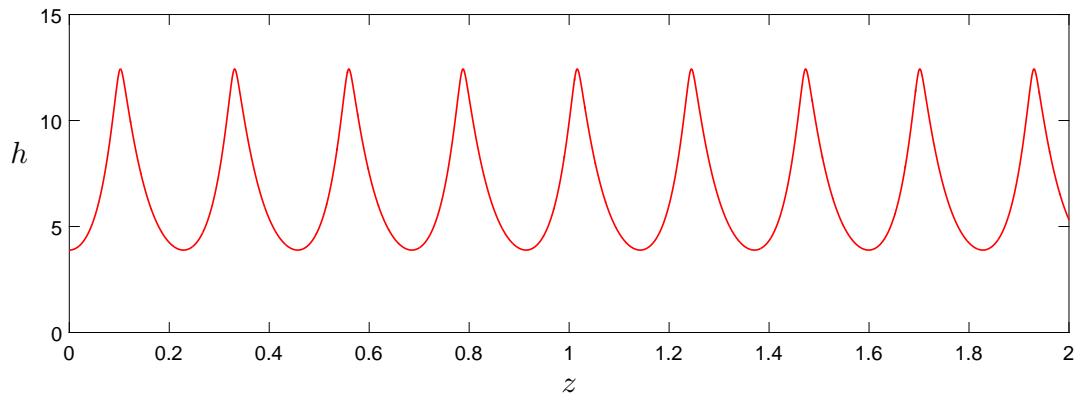
For the first set of parameters shown in Figure 4.10 we get three saddle-node bifurcations, three homoclinic bifurcations and a Hopf bifurcation. For the second set of parameters shown in Figure 4.11 we have three saddle-node bifurcations, five homoclinic bifurcations and two Hopf bifurcations. As we have seen from these two examples, there are numerous possible bifurcation diagrams we can get depending on the parameters.

#### 4.4 CONCLUSION

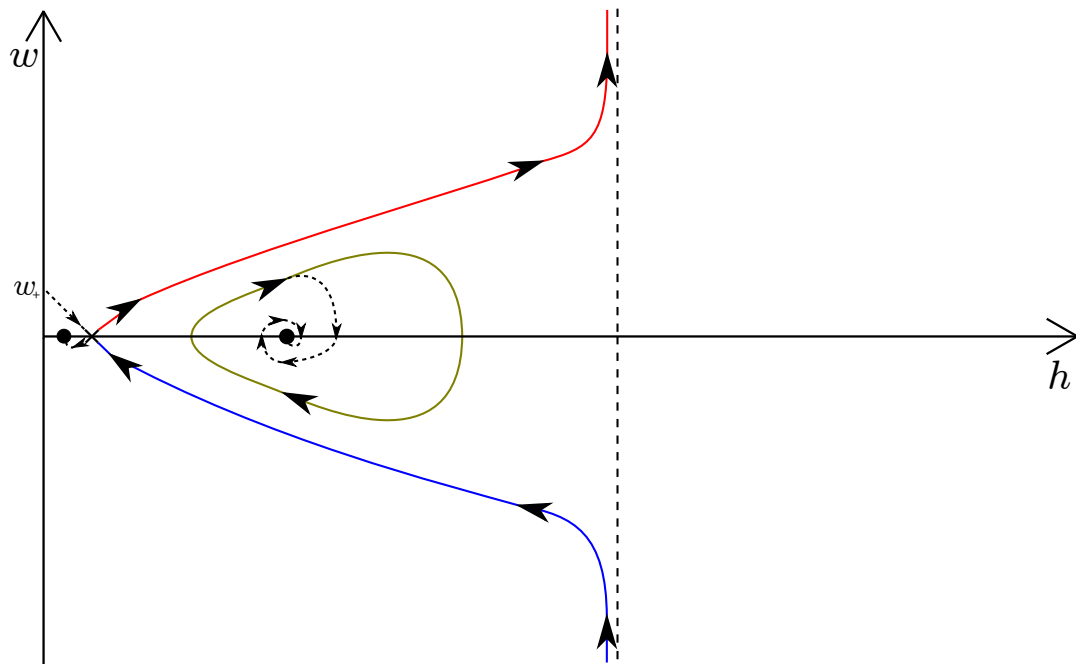
We have investigated the existence of periodic travelling wave solutions and found that for  $\delta U \approx 1$  there are two previously unknown equilibrium points ( $H_-$  and  $H_+$ ) for our system of equations that come into existence near  $\epsilon^{-1}$ . By finding asymptotic expansions for these new equilibrium points we were able to deduce that, for small  $\epsilon$ ,  $H_-$  was a saddle point and  $H_+$  a node or spiral where a Hopf bifurcation may occur. Hence, from our equilibrium points we have the possibility of:

- Hopf bifurcations at  $H_3$  and  $H_+$ ,
- homoclinic bifurcations at  $H_2$  and  $H_-$ ,
- heteroclinic bifurcations between  $H_2$  and  $H_-$
- saddle-node bifurcations between  $H_-$  and  $H_+$ ,  $H_3$  and  $H_-$  and between  $H_2$  and  $H_3$ , and
- periodic saddle-node bifurcations between stable and unstable limit cycles.

Finally we solved the system of equations numerically and found high amplitude periodic solutions. We investigated the phase plane for two sets

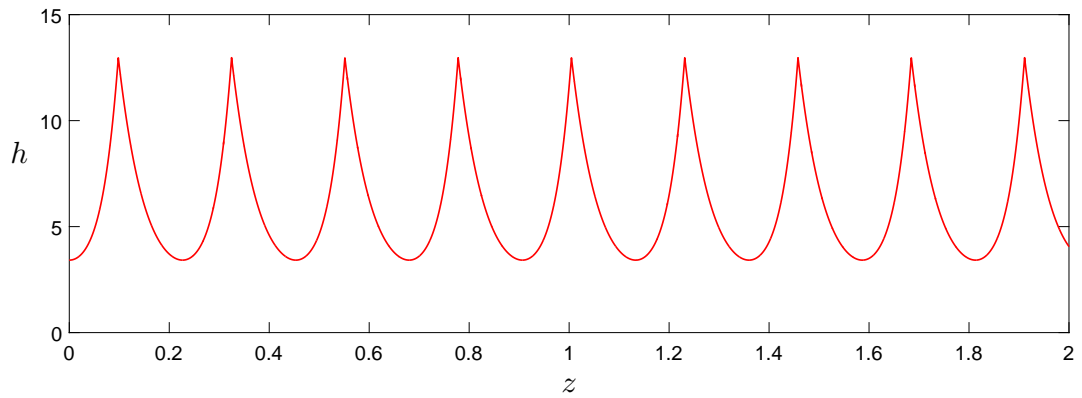


(a) The periodic solution between Hopf1 and the point at which the limit cycle reaches the line of singularities.

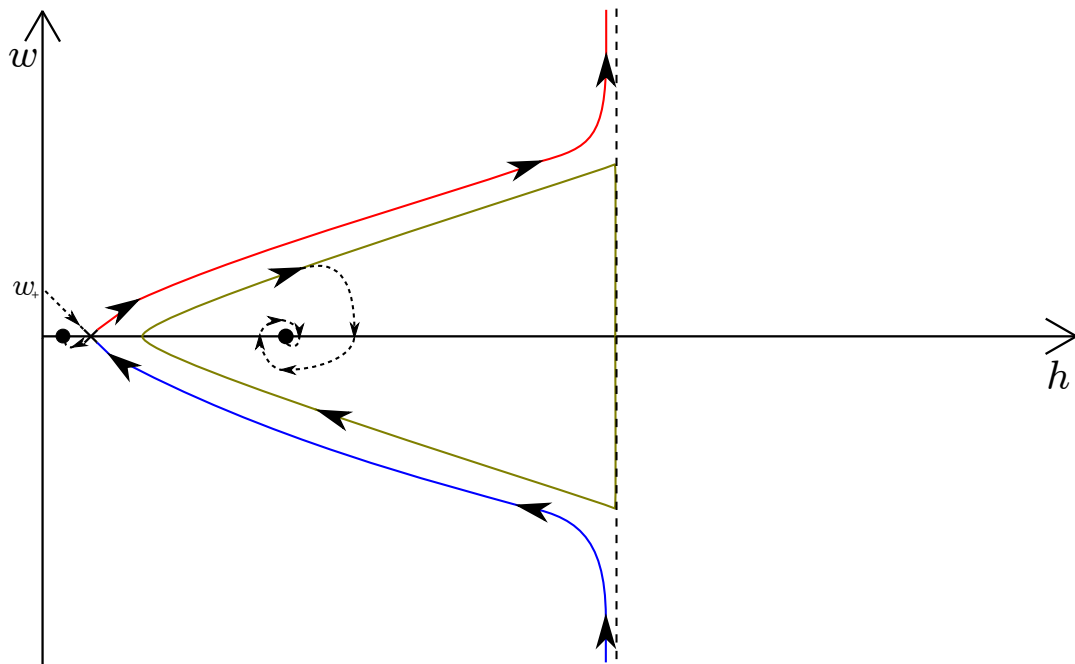


(b) The phase plane between Hopf1 and the point at which the limit cycle reaches the line of singularities.

Figure 4.20.:  $U = 2.730$ .

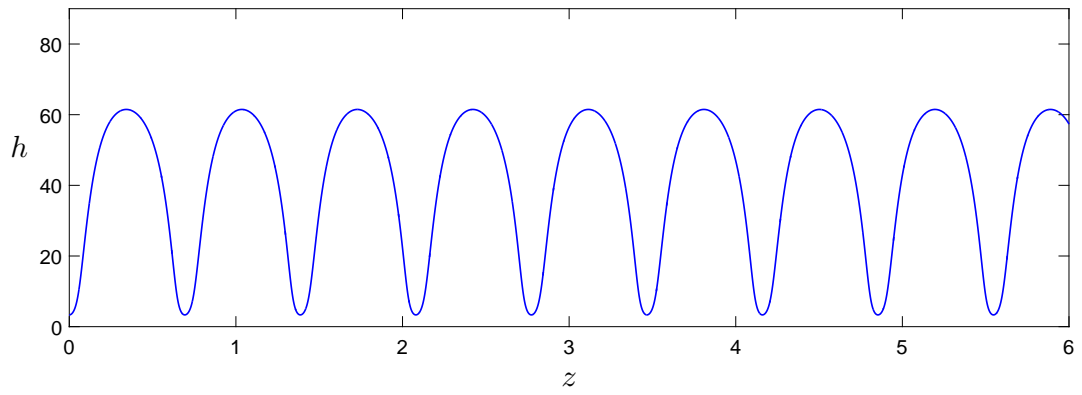


(a) The periodic solution just before the limit cycle reaches the line of singularities.

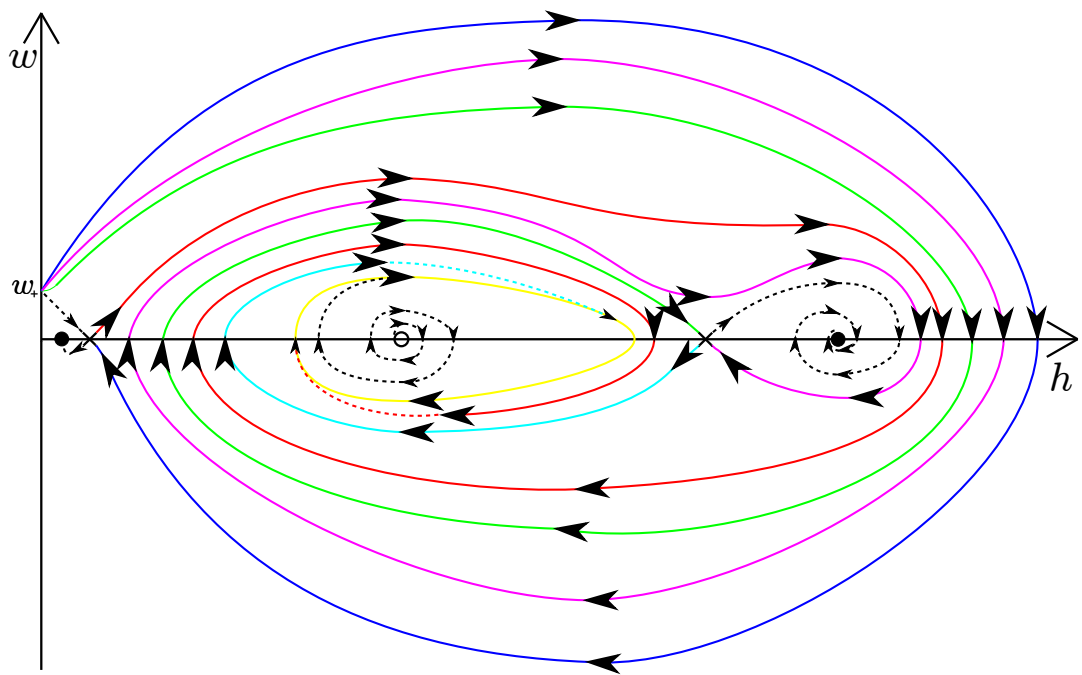


(b) The phase plane at the point when the limit cycle reaches the line of singularities.

Figure 4.21.:  $U = 2.710$ .

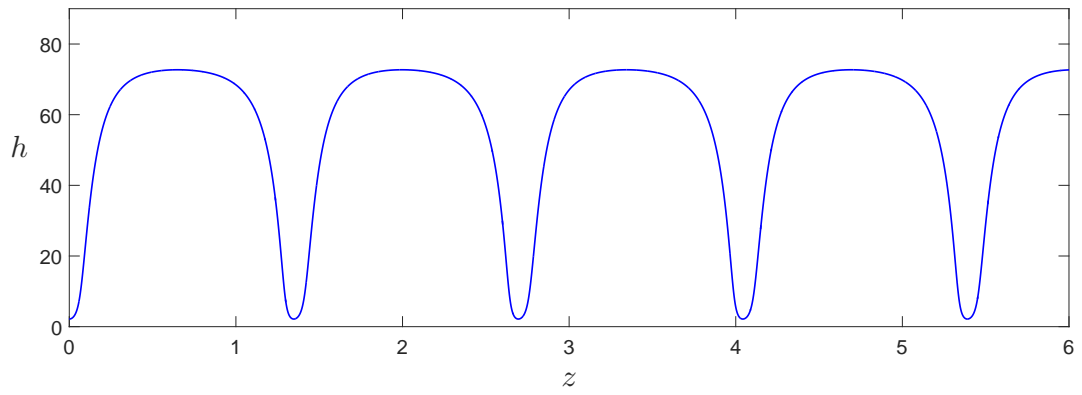


(a) The periodic solution between Hopf2 and hom1.

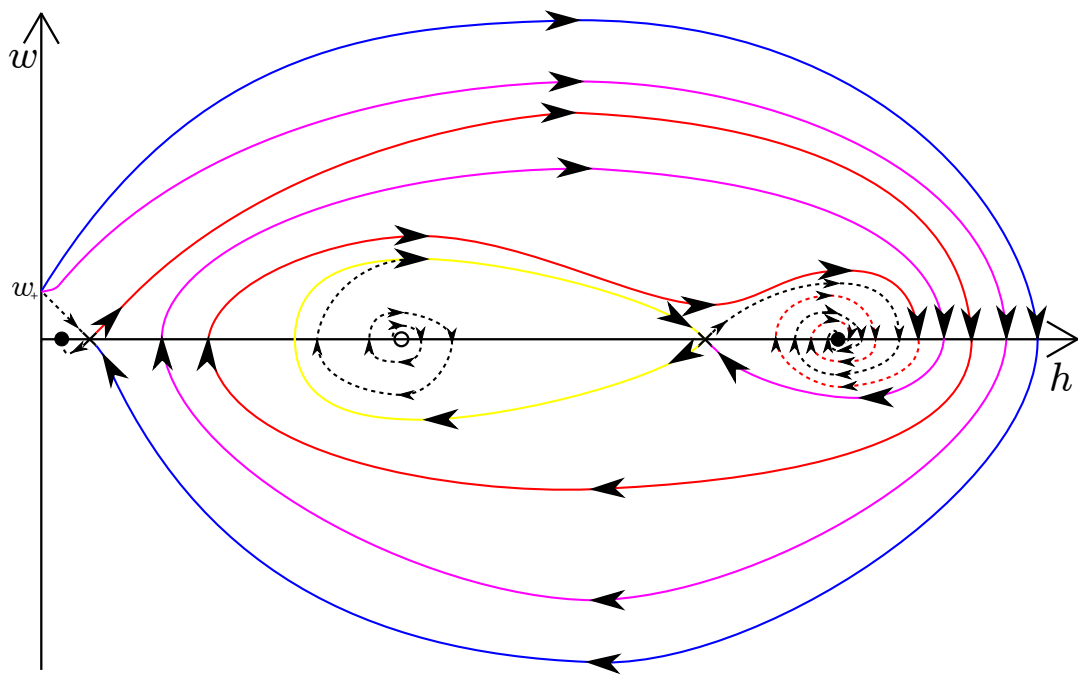


(b) The phase plane between Hopf2 and hom1.

Figure 4.22.:  $U = 4.250$ .

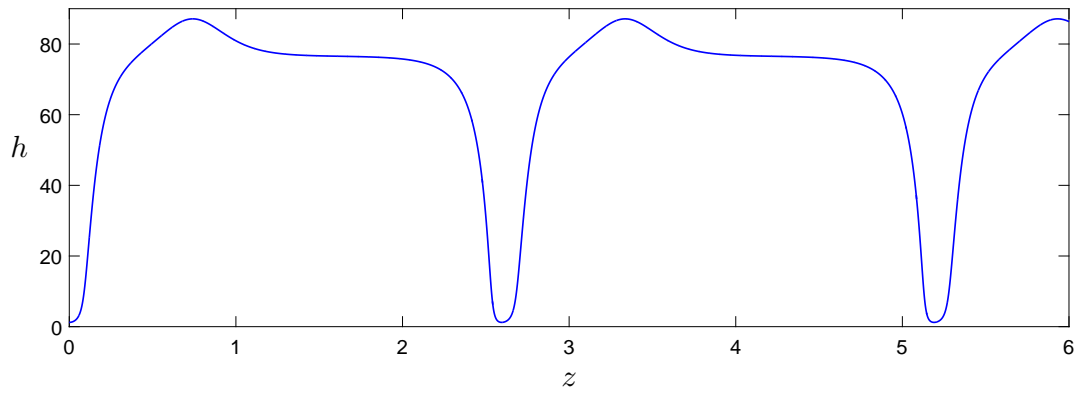


(a) The periodic solution just before  $\text{hom}_1$ .

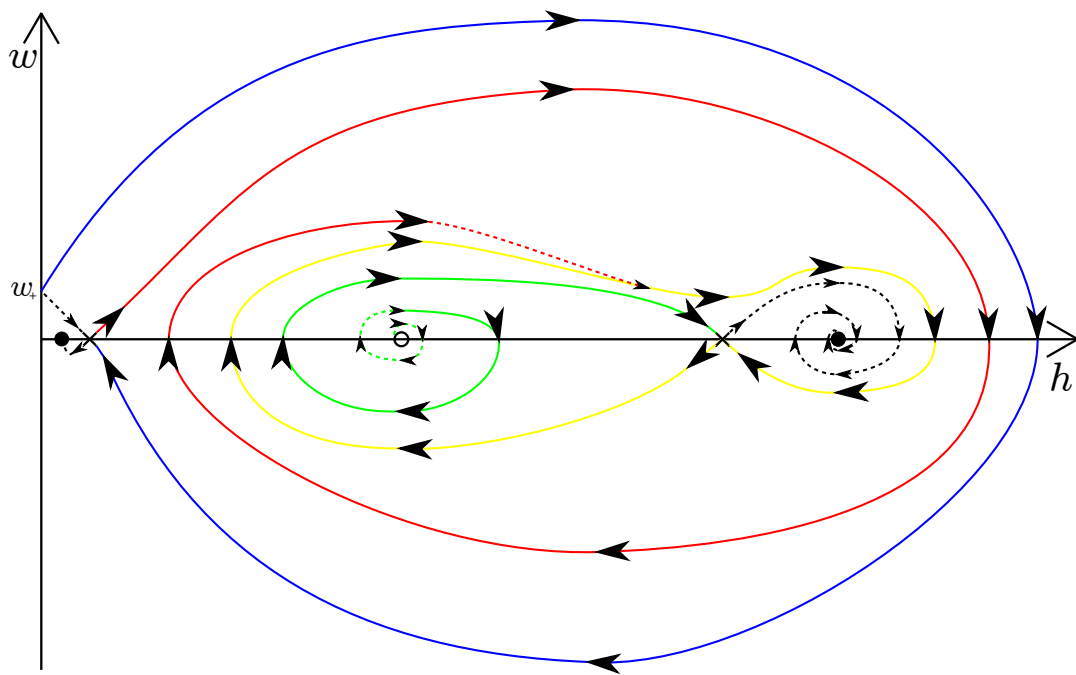


(b) The phase plane at  $\text{hom}_1$ .

Figure 4.23.:  $U = 4.194$ .

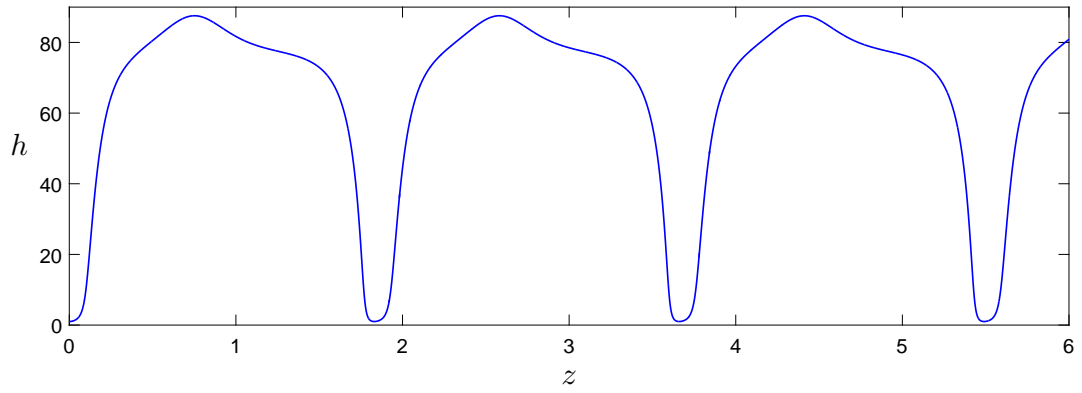


(a) The periodic solution just after  $\text{hom}2$ .

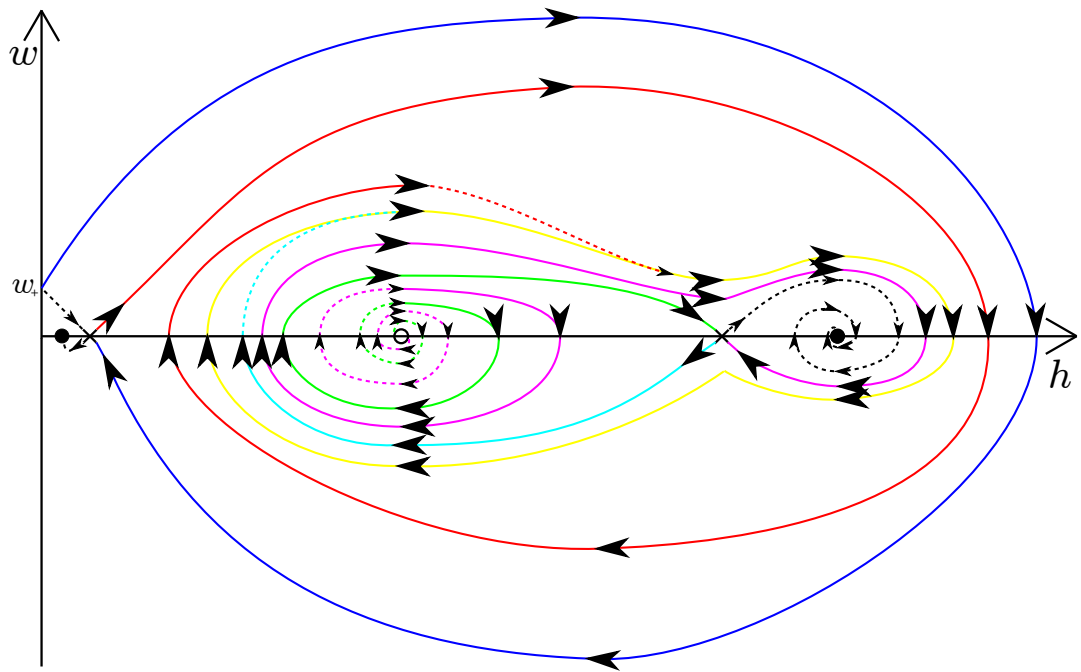


(b) The phase plane at  $\text{hom}2$ .

Figure 4.24.:  $U = 4.100$ .

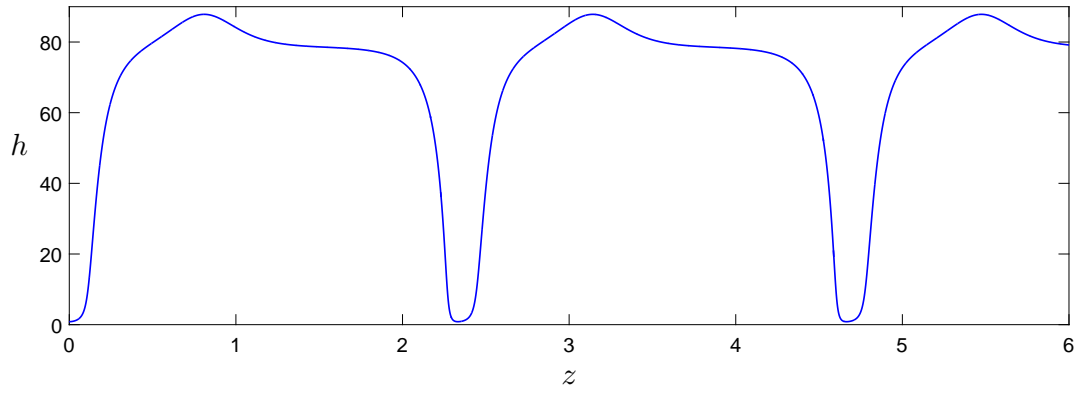


(a) The periodic solution between hom2 and hom3.

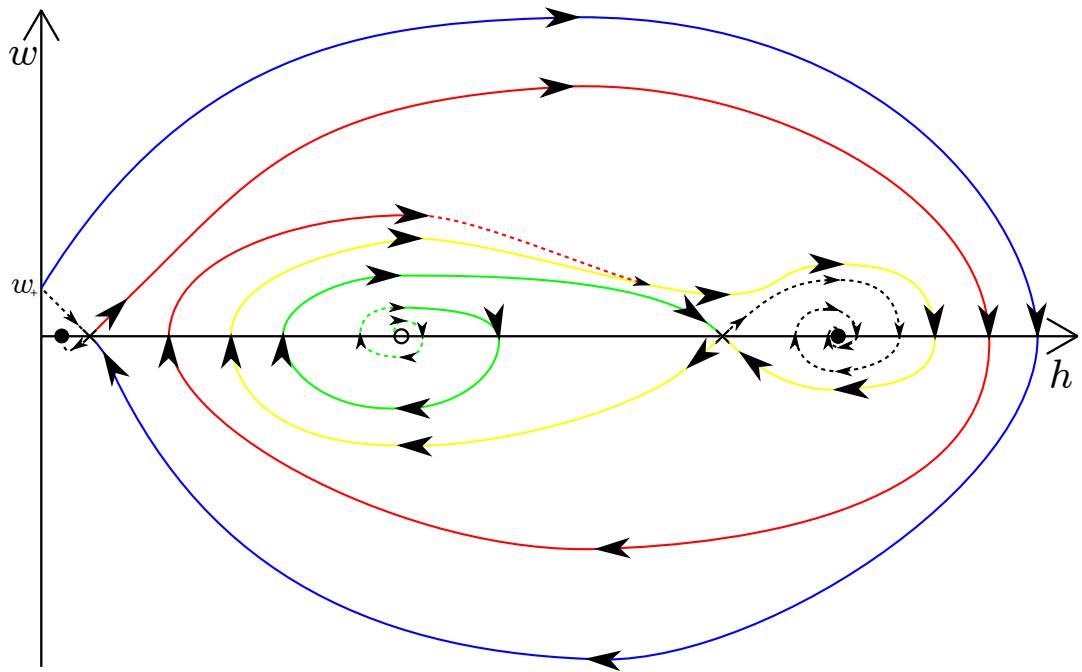


(b) The phase plane between hom2 and hom3.

Figure 4.25.:  $U = 4.067$ .

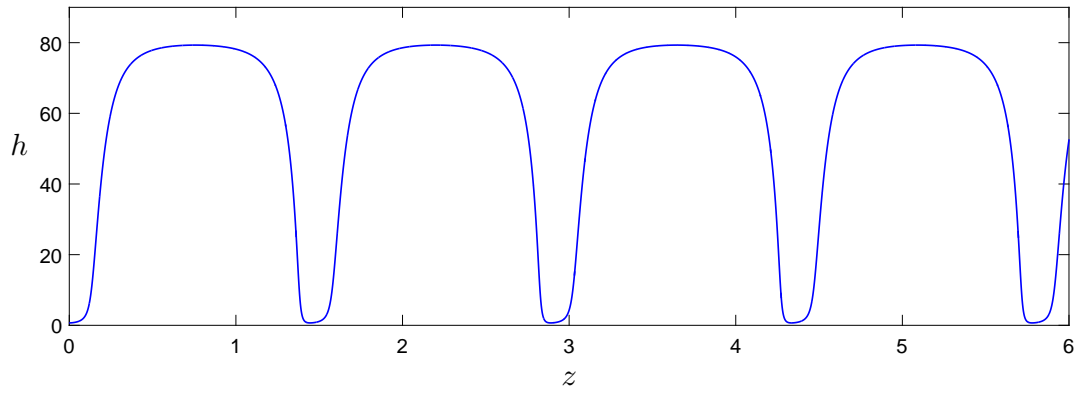


(a) The periodic solution just before  $\text{hom}_3$ .

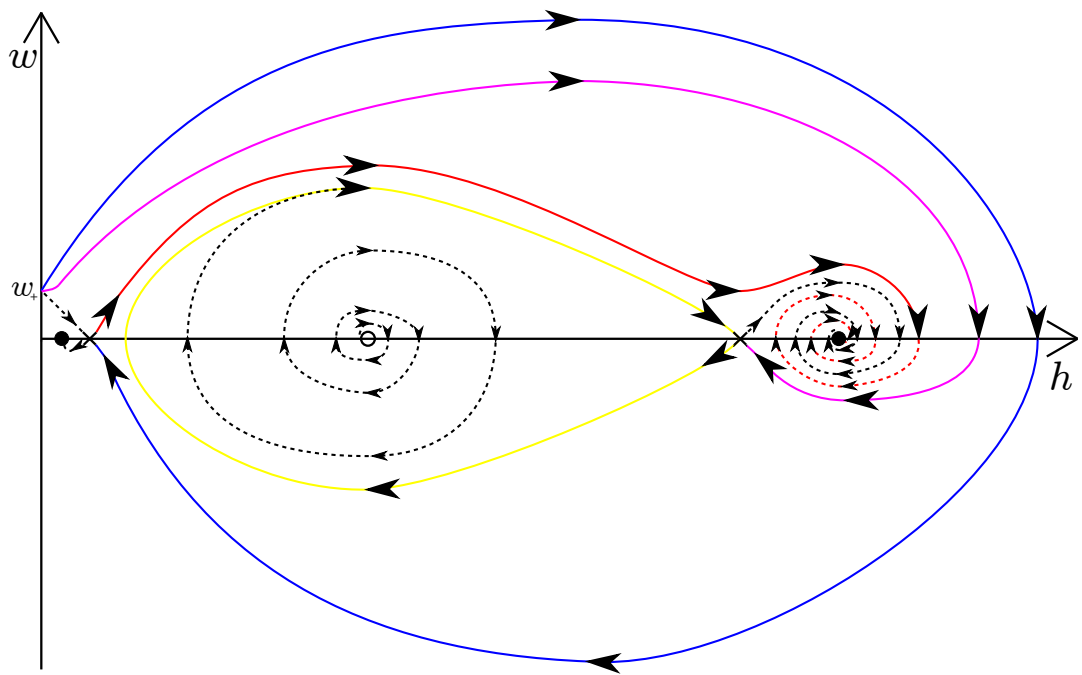


(b) The phase plane at  $\text{hom}_3$ .

Figure 4.26.:  $U = 4.033$ .

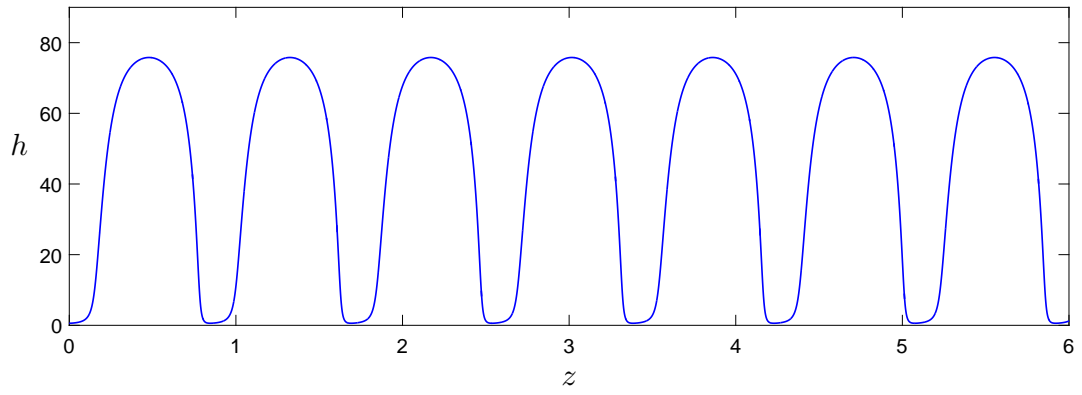


(a) The periodic solution just after  $\text{hom}_4$ .

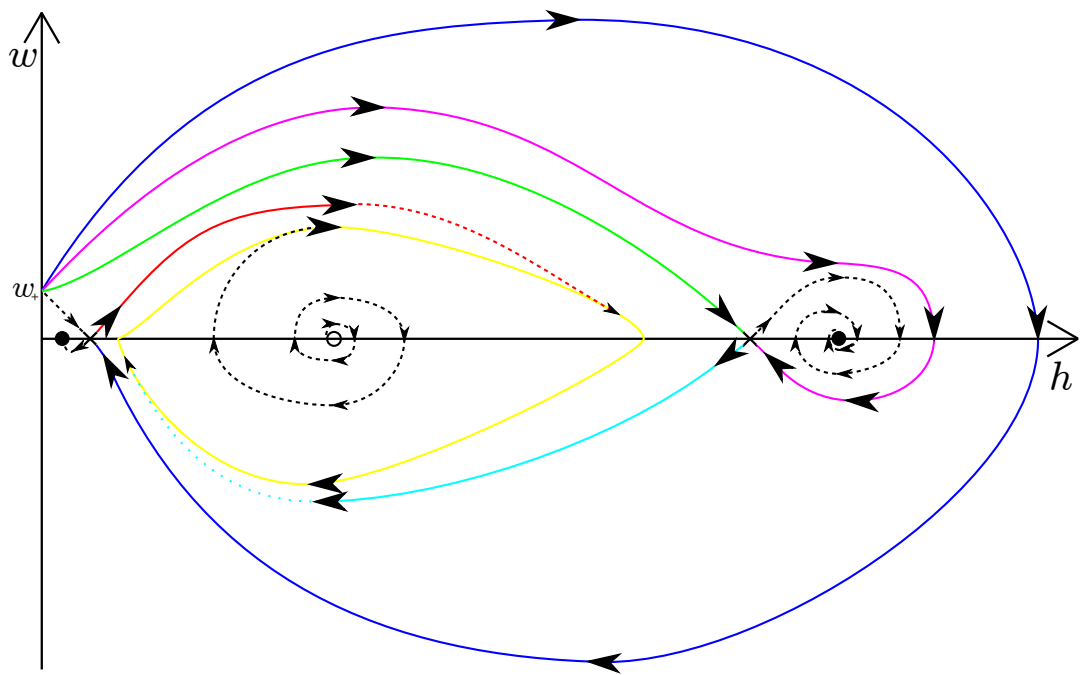


(b) The phase plane at  $\text{hom}_4$ .

Figure 4.27.:  $U = 3.989$ .

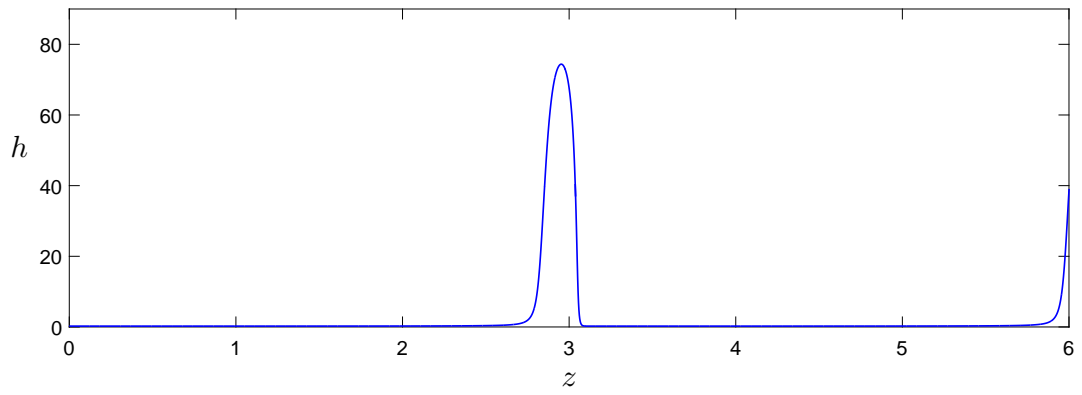


(a) The periodic solution between hom<sub>4</sub> and hom<sub>5</sub>.

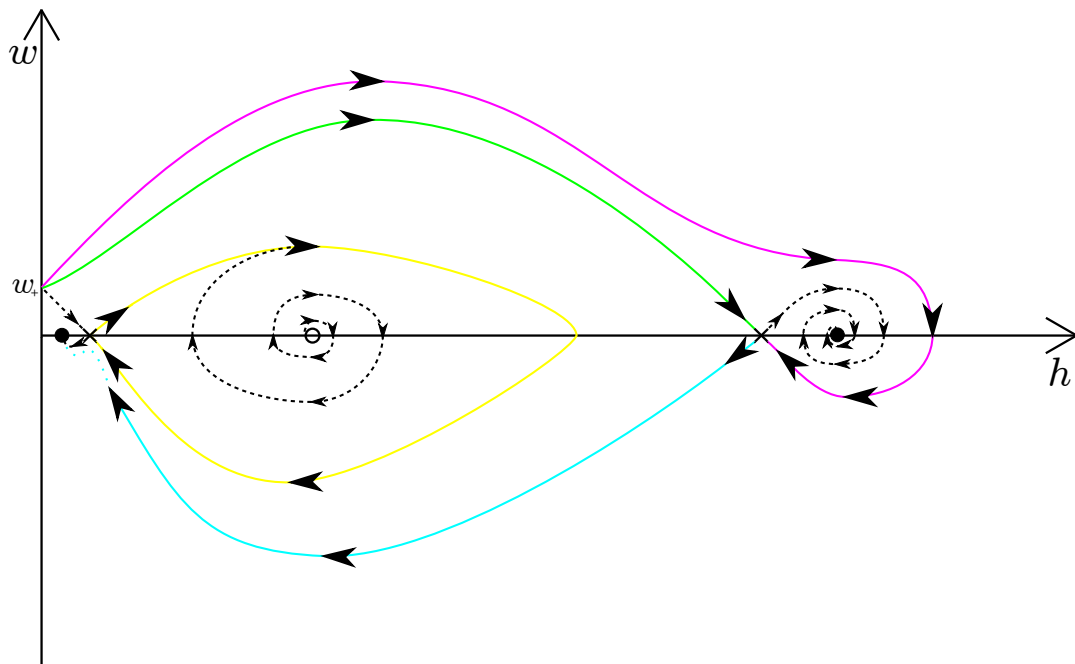


(b) The phase plane between hom<sub>4</sub> and hom<sub>5</sub>.

Figure 4.28.:  $U = 3.950$ .



(a) The periodic solution just before  $\text{hom}_5$ .



(b) The phase plane at  $\text{hom}_5$ .

**Figure 4.29.:**  $U = 3.581$ .

of parameters while varying  $U$ . In one we found one Hopf bifurcation, two homoclinic bifurcations and a periodic saddle-node bifurcation which resulted in two separate regions in which periodic solutions can exist and which contain both stable and unstable limit cycle solutions which result in a stable-unstable limit cycle annihilation. In the other we found two Hopf bifurcations and five homoclinic bifurcations which resulted in four separate regions in which periodic solutions can exist. As we have many parameters and the phase planes are extremely complicated, an exhaustive catalogue of possibilities is not feasible, hence further research in this area is needed in order to achieve an understanding of the whole phase portrait.

By using periodic travelling wave theory we now have more insight into how the parameters affect the system and have shown the possibility for the existence of slugs, such as those shown in Figure 4.14a. However periodic travelling wave theory does not tell us about the stability of those travelling waves in the full system, hence we will solve our governing equations as an initial value problem.

---

## INITIAL VALUE PROBLEM

---

In order to improve our understanding of how slugs form and the effects our parameters have we will now solve the governing equations as an initial value problem. We will use the finite-difference method derived by Kurganov and Tadmor [114] combined with a second-order Runge-Kutta method which requires our equations in the form

$$\frac{\partial}{\partial t}u(x,t) + \frac{\partial}{\partial x}f(u(x,t)) = \frac{\partial}{\partial x}Q[u(x,t), u_x(x,t)] + R(u(x,t)). \quad (5.0.1)$$

Hence, we will begin this chapter by re-writing our equations from Chapter 2 so that they are in this form. We will use periodic boundary conditions to analyse the effect of varying the spatial step size,  $\Delta x$ , in order to choose a value that will give us the necessary accuracy and a practical run-time. We will then investigate how rapidly small disturbances to the uniform flow grow and compare the results with those predicted in Chapter 3 in order to verify our earlier work. We will then use solutions found using `bvp5c` as our initial condition in the IVP problem to investigate the stability of those travelling waves found in Chapter 4. Finally, we will use inlet and outlet conditions to simulate the flow through a channel for  $F_0 > F_c$  and investigate the effects of varying our parameters.

By using more precise information on the local propagation speeds, Kurganov and Tadmor [114] have derived a second order accurate scheme that does not rely on the characteristics of the problem other than the local wave

speeds. It does not generate spurious oscillations and, of particular importance in our work, is able to capture shocks. As it is a central scheme it is not tied to the specific eigenstructure of the problem so is straightforward to use and, compared with other similar schemes, has a much smaller numerical viscosity.

## 5.1 FORMULATION OF EQUATIONS

In Chapter 2 we derived the system of equations for our model. By combining (2.2.15) and (2.2.16) using (2.2.17) but not (2.1.10), as we originally did, and dropping the bars from  $\bar{u}$  for convenience, we have the equations of motion as

$$h_t + [hu_l]_x = 0, \quad (5.1.1)$$

$$\begin{aligned} & [\rho_l u_l - \rho_g u_g]_t + \left[ \frac{1}{2} \rho_l u_l^2 - \frac{1}{2} \rho_g u_g^2 + (\rho_l - \rho_g) g h \right]_x \\ &= -\frac{\rho_l c_l u_l^2}{h} + \frac{\rho_g c_g u_g^2}{a-h} + \frac{a \rho_g c_l^g}{h(a-h)} (u_g - u_l) |u_g - u_l| + \frac{\mu_l}{h} [hu_{lx}]_x \\ & \quad - \frac{\mu_g}{a-h} [(a-h)u_{gx}]_x, \end{aligned} \quad (5.1.2)$$

and, as in (2.1.10),

$$u_g = \frac{au_h - hu_l}{a-h}. \quad (5.1.3)$$

Using the scales (2.3.1), dimensionless constants (2.3.2), defining

$$u = \frac{u_g}{u_l^0}, \quad (5.1.4)$$

and dropping the primes for convenience, (5.1.1), (5.1.2) and (5.1.3) non-dimensionalise to

$$h_t + [hv]_x = 0, \quad (5.1.5)$$

$$\begin{aligned}
 [v - \rho u]_t + \left[ \frac{1}{2} (v^2 - \rho u^2) + \frac{1 - \rho}{F_0^2} h \right]_x \\
 = \frac{1}{R_l h} [h v_x]_x - \frac{\rho}{R_g (1 - \epsilon h)} [(1 - \epsilon h) u_x]_x - \frac{v^2}{h} \\
 + \frac{\rho c_l^g}{c_l} \left( \frac{u^2}{\lambda (1 - \epsilon h)} + \frac{(u - v) |u - v|}{h (1 - \epsilon h)} \right), \quad (5.1.6)
 \end{aligned}$$

and

$$u = \frac{1 - \epsilon \delta h v}{\delta (1 - \epsilon h)}. \quad (5.1.7)$$

At the inlet we assume the flow is at an equilibrium, hence (5.1.6) reduces to

$$\frac{\rho c_l^g}{c_l} = \frac{\lambda \delta^2 (1 - \epsilon)^3}{(1 - \epsilon \delta)^2 + \lambda (1 - \delta)^2}, \quad (5.1.8)$$

which when substituted back into (5.1.6) gives

$$\begin{aligned}
 [v - \rho u]_t + \left[ \frac{1}{2} (v^2 - \rho u^2) + \frac{1 - \rho}{F_0^2} h \right]_x \\
 = \frac{1}{R_l h} [h v_x]_x - \frac{\rho}{R_g (1 - \epsilon h)} [(1 - \epsilon h) u_x]_x - \frac{v^2}{h} \\
 + \frac{\delta^2 (1 - \epsilon)^3}{(1 - \epsilon \delta)^2 + \lambda (1 - \delta)^2} \left( \frac{u^2}{1 - \epsilon h} + \frac{\lambda (u - v) |u - v|}{h (1 - \epsilon h)} \right). \quad (5.1.9)
 \end{aligned}$$

It is important to note that if the liquid forms a slug and begins to reach the top of the channel ( $h \rightarrow \epsilon^{-1}$ ) the governing equations become invalid. At this point the shear stresses between the wall and the gas and between the gas and the liquid will decrease to zero as the liquid height increases to the top of the channel. As our model does not take this into account we must make a small modification to our equations in order for them to be solved numerically. We will multiply the terms representing the gas-wall and gas-liquid shear by

$$1 - \exp\left(-\frac{(1 - \epsilon h)^3}{\epsilon^3}\right), \quad (5.1.10)$$

which will only have an effect on the solutions as they near the top of the channel. As the gas-wall and gas-liquid shear terms contain  $(1 - \epsilon h)^{-3}$  we have used  $(1 - \epsilon h)^3 \epsilon^{-3}$  so that (5.1.10) takes effect at the same rate. Applying (5.1.10) to (5.1.9) gives

$$\begin{aligned}
 & [v - \rho u]_t + \left[ \frac{1}{2} (v^2 - \rho u^2) + \frac{1 - \rho}{F_0^2} h \right]_x \\
 &= \frac{1}{R_l h} [h v_x]_x - \frac{\rho}{R_g (1 - \epsilon h)} [(1 - \epsilon h) u_x]_x - \frac{v^2}{h} \\
 & \quad + \frac{\delta^2 (1 - \epsilon)^3}{(1 - \epsilon \delta)^2 + \lambda (1 - \delta)^2} \left( \frac{u^2}{1 - \epsilon h} + \frac{\lambda (u - v) |u - v|}{h (1 - \epsilon h)} \right) \left( 1 - e^{-\frac{(1 - \epsilon h)^3}{\epsilon^3}} \right).
 \end{aligned} \tag{5.1.11}$$

Note that this is a numerical fix that should not affect the formation of slugs. We now define

$$q = v - \rho u, \tag{5.1.12}$$

which, when combined with (5.1.7), gives

$$v = \frac{\rho + \delta (1 - \epsilon h) q}{\delta [1 - (1 - \rho) \epsilon h]}, \tag{5.1.13}$$

and

$$u = \frac{1 - \epsilon \delta h q}{\delta [1 - (1 - \rho) \epsilon h]}, \tag{5.1.14}$$

where  $v = v(h, q)$  and  $u = u(h, q)$ . Hence, by defining

$$f_h = h v, \tag{5.1.15}$$

$$f_q = \frac{1}{2} (v^2 - \rho u^2) + \frac{1 - \rho}{F_0^2} h, \tag{5.1.16}$$

$$Q_v = h v_x, \tag{5.1.17}$$

$$Q_u = (1 - \epsilon h)u_x, \quad (5.1.18)$$

$$R = -\frac{v^2}{h} + \frac{\delta^2(1 - \epsilon)^3}{(1 - \epsilon\delta)^2 + \lambda(1 - \delta)^2} \left( \frac{u^2}{1 - \epsilon h} + \frac{\lambda(u - v)|u - v|}{h(1 - \epsilon h)} \right) \left( 1 - e^{-\frac{(1 - \epsilon h)^3}{\epsilon^3}} \right), \quad (5.1.19)$$

where  $f_h = f_h(h, q)$ ,  $f_q = f_q(h, q)$ ,  $Q_v = Q_v(h, q, h_x, q_x)$ ,  $Q_u = Q_u(h, q, h_x, q_x)$  and  $R = R(h, q)$ , (5.1.5) and (5.1.11) become

$$h_t + f_{h_x} = 0, \quad (5.1.20)$$

and

$$q_t + f_{q_x} = \frac{1}{R_1 h} Q_{v_x} - \frac{\rho}{R_g(1 - \epsilon h)} Q_{u_x} + R. \quad (5.1.21)$$

We can now use the finite difference method derived by Kurganov and Tadmor [114] combined with a second-order Runge-Kutta method.

### 5.1.1 Spatial Step Size Analysis

For channel length  $CL$ , the periodic boundary conditions become

$$h(0, t) = h(CL, t), \quad q(0, t) = q(CL, t). \quad (5.1.22)$$

Using `bvp5c` as before in Chapter 4, we can solve for a periodic travelling wave which we then use as the initial condition with periodic boundary conditions. We will let the code run until the wave has become steady then calculate its propagation speed by measuring the distance the peak of the wave has travelled. In order to get an accurate value of  $U$  we will solve for a quadratic at the peak of the waves and use the location of the quadratic's maximum in order to give an accurate value for the peak's location. We will then use this value of  $U$  in `bvp5c`, solving for  $B$ , in order to calculate the

$\Delta x$	$U$	$B$
0.01	1.97282	-0.82502
0.008	1.98279	-0.83653
0.005	1.99702	-0.85311
0.0025	2.00662	-0.86438
0.001	2.00966	-0.86797

**Table 5.1.:** A comparison of  $U$  and  $B$  for  $\epsilon = 0.1$ ,  $\delta = 0.5$ ,  $F_0 = 5$ ,  $R_l = 50$ ,  $R_g = 50$ ,  $\lambda = 1$ ,  $\rho = 0.1$ ,  $U = 2$ ,  $B = -0.8566$ ,  $L = 1$  and varying  $\Delta x$ .

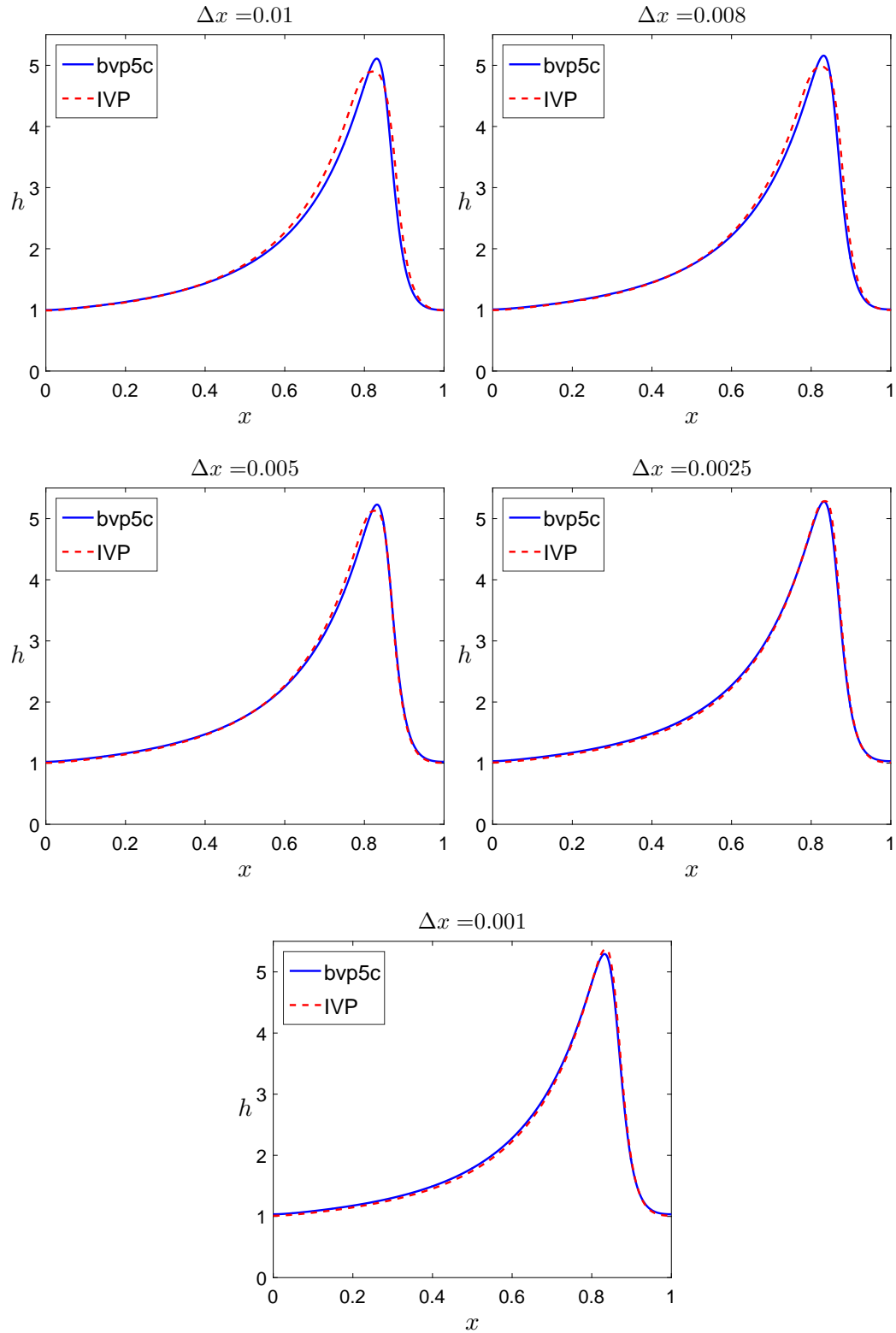
corresponding periodic travelling wave which we can compare to our IVP solution.

Table 5.1 shows the values of  $U$  and  $B$  for  $\epsilon = 0.1$ ,  $\delta = 0.5$ ,  $F_0 = 5$ ,  $R_l = 50$ ,  $R_g = 50$ ,  $\lambda = 1$ ,  $\rho = 0.1$ ,  $U = 2$ ,  $B = -0.8566$ ,  $L = 1$  and varying  $\Delta x$  and Figure 5.1 shows our IVP solutions compared to the `bvp5c` solutions. In order to decrease computing time we want to use the largest  $\Delta x$  possible without losing accuracy. We can see from Figure 5.1 that for  $\Delta x > 0.005$  the IVP solution is not resolving the steep front face of the wave accurately, hence we will use  $\Delta x = 0.005$ . As can be seen in Table 5.1, using  $\Delta x = 0.005$  will result in a slightly slower propagation speed in the IVP when compared to solutions found using `bvp5c`, hence when we make these comparisons we must take this into account.

### 5.1.2 IVP Linear Stability

We will compare solutions from our IVP problem with our work in Chapter 3 in order to check they are consistent. To do this, recalling from Chapter 3 that

$$h = 1 + \bar{h}, \quad (5.1.23)$$



**Figure 5.1.:** A comparison of the bvp5c solution to our IVP solution for  $\epsilon = 0.1$ ,  $\delta = 0.5$ ,  $F_0 = 5$ ,  $R_l = 50$ ,  $R_g = 50$ ,  $\lambda = 1$ ,  $\rho = 0.1$ ,  $U = 2$ ,  $B = -0.8566$ ,  $L = 1$  and varying  $\Delta x$ .

where

$$\bar{h}(x, t) = Ae^{ikx + \omega t}, \quad (5.1.24)$$

we set our initial condition to be the uniform flow plus a small disturbance,  $\bar{h}$ , given by

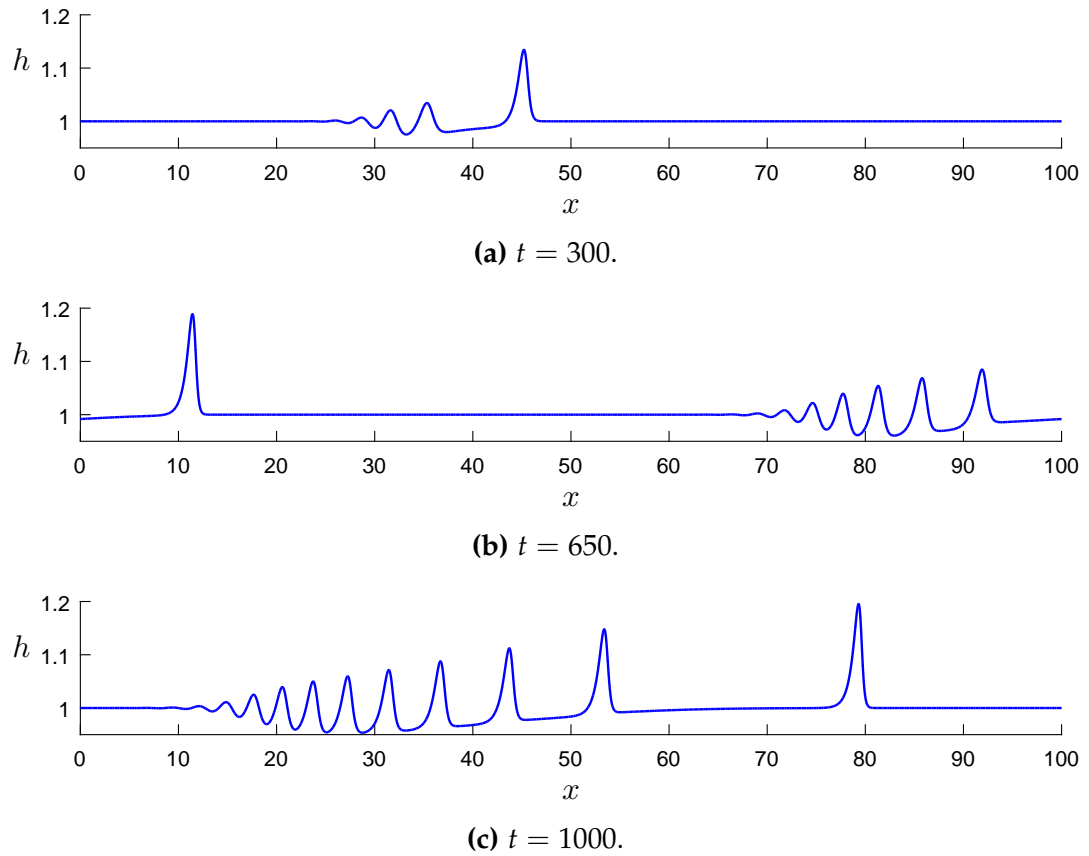
$$\bar{h}(t = 0) = 0.1 \exp\left(-5\left(x - \frac{CL}{2}\right)^2\right). \quad (5.1.25)$$

Figure 5.2 shows the solutions at multiple times for  $\epsilon = 0.01$ ,  $\delta = 0.3$ ,  $F_0 = 3.2$ ,  $R_l = 50$ ,  $R_g = 50$ ,  $\lambda = 1$  and  $\rho = 0.1$ . For this parameter set  $F_c = 3.048$  and the most unstable wavelength is 3.808, which can be seen to be close to the wavelength of the disturbances in Figure 5.2 when they are in their early stages of growth. However, due to the non-linear effects, the larger waves propagate more quickly than the smaller ones which causes the wavelengths to increase after a long enough time.

Figure 5.3 shows the solution at  $t = 9$  for the same parameter set except with  $F_0 = 10$ , for which the most unstable wavelength is 0.792. As the value of  $F_0$  is significantly larger than  $F_c$ , the non-linear effects work more rapidly, however again in the early stages of the growth of the disturbances their wavelength is close to that of the most unstable wavelength. In both cases our predicted most unstable wavelength gives a close approximation to the wavelength of our disturbances in their early stages of growth, hence we may assume our linear stability analysis and our numerical solution are consistent.

## 5.2 ANALYSIS OF THE STABILITY OF PERIODIC TRAVELLING WAVES

In Chapter 4 we studied the existence of periodic travelling wave solutions, however periodic travelling wave theory does not tell us about the stability of those travelling waves in the full system. We will now use some of the



**Figure 5.2.:** The solutions for  $\epsilon = 0.01$ ,  $\delta = 0.3$ ,  $F_0 = 3.2$ ,  $R_l = 50$ ,  $R_g = 50$ ,  $\lambda = 1$  and  $\rho = 0.1$  at various times.

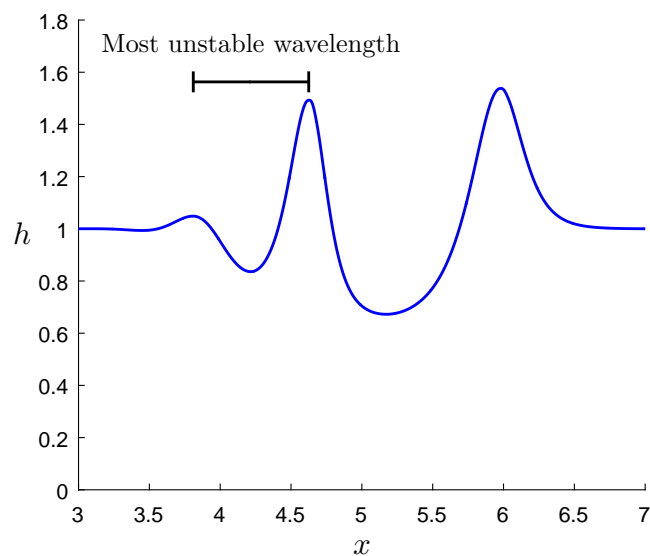


**Figure 5.3.:** The solution at  $t = 9$  for  $\epsilon = 0.01$ ,  $\delta = 0.3$ ,  $F_0 = 10$ ,  $R_l = 50$ ,  $R_g = 50$ ,  $\lambda = 1$  and  $\rho = 0.1$ .

solutions we found earlier in Section 4.3 as our initial condition in the IVP problem with periodic boundary conditions in order to investigate their stability.

Throughout this section we will refer to the parameter set  $\epsilon = 0.1$ ,  $\delta = 0.5$ ,  $F_0 = 6.7$ ,  $R_l = 50$ ,  $R_g = 50$ ,  $\lambda = 0.4$  and  $\rho = 0.1$  as Parameter Set 1, and the parameter set  $\epsilon = 0.01$ ,  $\delta = 0.3$ ,  $F_0 = 25$ ,  $R_l = 50$ ,  $R_g = 10$ ,  $\lambda = 0.37$  and  $\rho = 0.1$  as Parameter Set 2. For Parameter Set 1 we will use `bvp5c` to compute solutions for  $U_1 = 2.099$ ,  $U_2 = 2.149$ ,  $U_3 = 2.189$ ,  $U_4 = 2.205$ ,  $U_5 = 2.348$ ,  $U_6 = 2.444$ ,  $U_7 = 2.498$  and  $U_8 = 2.490$  where for  $U_7$  we use the stable limit cycle solution and for  $U_8$  we use the unstable limit cycle solution. For Parameter Set 2 we will use  $U_1 = 4.298$ ,  $U_2 = 4.251$ ,  $U_3 = 4.200$ ,  $U_4 = 4.060$ ,  $U_5 = 3.985$ ,  $U_6 = 3.808$ ,  $U_7 = 3.560$  and  $U_8 = 2.748$ . For both parameter sets we will use  $B = -0.7$ . Figures 5.4 and 5.5 show the bifurcation diagrams for Parameter Sets 1 and 2, respectively, with the values of  $U$  we are using in `bvp5c` marked by purple lines. In Figure 5.4 Region A refers to the values of  $U$  between the Hopf bifurcation and the first homoclinic bifurcation, Region B refers to the values of  $U$  between the second and third homoclinic bifurcations and Region C refers to the values of  $U$  between the third homoclinic bifurcation and the point where the stable and unstable limit cycles annihilate each other. In Figure 5.5 Region C refers to the values of  $U$  between the Hopf bifurcation and the first homoclinic bifurcation, Region B refers to the values of  $U$  between the second and third homoclinic bifurcations and Region A refers to the values of  $U$  between the fourth and fifth homoclinic bifurcations.

Using `bvp5c` we find periodic solutions for the parameters specified. In order to use these as our initial conditions for our IVP we will combine ten of each solution, one after the other, creating a channel of length  $10L$ , where  $L$  is the length of one periodic solution, comprising ten periodic and identical roll waves. We then use these initial conditions in our IVP and let it run until the structure of the roll waves in the IVP has become time-independent.

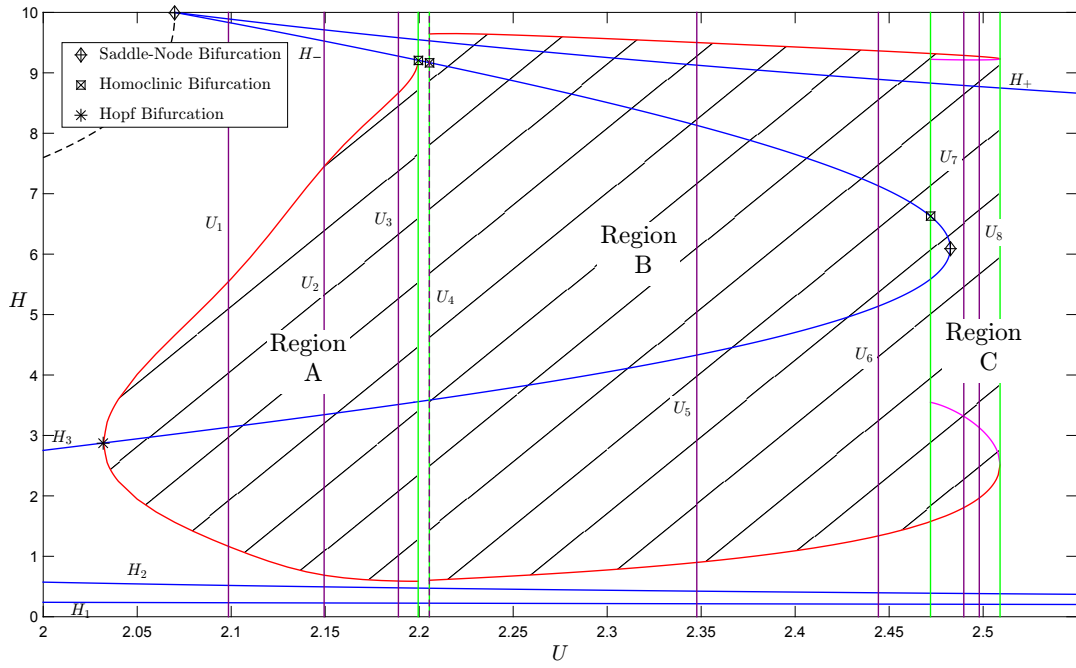


**Figure 5.4.:** The bifurcation diagram for Parameter Set 1 with the values of  $U_1, U_2, U_3, U_4, U_5, U_6, U_7$  and  $U_8$  marked by the purple lines.

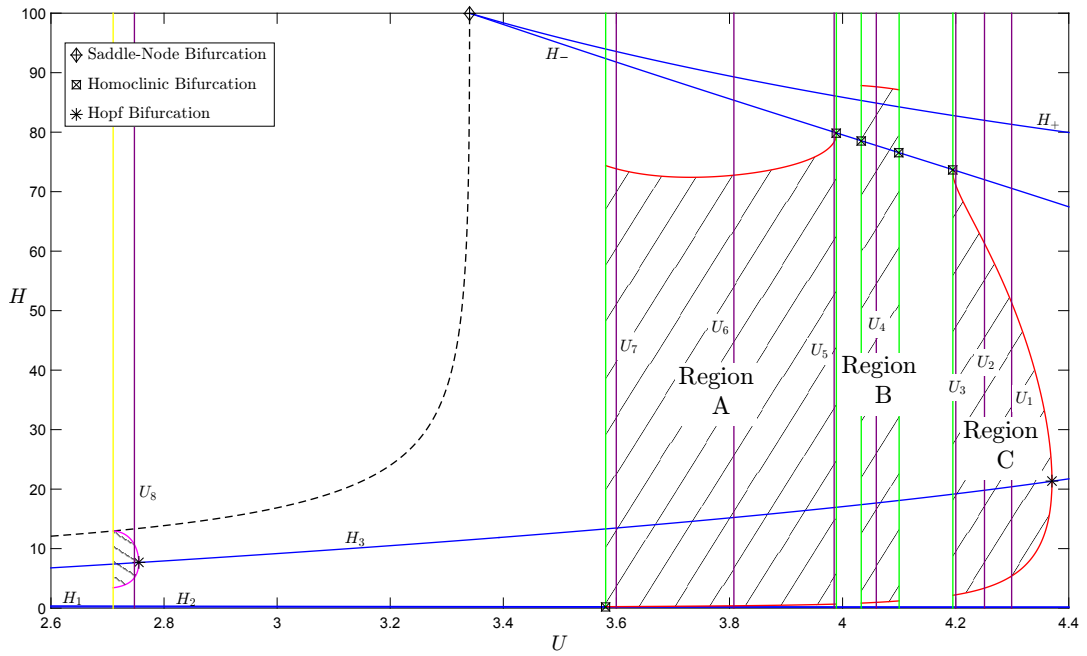


**Figure 5.5.:** The bifurcation diagram for Parameter Set 2 with the values of  $U_1, U_2, U_3, U_4, U_5, U_6, U_7$  and  $U_8$  marked by the purple lines.

Figure	bvp5c $U$	IVP $U$	IVP $B$	Figure	bvp5c $U$	IVP $U$	IVP $B$
5.9a	2.099	2.077	-0.692	5.10a	4.298	3.888	-0.979
5.9b	2.149	2.123	-0.698	5.10b	4.251	3.817	-0.712
5.9c	2.189	2.186	-0.681	5.10c	4.200	N/A	N/A
5.9d	2.205	2.180	-0.599	5.10d	4.060	N/A	N/A
5.9e	2.348	2.298	-0.780	5.10e	3.985	N/A	N/A
5.9f	2.444	N/A	N/A	5.10f	3.808	3.723	-0.822
5.9g	2.498	N/A	N/A	5.10g	3.560	3.560	-0.926
5.9h	2.490	2.345	0.117	5.10h	2.748	N/A	N/A

**Table 5.2.:** A comparison of  $U$  and  $B$  from bvp5c compared to those from the IVP for Parameter Set 1.

**Table 5.3.:** A comparison of  $U$  and  $B$  from bvp5c compared to those from the IVP for Parameter Set 2.

Tables 5.2 and 5.3 show the resulting values of  $U$ , calculated by measuring the distance travelled in the IVP (using the method of fitting a quadratic to the top of the wave as described in Section 5.1), and  $B$ , calculated using  $B = \text{average}(h(v - U))$ . We can see that the propagation speeds found in the IVP are slightly slower than those in the initial conditions, as we expect from our work in Section 5.1.

The values of  $U$  and  $B$  for Parameter Set 1 for  $U \approx 2.444$  and  $U \approx 2.498$  and Parameter Set 2 for  $U \approx 2.748$  are not given as the flow has developed into a stratified flow regime. The values of  $U$  and  $B$  for Parameters Set 2 for  $U \approx 4.200$ ,  $U \approx 4.060$  and  $3.985$  are not given as they are unsteady periodic solutions which do not have a permanent form.

Plots of the values for  $U$  from bvp5c compared to those found from the IVP and where they lie in the bifurcation diagram are shown in Figures 5.7 and 5.8. Figures 5.9 and 5.10 show plots of the initial conditions, found using bvp5c, compared to the solutions found using the IVP.

For Parameter Set 1 we can see from Table 5.2 and Figures 5.7 and 5.9 that only bvp5c solutions in Region A are stable in the IVP. For solutions

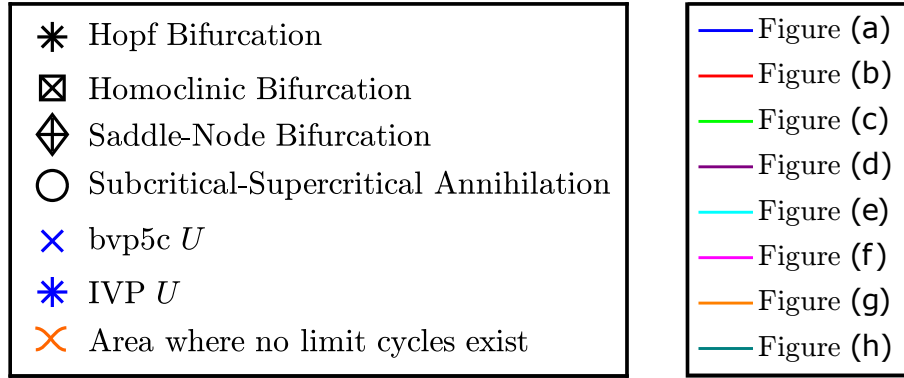


Figure 5.6.: Legends for Figures 5.7 and 5.8.

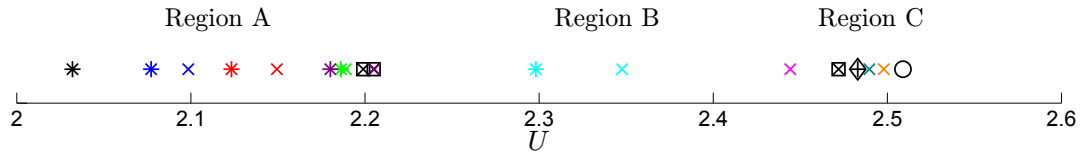


Figure 5.7.: The values of  $U$  from bvp5c compared to those computed in the IVP for Parameter Set 1.

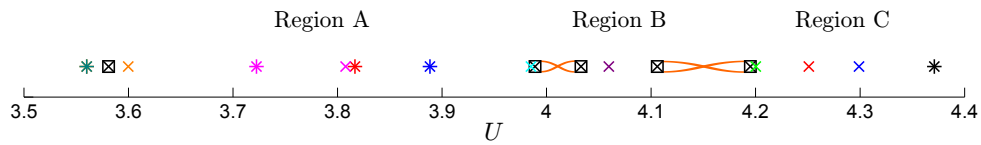
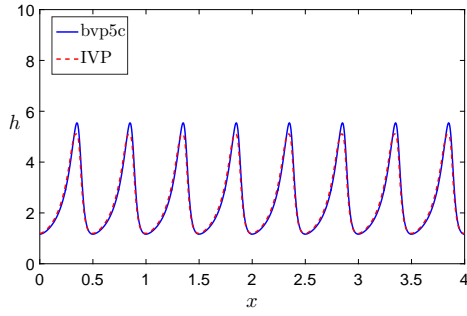
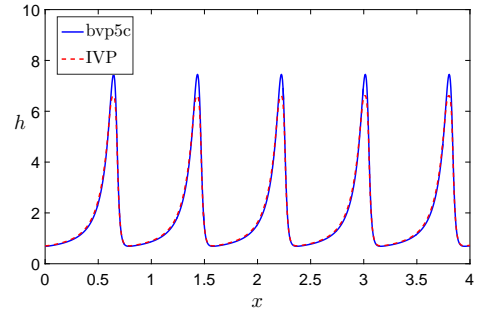


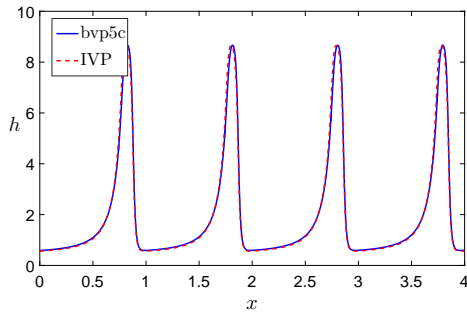
Figure 5.8.: The values of  $U$  from bvp5c compared to those computed in the IVP for Parameter Set 2.



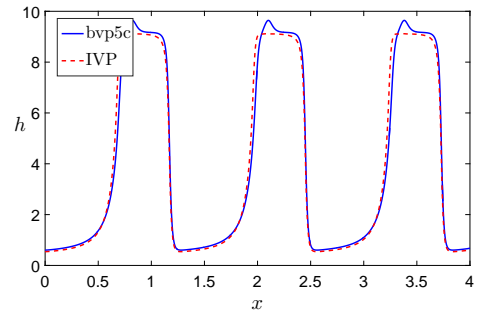
(a)  $U_1 \approx 2.099, L = 0.5.$



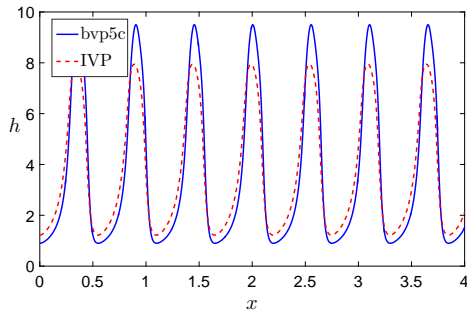
(b)  $U_2 \approx 2.149, L = 0.79.$



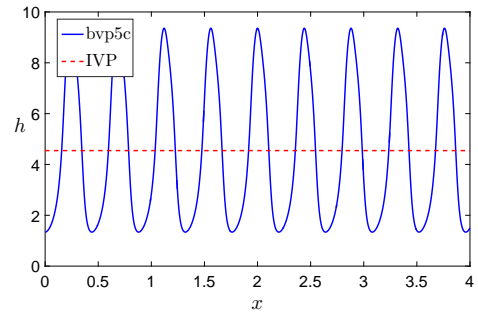
(c)  $U_3 \approx 2.189, L = 0.99.$



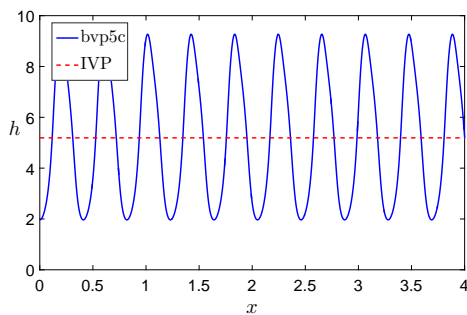
(d)  $U_4 \approx 2.205, L = 1.28.$



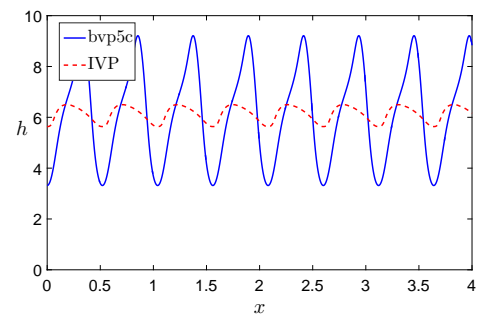
(e)  $U_5 \approx 2.348, L = 0.55.$



(f)  $U_6 \approx 2.444, L = 0.44.$

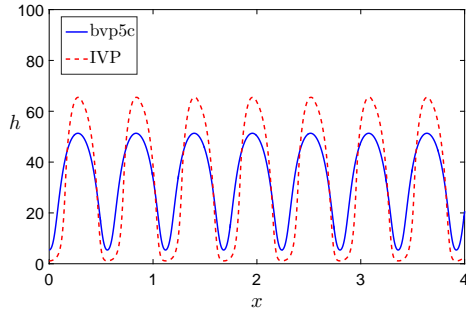


(g)  $U_7 \approx 2.498, L = 0.41.$

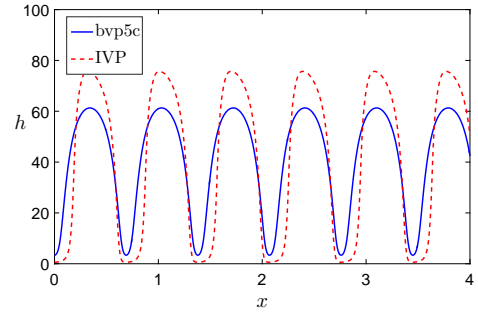


(h)  $U_8 \approx 2.490, L = 0.52, \text{unstable limit cycle.}$

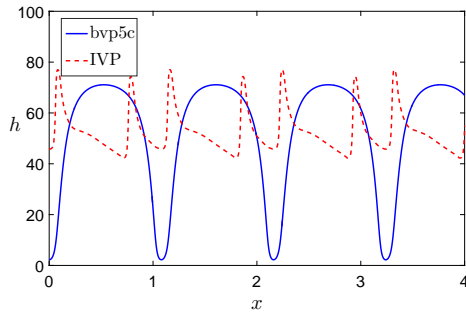
**Figure 5.9.:** A comparison of the limit cycles solutions using bvp5c for Parameter Set 1 to the solution from the IVP.



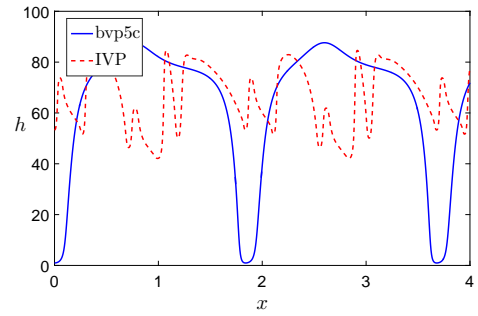
(a)  $U_1 \approx 4.298, L = 0.56.$



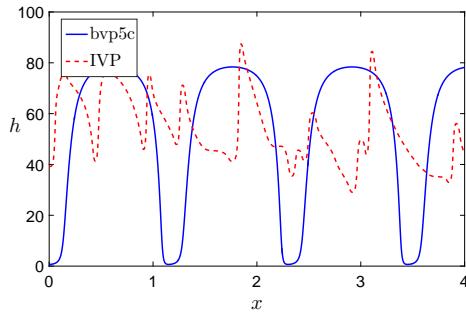
(b)  $U_2 \approx 4.251, L = 0.69.$



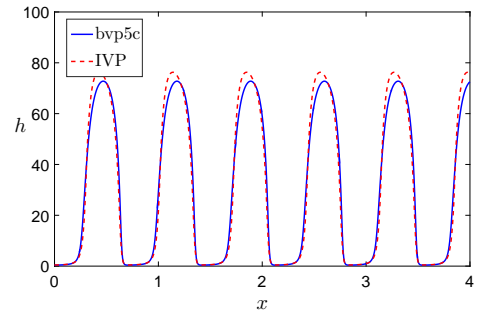
(c)  $U_3 \approx 4.200, L = 1.08.$



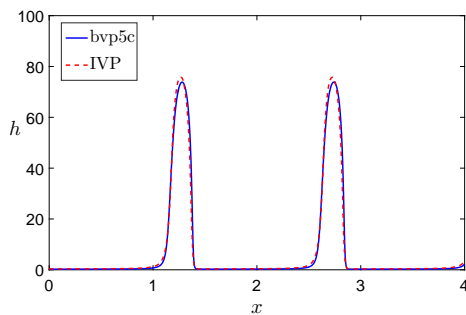
(d)  $U_4 \approx 4.060, L = 1.84.$



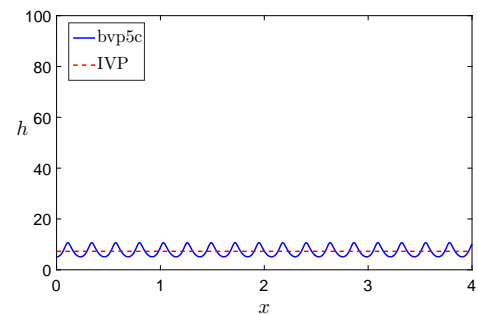
(e)  $U_5 \approx 3.985, L = 1.15.$



(f)  $U_6 \approx 3.808, L = 0.71.$



(g)  $U_7 \approx 3.560, L = 1.46.$



(h)  $U_8 \approx 2.748, L = 0.23,$  unstable limit cycle.

**Figure 5.10.:** A comparison of the limit cycles solutions using bvp5c for Parameter Set 2 to the solution from the IVP.

in this region Figures 5.9a, 5.9b and 5.9c show the solutions from the IVP very closely resemble those from bvp5c and from Table 5.2 we can see how close the values of  $U$  and  $B$  are in the IVP compared to those from bvp5c. Figure 5.9d shows a close match between the IVP and bvp5c solution just after the second homoclinic bifurcation, in Region B. However, Table 5.2 shows that the value of  $B$  is significantly different and Figure 5.7 shows the value of  $U$  lies in Region A, not Region B. Although the bvp5c solution was just after the second homoclinic bifurcation, the solution from the IVP resembles that of bvp5c just before the first homoclinic bifurcation for a different value of  $B$ . As  $U$  is increased further into Region B we again get a stable solution in the IVP, however we can see from Table 5.2 that the value of  $U$  and  $B$  from the IVP is significantly different from the bvp5c solution. Again the solution from the IVP is actually from Region A, but for a different value of  $B$ . As the value of  $U$  is increased further we can see from Table 5.2 and Figures 5.9f and 5.9g that the solution in the IVP has become a stratified flow regime and no longer produces waves. Finally, from Table 5.2 and Figure 5.9h we can see that the subcritical bvp5c solution in Region C produces a stable solution in the IVP, however the values of  $U$  and  $B$  are significantly different. As the value of  $B$  in the IVP is positive, this represents a wave for which the liquid is moving faster than the wave propagation speed which is a situation that we would not expect to encounter as the flow is driven by the gas.

For Parameter Set 2 we can see from Table 5.3 and Figures 5.8 and 5.10 that, although bvp5c solutions from Regions A and C produce stable solutions in the IVP, these solutions have significantly different values of  $U$  and  $B$ . This is to be expected as, from Section 3,  $F_{NH} = 12.671$  for this parameter set so the IVP model is ill-posed for these simulations. However, we can see from Figures 5.10f and 5.10g the solutions from the IVP very closely resemble those from bvp5c in Region A. Also, from Figure 5.8 we can see that for solutions in Region C from bvp5c, the IVP produces stable

solutions from Region A. As with Parameter Set 1, it appears that only `bvp5c` solutions for  $U \approx 1/\delta$  produce stable solutions in the IVP.

### 5.3 CHANNEL SIMULATIONS

In order to simulate the flow through a channel, instead of using (5.1.22), we will define our outlet condition as

$$h(CL, t)_x = 0, \quad v(CL, t)_x = 0, \quad (5.3.1)$$

and our inlet condition to be the uniform flow plus some small amplitude random noise, Chang et al. [36], such that

$$h_1 = 1 + 0.001 \sum_{k=1}^M \sin \left( \left[ \omega_{\min} + \frac{k}{M} (\omega_{\max} - \omega_{\min}) \right] t + 2\pi r_k \right), \quad (5.3.2)$$

$$v_1 = \frac{1}{h_1}, \quad (5.3.3)$$

where  $\omega_{\min}$  and  $\omega_{\max}$  are constants and  $r$  is a vector of length  $M$  of random numbers between 0 and 1 such that  $h_1$  is the uniform flow with some small noise at the inlet. We will use  $\omega_{\min} = 0.1$ ,  $\omega_{\max} = 10$  and  $M = 250$  unless otherwise stated.

We expect the noise with wavelength closest to the most unstable wavelength to dominate the flow close to the inlet. If this noise is able to escape the linear instability, as discussed in Chapter 3, it will grow to form a wave packet, such as those shown in Figure 5.2. If the front of the localised coherent structure propagates down the channel faster than the structure, it will be destroyed returning to the steady state solution. However, if it does not, the structure will grow, as in Figure 5.2l, and may form roll waves and possibly slugs.

We have seen when using `bvp5c` that for  $\epsilon = 0.1$ ,  $\delta = 0.5$ ,  $F_0 = 6.7$ ,  $R_l = 50$ ,  $R_g = 50$ ,  $\lambda = 0.4$  and  $\rho = 0.1$  we can compute both periodic roll

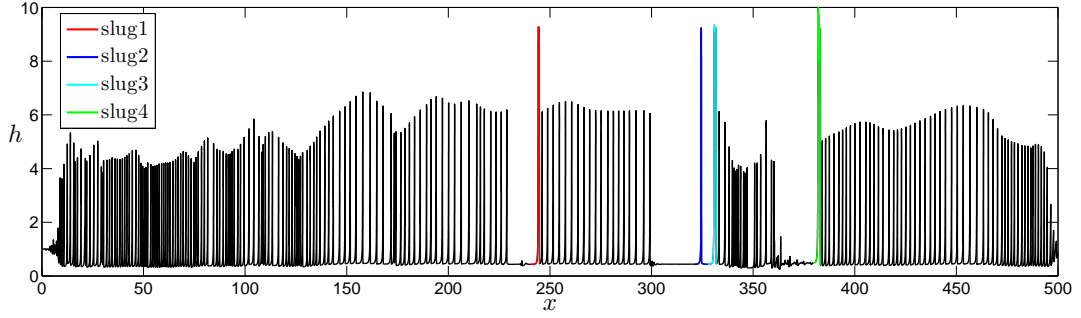
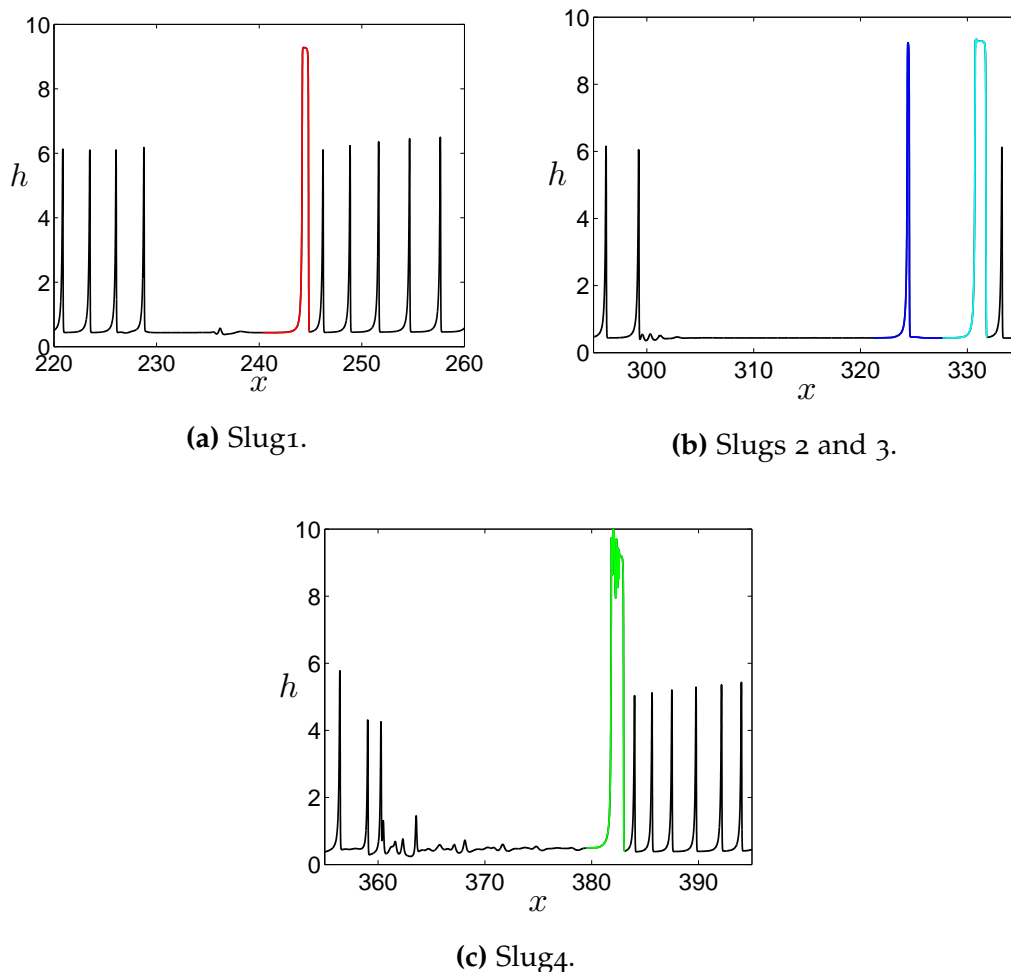


**Figure 5.11.:** The solution at  $t = 900$  for  $\epsilon = 0.1$ ,  $\delta = 0.5$ ,  $F_0 = 6.7$ ,  $R_l = 50$ ,  $R_g = 50$ ,  $\lambda = 0.4$  and  $\rho = 0.1$ .

wave solutions and slug solutions. We will now use these parameters and compute the solution in a channel with  $CL = 500$ . Assuming a channel of height  $a = 1\text{m}$  this gives us  $u_l^0 = 6.636\text{m/s}$ ,  $u_g^0 = 14.009\text{m/s}$ ,  $h_0 = 0.1\text{m}$  and dimensional channel length of  $33.5\text{km}$ . Figure 5.11 shows the solution at  $t = 900$ , which in dimensional time is approximately 2.5 hours. We can see that the majority of the channel is full of roll waves, but there are four slugs and each of these is followed by a region with little liquid. We will refer to the slug coloured red as slug1, the slug coloured dark blue as slug2, the slug coloured light blue as slug3 and the slug coloured green as slug4. Figure 5.12 shows a close up of these slugs where it must be noted that although the slugs appear to have near vertical slopes, this due to the scalings used and is not the case. For example, the dimensional length of the front slope of slug1 between  $h = 2$  and  $h = 8$  is  $2.6\text{m}$ , hence gives an angle of approximately  $13^\circ$ .

Note that the top of slug4, as seen in Figure 5.12c, is well resolved. As the liquid gets near to the top of the channel it would in reality transition into a local bubbly flow regime which our long wavelength model cannot capture. As a result of this we are left with high frequency oscillations at the top of the slug due to local ill-posedness, so the structure of the tops of these waves is not accurate, though the overall structure is.

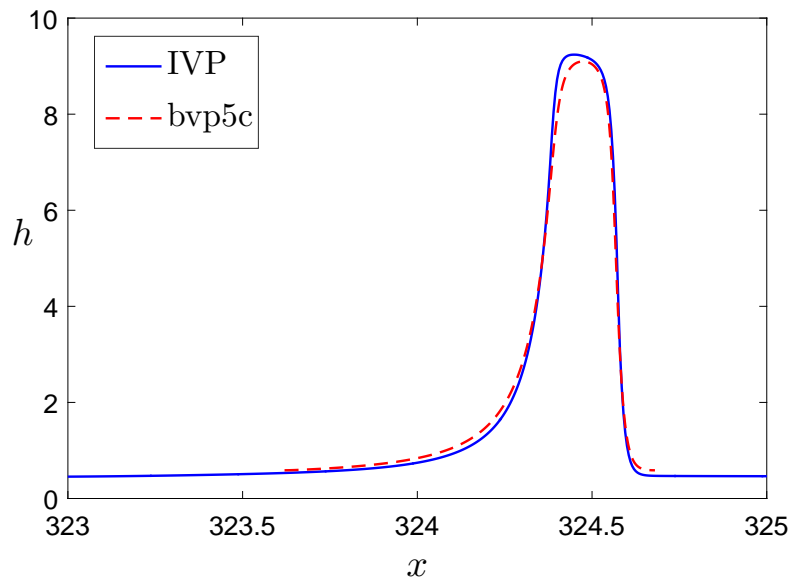
Using `bvp5c` we can solve for solutions that resemble those in the IVP solution. The value of  $U$  is found by measuring the distance travelled by



**Figure 5.12.:** The slugs at  $t = 900$  for  $\epsilon = 0.1$ ,  $\delta = 0.5$ ,  $F_0 = 6.7$ ,  $R_l = 50$ ,  $R_g = 50$ ,  $\lambda = 0.4$  and  $\rho = 0.1$ .

the slug and then using  $B = \text{average}(h(v - U))$  for an approximation of the value for  $B$ . Figure 5.13 shows the `bvp5c` solution for  $U \approx 2.192$  and  $B = -0.7$  plotted over the top of Slug 2 at  $t = 900$ , from which we can see how similar the solutions are. Hence, although our work in Chapter 4 used a system of ODE's, the periodic travelling wave solutions we found do exist in the full problem.

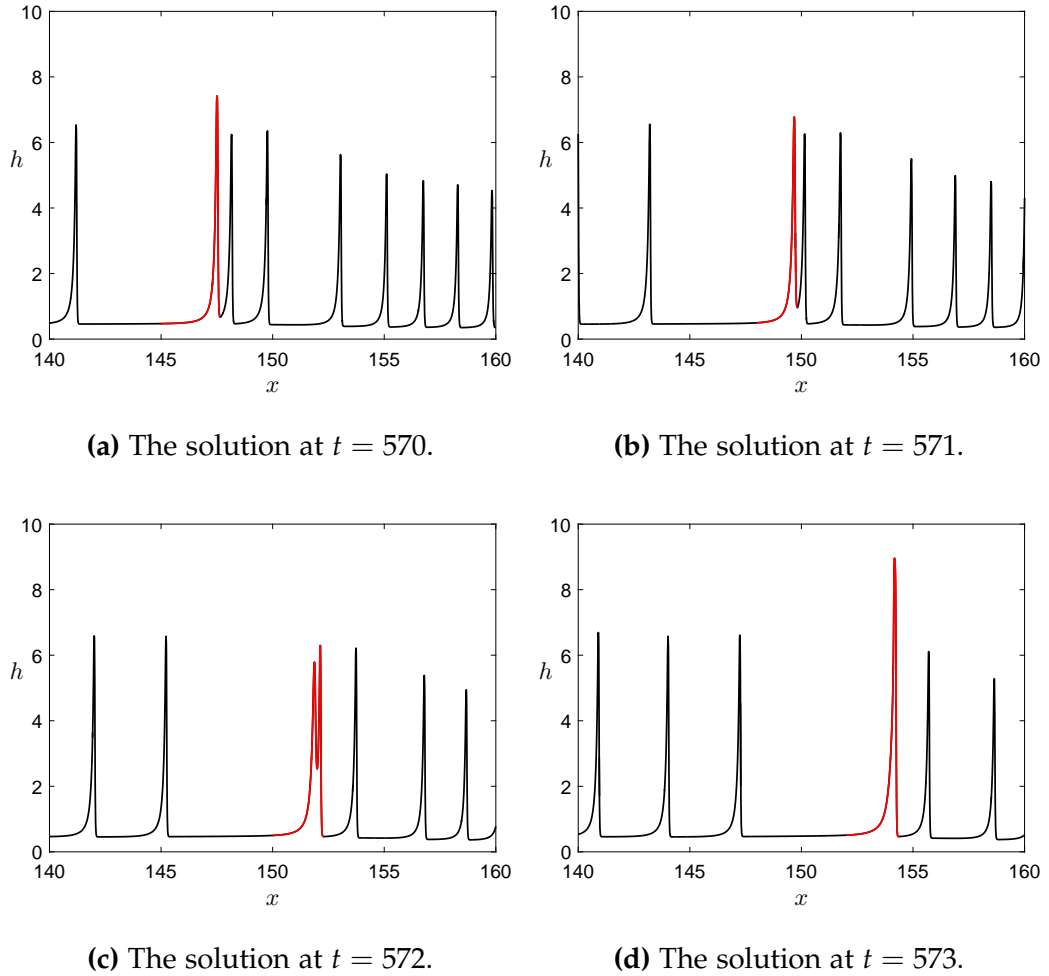
These slugs begin as roll waves, but propagate slightly faster than the roll waves in front of them. When they catch up with a roll wave and begin to absorb the tail of the slower moving roll wave they are slowed down and some of their mass is drained out of their back. At this point either their mass and velocity is decreased such that they return to their equilibrium roll



**Figure 5.13.:** Slug 2 compared to the solution found using bvp5c for  $U \approx 2.192$  and  $B = -0.7$ .

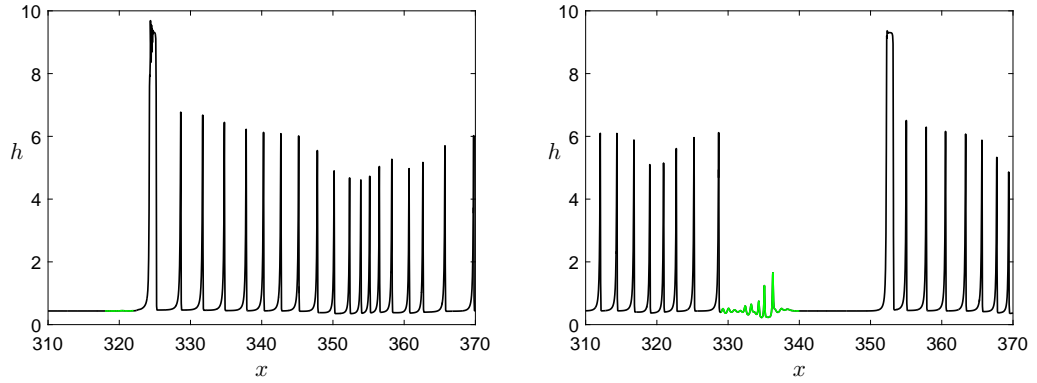
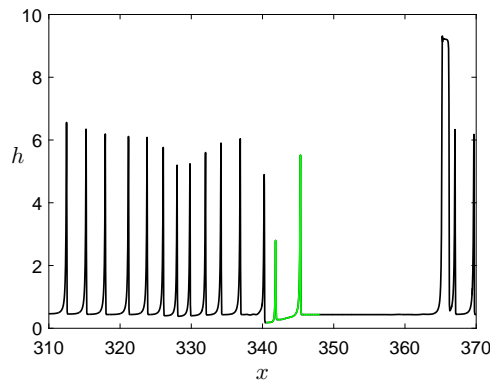
wave state, or they are able to absorb the slower moving roll wave. If they are able to absorb the slower roll wave they will continue down the channel until they catch up with the next roll wave and the process is repeated. A slug is formed if the faster moving roll wave is able to repeatedly absorb the slower moving roll waves in front of it such that the mass it gains from absorbing slower roll waves is greater than the mass that is drained out of its back. The slug then continues down the channel increasing in size each time it absorbs a roll wave. Hence, in general, the slugs further down the channel will be larger than those further up the channel.

In order to determine conditions under which two roll waves will attract and form one larger roll wave, or repel settling into their equilibrium roll wave state, we could perform interaction experiments. Further, in simulations for which slugs are produced, if the channel length is large enough, eventually the system will be dominated by a series of large slugs which may be separated with well-defined distances. From this we could perform detailed statistical analysis in order to predict them analytically. These areas are not explored here, hence are areas where further research is needed.



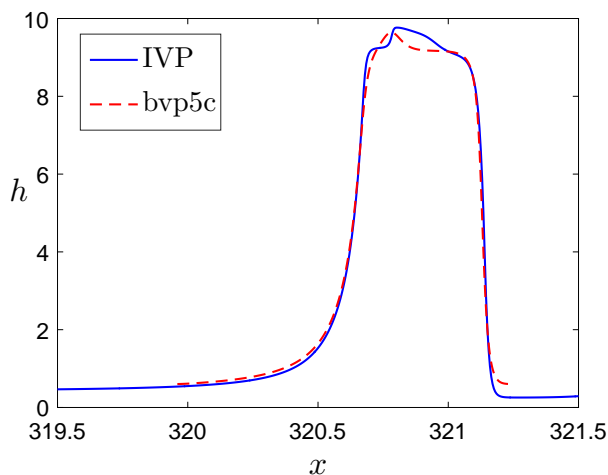
**Figure 5.14.:** The solutions as a slug is formed at  $t = 570, 571, 572$  and  $573$  for  $\epsilon = 0.1, \delta = 0.5, F_0 = 6.7, R_l = 50, R_g = 50, \lambda = 0.4$  and  $\rho = 0.1$ .

The slug forming process is shown in Figure 5.14 where the roll wave of interest is shown in red. We can see in Figures 5.14a the roll wave of interest catching up with a roll wave in front of it. As it absorbs the tail of the slower moving roll wave, in Figure 5.14b, we can see that its size has decreased due to mass draining out of its back as it is slowed down. In this case, the loss of mass and velocity is not large enough to return the roll of interest to its equilibrium roll wave state and it is able to absorb the slower roll wave, shown in Figure 5.14c. After the absorption, as in Figure 5.14d, it has increased in size and will continue down the channel until it reaches the next roll wave and repeats the process forming a slug.

(a) The solution at  $t = 651$ .(b) The solution at  $t = 664$ .(c) The solution at  $t = 670$ .

**Figure 5.15.:** The solutions as the slug leaves liquid behind at  $t = 651, 664$  and  $670$  for  $\epsilon = 0.1, \delta = 0.5, F_0 = 6.7, R_l = 50, R_g = 50, \lambda = 0.4$  and  $\rho = 0.1$ .

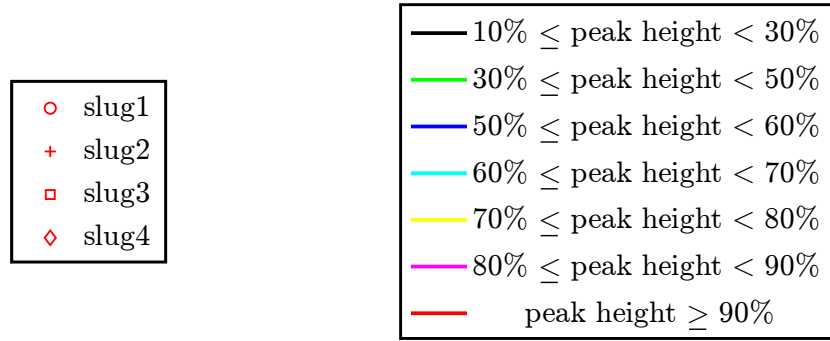
As can be seen in Figure 5.12, slug<sub>1</sub>, slug<sub>2</sub> and slug<sub>3</sub> are followed by almost flat regions of liquid, however slug<sub>4</sub> is followed by a noisy region. This is due to the slugs leaving small amounts of liquid behind after absorbing roll waves. This liquid then begins to grow in amplitude and may form roll waves. As the roll waves in front of slug<sub>4</sub> are closer together than those in front of slug<sub>1</sub> or slug<sub>3</sub>, slug<sub>4</sub> is absorbing roll waves more frequently and hence leaving more liquid behind. The region behind slug<sub>2</sub> is so flat because the liquid left behind by slug<sub>3</sub> when it absorbs roll waves is then absorbed by slug<sub>2</sub> before it has begun to grow. Figure 5.15 shows the same slug we saw formed in Figure 5.14 at a later time after it has travelled further



**Figure 5.16.:** A slug at  $t = 962$  compared to the solution found using `bvp5c` for  $U \approx 2.206$  and  $B = -0.7$ .

down the channel and increased in size. As it catches and absorbs the roll waves in front of it, it leaves behind a small amount of liquid (shown in green), shown in Figure 5.15a where, for the discharge,  $U \approx 0.9$ . This liquid begins to grow in amplitude and propagate faster, shown in Figure 5.15b where, for the discharge,  $U \approx 1.05$ . The discharge continues to grow in amplitude and propagate faster and, if the roll waves following the slug are far enough behind, will form roll waves. When the leading roll wave behind the slug catches up with this slower moving liquid it is slowed down and decreases in size as its momentum is transferred to the discharge, shown in Figure 5.15c, which is then able to grow into a roll wave with  $U \approx 1.945$ , the same propagation speed as the following roll waves.

In Chapter 4 we saw periodic travelling waves with 'bump'-like peaks, such as those shown in Figure 4.15a. We have seen in Section 5.2 that these solutions are not stable in the IVP, however we do find similar solutions in the IVP. Figure 5.16 shows a slug in the IVP at  $t = 962$  compared to the `bvp5c` solution for  $U \approx 2.206$  (from Section 5.2 Figure 5.9d). The slugs in the IVP take this shape after catching and absorbing a roll wave as the additional liquid from the roll wave is added to the slug. Hence the `bvp5c`

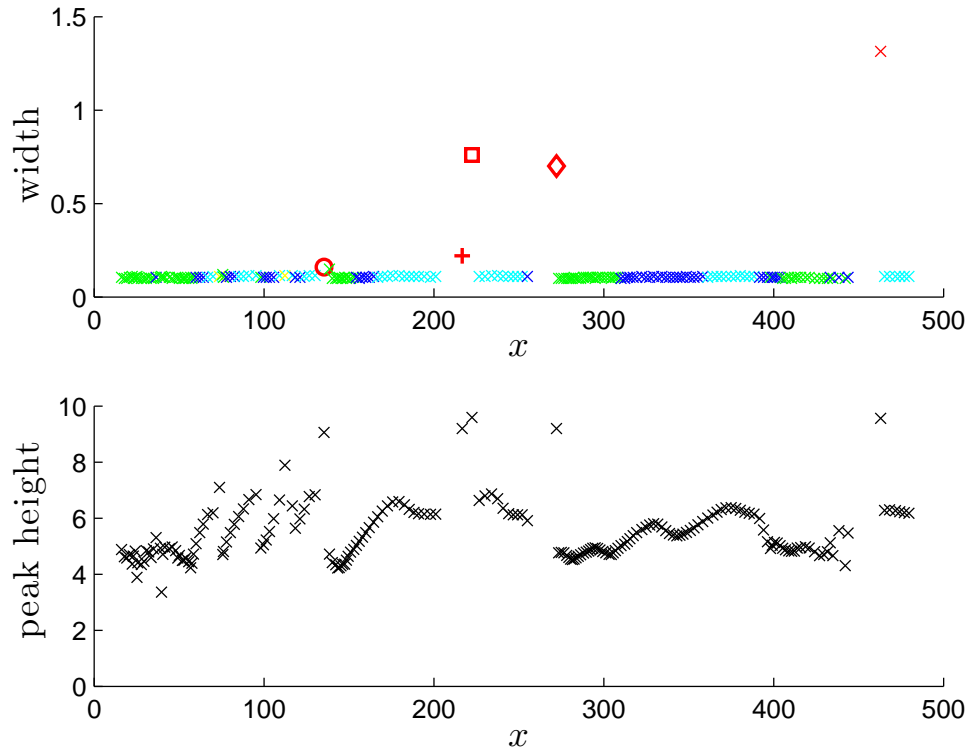
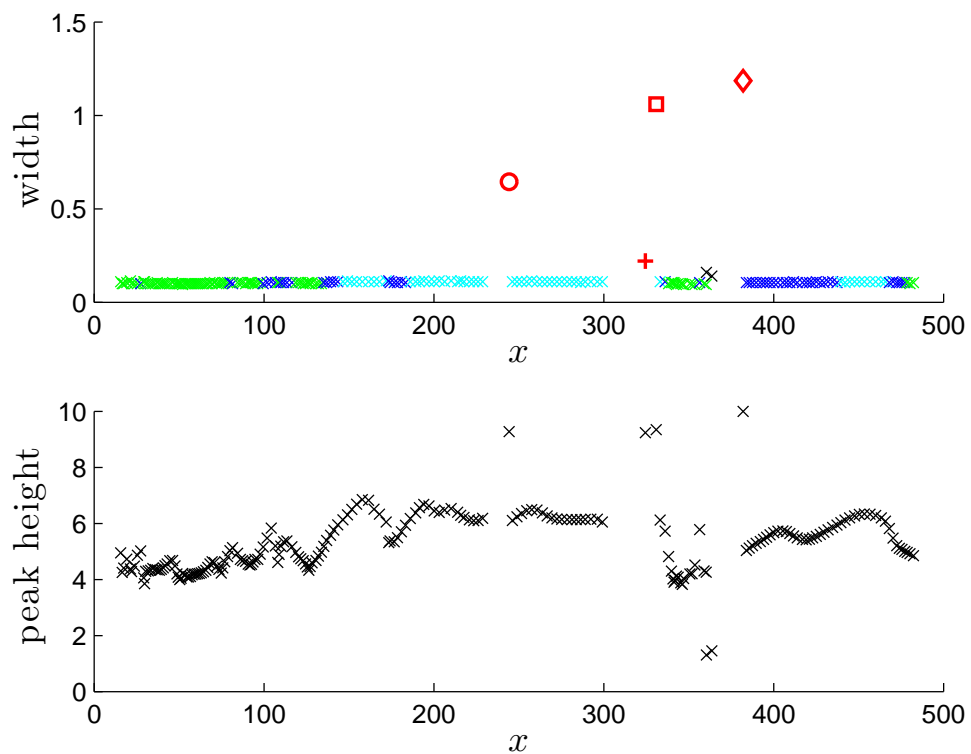


**Figure 5.17.:** Legend for width figures.

solutions that take this shape are temporally stable and not unstable as our work in Section 5.2 found.

In order to investigate these slugs further we will define the ‘width’ of a wave as the width at the point halfway between its peak and trough. Figure 5.18 shows the widths and peak heights of the waves plotted against their location in a channel of  $CL = 500$  for  $\epsilon = 0.1$ ,  $\delta = 0.5$ ,  $F_0 = 6.7$ ,  $R_l = 50$ ,  $R_g = 50$ ,  $\lambda = 0.4$  and  $\rho = 0.1$  at  $t = 850$  and  $t = 900$ . We can see that, with the exception of slug2, the slugs have increased in width as they have propagated down the channel as expected. Slug2 has not grown as it is located close behind slug3 (shown in Figure 5.12b), hence there are no roll waves for it to absorb in order for it to increase in size as it propagates down the channel.

Figure 5.19 shows the widths and peak heights of the waves plotted at numerous times throughout the simulation. Looking at the width figure in the region where  $0 < x < 100$  we can see there are only black, green and dark blue marks all with narrow width indicating that this part of the channel only contains roll waves. In the region where  $100 < x < 150$  we begin to see some red and pink marks with narrow width indicating that slugs have begun to form and have gained height, but are not much wider than the roll waves around them. As  $x$  increases past 150 we can see the red and pink marks have larger widths the further down the channel they are due to the slugs absorbing roll waves as they travel down the channel. By looking at the peak height figure we can also see that from  $x \approx 250$  the

(a)  $t = 850$ .(b)  $t = 900$ .

**Figure 5.18.:** The width and peak height against location in the channel of waves for  $\epsilon = 0.1$ ,  $\delta = 0.5$ ,  $F_0 = 6.7$ ,  $R_l = 50$ ,  $R_g = 50$ ,  $\lambda = 0.4$  and  $\rho = 0.1$ .

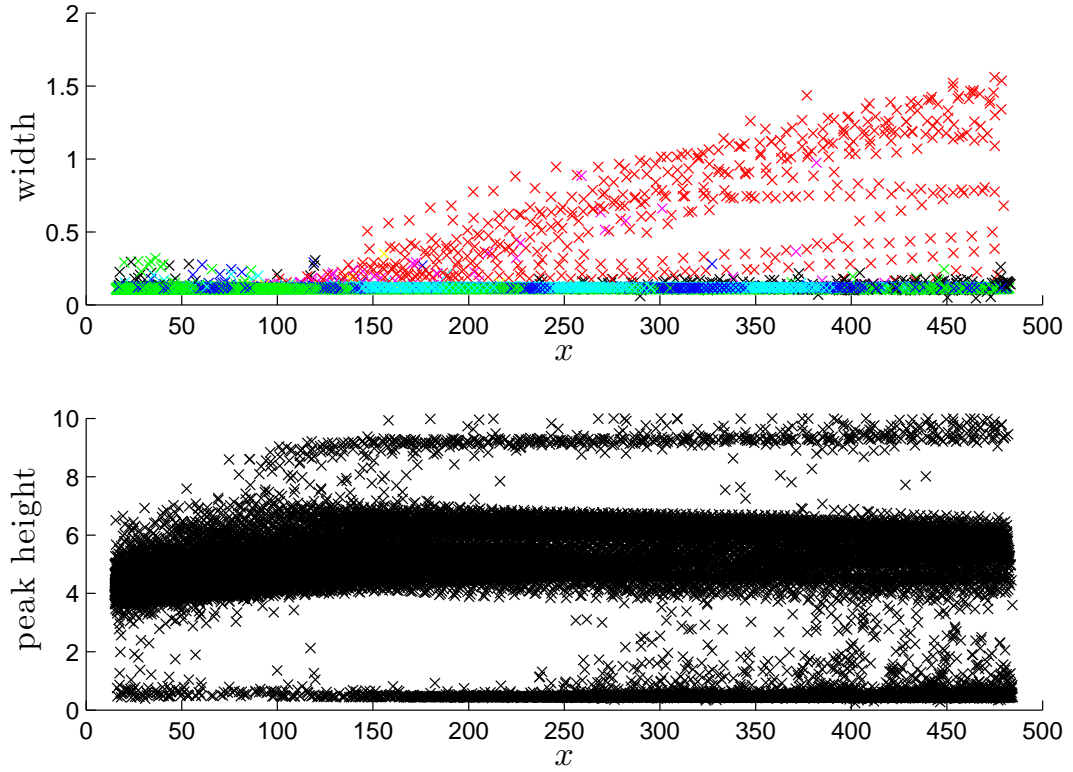


**Figure 5.19.:** The width and peak height against location in the channel of waves at numerous times for  $\epsilon = 0.1$ ,  $\delta = 0.5$ ,  $F_0 = 6.7$ ,  $R_l = 50$ ,  $R_g = 50$ ,  $\lambda = 0.4$  and  $\rho = 0.1$ .

slugs are far enough ahead of any following roll waves that the liquid they leave behind is beginning to grow and form roll waves.

### 5.3.1 Varying Parameters

We know that for  $a = 1\text{m}$ ,  $u_l^0 = 6.636\text{m/s}$ ,  $u_g^0 = 14.009\text{m/s}$  and  $h_0 = 0.1\text{m}$  we generate slug solutions. We want to know which of the parameters affect the system so will keep  $a = 1\text{m}$  and solve for all combinations of  $u_l^0 = 6, 6.636$  and  $7$ ;  $u_g^0 = 12, 14$  and  $14.7$ ; and  $h_0 = 0.05, 0.1$  and  $0.15$ . From  $a = 1\text{m}$ ,  $u_l^0 = 6.636\text{m/s}$ ,  $u_g^0 = 14.009\text{m/s}$  and  $h_0 = 0.1\text{m}$  and  $\epsilon = 0.1$ ,  $\delta = 0.5$ ,  $F_0 = 6.7$ ,  $R_l = 50$ ,  $R_g = 50$ ,  $\lambda = 0.4$  and  $\rho = 0.1$  we can solve for  $c_l$ ,  $\mu_l$  and  $\mu_g$  which we will use in order to calculate our dimensionless parameters.

The results of these simulations are shown in Table 5.4 for which slugs do form, Table 5.5 for which no slugs form and Table 5.6 which will be discussed later. The  $F_r$  column heading is the Froude ratio, which we define as

$$F_r = \frac{F_0 - F_c}{F_{NH} - F_c}. \quad (5.3.4)$$

The 'D.S.' column heading is the Data Set the parameters correspond to. The 'R.W.  $h\%$ ' and 'R.W. Width' column headings are the average roll wave height as a percentage of the channel height of roll waves for  $x > 200$  and the average width of these roll waves, respectively. The solutions with 'N/A' in these columns are almost entirely made up of slugs with very few roll waves, hence an average roll wave height and width cannot be given. The 'Avg Slugs' column heading is the average number of slugs per unit time during the simulation after  $t = 500$ , when the flow has fully formed. The 'Slug Width' column heading is the average width of the slugs as they reach the outlet, hence are at their maximum width for the simulation. Here a slug is considered to have height  $\geq 0.75/\epsilon$  and width at least twice that of the average roll wave width throughout the channel.

From these tables, plots of the solutions at  $t = 3000$  for  $CL = 1000$  (shown in the Appendix in Figure A.1) and plots of width and peak height against location in the channel (shown in the Appendix in Figure A.2), we can see that, with the exception of Data Sets 13, 23 and 25, slugs form when  $\delta > 0.5$  and the Data Sets containing the most slugs also have the largest values of  $\delta$ . However, due to the high number of slugs that form in these simulations there are not many roll waves for them to absorb and they do not grow much in size. The widest slugs form when  $\delta \approx 0.5$ ; in these Data Sets when the slugs form there are lots of roll waves in the channel for them to catch up with and absorb. This can be seen by comparing Data Sets 8, which has  $\delta = 0.609$ , and 14, which has  $\delta = 0.500$ . In Table 5.4 and Figures 5.20a and 5.20b we can see that Data Set 8 produces a lot more slugs than Data Set 14. In Figure 5.21a we can see that lots of slugs are formed in the region

D.S.	$h_0 (= \epsilon)$	$u_l^0$	$u_g^0$	$\delta$	$F_0$	$F_r$	$R_l (= R_g)$	$\lambda$	R.W. $h\%$	R.W. Width	Avg Slugs	Slug Width
1	0.05	6	12	0.513	8.567	0.580	19.658	0.790	40	0.195	0.118	0.563
2	0.1	6	12	0.526	6.058	0.580	44.524	0.392	56	0.141	0.333	1.095
3	0.15	6	12	0.541	4.946	0.590	71.601	0.259	67	0.114	3.314	0.448
4	0.05	6.636	12	0.566	9.475	0.510	22.149	0.790	42	0.180	4.902	0.815
5	0.1	6.636	12	0.579	6.700	0.520	50.113	0.392	43	0.132	14.039	0.922
6	0.15	6.636	12	0.593	5.470	0.520	80.545	0.259	71	0.112	24.588	0.641
7	0.05	7	12	0.596	9.995	0.480	23.593	0.790	N/A	N/A	8.627	0.688
8	0.1	7	12	0.609	7.067	0.480	53.352	0.392	N/A	N/A	23.471	0.795
9	0.15	7	12	0.622	5.771	0.480	85.725	0.259	65	0.107	32.471	0.733
13	0.05	6.636	14	0.487	9.475	0.750	22.149	0.806	38	0.164	0.706	1.140
14	0.1	6.636	14	0.500	6.700	0.770	50.113	0.400	56	0.117	3.941	1.076
16	0.05	7	14	0.513	9.995	0.710	23.593	0.806	35	0.167	3.882	1.256
17	0.1	7	14	0.526	7.067	0.720	53.352	0.400	43	0.115	9.294	1.183
18	0.15	7	14	0.541	5.771	0.740	85.725	0.265	71	0.093	12.667	0.415
23	0.1	6.636	14.7	0.478	6.700	0.870	50.113	0.403	51	0.107	0.863	0.935
25	0.05	7	14.7	0.489	9.995	0.800	23.593	0.811	40	0.158	0.588	0.944
26	0.1	7	14.7	0.503	7.067	0.820	53.352	0.403	52	0.108	4.706	1.300
27	0.15	7	14.7	0.517	5.771	0.840	85.725	0.266	69	0.086	1.098	0.413

Table 5.4.: Data for which slugs form.

D.S.	$h_0 (= \epsilon)$	$u_l^0$	$u_g^0$	$\delta$	$F_0$	$F_r$	$R_l (= R_g)$	$\lambda$	R.W. $h\%$	R.W. Width
10	0.05	6	14	0.441	8.567	0.830	19.658	0.806	34	0.169
12	0.15	6	14	0.469	4.946	0.880	71.601	0.265	64	0.086
19	0.05	6	14.7	0.421	8.567	0.930	19.658	0.811	33	0.159
20	0.1	6	14.7	0.434	6.058	0.960	44.524	0.403	47	0.102
21	0.15	6	14.7	0.448	4.946	0.990	71.601	0.266	67	0.079
22	0.05	6.636	14.7	0.464	9.475	0.840	22.149	0.811	37	0.158
24	0.15	6.636	14.7	0.492	5.470	0.890	80.545	0.266	68	0.084

Table 5.5.: Data for which no slugs form.

D.S.	$h_0 (= \epsilon)$	$u_l^0$	$u_g^0$	$\delta$	$F_0$	$F_r$	$R_l (= R_g)$	$\lambda$	R.W. $h\%$	R.W. Width
11	0.1	6	14	0.455	6.058	0.850	44.524	0.400	49	0.113
15	0.15	6.636	14	0.515	5.470	0.790	80.545	0.265	65	0.091

Table 5.6.: Other.

$0 < x < 200$  which begin to grow until  $x \approx 200$  at which point there are no longer any roll waves left to be absorbed and the slugs are unable to grow further. In Figure 5.21b we can see again that the slugs form in the region  $0 < x < 200$ , however as fewer slugs have formed they are able to continue to grow throughout the whole length of the channel.

These simulations were completed for two different  $r$  vectors in order to check the results were consistent. For one  $r$  vector Data Set 15 produced no slugs, however for the other it produced a few slugs. This may be due to the chaotic nature of the system, or the first  $r$  vector may have needed to be run for longer in order to produce a slug. When Data Set 11 was run it produced a few larger roll waves which did not continue to develop into full slugs; this again could mean if it was run for longer we would get a slug. Hence, the results from these Data Sets have been omitted.

## 5.4 EFFECTS OF VARYING THE PARAMETERS

We will begin by setting  $\epsilon = 0.1$ ,  $R_l = 50$ ,  $R_g = 50$ ,  $\rho = 0.1$  and solving our IVP for all combinations of  $\delta = 0.35, 0.4, 0.45, 0.5, 0.55, 0.6$  and  $0.65$  and  $\lambda = 0.2, 0.4, 0.6, 0.8, 1, 2, 5, 7, 10$  and  $20$ . For each data set we will select the value of  $F_0$  such that  $F_r = 0.95$  in order to maximise the probability of producing slug solutions. The results of these simulations are shown in Table 5.7 for which slugs do form and Table 5.8 for which no slugs form.

From these tables we can see that slugs only form in data sets which have  $\delta \geq 0.5$  and as  $\lambda$  is increased, only the data sets containing the larger values of  $\delta$  result in slug solutions. We can also see that in the data sets that do form slugs, they form lots of slugs leaving very few roll waves throughout the channel due to the large value of  $F_0$ . From this we can conclude that the value of  $\lambda$  has a large influence on whether or not slugs will form, but not much effect on how many will form.

Figure 5.22 shows a plot of  $\delta$  against  $\lambda$  against average slugs per unit time with  $\lambda = 20$  omitted as we found no slugs for these data sets. We can see

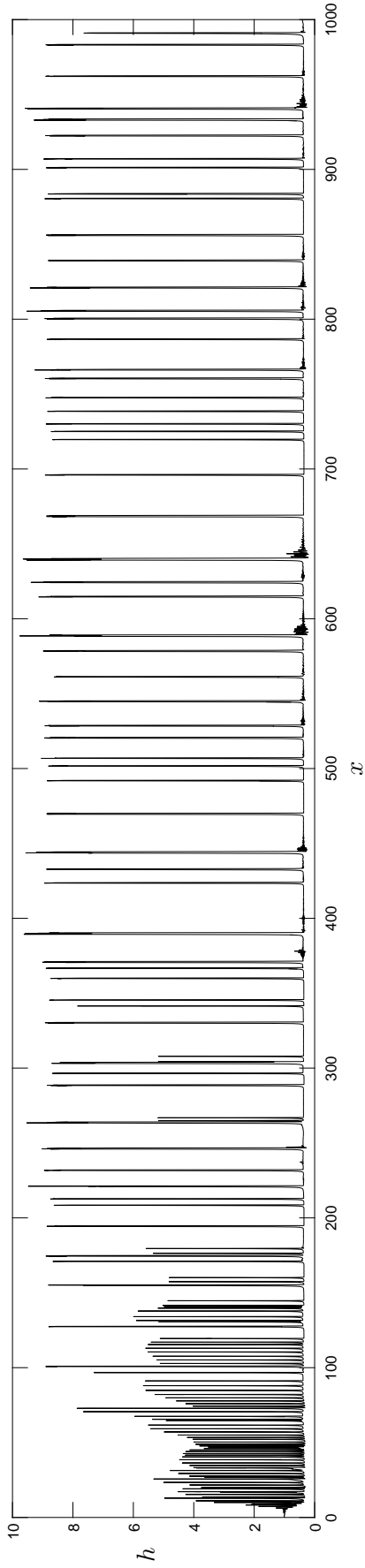


Figure 5.20a.: The solution of Data Set 8 at  $t = 3000$ .

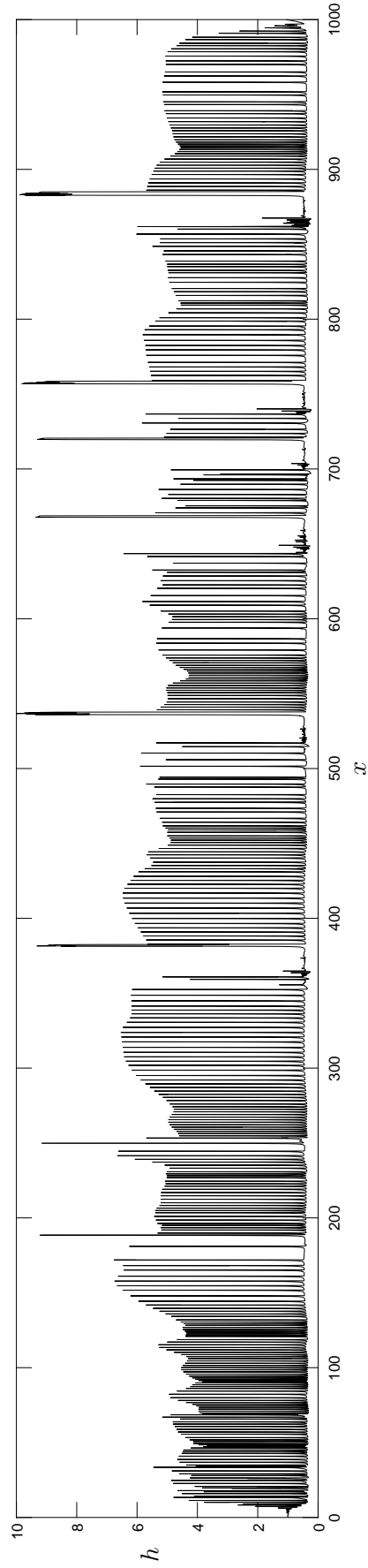
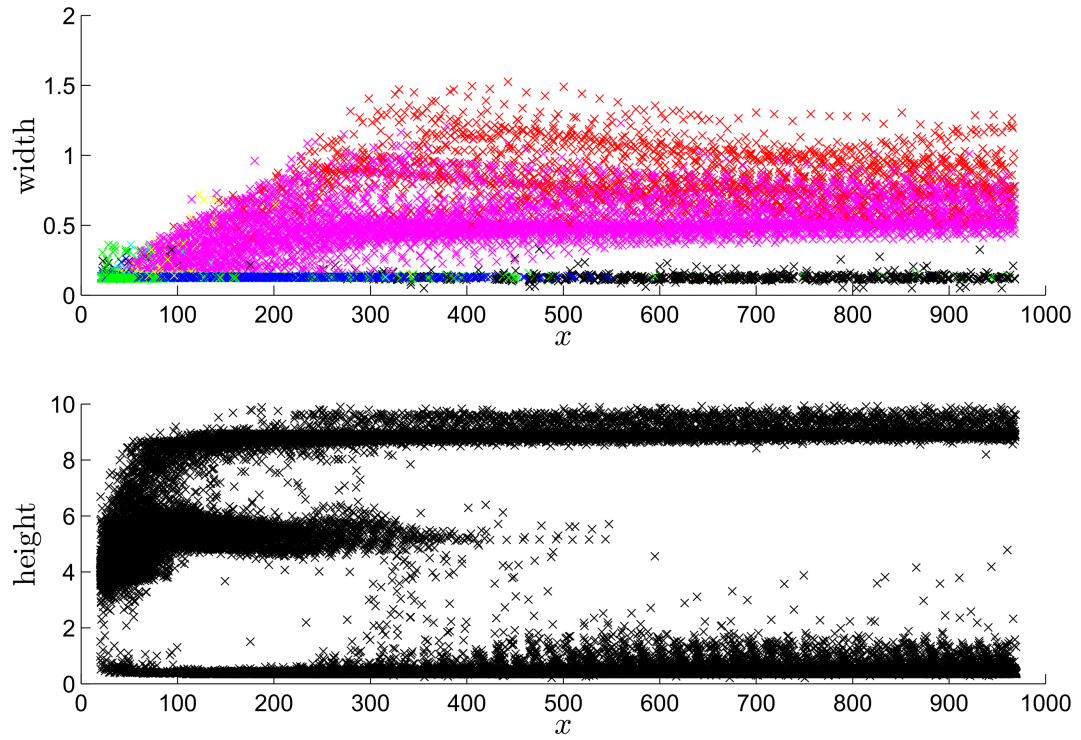
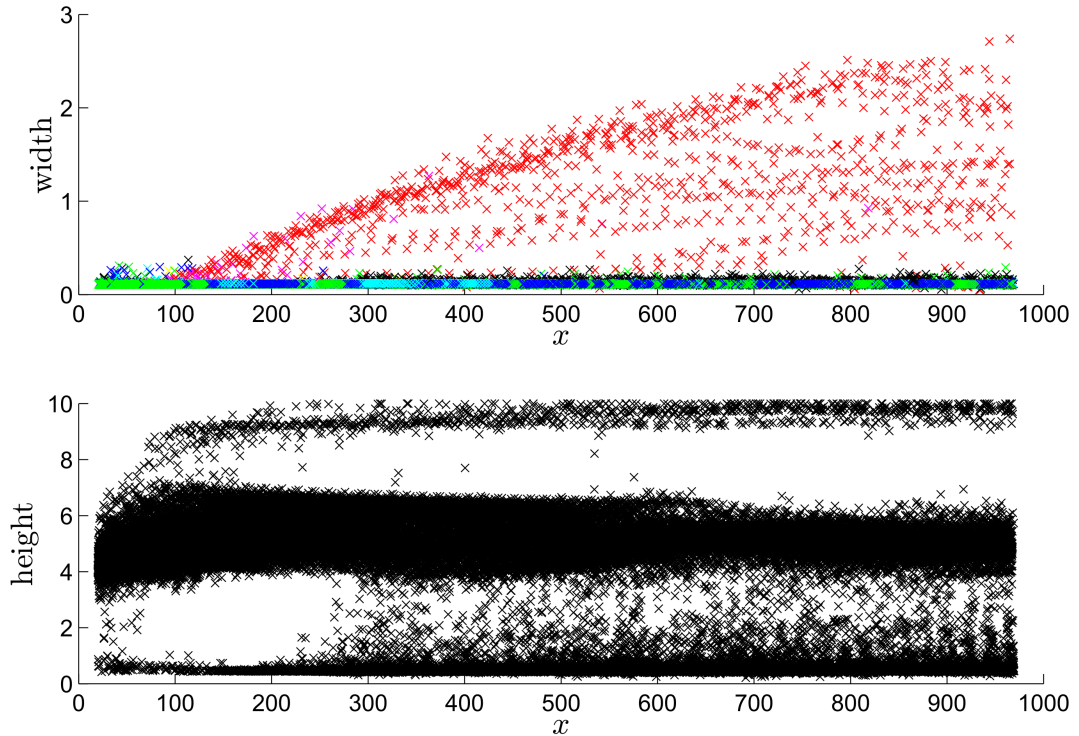


Figure 5.20b.: The solution of Data Set 14 at  $t = 3000$ .



**Figure 5.21a.:** The width and peak height against location in the channel of waves for Data Set 8.



**Figure 5.21b.:** The width and peak height against location in the channel of waves for Data Set 14.

5.4 EFFECTS OF VARYING THE PARAMETERS

D.S.	$\delta$	$F_0$	$\lambda$	R.W. $h\%$	R.W. Width	Avg Slugs	Slug Width
4	0.5	7.826	0.2	50	0.100	11.000	1.060
5	0.55	9.546	0.2	N/A	N/A	42.039	0.527
6	0.6	11.696	0.2	N/A	N/A	68.647	0.389
7	0.65	14.460	0.2	N/A	N/A	92.176	0.335
11	0.5	7.832	0.4	49	0.103	8.804	1.415
12	0.55	9.553	0.4	N/A	N/A	37.745	0.536
13	0.6	11.702	0.4	N/A	N/A	61.235	0.429
14	0.65	14.466	0.4	N/A	N/A	88.373	0.331
18	0.5	7.839	0.6	51	0.109	8.020	1.417
19	0.55	9.559	0.6	N/A	N/A	35.176	0.583
20	0.6	11.708	0.6	N/A	N/A	56.843	0.444
21	0.65	14.471	0.6	N/A	N/A	85.627	0.339
25	0.5	7.845	0.8	52	0.105	6.294	1.469
26	0.55	9.565	0.8	N/A	N/A	34.490	0.569
27	0.6	11.714	0.8	N/A	N/A	53.294	0.471
28	0.65	14.477	0.8	N/A	N/A	85.529	0.331
32	0.5	7.851	1	50	0.107	5.196	1.502
33	0.55	9.571	1	N/A	N/A	33.941	0.569
34	0.6	11.720	1	N/A	N/A	49.490	0.468
35	0.65	14.482	1	N/A	N/A	84.863	0.326
39	0.5	7.878	2	54	0.109	0.275	0.985
40	0.55	9.598	2	N/A	N/A	21.451	0.654
41	0.6	11.746	2	N/A	N/A	42.510	0.492
42	0.65	14.507	2	N/A	N/A	66.647	0.400
47	0.55	9.660	5	51	0.118	1.451	1.230
48	0.6	11.810	5	N/A	N/A	24.490	0.606
49	0.65	14.571	5	N/A	N/A	46.667	0.469
55	0.6	11.843	7	46	0.114	10.529	0.517
56	0.65	14.606	7	N/A	N/A	39.784	0.451
63	0.65	14.649	10	N/A	N/A	23.431	0.509

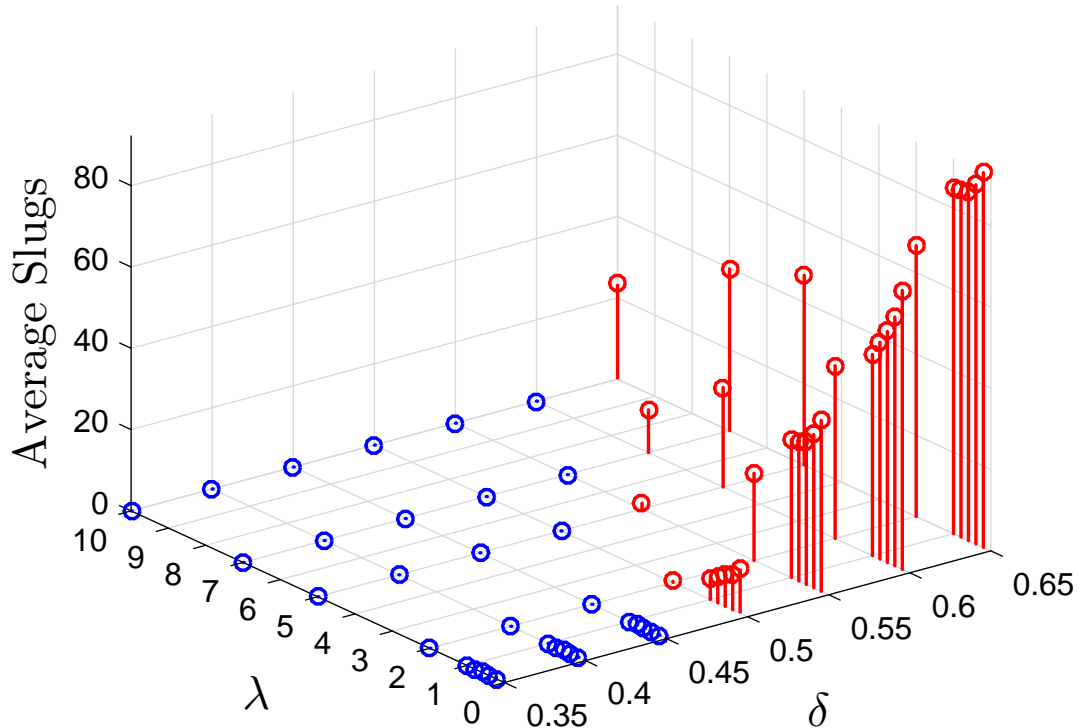
Table 5.7.: Data for which slugs form when varying  $\delta$  and  $\lambda$ .

D.S.	$\delta$	$F_0$	$\lambda$	R.W. $h\%$	R.W. Width
1	0.35	4.25	0.2	45	0.087
2	0.4	5.24	0.2	46	0.094
3	0.45	6.42	0.2	49	0.098
8	0.35	4.26	0.4	45	0.087
9	0.4	5.25	0.4	46	0.095
10	0.45	6.42	0.4	48	0.099
15	0.35	4.26	0.6	45	0.087
16	0.4	5.26	0.6	45	0.095
17	0.45	6.43	0.6	48	0.100
22	0.35	4.27	0.8	45	0.087
23	0.4	5.26	0.8	45	0.095
24	0.45	6.44	0.8	47	0.101
29	0.35	4.27	1	44	0.087
30	0.4	5.27	1	45	0.095
31	0.45	6.44	1	46	0.101
36	0.35	4.29	2	46	0.084
37	0.4	5.29	2	45	0.094
38	0.45	6.47	2	47	0.102
43	0.35	4.33	5	49	0.077
44	0.4	5.34	5	47	0.089

D.S.	$\delta$	$F_0$	$\lambda$	R.W. $h\%$	R.W. Width
45	0.45	6.52	5	47	0.099
46	0.5	7.94	5	49	0.107
50	0.35	4.34	7	51	0.075
51	0.4	5.35	7	49	0.086
52	0.45	6.54	7	48	0.097
53	0.5	7.96	7	48	0.107
54	0.55	9.69	7	50	0.114
57	0.35	4.35	10	52	0.074
58	0.4	5.36	10	50	0.083
59	0.45	6.56	10	49	0.094
60	0.5	7.99	10	47	0.105
61	0.55	9.72	10	47	0.113
62	0.6	11.9	10	53	0.118
64	0.35	4.36	20	55	0.071
65	0.4	5.38	20	51	0.079
66	0.45	6.59	20	49	0.089
67	0.5	8.03	20	46	0.101
68	0.55	9.78	20	43	0.111
69	0.6	12	20	40	0.120
70	0.65	14.7	20	44	0.123

Table 5.8.: Data for which no slugs form when varying  $\delta$  and  $\lambda$ .



**Figure 5.22.:**  $\delta$  against  $\lambda$  against average slugs per unit time where blue represents no slugs.

a clear boundary between values of  $\delta$  and  $\lambda$  that form slugs and those that do not and that for a given value of  $\lambda$ , increasing  $\delta$  increases the number of slugs.

Focusing on the 'Average Slugs' and 'Slug Width' columns in Table 5.7 we can see that, as we found in Section 5.3, the width of the slugs decreases as the number of slugs increases. Figure 5.23 shows plots of the solutions at  $t = 1000$  and the width of the waves against peak height location throughout the simulation (using the legend from Figure 5.17) for Data Sets 32, 33, 34 and 35 which have the same parameters except for  $\delta$ . From Figure 5.23a we can see the channel mainly consists of roll waves and has a few slugs which have a large region of separation between each other. As there are still roll waves left at  $x = 500$ , the slugs would continue to grow in width if we had used a longer channel so the value given for 'Slug Width' in Table 5.7 does not represent the maximum possible width of a slug for this parameter set. When  $\delta$  is increased to 0.55 we can see from Figure 5.23b the solution

now consists almost entirely of slugs, some of which are actually at their widest at  $x \approx 200$  and slowly decrease in width throughout the channel. This is due to there still being some roll waves up to  $x \approx 200$  allowing the slugs to grow up until this point, after which, due to them leaving some discharge behind (as in Figure 5.15), they decrease in size until their width is approximately 0.569. At this point they reach an equilibrium between the discharge they leave behind and the liquid they absorb from the discharge left behind by the slug in front. As  $\delta$  is increased further to 0.6 and 0.65, shown in Figures 5.23c and 5.23d respectively, we see the same effects as for  $\delta = 0.55$ . As  $\delta$  has increased, the distance along the channel for which there are roll waves has decreased due to the increased amount of slugs produced. As there are significantly less roll waves for the slugs to absorb we now see that, not only are the slugs narrower, they are also shorter (shown by the large quantity of purple in Figure 5.23d). This leads us to conclude that, although increasing  $\delta$  increases the number of slugs, we get the widest slugs for values of  $\delta$  closest to the boundary between Data Sets that slug and those that do not at  $\delta \approx 0.5$ .

In order to understand what is happening at the  $\delta \approx 0.5$  boundary between Data Sets that produce slugs and those that do not we will consider all combinations of  $\delta = 0.45, 0.46, 0.47, 0.48, 0.49$  and  $0.5$ ,  $\lambda = 0.2, 0.4, 0.6, 0.8$  and  $1$  and  $F_0 = 5, 5.5, 6, 6.5, 7, 7.5$ , and  $8$  excluding values where  $F_0 > F_{NH}$ . (The tables corresponding to these Data Sets are given in the Appendix where Table A.1 shows the Data Sets that produced slugs and Table A.2 shows the Data Sets that produced no slugs.) Figure 5.24 shows plots of  $\delta$  against  $F_0$  against the average number of slugs per unit time for each value of  $\lambda$ . From these we see that, for Data Sets that produce slugs, increasing either  $\delta$  and  $F_0$  increases the number of slugs produced. Looking at the 'Slug Width' column in Table A.1 it appears that increasing  $\delta$  and  $F_0$  increases the width of the slugs, however this is due to our channel not being long enough for the slugs to reach their maximum width. The smaller values of  $\delta$  and  $F_0$  result in slower moving slugs so they take longer to catch

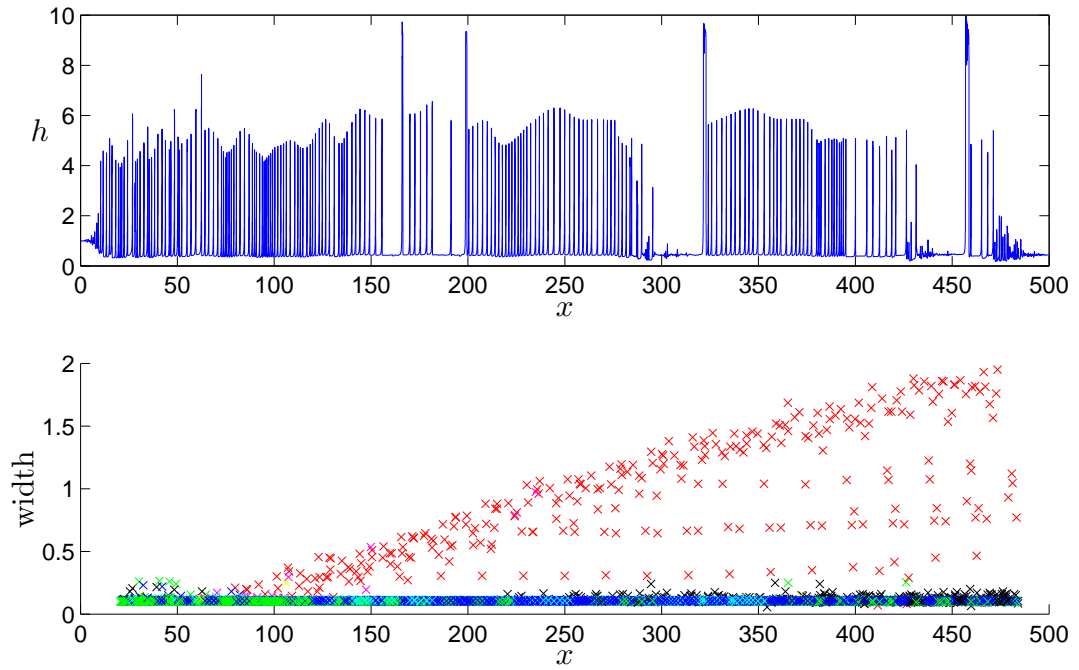


**Figure 5.23a.:** The solution of Data Set 32 ( $\delta = 0.5$ ) at  $t = 1000$  and the width of the waves against peak height location throughout the simulation.

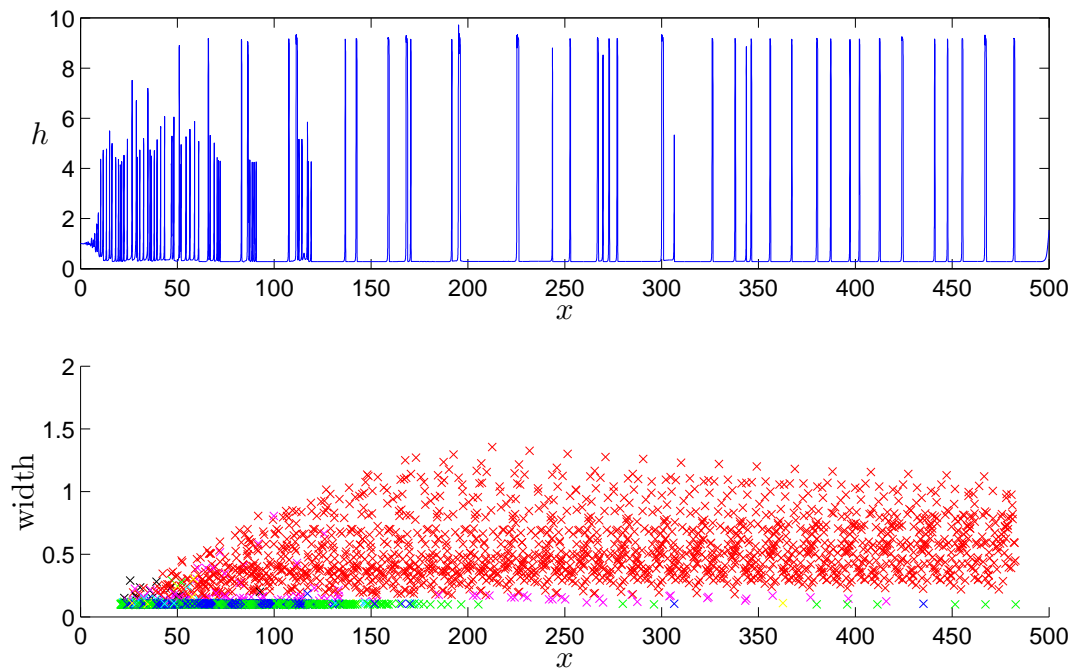


**Figure 5.23b.:** The solution of Data Set 33 ( $\delta = 0.55$ ) at  $t = 1000$  and the width of the waves against peak height location throughout the simulation.

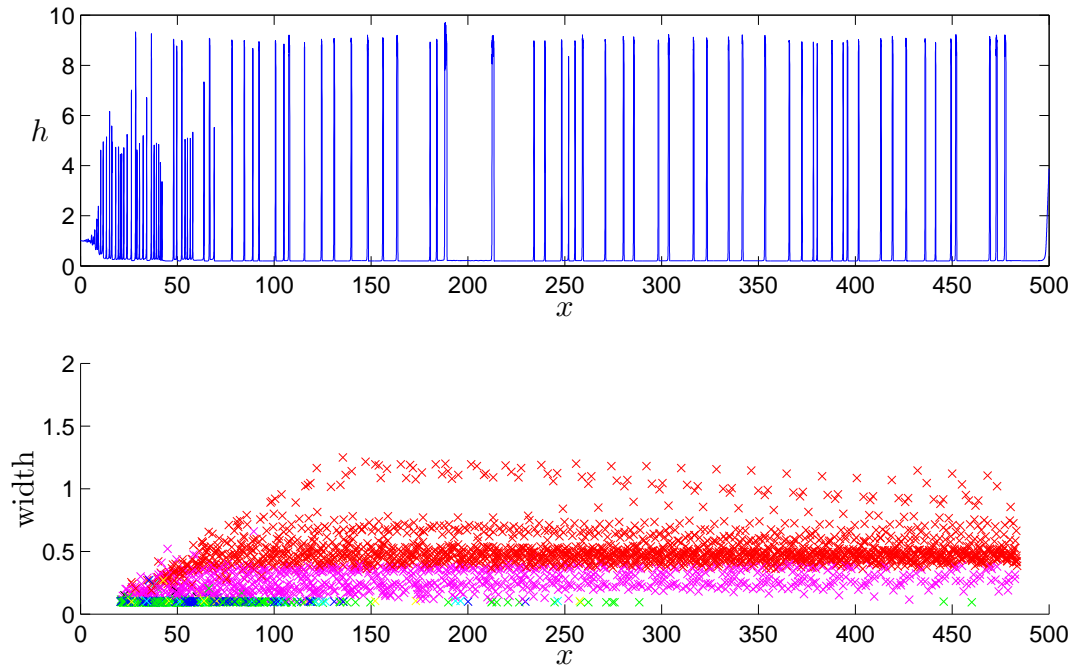


**Figure 5.23c.:** The solution of Data Set 34 ( $\delta = 0.6$ ) at  $t = 1000$  and the width of the waves against peak height location throughout the simulation.

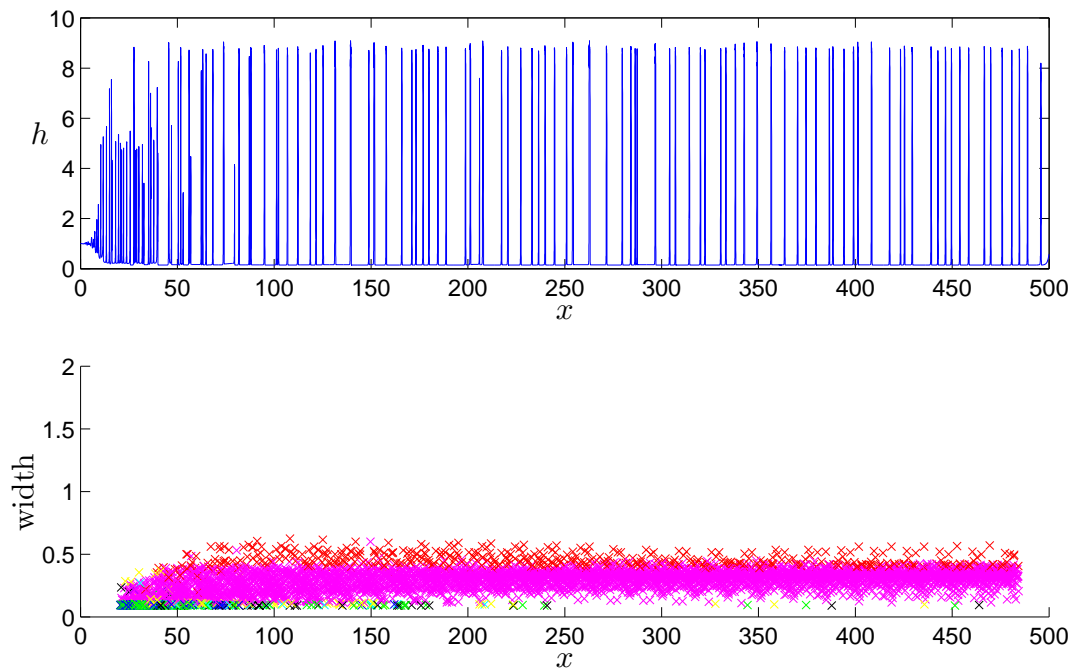


**Figure 5.23d.:** The solution of Data Set 35 ( $\delta = 0.65$ ) at  $t = 1000$  and the width of the waves against peak height location throughout the simulation.

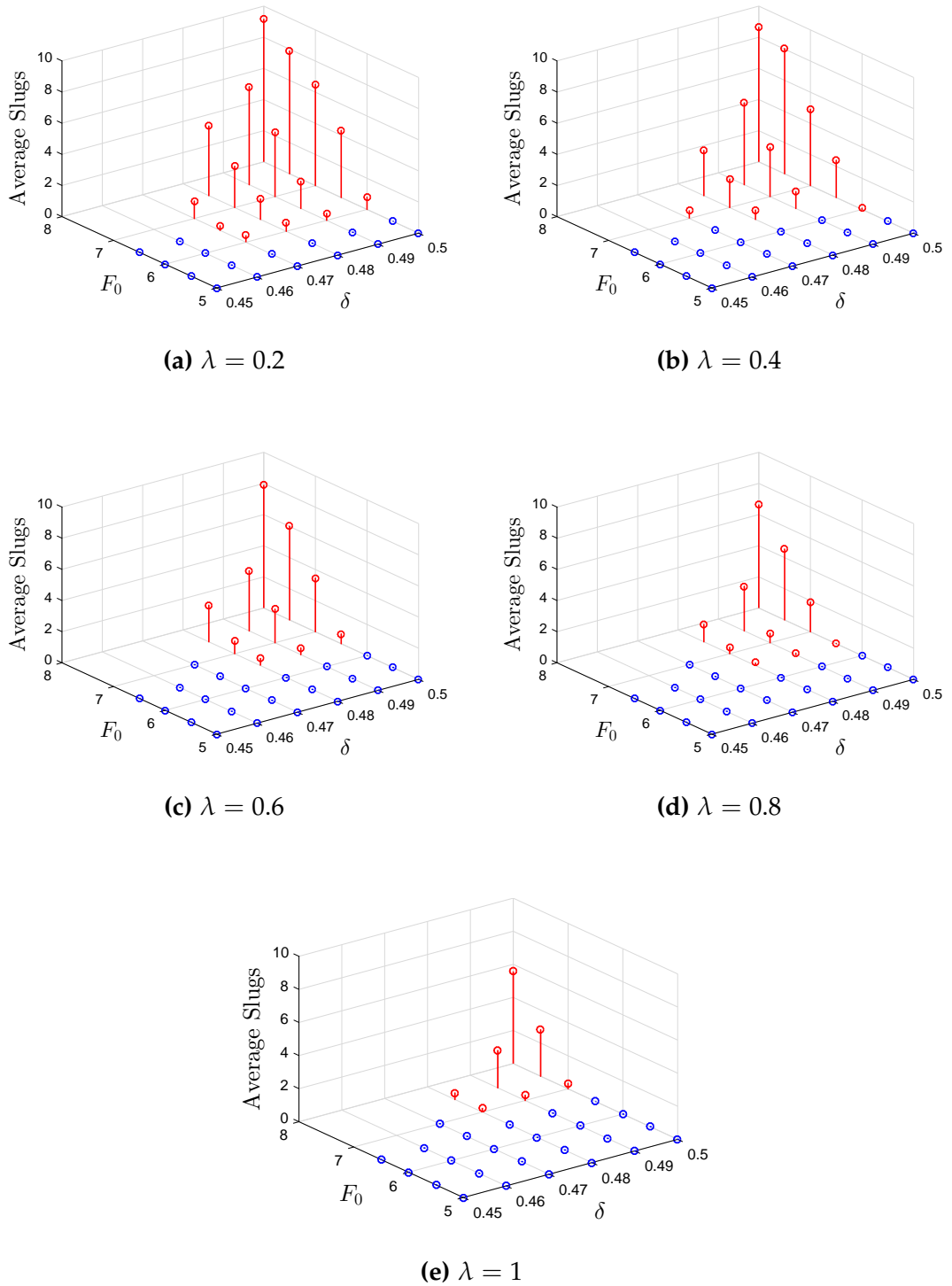


**Figure 5.24.:** The average number of slugs per unit time compared to  $F_0$  and  $\delta$  where blue represents no slugs.

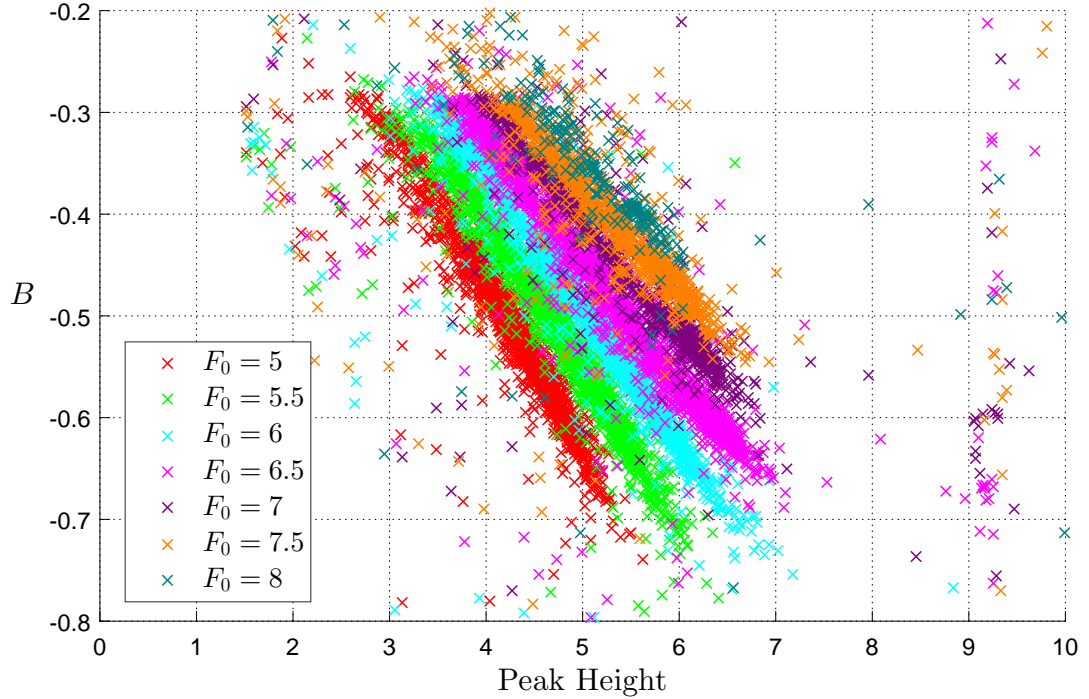


**Figure 5.25.:** The wave peak height against  $B$  for  $\epsilon = 0.1$ ,  $\delta = 0.5$ ,  $\lambda = 0.4$ ,  $R_l = 50$ ,  $R_g = 50$ ,  $\rho = 0.1$  and varying  $F_0$ .

and absorb roll waves, but as there are less slugs in these simulations there are more roll waves to be absorbed resulting in larger slugs if the channel is long enough.

We will now focus on Data Sets 58, 59, 60, 61, 62, 63 and 64 for which  $\lambda = 0.4$  and  $\delta = 0.5$ . From Figure 5.24b we see that we get slugs for  $F_0 \geq 6$ . For each value of  $F_0$  we can calculate the value of  $U$  for each wave by measuring how far it has travelled down the channel in one  $t$  (using the method of fitting a quadratic to the top of the wave as described in Section 5.1) and hence calculate its value of  $B$ . Note that due to the turbulent tops of the slugs, the values of  $U$  and  $B$  calculated will not be accurate. Figures 5.25, 5.26 and 5.27 show plots of the peak height against  $B$ ,  $U$  against  $B$  and  $U$  against peak height, respectively, and Figures 5.28a - 5.28g show the corresponding bifurcation diagrams for  $-0.8 \leq B \leq -0.2$  from our work on periodic travelling waves in Chapter 4.

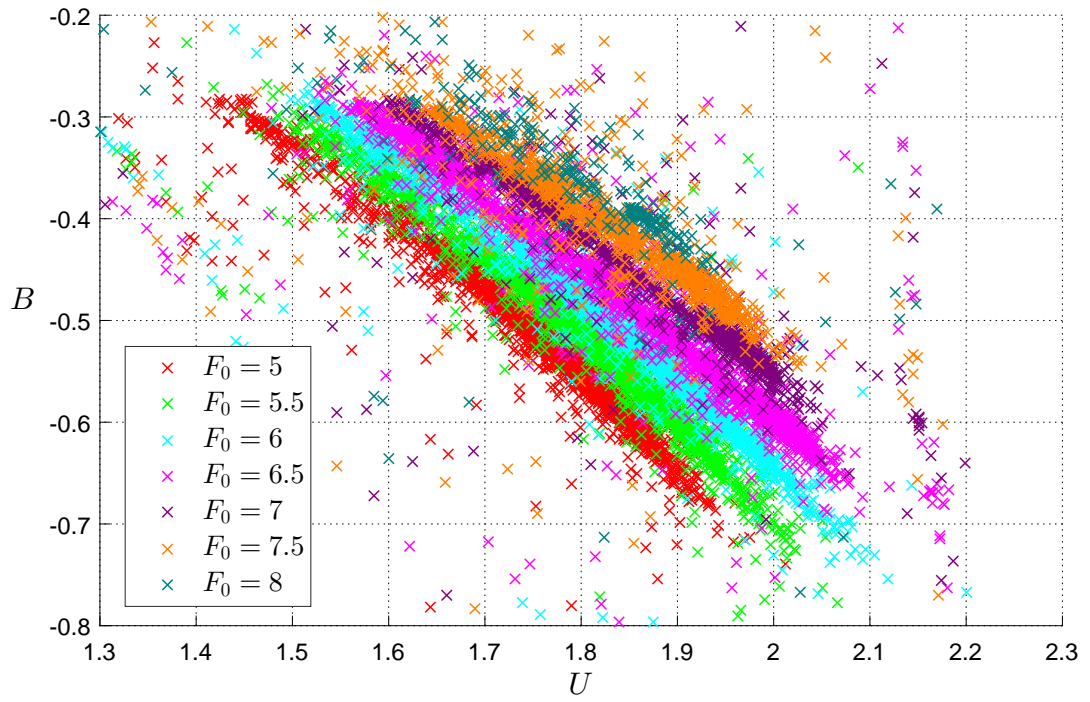


**Figure 5.26.:** The propagation speed,  $U$ , against  $B$  for  $\epsilon = 0.1$ ,  $\delta = 0.5$ ,  $\lambda = 0.4$ ,  $R_l = 50$ ,  $R_g = 50$ ,  $\rho = 0.1$  and varying  $F_0$ .

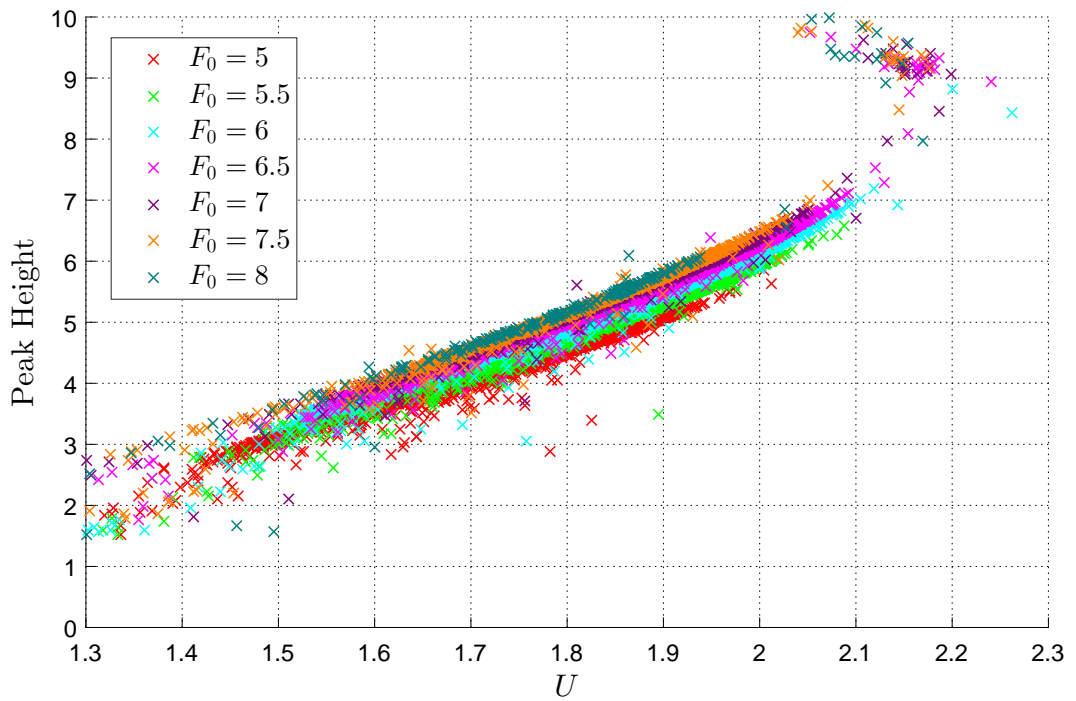


**Figure 5.27.:** The propagation speed,  $U$ , against wave peak height for  $\epsilon = 0.1$ ,  $\delta = 0.5$ ,  $\lambda = 0.4$ ,  $R_l = 50$ ,  $R_g = 50$ ,  $\rho = 0.1$  and varying  $F_0$ .

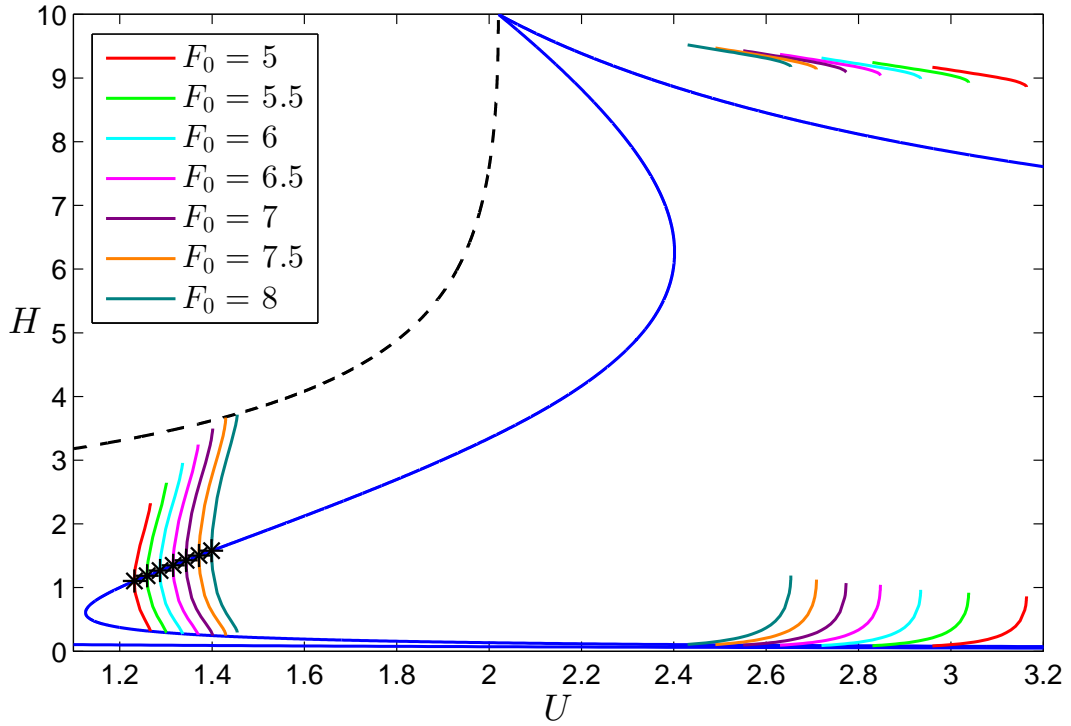


**Figure 5.28a.:** The bifurcation diagram for  $\epsilon = 0.1, \delta = 0.5, \lambda = 0.4,$   
 $R_l = 50, R_g = 50, \rho = 0.1,$  varying  $F_0$  and  $B = -0.2.$

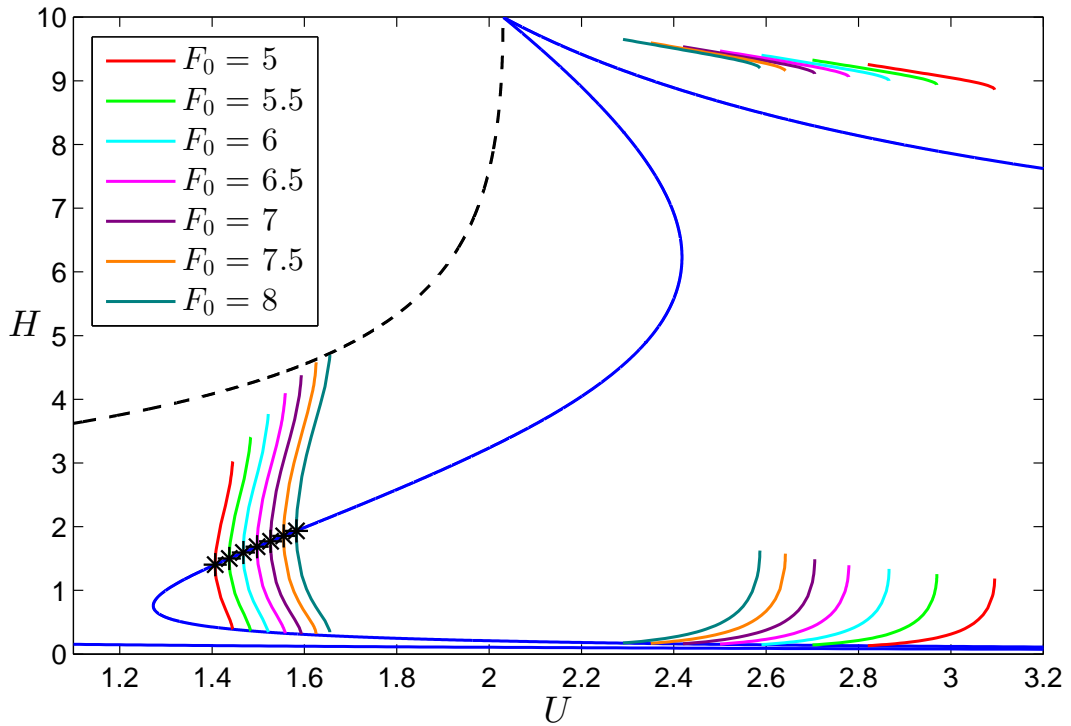


**Figure 5.28b.:** The bifurcation diagram for  $\epsilon = 0.1, \delta = 0.5, \lambda = 0.4,$   
 $R_l = 50, R_g = 50, \rho = 0.1,$  varying  $F_0$  and  $B = -0.3.$

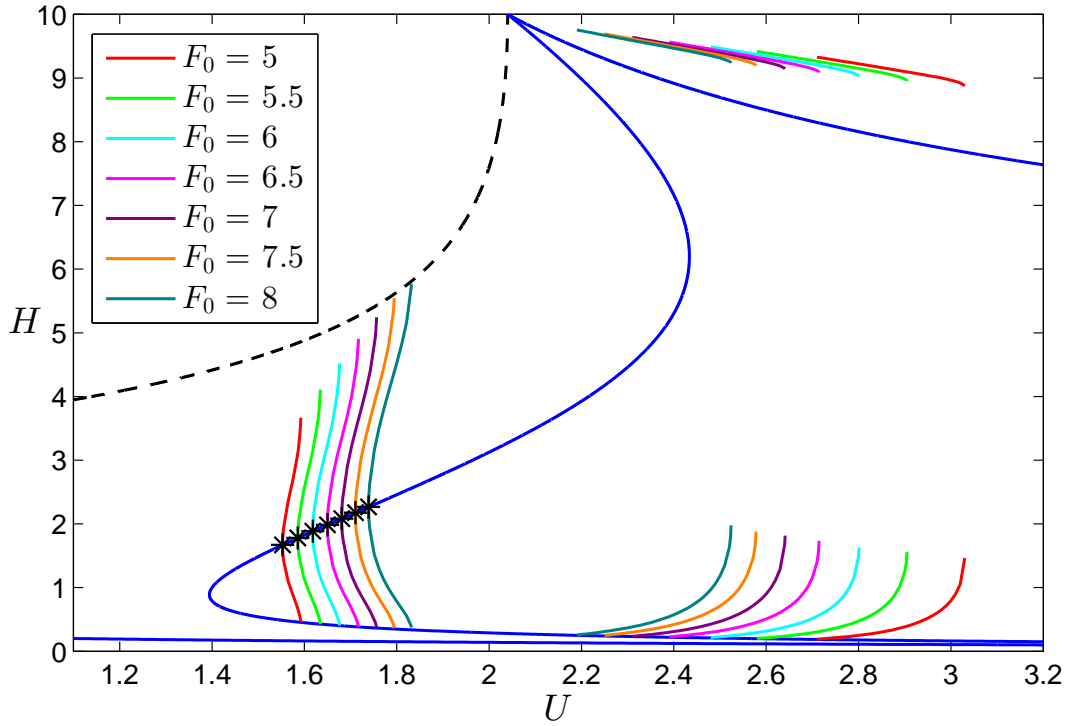


**Figure 5.28c.:** The bifurcation diagram for  $\epsilon = 0.1, \delta = 0.5, \lambda = 0.4,$   
 $R_l = 50, R_g = 50, \rho = 0.1,$  varying  $F_0$  and  $B = -0.4.$

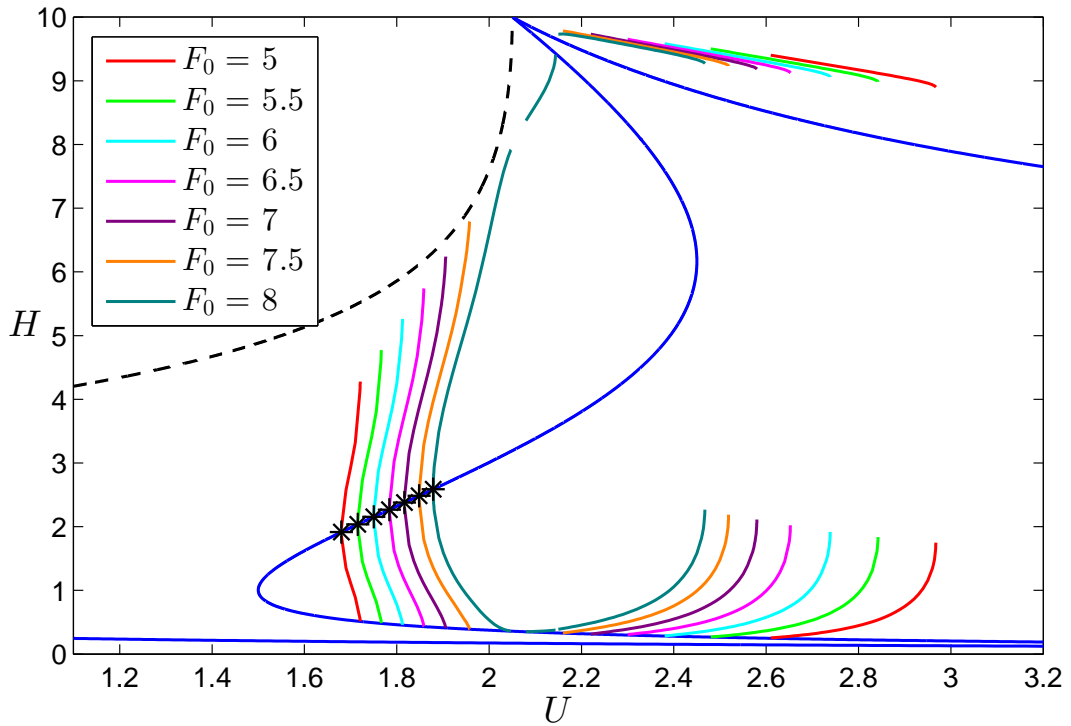


**Figure 5.28d.:** The bifurcation diagram for  $\epsilon = 0.1, \delta = 0.5, \lambda = 0.4,$   
 $R_l = 50, R_g = 50, \rho = 0.1,$  varying  $F_0$  and  $B = -0.5.$

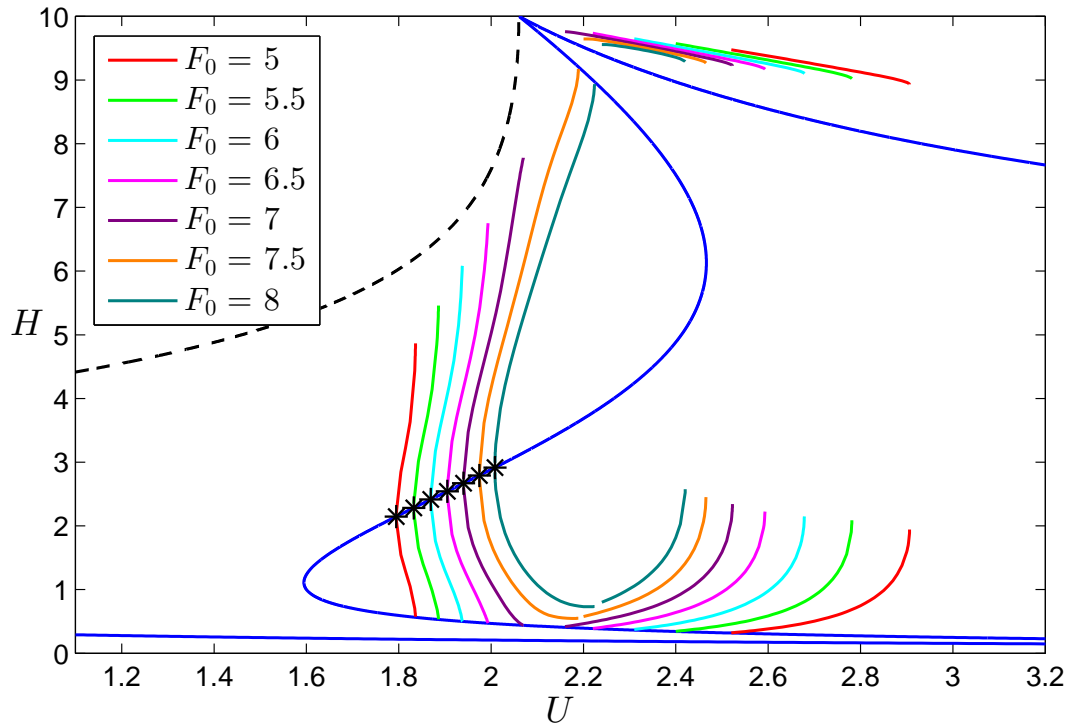


**Figure 5.28e.:** The bifurcation diagram for  $\epsilon = 0.1$ ,  $\delta = 0.5$ ,  $\lambda = 0.4$ ,  
 $R_l = 50$ ,  $R_g = 50$ ,  $\rho = 0.1$ , varying  $F_0$  and  $B = -0.6$ .

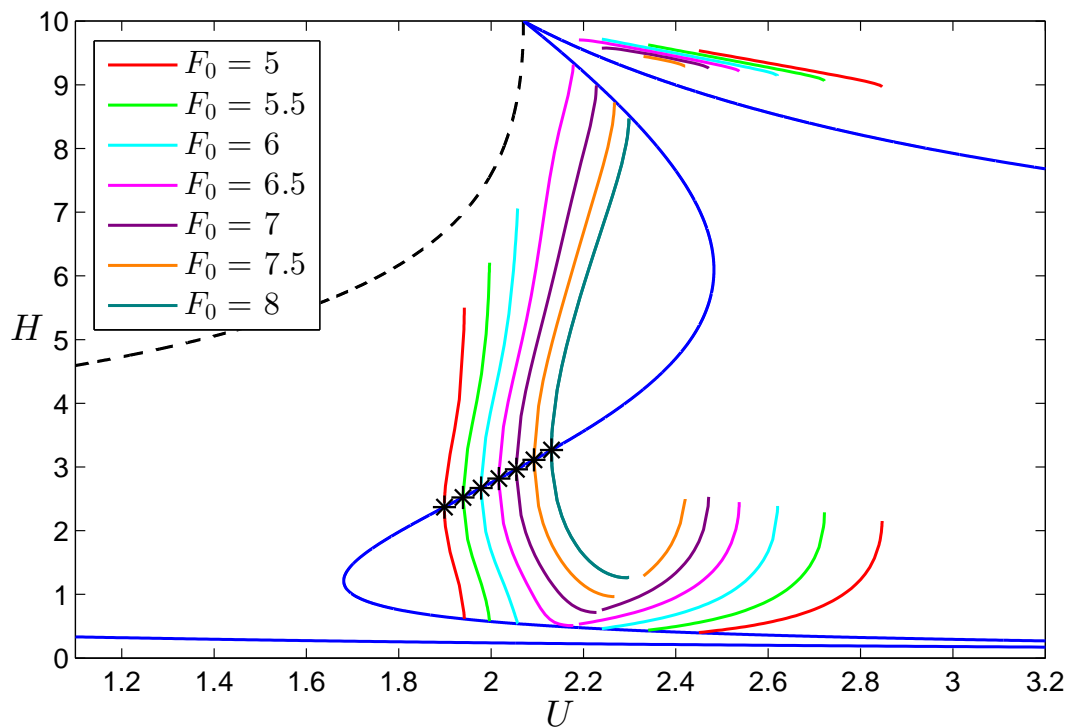


**Figure 5.28f.:** The bifurcation diagram for  $\epsilon = 0.1$ ,  $\delta = 0.5$ ,  $\lambda = 0.4$ ,  
 $R_l = 50$ ,  $R_g = 50$ ,  $\rho = 0.1$ , varying  $F_0$  and  $B = -0.7$ .

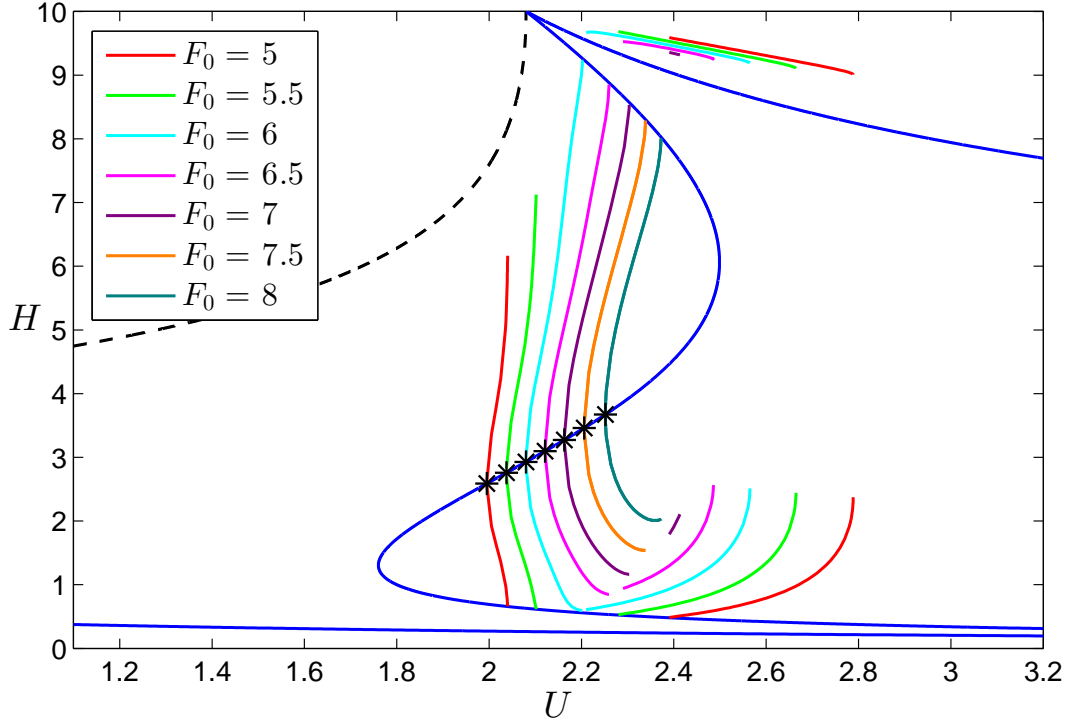


**Figure 5.28g.:** The bifurcation diagram for  $\epsilon = 0.1$ ,  $\delta = 0.5$ ,  $\lambda = 0.4$ ,  
 $R_l = 50$ ,  $R_g = 50$ ,  $\rho = 0.1$ , varying  $F_0$  and  $B = -0.8$ .

From Figures 5.25 - 5.27 we can see that the roll waves start with  $B \approx -0.3$  and  $U \approx 1.5$  and as they grow their value of  $B$  decreases and their value of  $U$  increases until the roll waves are able to form slugs. As  $F_0$  is increased, the roll wave peak height and value of  $U$  needed in order to produce a slug is decreased whilst the value of  $B$  is increased. This means for larger  $F_0$  it is easier to produce slugs, as we found in our earlier work. By comparing Figure 5.25 to Figures 5.28a - 5.28g, we can see that for each value of  $B$  the roll waves correspond to the maximum value of  $U$  and peak height possible in the corresponding bifurcation diagram, therefore for them to grow further their value of  $B$  must decrease.

From (4.3.7) we must have  $U = 2 + \tilde{A}$  for  $0 < \tilde{A} \ll 1$  in order to produce slugs. Hence, for each value of  $F_0$ , we produce slugs if the waves have grown sufficiently large when  $U = 2 + \tilde{A}$ . As can be seen in Figures 5.28a - 5.28g this happens for  $F_0 \geq 6$ , but not for  $F_0 = 5.5$  or 5 hence we do not produce slugs in the IVP for these parameter sets.

We will now solve the IVP for all combinations of

$$\epsilon = 0.025, 0.05, 0.1$$

$$\delta = 0.2, 0.3, 0.4, 0.5, 0.6$$

$$F_r = 0.4, 0.6, 0.8$$

$$R_l = 30, 50, 70$$

$$R_g = 30, 50, 70, 100$$

$$\lambda = 0.5, 1, 2, 5$$

$$\rho = 0.1$$

in order to investigate the effects of varying all the parameters. Figure 5.29 shows plots of the average number of slugs per unit time compared to  $F_0$  and  $\delta$  and again we get no slugs unless  $\delta \geq 0.5$ . From equations (3.1.10) and (3.1.12) we know  $F_{NH} = F_{NH}(\epsilon, \delta, \rho)$  and  $F_c = F_c(\epsilon, \delta, \lambda, \rho)$  hence for our Data Sets we have multiple solutions with the same values of  $\delta$  and  $F_0$ , but different values of  $R_l$  and  $R_g$ .

Focusing on  $\lambda = 1$  and  $\delta = 0.5$ , Figure 5.29a shows that some of these Data Sets have produced slug solutions, however the number of slugs does not appear to increase as  $F_0$  is increased as our previous work would imply. This is due to the Data Sets we are comparing here having different values of  $\epsilon$ . Figure 5.30 shows the average number of slugs per unit time compared to  $F_0$  and  $\epsilon$  for  $\lambda = 1$  and  $\delta = 0.5$ . For each value of  $\epsilon$ , increasing  $F_0$  does increase the number of slugs, however we require a larger value of  $F_0$  as  $\epsilon$  is decreased in order to begin finding slug solutions. For the Data Sets shown in Figure 5.30,  $F_{min} = 6.246$  for  $\epsilon = 0.1$ ,  $F_{min} = 8.947$  for  $\epsilon = 0.05$  and  $F_{min} = 12.507$  for  $\epsilon = 0.025$ , where  $F_{min}$  is the smallest value of  $F_0$  for which we found slug solutions. As  $F_0 = u_l^0 / \sqrt{gh_0}$  we would expect a larger value of  $F_0$  for a smaller value of  $\epsilon$  and as  $F_{NH}$  increases as  $\epsilon$  decreases, we are able to solve our IVP for these values of  $F_0$  unlike earlier in this section where we could not go above  $F_0 \approx 9$ .

Finally, we can investigate the effects of our effective Reynolds numbers by fixing all our parameters other than  $R_l$  and  $R_g$ . Unlike our other parameters which have had clear monotonic effects on our solutions, the effects of

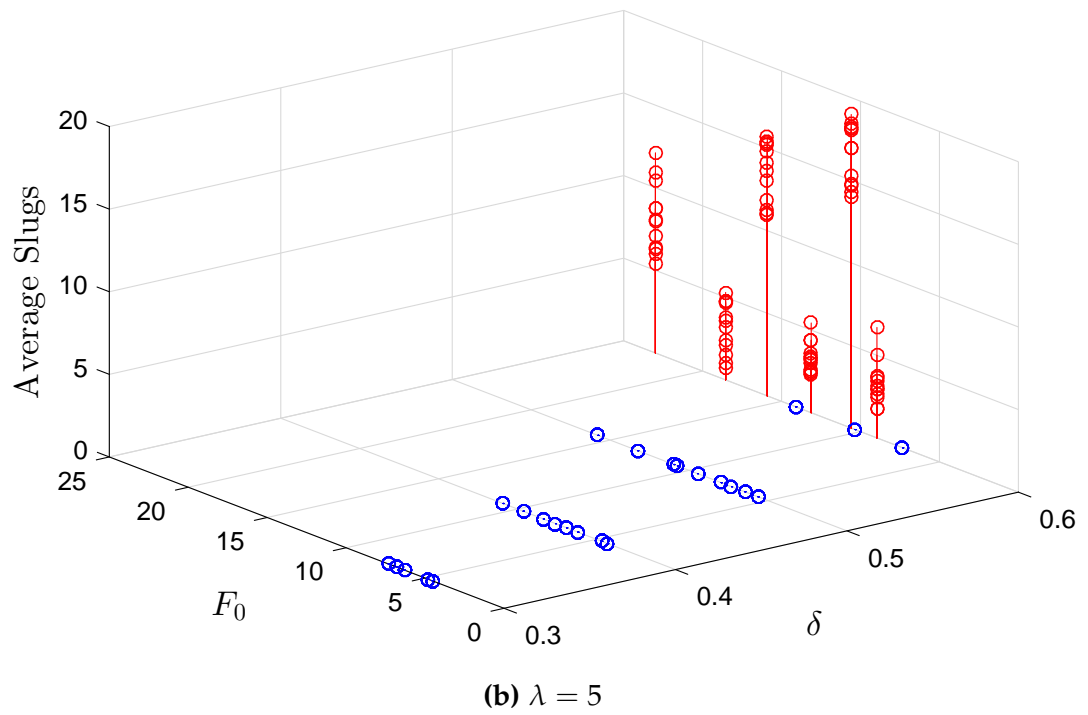
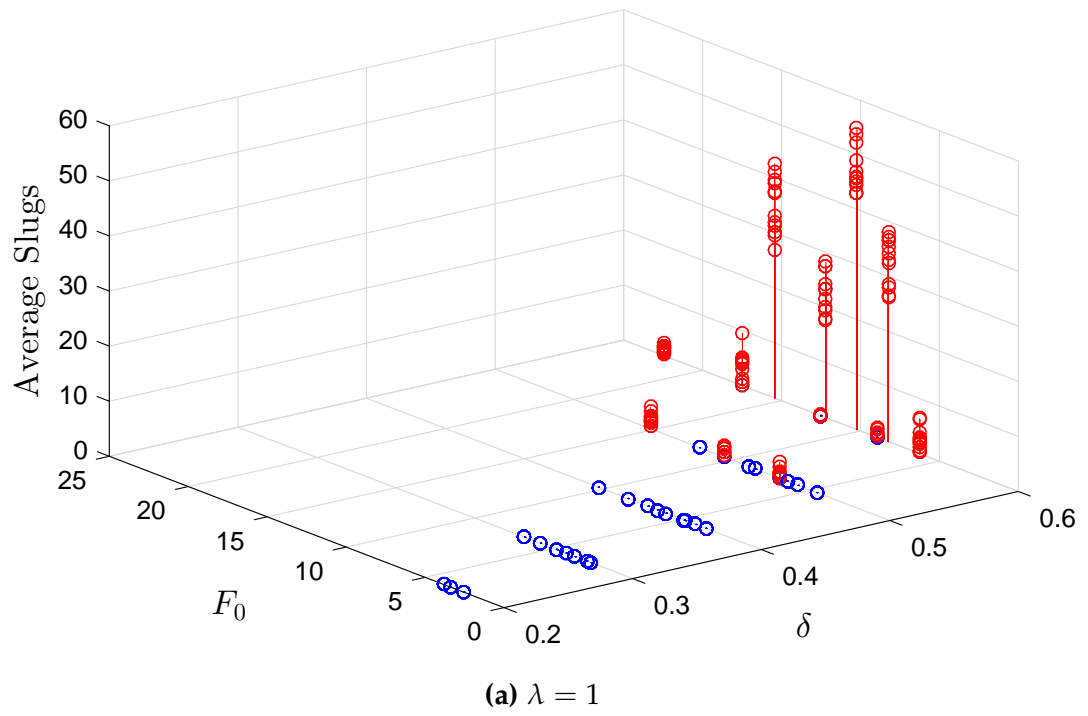


**Figure 5.29.:** The average number of slugs per unit time compared to  $F_0$  and  $\delta$  where blue represents no slugs.

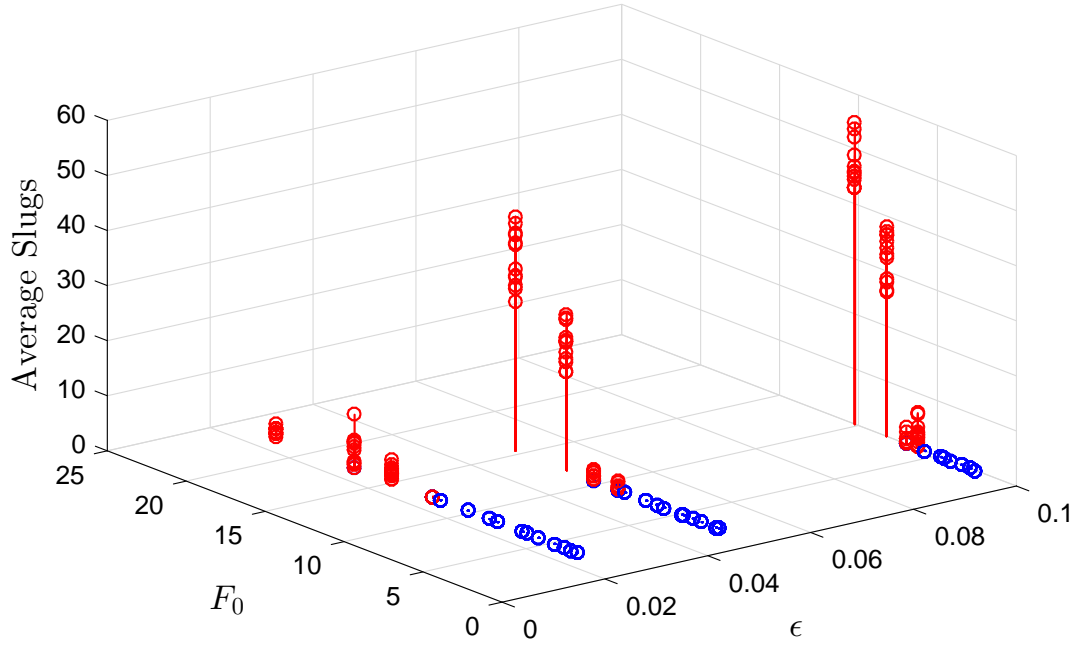


**Figure 5.30.:** The average number of slugs per unit time compared to  $F_0$  and  $\epsilon$  for  $\lambda = 1$  and  $\delta = 0.5$  where blue represents no slugs.

varying  $R_l$  and  $R_g$  differ depending on the other parameters, as shown in Figure 5.31. In Figure 5.31a the number of slugs increases as  $R_l$  increases or  $R_g$  decreases, in Figure 5.31b the number of slugs increases as either  $R_l$  or  $R_g$  decreases, in Figure 5.31c the number of slugs increases as either  $R_l$  or  $R_g$  increases and in Figure 5.31d the number of slugs increases as  $R_l$  decreases or  $R_g$  increases.

## 5.5 CONCLUSION

We have re-written our equations of motion from Chapter 2 into the form required to apply the finite-difference method derived by Kurganov and Tadmor [114] which we combined with a second-order Runge-Kutta method in order to solve our equations as an initial value problem. We performed spatial step size analysis on our IVP and found  $\Delta x = 0.005$  to be the optimum size in order to decrease computing time without losing accuracy. We then set the initial condition in the IVP to be the uniform flow plus some

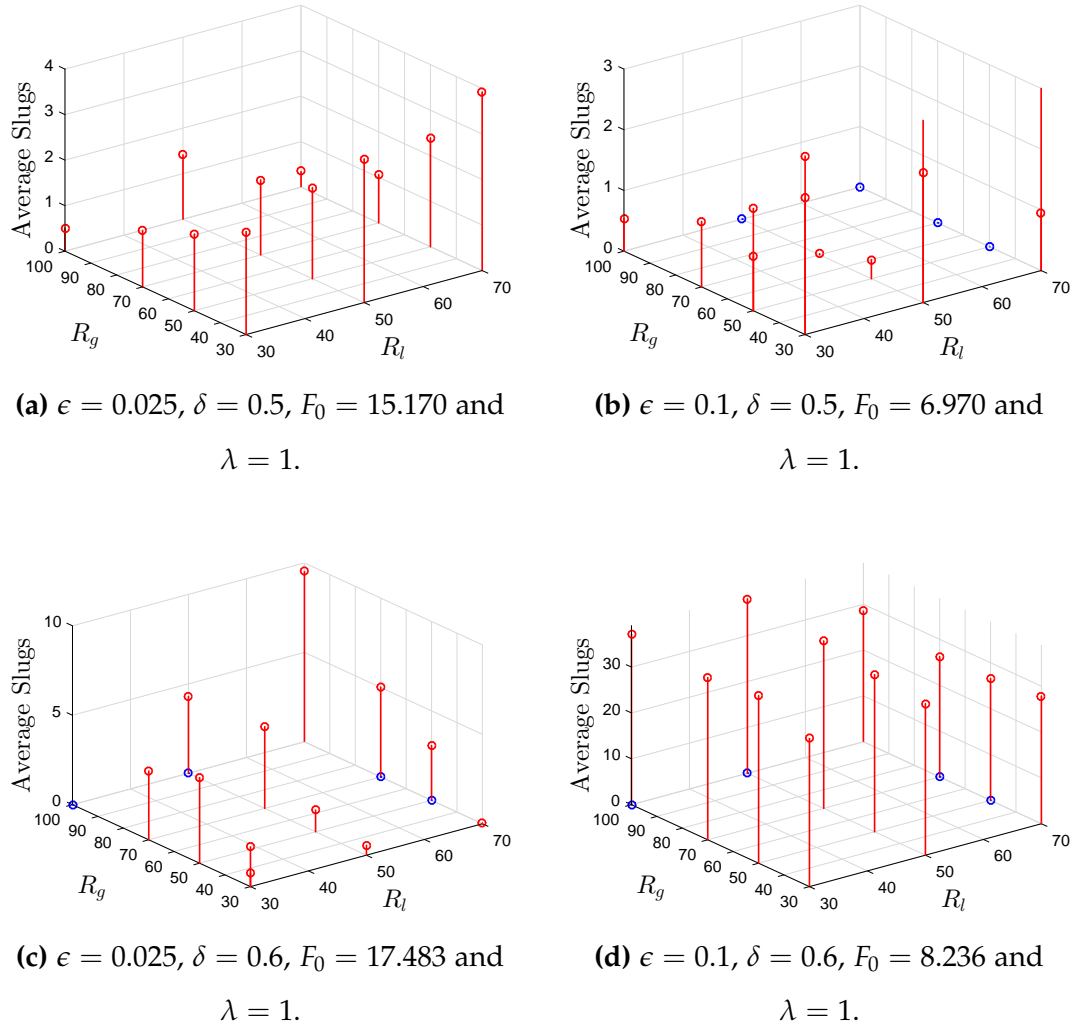


**Figure 5.31.:** The average number of slugs per unit time compared to  $R_l$  and  $R_g$  where blue represents no slugs.

small noise and found our work in Chapter 3 gave a very close prediction of the maximum growth rate. By using the solutions from `bvp5c` found in Section 4.3 as our initial condition in the IVP problem with periodic boundary conditions, we were able to determine their stability. From this we found regions within the bifurcation diagrams where the solutions, which contained both roll waves and slugs, were stable.

We then defined an inlet condition, the uniform flow plus some small amplitude random noise, and an outlet condition in order to simulate flow through a channel. We first used one of the parameter sets we had used in Section 4.3 in the IVP which resulted in the channel being predominantly

full of roll waves with a few slugs. By following these slugs as they travelled through the channel we saw that they begin as roll waves which propagate faster than the roll waves in front of them and as they catch the roll wave in front they absorb it, increasing in size to form a slug. They continue this process as they travel down the channel, increasing in size every time they absorb a roll wave, but also leaving a small amount of liquid behind. This liquid then begins to grow in amplitude and, if there is sufficient space behind the slug before the following roll waves, will form into roll waves.

In this simulation we were also able to see the effects of two slugs being close together. The lead slug propagates down the channel absorbing roll waves and growing in size, however the slug following behind it is unable to grow as there are no roll waves for it to absorb. This results in the slug being large in amplitude, but not much wider than the roll waves in the channel.

We then varied the parameters slightly in order to investigate the effects this had on our simulations. We found that the parameter sets with the larger values of  $\delta$  produced the most slugs, whereas those where  $\delta \approx 0.5$  produced the widest slugs. This is because in solutions which only produce a few slugs there are lots of roll waves for them to absorb as they travel down the channel, so they are constantly growing in size. In the solutions which produce lots of slugs, the roll waves are quickly absorbed early in the channel meaning once a slug has formed there are no more roll waves left in front of it and its width is not many times more than that of a roll wave.

By varying  $\delta$  and  $\lambda$  we were able to determine that,  $\delta \approx 0.5$  is a critical limit for our IVP which separates Data Sets which may lead to slugs and those which will not. It is at this ratio of liquid to homogeneous velocity that the liquid momentum is able to overcome the interfacial shear forces in order to grow into slugs. We then fixed  $\lambda$  and focused on a small range of  $\delta$  at this limit while varying  $F_0$  and applied our work from Chapter 4. Through this we found that, for a wave with propagation speed  $U$ , the solutions with smaller values of  $F_0$  had smaller waves compared to a wave

with the same value of  $U$  from a solution with a larger value of  $F_0$ . This meant that when  $U \approx 1/\delta + A$ , the waves with smaller values of  $F_0$  were not large enough to build into slugs.

Finally, we investigated the effects of varying all the parameters and found our work throughout this chapter to be consistent for a larger parameter range. We also found that as  $\epsilon$  decreases we require larger values of  $F_0$  in order to produce slug solutions, however as  $F_0 = u_l^0 / \sqrt{gh_0}$  we would expect to have larger values of  $F_0$  and as  $F_{NH}$  increases as  $\epsilon$  decreases we are able to solve our IVP for these values.

Currently, due to the way the equations have been derived and the code programmed, it is not possible for the liquid to touch the top of the channel as this results in denominators in our equations becoming zero. Hence, further research is needed into solutions where the liquid completely fills the channel locally.

---

## THE EFFECT OF INCLINATION IN THE THIN LAYER LIMIT

---

As subsea natural gas pipelines lie on the seabed they must follow the topography of the sea floor which may destabilise the flow (as discussed in Subsection 1.2.4). Further, as the pipeline comes to shore it will be at a slight incline before reaching a processing plant, so the effects of uphill inclination are of particular importance. Hence, in this chapter we will investigate how topography affects the formation of slugs. In order to do this we must first amend our equations from Chapter 2, which will be done by writing the conservation of mass and conservation of momentum equations in terms of a curvilinear co-ordinate system and taking the thin layer limit. We will then consider the channel to be at a constant angle and, by investigating the existence of periodic travelling waves and solving the system as an IVP, will explore how changes to the angle affect the solutions. Finally, we will solve the IVP for an undulating topography to investigate how combining uphill, downhill and horizontal sections of channel may result in a transition to a slug flow regime.

### 6.1 EQUATION DERIVATION

We will now consider a curved channel of height  $a$  in terms of a two-dimensional Cartesian co-ordinate system  $(X, Y)$  with the  $Y$  axis pointing

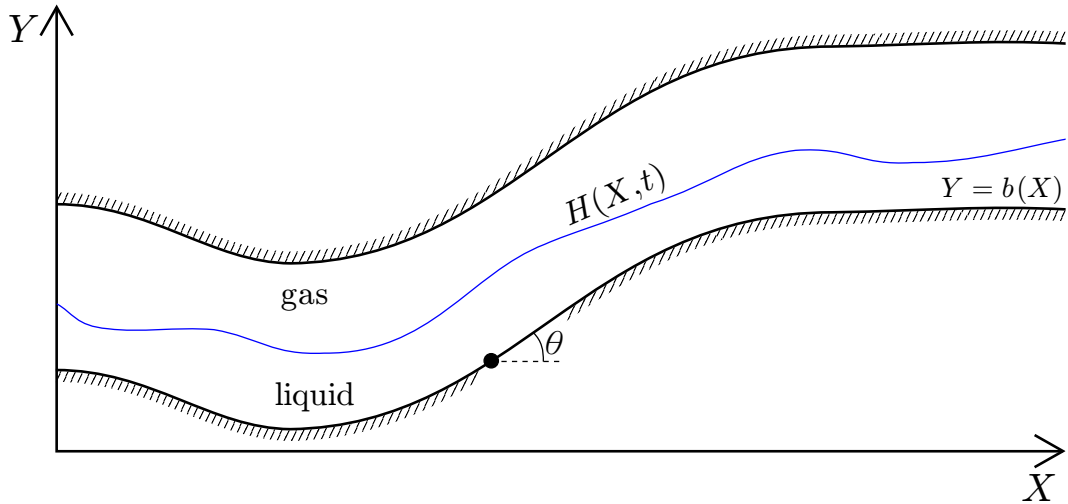


Figure 6.1.: The Cartesian co-ordinate system.

vertically upwards with its bottom located at  $Y = b(X)$ . A layer of liquid will flow along the bottom of the channel; the free surface of this layer will be at  $Y = H(X, t)$ , with  $t$  being time, as shown in Figure 6.1. The base of the channel is at angle  $\theta = \arctan(b'(X))$  to the horizontal on the downstream side, hence  $-\pi/2 < \theta < \pi/2$  where  $\theta$  is positive where the channel is going uphill and negative where the channel is going downhill.

Let us now consider the same curved channel but express it in terms of a curvilinear co-ordinate system  $(x, y)$  with the  $y$  axis pointing perpendicular to the channel bottom and the  $x$  axis pointing tangential to the channel bottom, measuring the distance travelled along it. Now the bottom of the channel is located at  $y = 0$  and the top is at  $y = a$ , while the free surface of the layer of liquid is located at  $y = h(x, t)$ , as shown in Figure 6.2. We will denote the velocity component tangential to the channel bottom, in the  $x$  direction, as  $u(x, y, t)$  (hereafter referred to as the tangential velocity) and the velocity component perpendicular to the channel bottom, in the  $y$  direction, as  $v(x, y, t)$ . A point,  $(x, y)$ , in the curvilinear coordinate system will be expressed in the Cartesian co-ordinate system as  $(X(x, y), Y(x, y))$ .

On the bottom of the channel we define

$$X(x, 0) = \zeta(x), \tag{6.1.1}$$

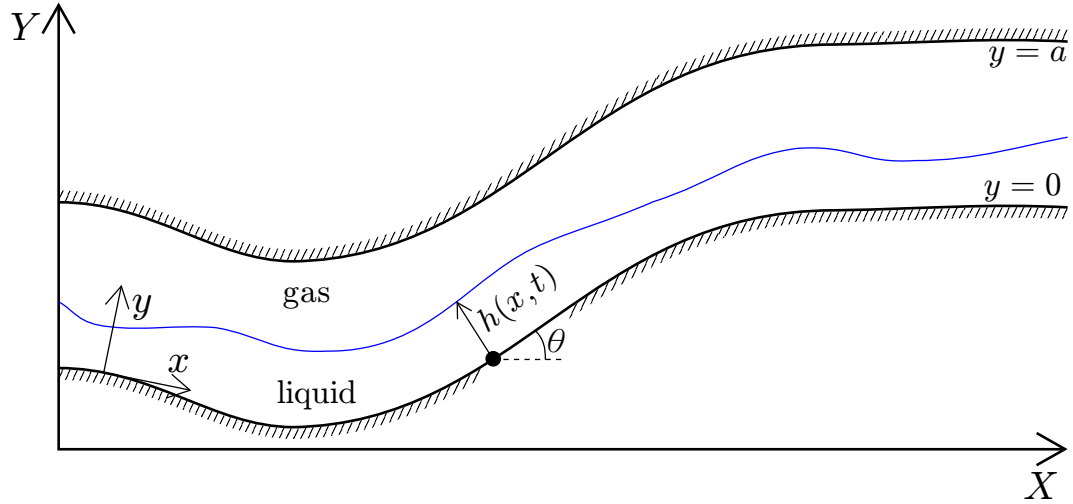


Figure 6.2.: The curvilinear co-ordinate system.

$$Y(x, 0) = \eta(x), \quad (6.1.2)$$

hence  $b(\zeta(x)) = \eta(x)$  and

$$X(x, y) = \zeta(x) - \eta'(x)y, \quad (6.1.3)$$

$$Y(x, y) = \eta(x) + \zeta'(x)y, \quad (6.1.4)$$

where  $\zeta'(x) = \cos \theta$  and  $\eta'(x) = \sin \theta$ . From Dressler [51] the curvature,  $\kappa$ , is given by

$$\kappa = \eta' \zeta'' - \zeta' \eta'', \quad (6.1.5)$$

$$= -\theta', \quad (6.1.6)$$

where  $\theta' = d\theta/dx$ , the scale factors are given by

$$s_x = 1 - \theta' y, \quad (6.1.7)$$

$$s_y = 1, \quad (6.1.8)$$

and, for any vector  $\mathbf{f} = (f_x, f_y)$  and scalar  $f$ , we have

$$\nabla f = \frac{1}{s_x} \frac{\partial f}{\partial x} \hat{\mathbf{x}} + \frac{\partial f}{\partial y} \hat{\mathbf{y}}, \quad (6.1.9)$$

$$\nabla \cdot \mathbf{f} = \frac{1}{s_x} \left[ \frac{\partial f_x}{\partial x} + \frac{\partial}{\partial y} (s_x f_y) \right], \quad (6.1.10)$$

$$\nabla^2 f = \frac{1}{s_x} \left[ \frac{\partial}{\partial x} \left( \frac{1}{s_x} \frac{\partial f}{\partial x} \right) + \frac{\partial}{\partial y} \left( s_x \frac{\partial f}{\partial y} \right) \right], \quad (6.1.11)$$

where  $\hat{\mathbf{x}}$  and  $\hat{\mathbf{y}}$  are the normal vectors in the  $x$  and  $y$  directions respectively.

Following the method we used in our original derivation in Chapter 2, we derive the non-dimensional equations as

$$(1 - c_l \theta' h) h_t + [h v]_x = 0, \quad (6.1.12)$$

$$\begin{aligned} & \left[ 1 - \frac{1}{2} c_l \theta' h + \frac{\rho \epsilon h}{1 - \epsilon h} \left( 1 - \frac{1}{2\epsilon} c_l \theta' [1 + \epsilon h] \right) \right] v_t \\ & + \left( v + \frac{\rho \epsilon h [2 - (1 + \epsilon h) \delta v]}{\delta (1 - \epsilon h)^2} \right) v_x + \left( \frac{1 - \rho}{F_0^2} \cos \theta - \frac{\rho \epsilon (1 - \delta v)^2}{\delta^2 (1 - \epsilon h)^3} \right) h_x \\ & = \frac{\rho c_l^g}{\delta^2 c_l} \left( \frac{(1 - \epsilon \delta h v)^2}{\lambda (1 - \epsilon h)^3} + \frac{(1 - \delta v) |1 - \delta v|}{h (1 - \epsilon h)^3} (1 - c_l \theta' h) \right) \\ & \quad - \frac{1 - \rho}{F_0^2} \frac{1 - c_l \theta' h}{c_l} \sin \theta - \frac{v^2}{h} + \frac{1}{h R_l} \left[ \frac{v_x}{h_0} \int_0^{h_0 h} \frac{1}{1 - \frac{c_l}{h_0} \theta' y} dy \right]_x \\ & \quad - \frac{\rho \epsilon}{R_g (1 - \epsilon h)} \left[ \left( \frac{1 - \delta v}{\delta (1 - \epsilon h)^2} \frac{h_x}{a} - \frac{h}{1 - \epsilon h} \frac{v_x}{a} \right) \int_{h_0 h}^a \frac{1}{1 - \frac{c_l}{h_0} \theta' y} dy \right]_x. \end{aligned} \quad (6.1.13)$$

By assuming  $\theta = O(c_l)$ , as is consistent with the small surface slope approximation that we made in (2.3.1) in our original derivation, we use the scale

$$\theta(x) = c_l \bar{\theta}(x), \quad (6.1.14)$$

where  $\bar{\theta} = O(1)$  and hence

$$\cos(c_l \bar{\theta}) \sim 1, \quad (6.1.15)$$

$$\sin(c_l \bar{\theta}) \sim c_l \bar{\theta}, \quad (6.1.16)$$

and

$$\frac{1}{1 - \frac{c_l^2 \bar{\theta}' y}{h_0}} \approx 1 + \frac{c_l^2 \bar{\theta}' y}{h_0}, \quad (6.1.17)$$

therefore (6.1.12) and (6.1.13) become

$$(1 - c_l^2 \bar{\theta}' h) h_t + [hv]_x = 0, \quad (6.1.18)$$

$$\begin{aligned} & \left[ 1 - \frac{1}{2} c_l^2 \bar{\theta}' h + \frac{\rho \epsilon h}{1 - \epsilon h} \left( 1 - \frac{1}{2\epsilon} c_l^2 \bar{\theta}' [1 + \epsilon h] \right) \right] v_t \\ & + \left( v + \frac{\rho \epsilon h [2 - (1 + \epsilon h) \delta v]}{\delta (1 - \epsilon h)^2} \right) v_x + \left( \frac{1 - \rho}{F_0^2} - \frac{\rho \epsilon (1 - \delta v)^2}{\delta^2 (1 - \epsilon h)^3} \right) h_x \\ & = \frac{\rho c_l^8}{\delta^2 c_l} \left( \frac{(1 - \epsilon \delta h v)^2}{\lambda (1 - \epsilon h)^3} + \frac{(1 - \delta v) |1 - \delta v|}{h (1 - \epsilon h)^3} (1 - c_l^2 \bar{\theta}' h) \right) \\ & - \frac{1 - \rho}{F_0^2} (1 - c_l^2 \bar{\theta}' h) \bar{\theta} - \frac{v^2}{h} + \frac{1}{h R_l} \left[ \left( 1 + \frac{1}{2} c_l^2 \bar{\theta}' h \right) h v_x \right]_x \\ & - \frac{\rho \epsilon}{R_g (1 - \epsilon h)} \left[ \left( \frac{1 - \delta v}{\delta (1 - \epsilon h)} h_x - h v_x \right) \left( 1 + \frac{1}{2\epsilon} c_l^2 \bar{\theta}' (1 + \epsilon h) \right) \right]_x. \quad (6.1.19) \end{aligned}$$

Assuming  $\bar{\theta}' \ll 1/c_l^2$ , the leading order non-dimensional equations of motion are

$$h_t + [hv]_x = 0, \quad (6.1.20)$$

$$\begin{aligned} & \left( 1 + \frac{\rho \epsilon h}{1 - \epsilon h} \right) v_t + \left( v + \frac{\rho \epsilon h [2 - (1 + \epsilon h) \delta v]}{\delta (1 - \epsilon h)^2} \right) v_x \\ & + \left( \frac{1 - \rho}{F_0^2} - \frac{\rho \epsilon (1 - \delta v)^2}{\delta^2 (1 - \epsilon h)^3} \right) h_x \\ & = -\frac{1 - \rho}{F_0^2} \bar{\theta} - \frac{v^2}{h} + \frac{\rho c_l^8}{\delta^2 c_l} \left( \frac{(1 - \epsilon \delta h v)^2}{\lambda (1 - \epsilon h)^3} + \frac{(1 - \delta v) |1 - \delta v|}{h (1 - \epsilon h)^3} \right) \\ & + \left( \frac{1}{h R_l} + \frac{\rho \epsilon}{(1 - \epsilon h) R_g} \right) [h v_x]_x - \frac{\rho \epsilon}{\delta (1 - \epsilon h) R_g} \left[ \frac{1 - \delta v}{1 - \epsilon h} h_x \right]_x, \quad (6.1.21) \end{aligned}$$

with steady state solution

$$h = 1, \quad v = 1, \quad (6.1.22)$$

when  $\bar{\theta} = 0$ . At equilibrium, (6.1.21) rearranges to give

$$\frac{\rho c_l^g}{\delta^2 c_l} = \frac{\lambda(1-\epsilon)^3}{(1-\epsilon\delta)^2 + \lambda(1-\delta)^2}, \quad (6.1.23)$$

which, when substituted back into (6.1.21), gives

$$\begin{aligned} & \left(1 + \frac{\rho\epsilon h}{1-\epsilon h}\right) v_t + \left(v + \frac{\rho\epsilon h[2 - (1+\epsilon h)\delta v]}{\delta(1-\epsilon h)^2}\right) v_x \\ & \quad + \left(\frac{1-\rho}{F_0^2} - \frac{\rho\epsilon(1-\delta v)^2}{\delta^2(1-\epsilon h)^3}\right) h_x \\ = & -\frac{1-\rho}{F_0^2}\bar{\theta} - \frac{v^2}{h} + \frac{\lambda(1-\epsilon)^3}{(1-\epsilon\delta)^2 + \lambda(1-\delta)^2} \left(\frac{(1-\epsilon\delta hv)^2}{\lambda(1-\epsilon h)^3} + \frac{(1-\delta v)|1-\delta v|}{h(1-\epsilon h)^3}\right) \\ & + \left(\frac{1}{hR_l} + \frac{\rho\epsilon}{(1-\epsilon h)R_g}\right) [hv_x]_x - \frac{\rho\epsilon}{\delta(1-\epsilon h)R_g} \left[\frac{1-\delta v}{1-\epsilon h} h_x\right]_x. \end{aligned} \quad (6.1.24)$$

In order to consider the small liquid layer limit we let  $\epsilon \rightarrow 0$  and  $\delta \rightarrow 0$  in (6.1.24), and assume  $\epsilon \ll \delta^2$ , hence the governing equations become

$$h_t + [hv]_x = 0, \quad (6.1.25)$$

$$v_t + vv_x + \frac{1-\rho}{F_0^2} h_x = -\frac{1-\rho}{F_0^2}\bar{\theta} - \frac{v^2}{h} + \frac{1}{1+\lambda} + \frac{\lambda}{(1+\lambda)h} + \frac{1}{hR_l} [hv_x]_x. \quad (6.1.26)$$

If  $\bar{\theta}$  is a constant, (6.1.26) may be written as

$$v_t + vv_x + \frac{1-\rho}{F_0^2} h_x = -\frac{v^2}{h} + \frac{1}{1+\bar{\lambda}} + \frac{\bar{\lambda}}{(1+\bar{\lambda})h} + \frac{1}{hR_l} [hv_x]_x, \quad (6.1.27)$$

where

$$\bar{\lambda} = \frac{F_0^2 + (1-\rho)\bar{\theta}}{F_0^2 - (1-\rho)\bar{\theta}} \lambda. \quad (6.1.28)$$

This gives us the same governing equations as derived by Needham et al. [132] with  $\lambda$  replaced with  $\bar{\lambda}$ . Note that

$$\bar{\lambda} \rightarrow \begin{cases} +\infty & \text{as } \bar{\theta} \rightarrow \left(\frac{F_0^2}{(1-\rho)\lambda}\right)^- \\ -\infty & \text{as } \bar{\theta} \rightarrow \left(\frac{F_0^2}{(1-\rho)\lambda}\right)^+ \\ -1 & \text{as } \bar{\theta} \rightarrow \pm\infty \end{cases}, \quad (6.1.29)$$

as shown in Figure 6.3.

In order to consider the stability of the uniform state, as in Chapter 3, we let

$$h = 1 + \bar{h}, \quad v = 1 + \bar{v}, \quad (6.1.30)$$

where  $\bar{h}, \bar{v} \ll 1$ . Using (6.1.30) in (6.1.25) and (6.1.27) gives us the linearised governing equation

$$\begin{aligned} \left(\frac{\partial}{\partial t} + c_+ \frac{\partial}{\partial x}\right) \left(\frac{\partial}{\partial t} + c_- \frac{\partial}{\partial x}\right) \bar{h} + 2 \left(\frac{\partial}{\partial t} + c_0 \frac{\partial}{\partial x}\right) \bar{h} \\ = \frac{1}{R_l} \left[ \frac{\partial}{\partial t} + \frac{1}{2} (c_+ + c_-) \frac{\partial}{\partial x} \right] \frac{\partial^2 \bar{h}}{\partial x^2}, \end{aligned} \quad (6.1.31)$$

where

$$c_{\pm} = 1 \pm \frac{\sqrt{1-\rho}}{F_0^2}, \quad c_0 = 1 + \frac{1}{2(1+\bar{\lambda})}. \quad (6.1.32)$$

Hence, by solving  $c_- < c_0 < c_+$ , we find the stability condition

$$F_0 < 2\sqrt{1-\rho} |1 + \bar{\lambda}| \equiv F_c, \quad (6.1.33)$$

according to which small disturbances to the uniform flow will decay when  $F_0 < F_c$ , but grow when  $F_0 > F_c$ .

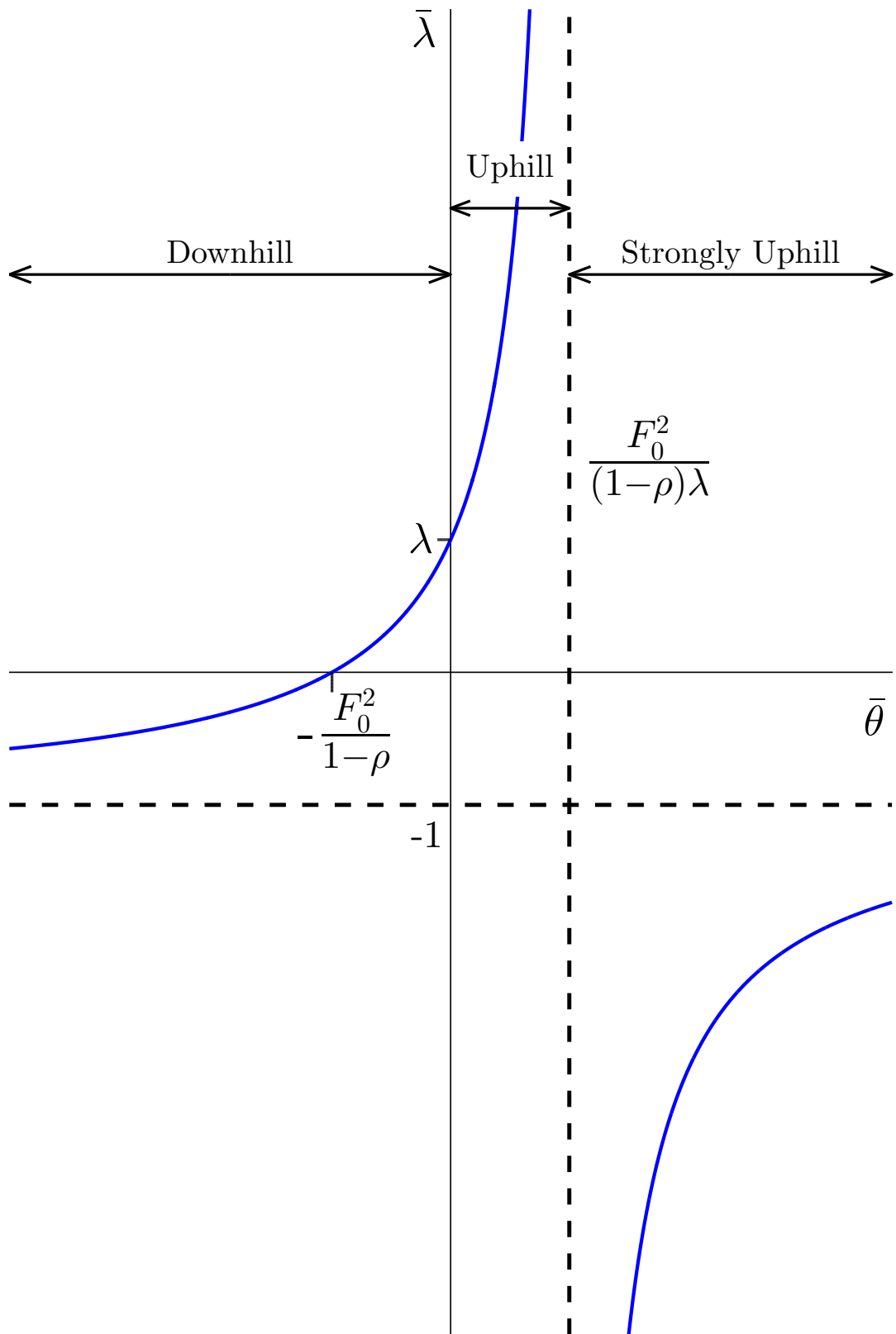


Figure 6.3.: Plot of  $\bar{\lambda}$  against  $\bar{\theta}$ .

## 6.2 PERIODIC TRAVELLING WAVE THEORY

As in Chapter 4 we look for periodic travelling wave solutions to our equations by introducing the travelling coordinate  $z = x - Ut$  and considering solutions of the form

$$h = h(z), \quad v = v(z), \quad (6.2.1)$$

where both  $h(z)$  and  $v(z)$  are periodic in  $z$ . On substitution of (6.2.1) into (6.1.25) and (6.1.27), we get

$$[h(v - U)]_z = 0, \quad (6.2.2)$$

$$(v - U)v_z + \frac{1 - \rho}{F_0^2} h_z = \frac{1}{1 + \bar{\lambda}} + \frac{\bar{\lambda}}{(1 + \bar{\lambda})h} - \frac{v^2}{h} + \frac{1}{R_l h} [hv_z]_z. \quad (6.2.3)$$

Integrating (6.2.2) leads us to

$$h(v - U) = B, \quad (6.2.4)$$

where  $B$  is a real constant. On rearranging (6.2.4), we obtain

$$v(z) = U + \frac{B}{h(z)}, \quad (6.2.5)$$

which, after substitution into (6.2.3), leads to

$$Bh_{zz} - \frac{B}{h} h_z^2 + \frac{R_l}{h} \left[ \frac{(1 - \rho)h^3}{F_0^2} - B^2 \right] h_z + \frac{R_l}{h} \left[ (B + Uh)^2 - \frac{(\bar{\lambda} + h)h^2}{1 + \bar{\lambda}} \right] = 0. \quad (6.2.6)$$

For analysis, it is convenient to rewrite (6.2.6) as the equivalent 2D autonomous dynamical system

$$h' = w, \quad (6.2.7)$$

$$w' = \frac{w^2}{h} - \frac{R_l}{Bh} \left[ \frac{(1-\rho)h^3}{F_0^2} - B^2 \right] w - \frac{R_l}{Bh} \left[ (B + Uh)^2 - \frac{(\bar{\lambda} + h)h^2}{1 + \bar{\lambda}} \right]. \quad (6.2.8)$$

Equilibrium points of (6.2.8) have  $w = 0$ ,  $h = h_0$ , where  $h_0$  satisfies

$$(B + Uh_0)^2 - \frac{(\bar{\lambda} + h_0)h_0^2}{1 + \bar{\lambda}} = 0, \quad (6.2.9)$$

which is a third order polynomial and hence has up to three real solutions.

For  $\bar{\lambda} > 0$ , as studied by Needham et al. [132] (discussed in Subsection 1.2.6), we find it has three equilibrium points,  $H_1$ ,  $H_2$  and  $H_3$ , where  $H_1 < H_2 < H_3$ , which are a stable node, a saddle and a spiral, respectively. A Hopf bifurcation may occur for  $B < 0$  and  $U_{\text{HB}} > 0$  on  $H_3$ , for which limit cycle solutions exist in  $U > U_{\text{HB}}$  which grow as  $U$  is increased and end in a homoclinic bifurcation with  $H_2$ . However, the case for  $\bar{\lambda} < 0$  was not examined by Needham et al. [132] and so we must investigate the equilibrium points in more detail in order to establish whether a Hopf bifurcation may occur and under what conditions.

It is convenient, for analysing (6.2.9), to rewrite it as

$$U_{0\pm} = \pm \sqrt{\frac{\bar{\lambda} + h_0}{1 + \bar{\lambda}}} - \frac{B}{h_0}, \quad (6.2.10)$$

and as  $U_{0\pm}$  must be real,

$$\text{if } -1 < \bar{\lambda} < 0, \quad \text{then } h_0 \geq -\bar{\lambda}, \quad (6.2.11)$$

$$\text{if } \bar{\lambda} < -1, \quad \text{then } h_0 \leq -\bar{\lambda}, \quad (6.2.12)$$

where

$$U_{0\pm}(h_0 = -\bar{\lambda}) = \frac{B}{\bar{\lambda}}. \quad (6.2.13)$$

The turning points of  $U_{0\pm}$  represent saddle-node bifurcations and are found by solving

$$0 = \pm \frac{1}{2\sqrt{1 + \bar{\lambda}}\sqrt{\bar{\lambda} + h_{\text{SN}}}} + \frac{B}{h_{\text{SN}}^2} \left( = \frac{dU_{0\pm}}{dh_0} \Big|_{h_0=h_{\text{SN}}} \right), \quad (6.2.14)$$

which can be rearranged to give

$$B_{\text{SN}} = \mp \frac{h_{\text{SN}}^2}{2\sqrt{1+\bar{\lambda}}\sqrt{\bar{\lambda}+h_{\text{SN}}}}. \quad (6.2.15)$$

By substituting (6.2.15) into (6.2.10) we get

$$U_{\text{SN}\pm} = \pm \left( \sqrt{\frac{\bar{\lambda}+h_{\text{SN}}}{1+\bar{\lambda}}} + \frac{h_{\text{SN}}}{2\sqrt{1+\bar{\lambda}}\sqrt{\bar{\lambda}+h_{\text{SN}}}} \right). \quad (6.2.16)$$

The turning points can be found to be maxima or minima by considering the sign of

$$\left. \frac{d^2 U_{0\pm}}{dh_0^2} \right|_{h_0=h_{\text{SN}}} = \mp \frac{1}{4\sqrt{1+\bar{\lambda}}(\bar{\lambda}+h_{\text{SN}})^{\frac{3}{2}}} - \frac{2B}{h_{\text{SN}}^3}, \quad (6.2.17)$$

which, using (6.2.15), simplifies to

$$\left. \frac{d^2 U_{0\pm}}{dh_0^2} \right|_{h_0=h_{\text{SN}}} = \pm \frac{4\bar{\lambda}+3h_{\text{SN}}}{4\sqrt{1+\bar{\lambda}}(\bar{\lambda}+h_{\text{SN}})^{\frac{3}{2}}h_{\text{SN}}}, \quad (6.2.18)$$

hence

$$\text{sign} \left( \left. \frac{d^2 U_{0\pm}}{dh_0^2} \right|_{h_0=h_{\text{SN}}} \right) = \pm \text{sign}(4\bar{\lambda}+3h_{\text{SN}}). \quad (6.2.19)$$

The eigenvalues of these equilibrium points are given by

$$\Lambda_{\pm} = \frac{1}{2} \left[ f_2 \pm \sqrt{f_2^2 + 4 \frac{df_3}{dh}} \right] \Big|_{h=h_0, U=U_0}, \quad (6.2.20)$$

where we have re-written (6.2.8) as

$$w' = f_1(h)w^2 + f_2(h)w + f_3(h), \quad (6.2.21)$$

and

$$\left. \frac{df_3}{dh} \right|_{h=h_0, U=U_{0\pm}} = \frac{R_l}{B(1+\bar{\lambda})h_0} \left[ h_0^2 \pm 2B\sqrt{1+\bar{\lambda}}\sqrt{\bar{\lambda}+h_0} \right]. \quad (6.2.22)$$

Hence, for a Hopf bifurcation, we must have  $df_3/dh < 0$  and  $f_2 = 0$ , which can be rearranged to give

$$h_{\text{HB}} = \left( \frac{B^2 F_0^2}{1 - \rho} \right)^{\frac{1}{3}}. \quad (6.2.23)$$

By using (6.2.11) and (6.2.12) in (6.2.23) we find

$$\text{if } -1 < \bar{\lambda} < 0, \quad \text{then } |B| > \frac{\sqrt{1 - \rho} (-\bar{\lambda})^{\frac{3}{2}}}{F_0} \equiv B_{\text{Hmin}}, \quad (6.2.24)$$

$$\text{if } \bar{\lambda} < -1, \quad \text{then } |B| < \frac{\sqrt{1 - \rho} (-\bar{\lambda})^{\frac{3}{2}}}{F_0} \equiv B_{\text{Hmax}}, \quad (6.2.25)$$

and by solving  $h_{\text{HB}} = h_{\text{SN}}$  for  $B$  we find that the Hopf bifurcation meets the saddle-node bifurcation when

$$B = \pm \frac{8(1 - \rho)^2}{F_0} \left( \frac{(1 + \bar{\lambda}) \bar{\lambda}}{F_0^2 - 4(1 - \rho)(1 + \bar{\lambda})} \right)^{\frac{3}{2}} \equiv B_{\text{HS}\pm}. \quad (6.2.26)$$

In order to determine the stability and direction of the limit cycles created from these Hopf bifurcations we must apply the Hopf bifurcation theorem. To translate the Hopf bifurcation to the origin, as required by the statement of the Hopf bifurcation theorem in King et al. [101], we introduce the variables

$$H = \omega(h - h_{\text{HB}}), \quad \mu = U - U_{\text{HB}}, \quad (6.2.27)$$

hence

$$h = \frac{1}{\omega}H + h_{\text{HB}}, \quad U = \mu + U_{\text{HB}}. \quad (6.2.28)$$

Substituting (6.2.28) into (6.2.7) and (6.2.8) gives

$$H' = \omega w, \quad (6.2.29)$$

and

$$w' = f_1(H; \mu)w^2 + f_2(H; \mu)w + f_3(H; \mu), \quad (6.2.30)$$

and  $\omega$  is found by solving

$$\omega = - \left. \frac{df_3(H; \mu)}{dH} \right|_{H=0, \mu=0}, \quad (6.2.31)$$

which gives

$$\omega = \sqrt{-\frac{R_l}{B} \left( \frac{h_{HB}}{1 + \bar{\lambda}} \pm \frac{2B}{h_{HB}} \sqrt{\frac{\bar{\lambda} + h_{HB}}{1 + \bar{\lambda}}} \right)}. \quad (6.2.32)$$

In order to apply the criterion given in King et al. [101], we need the quantity

$$\begin{aligned} a = & \frac{1}{16} (H'_{HHH} + w'_{HHw} + H'_{Hkw} + w'_{kw}) \\ & - \frac{1}{16\omega} [H'_{Hkw} (H'_{HH} + H'_{kw}) - w'_{Hkw} (w'_{HH} + w'_{kw}) - H'_{HH} w'_{HH} + H'_{kw} w'_{kw}], \end{aligned} \quad (6.2.33)$$

which becomes

$$a = \frac{3R_l^2 B^2}{8h_{HB}^5 \omega^4} \left( 1 \pm \frac{2h_{HB}}{B} \sqrt{\frac{\bar{\lambda} + h_{HB}}{1 + \bar{\lambda}}} \right). \quad (6.2.34)$$

Furthermore, separating the real and imaginary part of the eigenvalues of the equilibrium points in the form  $\Lambda_{\pm} = \alpha(\mu) \pm i\beta(\mu)$ , we find

$$\alpha(\mu) = -R_l \frac{(1 - \rho) (H(\mu) + \omega h_{HB})^3 - \omega^3 B^2 F_0^2}{B\omega^2 (H(\mu) + \omega h_{HB}) F_0^2}, \quad (6.2.35)$$

$$\alpha'(\mu = 0) = -\frac{3R_l B}{h_{HB}^2 \omega} \left. \frac{dH}{d\mu} \right|_{\mu=0}. \quad (6.2.36)$$

Hence

$$\text{sign}(a\alpha'(0)) = \text{sign} \left( - \left[ B \pm 2h_{HB} \sqrt{\frac{\bar{\lambda} + h_{HB}}{1 + \bar{\lambda}}} \right] \left. \frac{dH}{d\mu} \right|_{\mu=0} \right), \quad (6.2.37)$$

and, as  $(1 - \rho) (H(\mu) + \omega h_{\text{HB}})^3 - \omega^3 B^2 F_0^2$  is monotone increasing with  $H(\mu)$ ,

$$\text{sign}(\alpha(\mu > 0)) = \text{sign} \left( -B \frac{dH}{d\mu} \Big|_{\mu=0} \right). \quad (6.2.38)$$

Using (6.2.23) in (6.2.37) we find that  $a\alpha'(0) = 0$  when

$$B = \pm 8 \sqrt{1 - \rho} F_0^2 \left( \frac{-\bar{\lambda}}{4F_0^2 - (1 - \rho)(1 + \bar{\lambda})} \right)^{\frac{3}{2}} \equiv B_{0\pm}. \quad (6.2.39)$$

From (6.2.23) it is clear that we get no Hopf Bifurcations if  $B = 0$ . However, in order to establish whether we may get them if  $B < 0$  or  $B > 0$  we must investigate each case individually.

### 6.2.1 $\bar{\lambda} < -1$ (Strongly Uphill)

#### 6.2.1.1 The case for $B < 0$

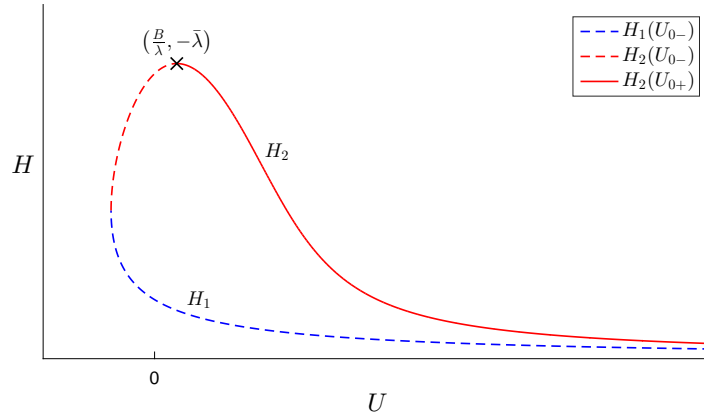


**Figure 6.4.:** The typical bifurcation diagram for  $B < 0$  and  $\bar{\lambda} < -1$  with the dashed and solid lines corresponding to  $U_{0-}$  and  $U_{0+}$ , respectively.

For  $B < 0$ , from (6.2.15) we see that there is a turning point on  $U_{0-}$  for which, by (6.2.12) and (6.2.19), gives

$$\frac{d^2 U_{0+}}{dh_0^2} > 0, \quad (6.2.40)$$

hence is a minimum. This gives us two branches of equilibrium points in  $U > 0$  which we will call  $H_1$  and  $H_2$  where  $H_1 < H_2$ , as shown in Figure 6.4. As can be seen in Figure 6.4,  $H_2$  is split into two sub-branches  $H_2(U_{0-})$  and  $H_2(U_{0+})$  which join at  $(B/\bar{\lambda}, -\bar{\lambda})$ .

From (6.2.22) we can see that

$$\text{sign} \left( \frac{df_3}{dh} \Big|_{h=h_0, U=U_{0-}} \right) = \text{sign} \left( h_0^2 - 2B\sqrt{1 + \bar{\lambda}}\sqrt{\bar{\lambda} + h_0} \right). \quad (6.2.41)$$

As  $h_0^2 - 2B\sqrt{1 + \bar{\lambda}}\sqrt{\bar{\lambda} + h_0}$  is monotone increasing for  $0 < h_0 < -\bar{\lambda}$  and  $h_0^2 - 2B\sqrt{1 + \bar{\lambda}}\sqrt{\bar{\lambda} + h_0} = 0$  when  $h_0 = h_{\text{SN}}$ , we can conclude that

$$\frac{df_3}{dh} \Big|_{h=h_0, U=U_{0-}} > 0 \quad \text{if } h_0 > h_{\text{SN}}, \quad (6.2.42)$$

$$\frac{df_3}{dh} \Big|_{h=h_0, U=U_{0-}} < 0 \quad \text{if } h_0 < h_{\text{SN}}, \quad (6.2.43)$$

and

$$\frac{df_3}{dh} \Big|_{h=h_0, U=U_{0+}} > 0. \quad (6.2.44)$$

Hence,  $H_2$  is a saddle and  $H_1$  is a node or spiral where, in order for a Hopf bifurcation to occur, we must have  $B > B_{\text{HS-}}$ .

Similarly to (6.2.41)

$$\text{sign} \left( \frac{dU_{0-}}{dh_0} \right) = \text{sign} \left( h_0^2 - 2B\sqrt{1 + \bar{\lambda}}\sqrt{\bar{\lambda} + h_0} \right), \quad (6.2.45)$$

and hence

$$\frac{dU_{0-}}{dh_0} > 0 \quad \text{if } h_0 > h_{\text{SN}}, \quad (6.2.46)$$

$$\frac{dU_{0-}}{dh_0} < 0 \quad \text{if } h_0 < h_{\text{SN}}, \quad (6.2.47)$$

therefore, for  $h_0 < h_{\text{SN}}$ ,  $U_{0-}$  is monotone decreasing in  $h_0$ .

Using (6.2.37) and (6.2.38) we find  $a\alpha'(0) < 0$  and  $\alpha(\mu < 0) > 0$ , hence the Hopf bifurcation theorem tells us  $(U_{\text{HB}}, h_{\text{HB}})$  is a subcritical Hopf bifurcation from which a unique limit cycle solution bifurcates in  $U > U_{\text{HB}}$ . An example of the bifurcation diagram is shown in Figure 6.5 where the stability of the equilibrium points is represented by solid/dashed lines for stable/unstable, respectively, and Figure 6.6 shows examples of limit cycle solutions for this parameter set.

By using these periodic travelling wave solutions as the initial condition in the IVP (6.1.25) and (6.1.27) with periodic boundary conditions, as we did in Section 5.2, we find these solutions produce unsteady periodic solutions which do not have a permanent form.

6.2.1.2 The case for  $B > 0$

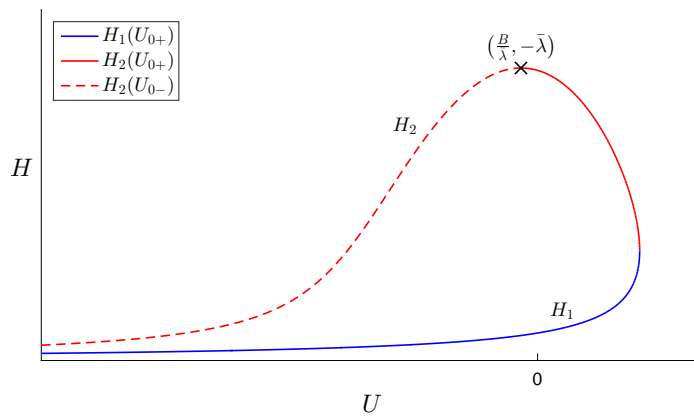
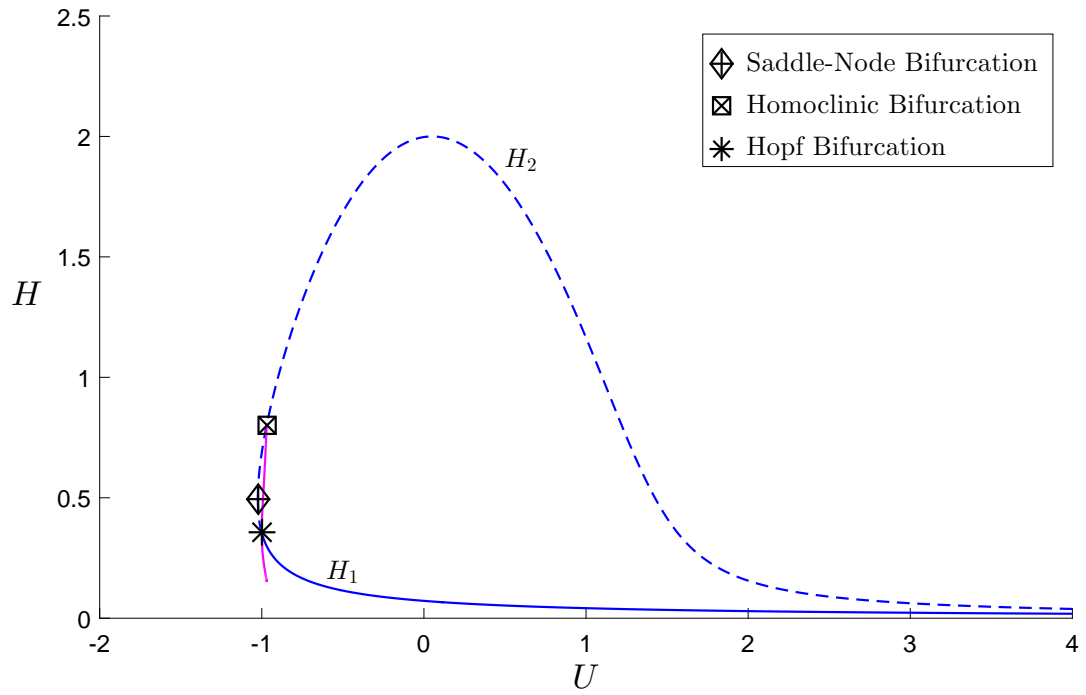


**Figure 6.7.:** The typical bifurcation diagram for  $B > 0$  and  $\bar{\lambda} < -1$  with the dashed and solid lines corresponding to  $U_{0-}$  and  $U_{0+}$ , respectively.

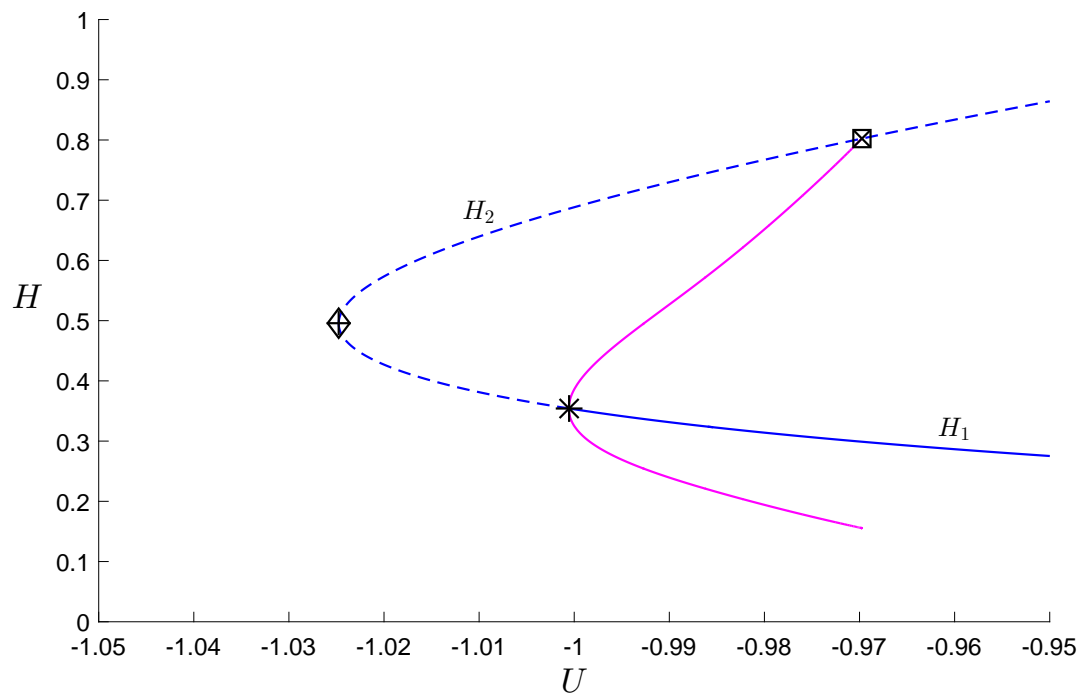
For  $B > 0$ , from (6.2.15) we see that there is a turning point on  $U_{0+}$  for which, by (6.2.12) and (6.2.19), gives

$$\frac{d^2 U_{0+}}{dh_0^2} < 0, \tag{6.2.48}$$

hence is a maximum. This gives us two equilibrium points in  $U > 0$  which we will call  $H_1$  and  $H_2$  where  $H_1 < H_2$ , as shown in Figure 6.7. As can be



(a) The complete bifurcation diagram.



(b) The bifurcation diagram zoomed in around the Hopf bifurcation.

**Figure 6.5.:** The bifurcation diagram for  $\bar{\lambda} = -2$ ,  $B = -0.1$ ,  $F_0 = 2$ ,  $R_l = 50$  and  $\rho = 0.1$ .

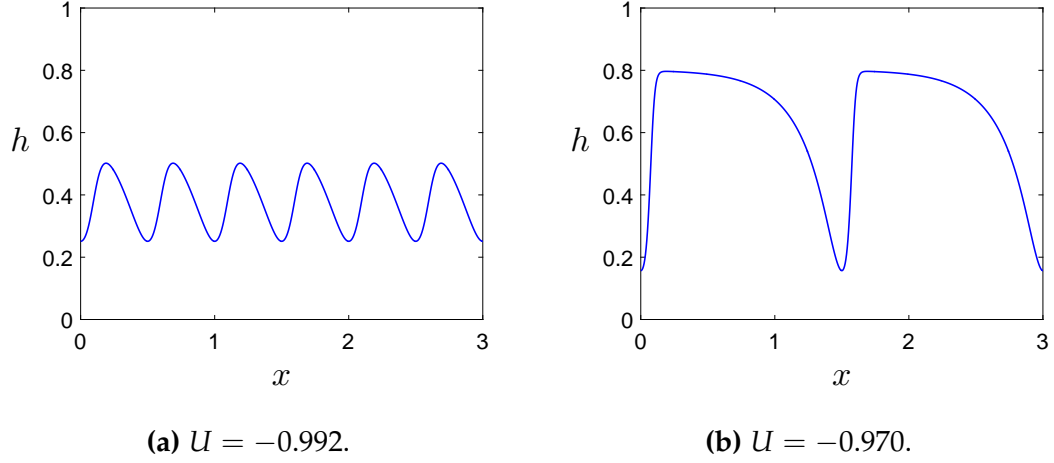


**Figure 6.6.:** The limit cycle solutions for  $\bar{\lambda} = -2$ ,  $B = -0.1$ ,  $F_0 = 2$ ,  
 $R_l = 50$  and  $\rho = 0.1$ .

seen in Figure 6.7,  $H_2$  is split into two parts  $H_2(U_{0-})$  and  $H_2(U_{0+})$  which join at  $(B/\bar{\lambda}, -\bar{\lambda})$ .

Similarly to our work in the previous subsection, from (6.2.41) onwards, we find that

$$\left. \frac{df_3}{dh} \right|_{h=h_0, U=U_{0+}} > 0 \quad \text{if } h_0 < h_{SN}, \quad (6.2.49)$$

$$\left. \frac{df_3}{dh} \right|_{h=h_0, U=U_{0+}} < 0 \quad \text{if } h_0 > h_{SN}, \quad (6.2.50)$$

$$(6.2.51)$$

and

$$\left. \frac{df_3}{dh} \right|_{h=h_0, U=U_{0-}} < 0. \quad (6.2.52)$$

Hence,  $H_1$  is a saddle and  $H_2$  is a node or spiral where, in order for a Hopf bifurcation to occur on  $U_{0+}$ , we must have  $B > B_{HS+}$ .

Again, similarly to our work in the previous subsection, from (6.2.45) onwards, we can find that

$$\text{sign} \left( \frac{dU_{0\pm}}{dh_0} \right) = -\text{sign} \left( h_0^2 \pm 2B\sqrt{1 + \bar{\lambda}}\sqrt{\bar{\lambda} + h_0} \right), \quad (6.2.53)$$

and hence

$$\frac{dU_{0+}}{dh_0} > 0 \quad \text{if } h_0 < h_{SN}, \quad (6.2.54)$$

$$\frac{dU_{0+}}{dh_0} < 0 \quad \text{if } h_0 > h_{SN}, \quad (6.2.55)$$

and

$$\frac{dU_{0-}}{dh_0} > 0. \quad (6.2.56)$$

Using (6.2.37) and (6.2.38) we find, for Hopf Bifurcations on  $H_2(U_{0+})$ ,  $aa'(0) > 0$  and  $\alpha(\mu > 0) > 0$ , hence the Hopf bifurcation theorem tells us  $(U_{HB+}, h_{HB})$  is a subcritical Hopf bifurcation from which a unique limit cycle solution bifurcates in  $U < U_{HB+}$ . For Hopf Bifurcations on  $H_2(U_{0-})$ , if  $B > B_{0+}$ ,  $aa'(0) < 0$  and  $\alpha(\mu < 0) > 0$ , hence the Hopf bifurcation theorem tells us  $(U_{HB-}, h_{HB})$  is a subcritical Hopf bifurcation from which a unique limit cycle solution bifurcates in  $U > U_{HB-}$ . Whereas if  $B < B_{0+}$ ,  $aa'(0) > 0$  and  $\alpha(\mu > 0) < 0$ , hence the Hopf bifurcation theorem tells us  $(U_{HB-}, h_{HB})$  is a supercritical Hopf bifurcation from which a unique limit cycle solution bifurcates in  $U < U_{HB-}$ .

An example of the bifurcation diagram is shown in Figure 6.8 where the stability of the equilibrium points is represented by solid/dashed lines for stable/unstable, respectively. A supercritical Hopf Bifurcation has occurred on  $H_2$  at  $U_{HB-} \approx -1.124$  (which corresponds to  $U_{0-}$  and will be referred to as Hopf1) resulting in a stable limit cycle in  $U < U_{HB-}$  (where we have used red in Figure 6.8 to represent stable). As  $U$  decreases, the limit cycles increase in amplitude until there is a homoclinic bifurcation at  $U_{hom-} \approx -1.1974$ .

Figure 6.9 shows another bifurcation diagram where all the parameters are the same except  $B$  which we have increased such that  $B > B_{HS+}$ , hence we now get two Hopf bifurcations. Comparing the two figures we can see Hopf1 has increased in  $U$  as we have increased  $B$  and again has produced

stable limit cycles as  $U$  is decreased before again ending in a homoclinic bifurcation. The second Hopf Bifurcation also occurred on  $H_2$  at  $U_{\text{HB}+} \approx 0.537$  (which corresponds to  $U_{0+}$  and will be referred to as Hopf2) resulting in an unstable limit cycle in  $U < U_{\text{HB}+}$  (where we have used pink in Figure 6.9 to represent unstable). As  $U$  decreases, the limit cycles increase in amplitude until there is a homoclinic bifurcation at  $U_{\text{hom}+} \approx 0.524$ .

As  $B$  is increased further we find that, while Hopf1 has continued to increase in  $U$ , Hopf2 has decreased in  $U$ , as shown in Figure 6.10a. As in the previous cases, Hopf1 has produced stable limit cycles which increase in amplitude as  $U$  is decreased, however we now find a homoclinic bifurcation which results in a small region in  $U$  where we generate unstable limit cycle solutions, shown in Figure 6.10b. These unstable limit cycle solutions decrease in amplitude as  $U$  decreases while the stable limit cycle solutions continue to increase in amplitude until we get a periodic saddle-node bifurcation and they annihilate each other (denoted by the point the red and pink lines meet).

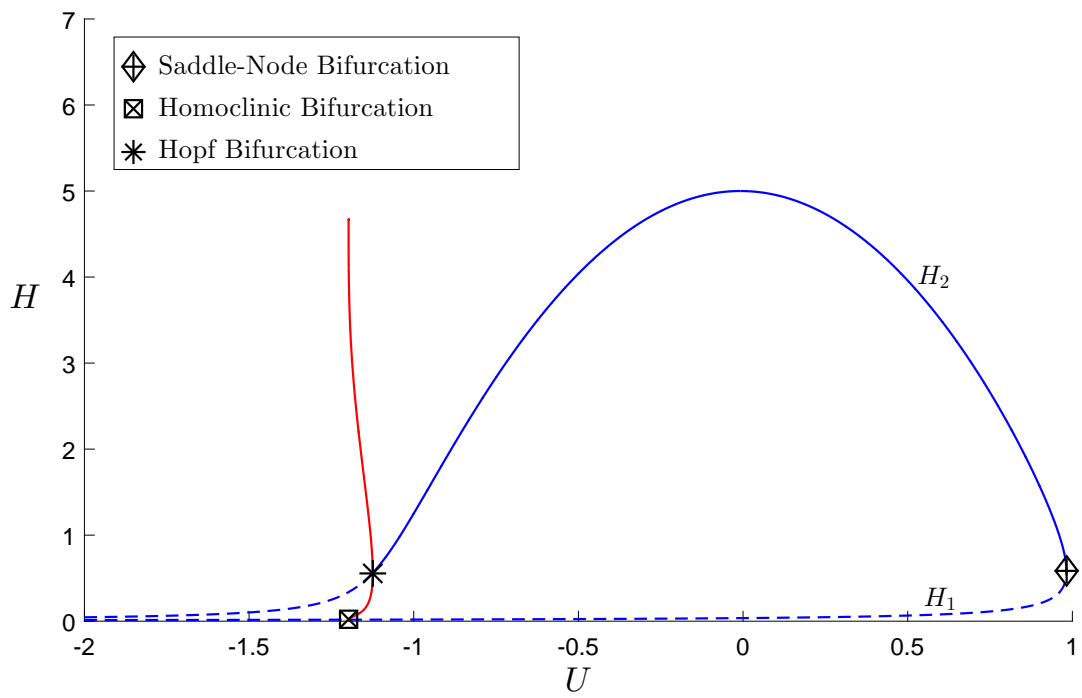
As we continue to increase  $B$  we find the region in  $U$  for which the unstable limit cycles produced from Hopf1 exist also increases, while the region in  $U$  for which the stable limit cycles exist decreases, shown in Figure 6.11. This continues as we increase  $B$  towards  $B_{0+}$ , at which point the region in  $U$  for which the stable limit cycles exist has become very small, whereas the region in  $U$  for which the unstable limit cycles exist has become large, shown in Figure 6.12. As  $B$  is increased past  $B_{0+}$  we no longer get any stable limit cycle solutions, shown in Figure 6.13, instead have two regions of unstable limit cycles which grow towards each other and move towards each other as  $B$  is increased further, shown in Figure 6.14.

As  $B$  is increased further, the homoclinic bifurcations points coalesce and the two regions of unstable limit cycle solutions join in a gluing bifurcation, creating one region, starting from and ending in a Hopf bifurcation, shown in Figure 6.15. This region in  $U$  of unstable limit cycles decreases in size as the two Hopf bifurcations continue to move towards each other as  $B$  is

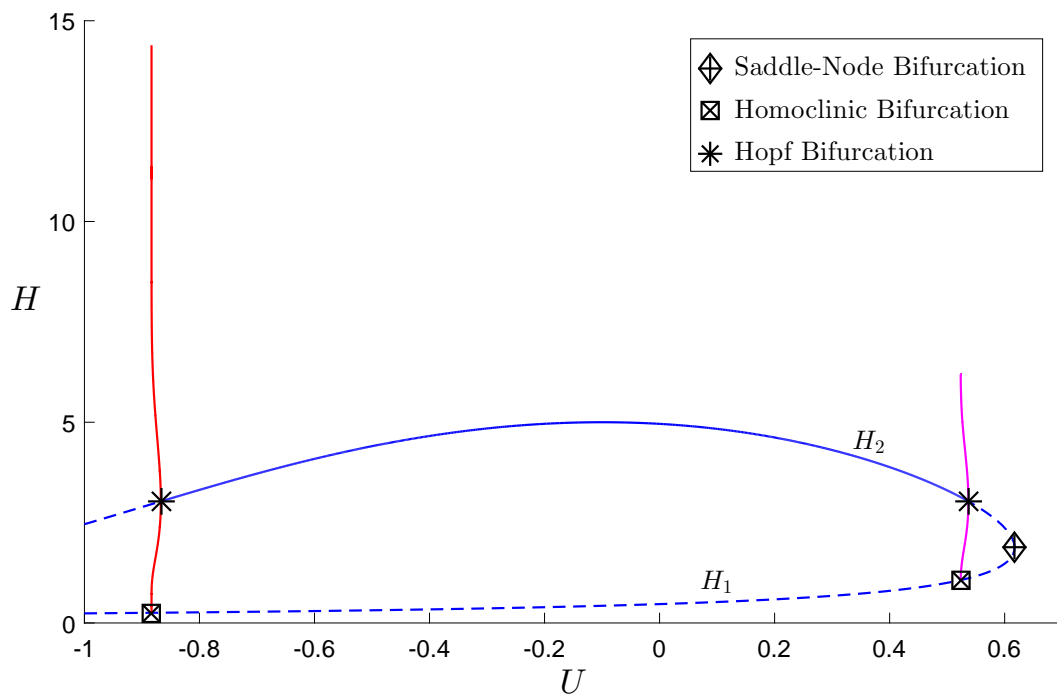
increased, shown in Figure 6.16, until there is a Hopf-Hopf bifurcation for  $B = B_{\max}$ .

Figure 6.17 shows a typical plot of the Hopf bifurcation points,  $U = U_{\text{HB-}}(B)$  and  $U = U_{\text{HB+}}(B)$ , the homoclinic bifurcation points,  $U = U_{\text{hom-}}(B)$  and  $U = U_{\text{hom+}}(B)$ , the saddle-node bifurcation point,  $U = U_{\text{SN}}(B)$ , and the minimum limit cycle point  $U = U_{\text{min-}}$ . We can see from Figure 6.17 that for most values of  $B$ ,  $U_{\text{min-}}(B) = U_{\text{hom-}}(B)$ . However for  $B \approx 1$ , as in Figure 6.18 (which shows an exaggerated version of the region around  $U = U_{\text{min-}}(B)$ ),  $U_{\text{min-}}(B) < U_{\text{hom-}}(B)$ , hence for these values of  $B$  we get stable limit cycles in  $U_{\text{min-}}(B) < U < U_{\text{HB-}}(B)$  and unstable limit cycles in  $U_{\text{min-}}(B) < U < U_{\text{hom-}}(B)$ . As  $B$  increases, the region  $U_{\text{min-}}(B) < U < U_{\text{HB-}}(B)$  decreases in size until  $B = B_{0+}$ , from which point  $U_{\text{min-}}(B) = U_{\text{HB-}}(B)$  and we only get unstable limit cycles in  $U > U_{\text{HB-}}(B)$ . As  $B$  is increased further we can see from Figure 6.17b that  $U_{\text{hom-}}(B)$  and  $U_{\text{hom+}}(B)$  head towards each other until they coalesce in a gluing bifurcation. Finally, we can see the point where  $U_{\text{HB-}}(B_{\max}) = U_{\text{HB+}}(B_{\max})$ , after which we no longer get Hopf bifurcations.

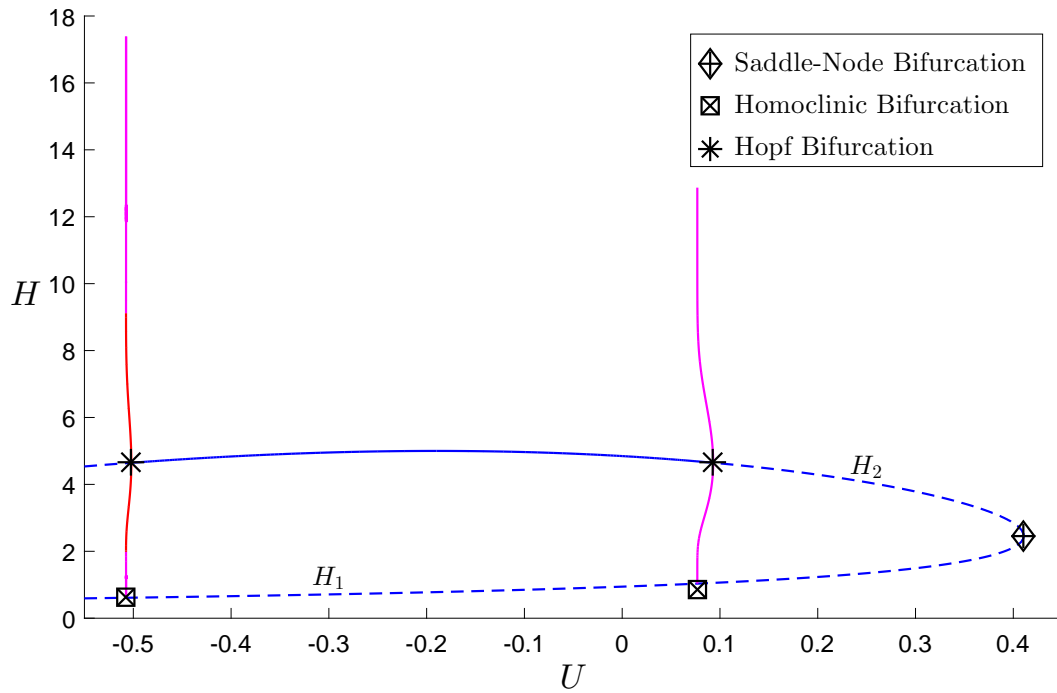
By using these periodic travelling wave solutions as the initial condition in the IVP (6.1.25) and (6.1.27) with periodic boundary conditions, as we did in Section 5.2, we find that solutions from Hopf1 produce unsteady periodic solutions which do not have a permanent form, whereas those from Hopf2 produce steady periodic solutions. An example for the solutions from Hopf2 for  $B = 0.5$ ,  $\bar{\lambda} = -5$ ,  $F_0 = 10$ ,  $R_l = 50$  and  $\rho = 0.1$  is shown in Table 6.1 and Figures 6.19 and 6.20. We can see from Table 6.1 that the values of  $U$  and  $B$  computed from the IVP are very close to those from bvp5c and, from Figure 6.20 we see the solutions are almost identical. In these figures, particularly Figure 6.20d, we can see that as they are travelling backwards relative to the flow (due to having  $B > 0$  and  $U > 0$ ) their structure is opposite in  $x$  to those we have previously seen.



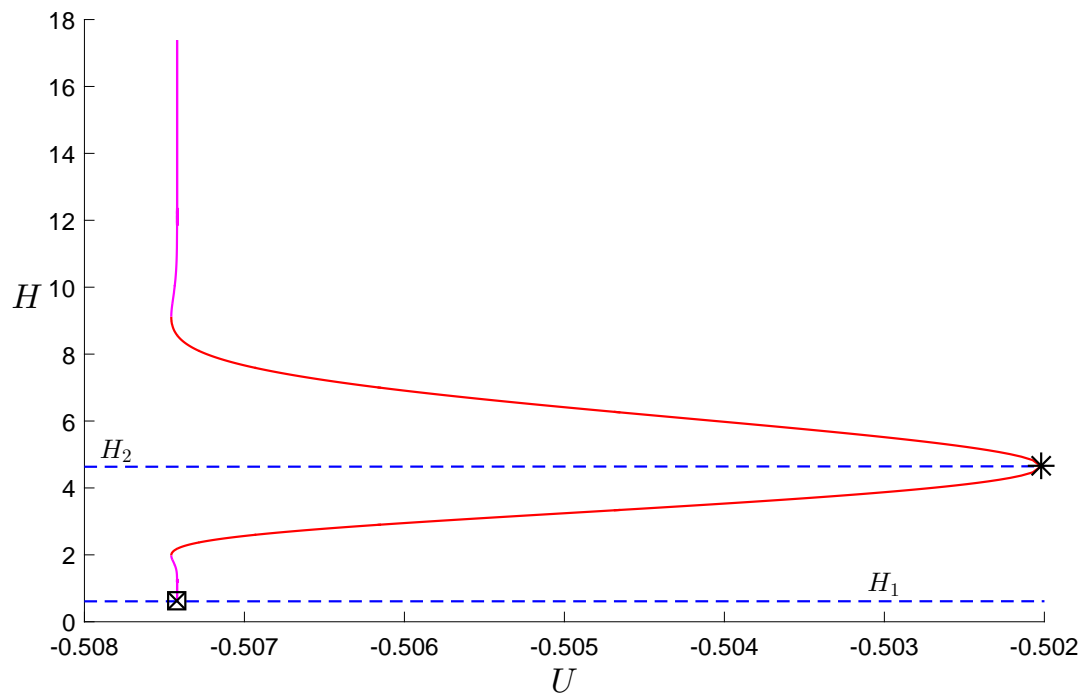
**Figure 6.8.:** The bifurcation diagram for  $B = 0.04$ ,  $\bar{\lambda} = -5$ ,  $F_0 = 10$ ,  $R_l = 50$  and  $\rho = 0.1$ .



**Figure 6.9.:** The bifurcation diagram for  $B = 0.5$ ,  $\bar{\lambda} = -5$ ,  $F_0 = 10$ ,  $R_l = 50$  and  $\rho = 0.1$ .

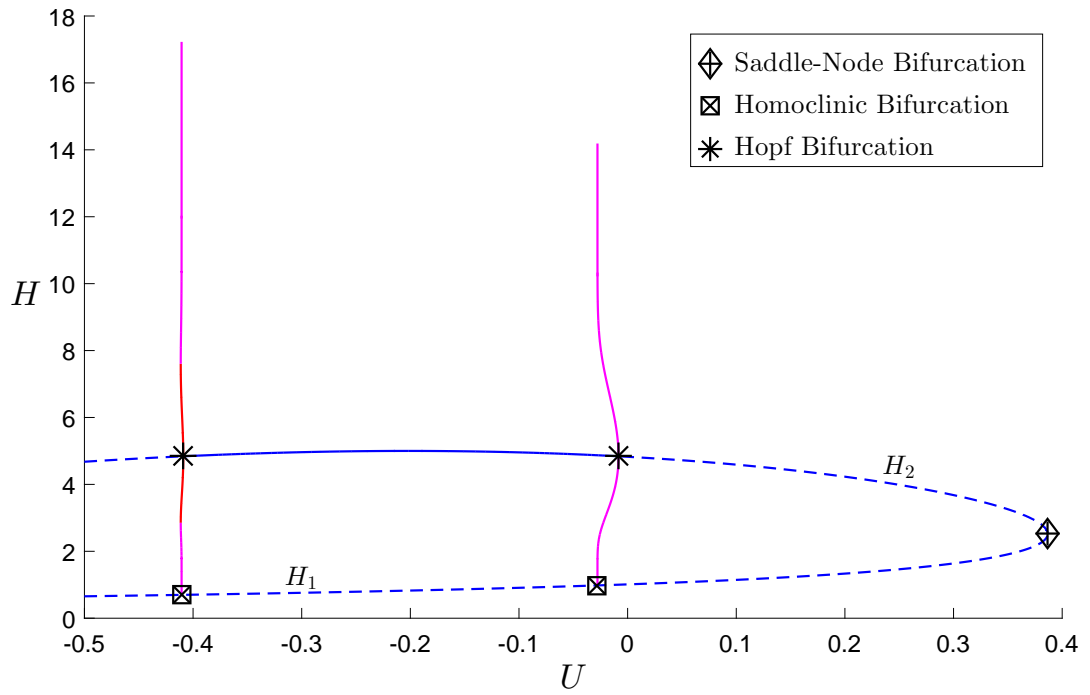


(a) The complete bifurcation diagram.

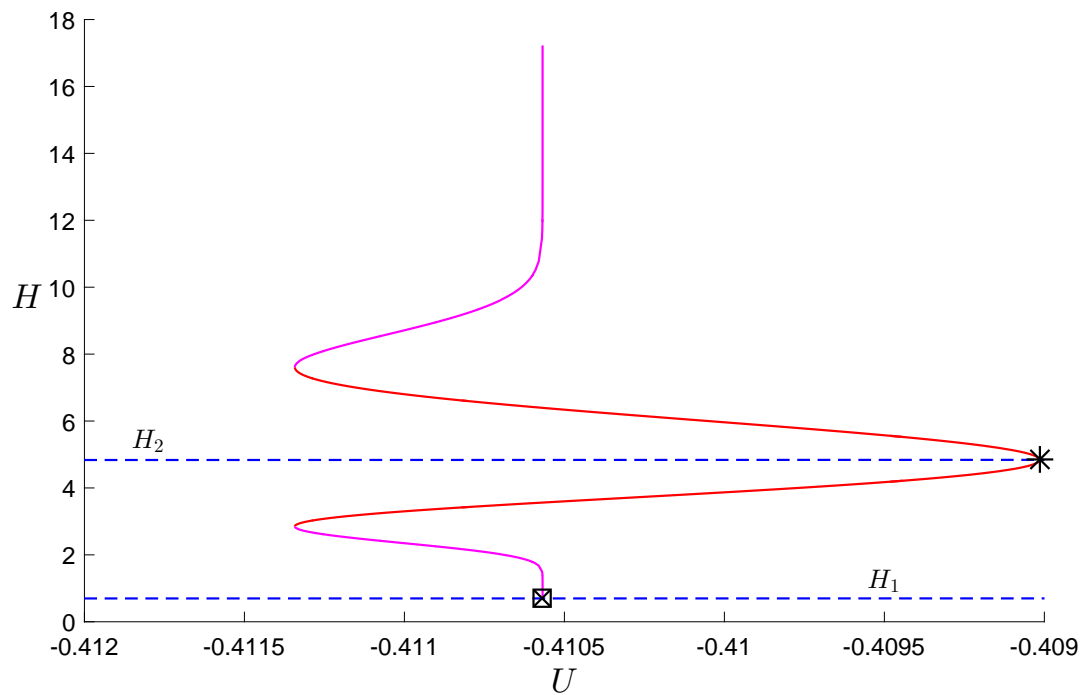


(b) The bifurcation diagram zoomed in around Hopf1.

**Figure 6.10.:** The bifurcation diagram for  $B = 0.95$ ,  $\bar{\lambda} = -5$ ,  $F_0 = 10$ ,  $R_l = 50$  and  $\rho = 0.1$ .

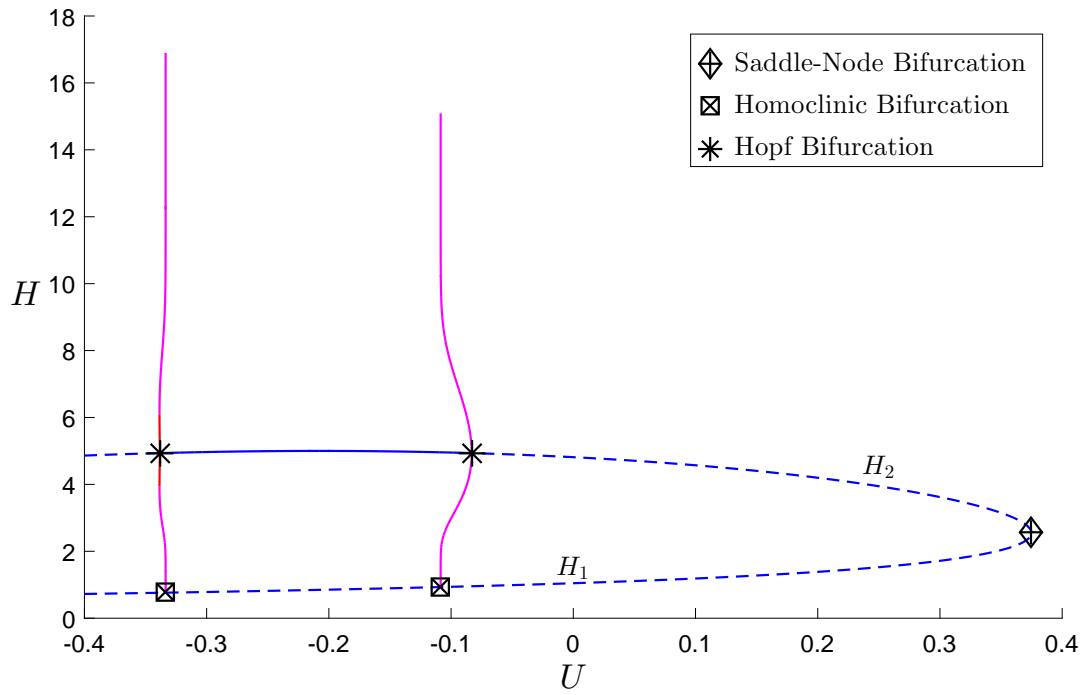


(a) The complete bifurcation diagram.

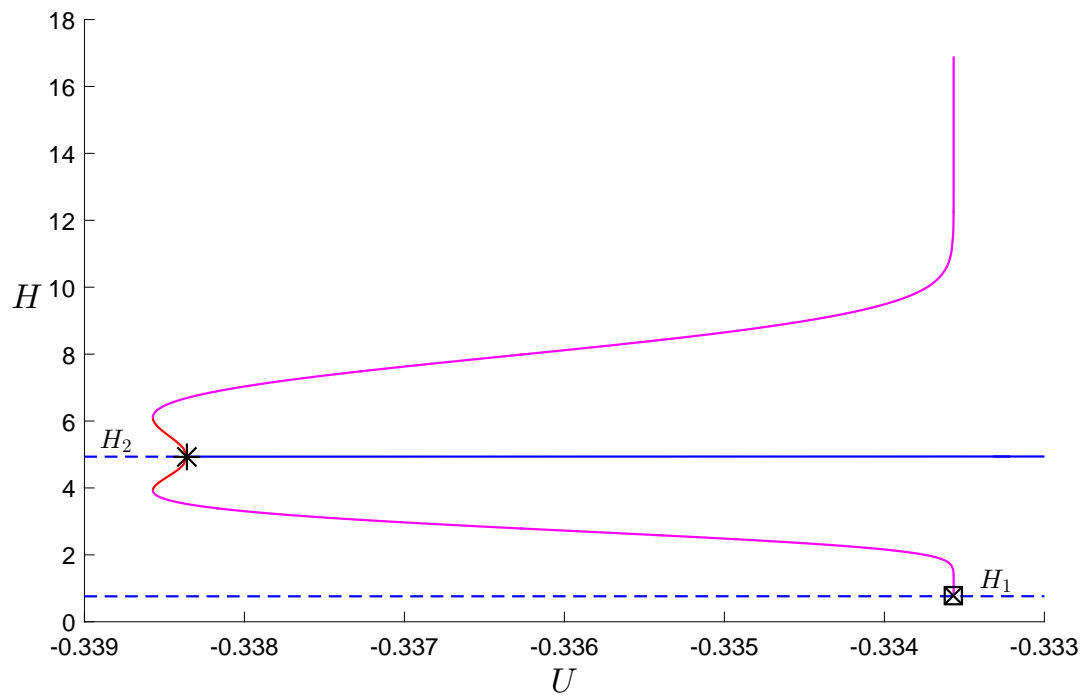


(b) The bifurcation diagram zoomed in around Hopf1.

**Figure 6.11.:** The bifurcation diagram for  $B = 1.01$ ,  $\bar{\lambda} = -5$ ,  $F_0 = 10$ ,  $R_l = 50$  and  $\rho = 0.1$ .



(a) The complete bifurcation diagram.



(b) The bifurcation diagram zoomed in around Hopf1.

**Figure 6.12.:** The bifurcation diagram for  $B = 1.04$ ,  $\bar{\lambda} = -5$ ,  $F_0 = 10$ ,  $R_l = 50$  and  $\rho = 0.1$ .

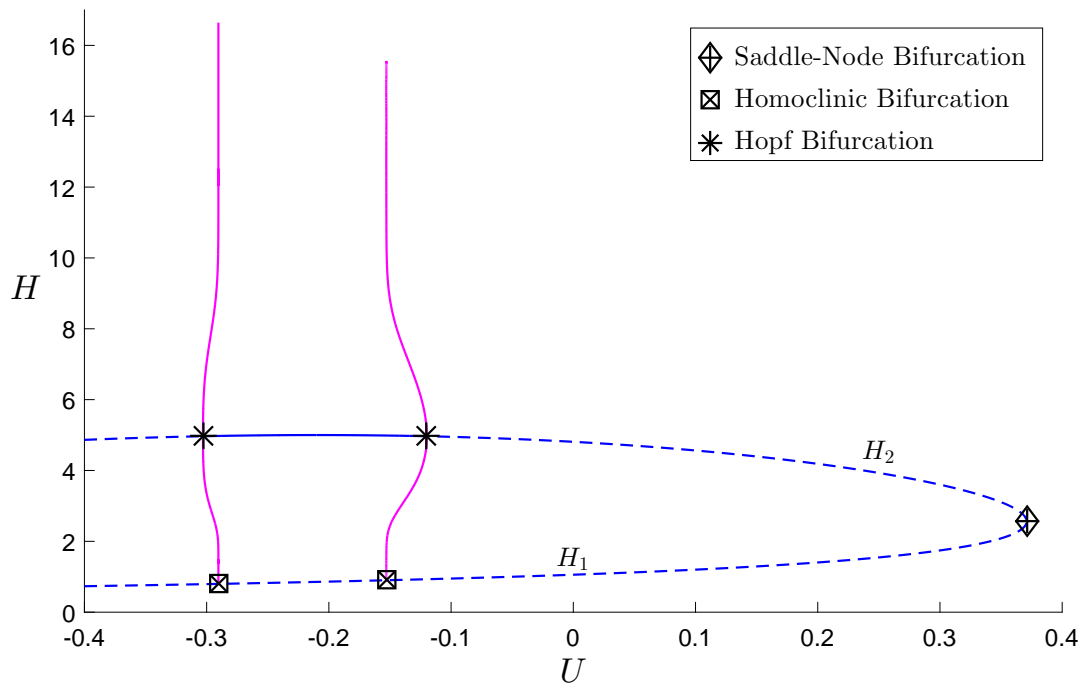


**Figure 6.13.:** The bifurcation diagram for  $B = 1.05$ ,  $\bar{\lambda} = -5$ ,  $F_0 = 10$ ,  $R_l = 50$  and  $\rho = 0.1$ .

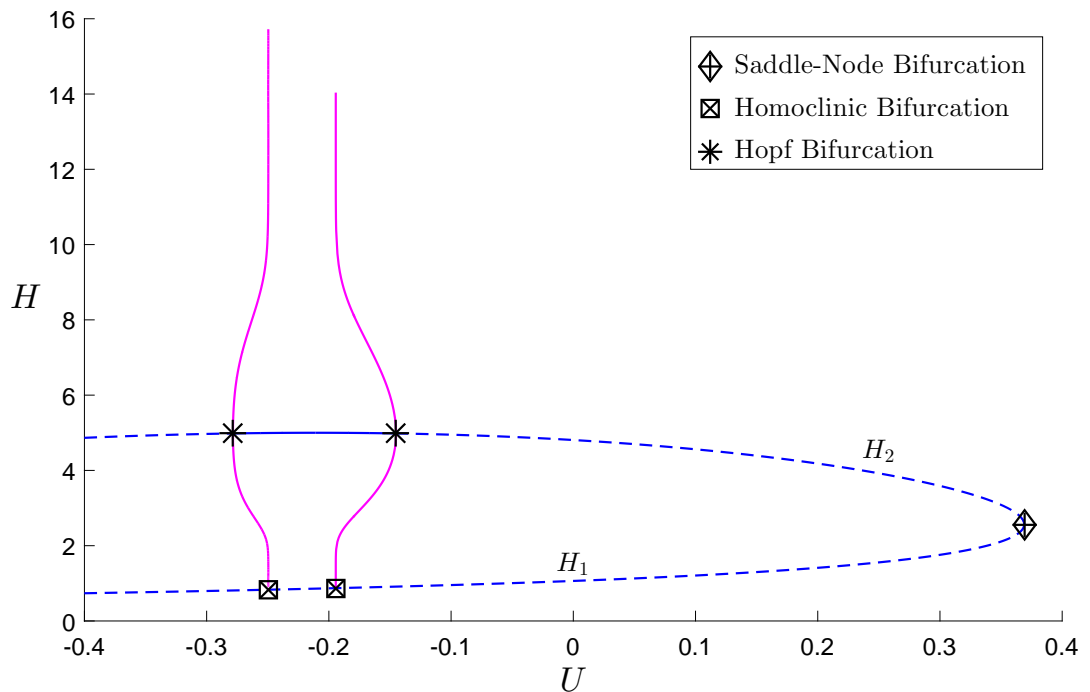


**Figure 6.14.:** The bifurcation diagram for  $B = 1.055$ ,  $\bar{\lambda} = -5$ ,  $F_0 = 10$ ,  $R_l = 50$  and  $\rho = 0.1$ .

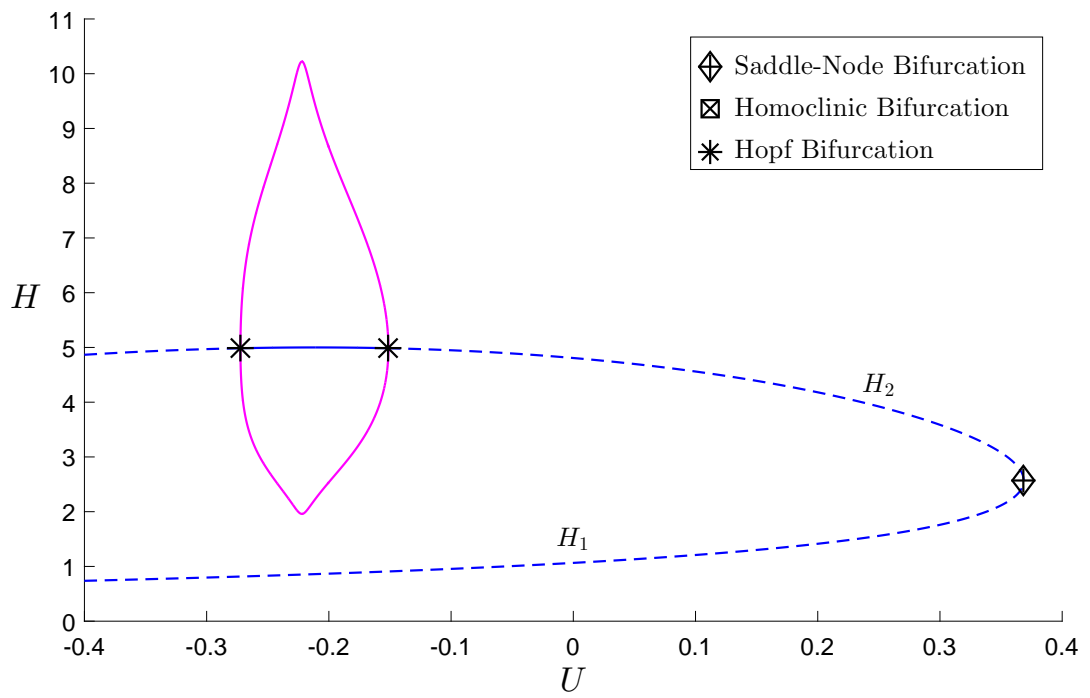


**Figure 6.15.:** The bifurcation diagram for  $B = 1.056$ ,  $\bar{\lambda} = -5$ ,  $F_0 = 10$ ,  $R_l = 50$  and  $\rho = 0.1$ .

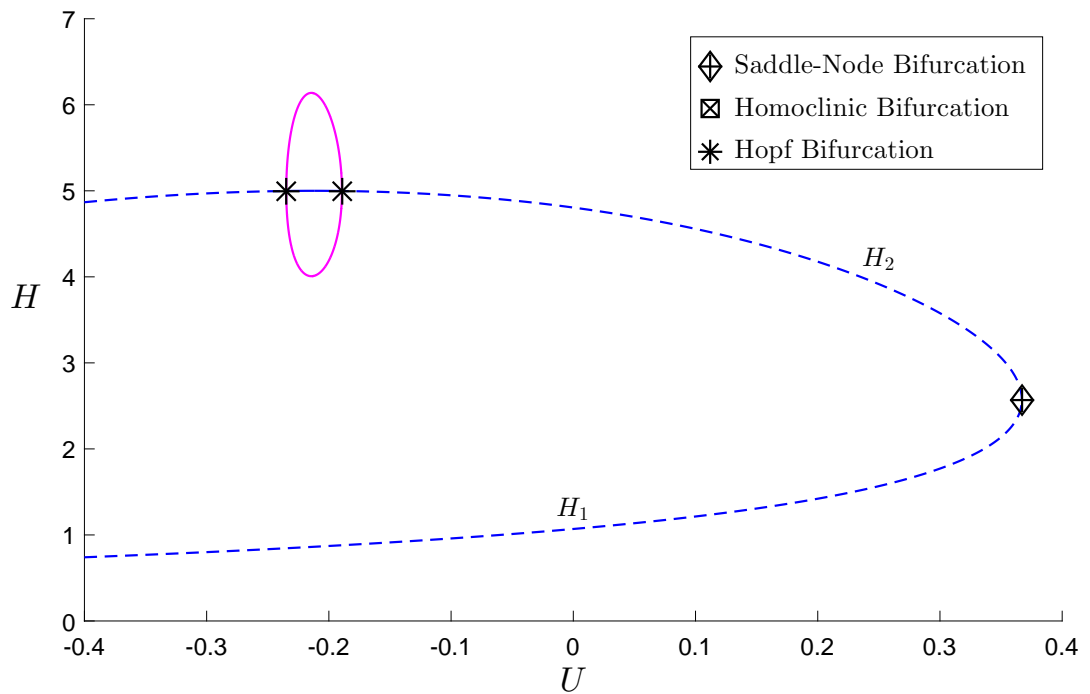
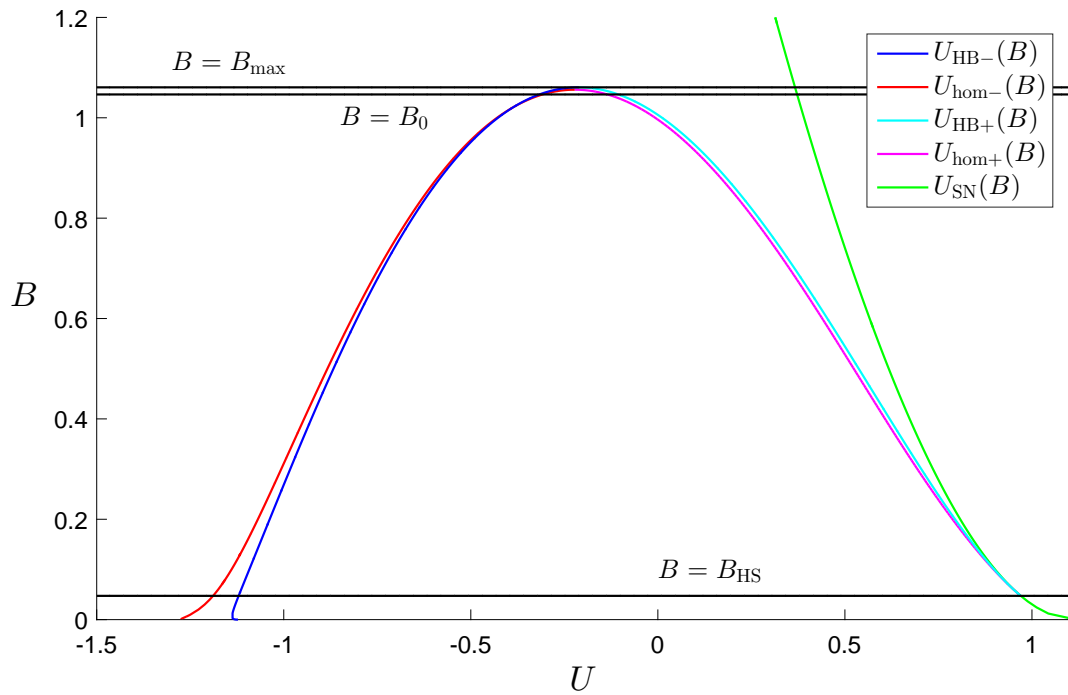
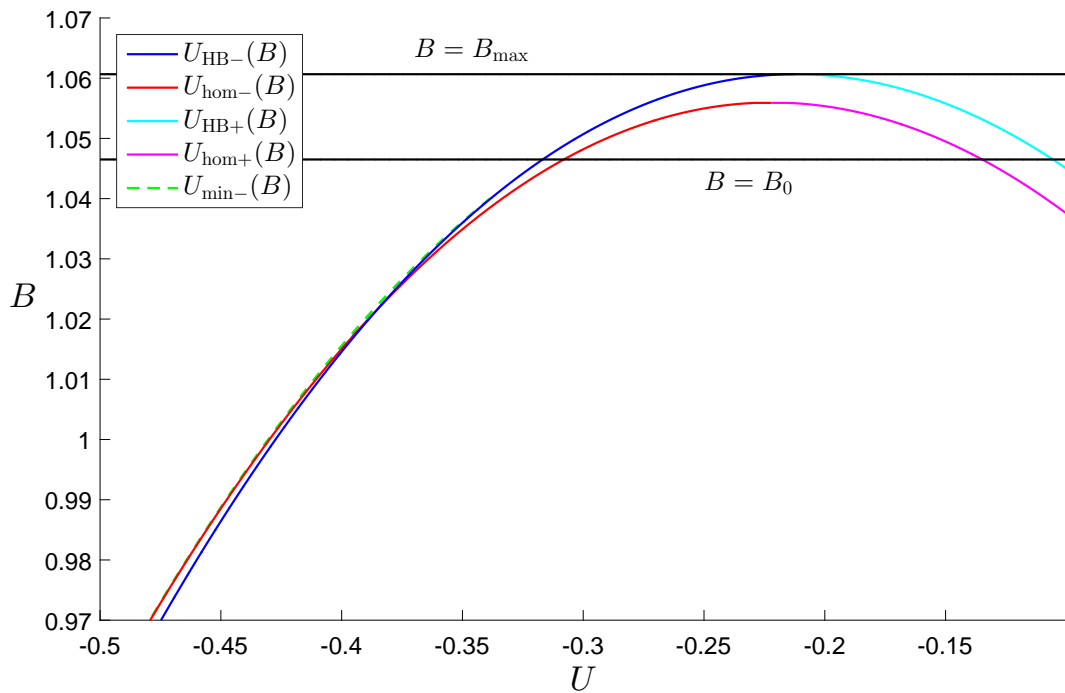


**Figure 6.16.:** The bifurcation diagram for  $B = 1.06$ ,  $\bar{\lambda} = -5$ ,  $F_0 = 10$ ,  $R_l = 50$  and  $\rho = 0.1$ .



(a) The complete bifurcation curves.



(b) The bifurcation curves zoomed in around  $B = B_{0+}$ .

**Figure 6.17.:** The bifurcation curves in the  $(U, B)$  plane for  $\bar{\lambda} = -5$ ,  $F_0 = 10$ ,  $R_l = 50$  and  $\rho = 0.1$ .

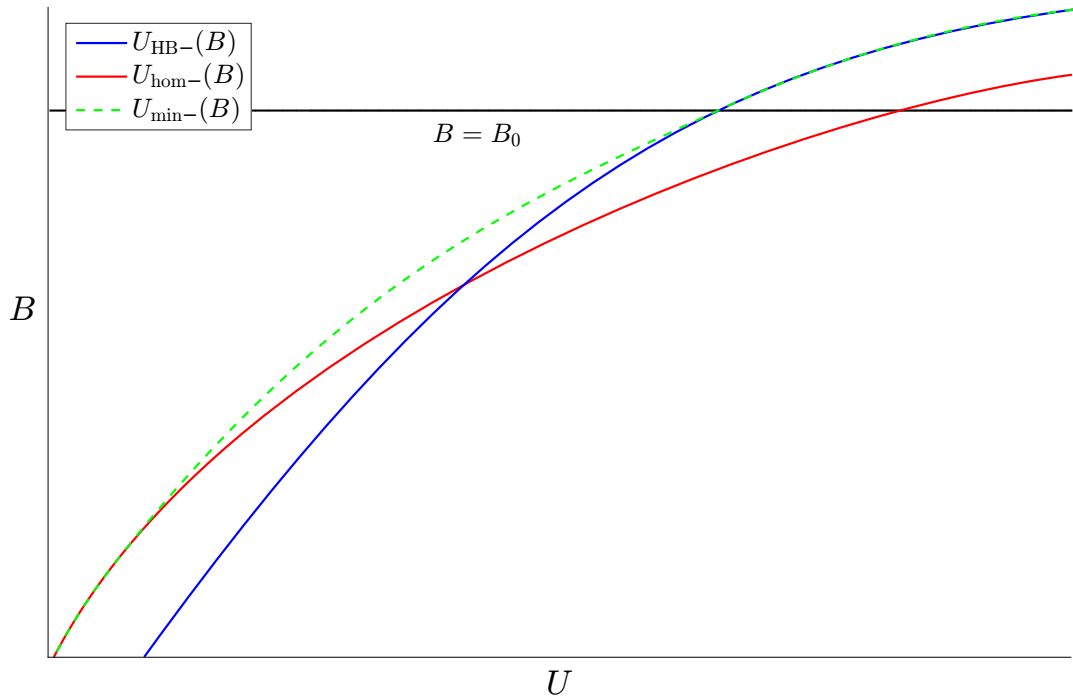


Figure 6.18.: The bifurcation curves zoomed in around  $U = U_{\min-}$ .

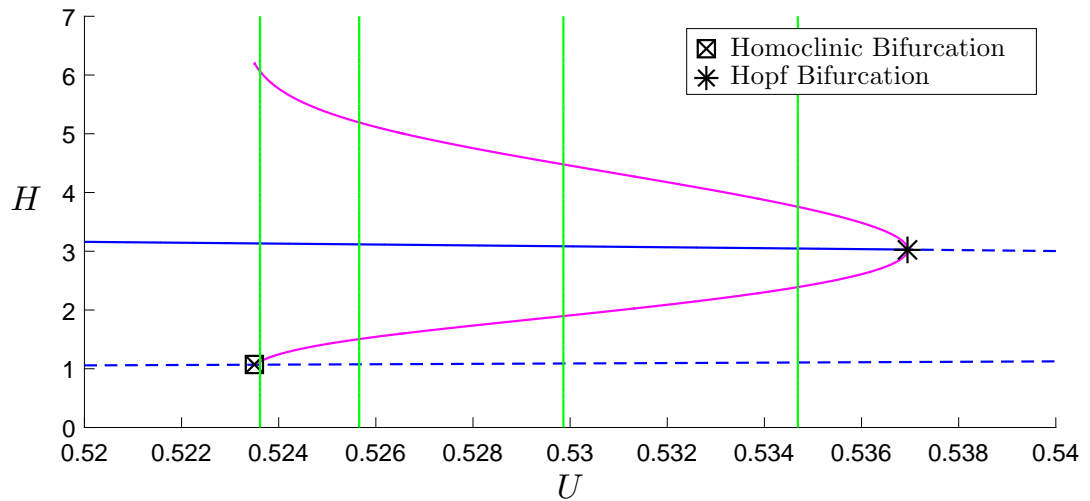
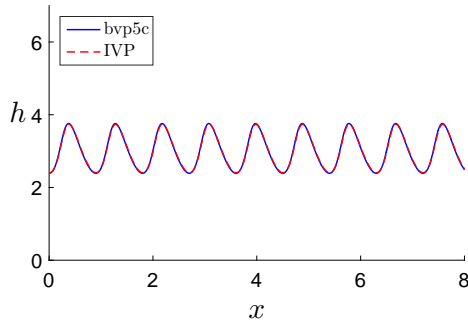


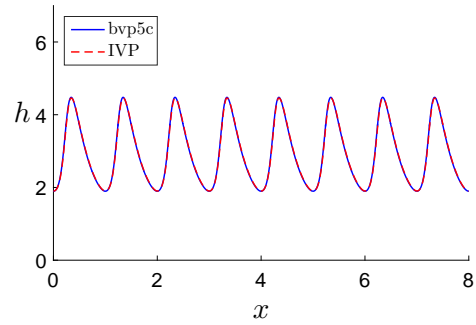
Figure 6.19.: The bifurcation diagram for  $B = 0.5$ ,  $\bar{\lambda} = -5$ ,  $F_0 = 10$ ,  $R_l = 50$  and  $\rho = 0.1$  zoomed in around Hopf2 with the values of  $U_1$ ,  $U_2$ ,  $U_3$  and  $U_4$  marked by the green lines.

Figure	bvp5c $U$	IVP $U$	IVP $B$
6.20a	0.53469	0.53494	0.49994
6.20b	0.52986	0.53011	0.50000
6.20c	0.52566	0.52601	0.49978
6.20d	0.52362	0.52415	0.49945

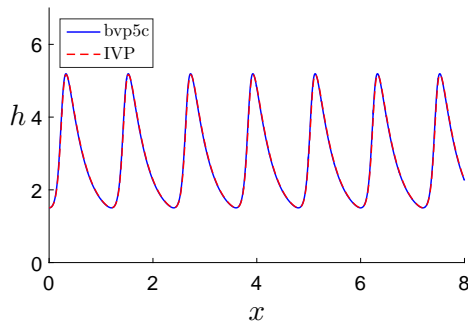
**Table 6.1.:** A comparison of  $U$  and  $B$  from bvp5c compared to those from the IVP for  $B = 0.5$ ,  $\bar{\lambda} = -5$ ,  $F_0 = 10$ ,  $R_l = 50$  and  $\rho = 0.1$ .



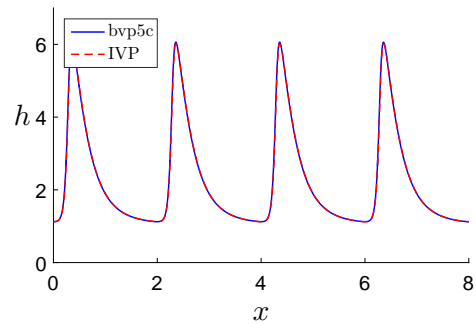
**(a)**  $U_1 \approx 0.53469$ ,  $L = 0.9$ .



**(b)**  $U_2 \approx 0.52986$ ,  $L = 1$ .



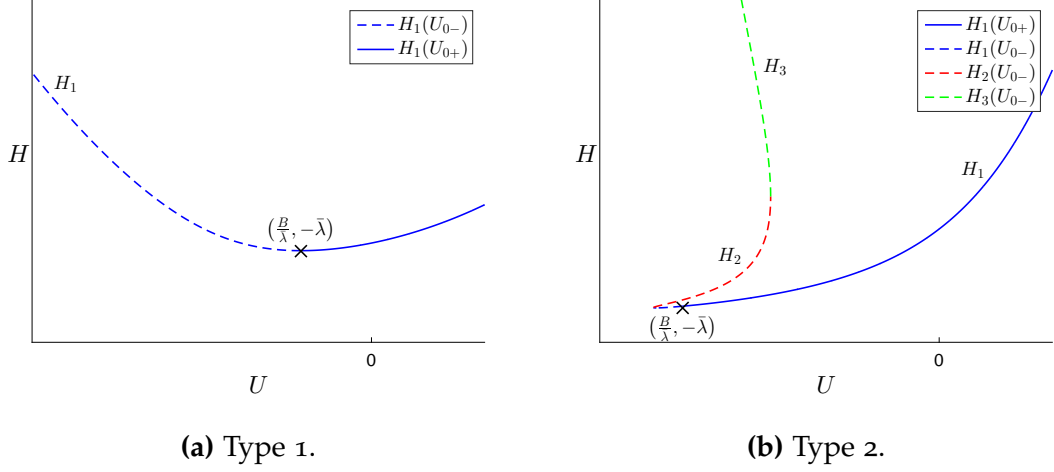
**(c)**  $U_3 \approx 0.52566$ ,  $L = 1.2$ .



**(d)**  $U_4 \approx 0.52362$ ,  $L = 2$ .

**Figure 6.20.:** A comparison between the limit cycle solutions obtained using bvp5c for  $B = 0.5$ ,  $\bar{\lambda} = -5$ ,  $F_0 = 10$ ,  $R_l = 50$  and  $\rho = 0.1$  and the corresponding solution from the IVP.

6.2.2  $-1 < \bar{\lambda} < 0$  (Downhill)

 6.2.2.1 The case for  $B > 0$ 


**Figure 6.21.:** The typical bifurcation diagrams for  $B > 0$  and  $-1 < \bar{\lambda} < 0$  with the dashed and solid lines corresponding to  $U_{0-}$  and  $U_{0+}$ , respectively.

For  $B > 0$ , from (6.2.15) we get no turning points on  $U_{0+}$ , hence  $U_{0+}$  gives one equilibrium point, which, by (6.2.22), is a saddle. For  $U_{0-}$ , from (6.2.15) we see that there are turning points which, when substituted into (6.2.10), gives

$$U_{\text{SN}} = -\sqrt{\frac{\bar{\lambda} + h_{\text{SN}}}{1 + \bar{\lambda}}} - \frac{h_{\text{SN}}}{2\sqrt{1 + \bar{\lambda}}\sqrt{\bar{\lambda} + h_{\text{SN}}}} < 0, \quad (6.2.57)$$

and can be solved to give

$$h_{\text{SN}\pm} = \frac{2}{9} \left[ U_{\text{SN}}^2 (1 + \bar{\lambda}) - 3\bar{\lambda} \pm (-U_{\text{SN}}) \sqrt{1 + \bar{\lambda}} \sqrt{U_{\text{SN}}^2 (1 + \bar{\lambda}) + 3\bar{\lambda}} \right]. \quad (6.2.58)$$

By (6.2.19), we have

$$\left. \frac{d^2 U_{0-}}{dh_0^2} \right|_{h_0=h_{\text{SN}}} \begin{cases} < 0 & \text{for } h_{\text{SN}} > -\frac{4}{3}\bar{\lambda} \\ > 0 & \text{for } h_{\text{SN}} < -\frac{4}{3}\bar{\lambda} \end{cases}, \quad (6.2.59)$$

hence for  $h_{\text{SN}} > -\frac{4}{3}\bar{\lambda}$  we get a maximum and for  $h_{\text{SN}} < -\frac{4}{3}\bar{\lambda}$  we get a minimum. These turning points represent saddle-node bifurcations which annihilate each other when  $\bar{\lambda} = \bar{\lambda}_{\text{SNA}}$ , where

$$\bar{\lambda}_{\text{SNA}} = -\frac{3}{8}B^{\frac{2}{3}} \left[ \left( \sqrt{B^2 + 16} + 4 \right)^{\frac{1}{3}} - \left( \sqrt{B^2 + 16} - 4 \right)^{\frac{1}{3}} \right], \quad (6.2.60)$$

at

$$h_{\text{SNA}} = -\frac{4}{3}\bar{\lambda}_{\text{SNA}}, \quad U_{\text{SNA}} = \sqrt{-\frac{3\bar{\lambda}_{\text{SNA}}}{1 + \bar{\lambda}_{\text{SNA}}}}. \quad (6.2.61)$$

From (6.2.60) and (6.2.61) we find we only get saddle-node bifurcations for

$$B > \frac{8\sqrt{3}}{9} \frac{\bar{\lambda}^2}{\sqrt{-\bar{\lambda}(1 + \bar{\lambda})}} \equiv B_{\text{SNA}}. \quad (6.2.62)$$

For  $B < B_{\text{SNA}}$  (as shown in Figure 6.21a), by using (6.2.62) in (6.2.22) we see that

$$\left. \frac{df_3}{dh} \right|_{h=h_0, U=U_0-} > \frac{R_l}{3Bh_0(1 + \bar{\lambda})\sqrt{-3\bar{\lambda}}} \left[ 3h_0^2\sqrt{-3\bar{\lambda}} - 16\bar{\lambda}^2\sqrt{\bar{\lambda}^2 + h_0} \right]. \quad (6.2.63)$$

By letting  $g(h_0) = 3h_0^2\sqrt{-3\bar{\lambda}} - 16\bar{\lambda}^2\sqrt{\bar{\lambda}^2 + h_0}$  and noting that

$$\frac{dg}{dh_0} = 0 \quad \text{for} \quad h_0 = -\frac{4}{3}\bar{\lambda}, \quad (6.2.64)$$

and

$$\left. \frac{d^2g}{dh_0^2} \right|_{h_0 = -\frac{4}{3}\bar{\lambda}} = 18\sqrt{-3\bar{\lambda}}, \quad (6.2.65)$$

hence  $h_0 = -\frac{4}{3}\bar{\lambda}$  is a minimum for which

$$g\left(h_0 = -\frac{4}{3}\bar{\lambda}\right) = 0. \quad (6.2.66)$$

Using this in (6.2.63) we see that

$$\left. \frac{df_3}{dh} \right|_{h=h_0, U=U_0-} > 0, \quad (6.2.67)$$

hence  $U_{0-}$  is a saddle. Therefore, for  $B < B_{\text{SNA}}$ , we only get one equilibrium point which is a saddle and so will not get any Hopf bifurcations.

For  $B > B_{\text{SNA}}$  (as shown in Figure 6.21b), by using (6.2.62) in (6.2.22) we see that

$$\left. \frac{df_3}{dh} \right|_{h=h_0, U=U_{0-}} > 0 \quad \text{as} \quad h_0 \rightarrow -\bar{\lambda}^+, \quad (6.2.68)$$

and

$$\left. \frac{df_3}{dh} \right|_{h=h_0, U=U_{0-}} > 0 \quad \text{as} \quad h_0 \rightarrow +\infty, \quad (6.2.69)$$

hence  $U_{0-}(h_0 = H_1)$  and  $U_{0-}(h_0 = H_3)$  are saddles and hence  $U_{0-}(h_0 = H_2)$  must be a node.

By noting that, on  $U = U_{0-}$ ,

$$\left. \frac{dH}{d\mu} \right|_{\mu=0} < 0 \quad \text{as} \quad h_0 \rightarrow -\bar{\lambda}^+, \quad (6.2.70)$$

and

$$\left. \frac{dH}{d\mu} \right|_{\mu=0} < 0 \quad \text{as} \quad h_0 \rightarrow +\infty, \quad (6.2.71)$$

hence for  $U = U_{0-}(h_0 = H_2)$

$$\left. \frac{dH}{d\mu} \right|_{\mu=0} > 0, \quad (6.2.72)$$

we may simplify (6.2.37) and (6.2.38) to

$$\text{sign}(a\alpha'(0)) = \text{sign} \left( 2h_{\text{HB}} \sqrt{\frac{\bar{\lambda} + h_{\text{HB}}}{1 + \bar{\lambda}}} - B \right), \quad (6.2.73)$$

and

$$\alpha(\mu > 0) < 0. \quad (6.2.74)$$

By (6.2.26), in order for  $h_{\text{SN}-} < h_{\text{HB}} < h_{\text{SN}+}$  we must have  $B > B_{\text{HS}+}$  and

$$F_0 < 2\sqrt{1 - \rho} (1 + \bar{\lambda}) \equiv F_{\text{HS}}, \quad (6.2.75)$$

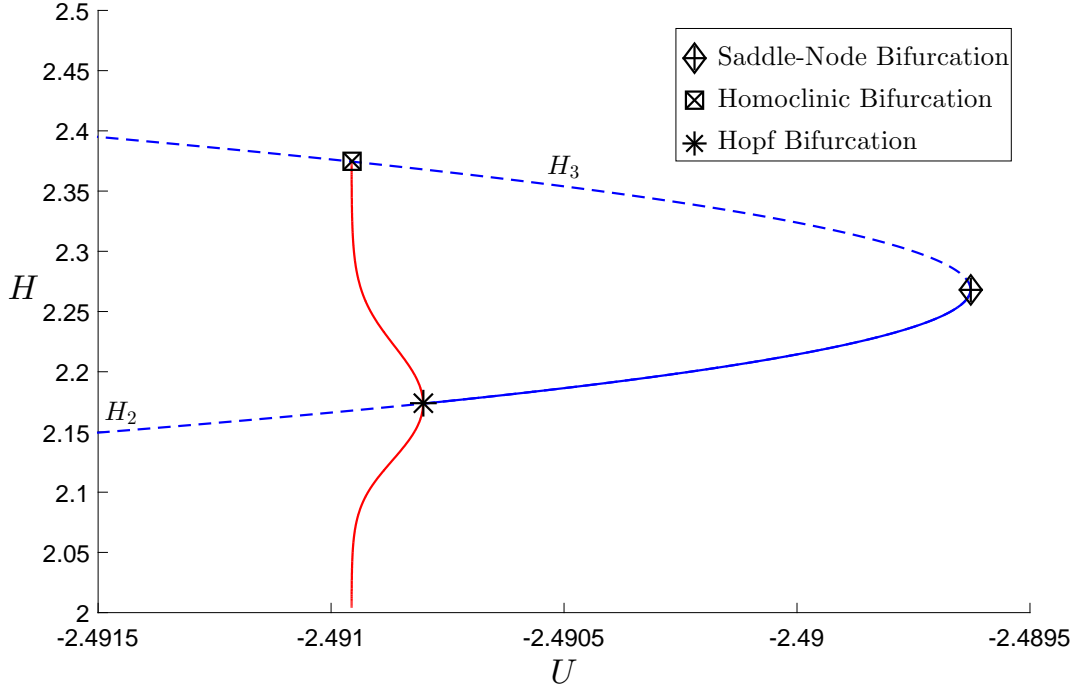


**Figure 6.22.:** The bifurcation diagram zoomed in around the Hopf bifurcation for  $B = 2$ ,  $\bar{\lambda} = -0.2$ ,  $F_0 = 1.52$ ,  $R_l = 50$  and  $\rho = 0.1$ .

and by (6.2.39),  $B_{0+} > B_{HS+}$  only when

$$F_0 < \sqrt{1 - \rho} \sqrt{1 + \bar{\lambda}} \equiv F_{B_0}, \quad (6.2.76)$$

for which  $F_{B_0} > F_c$  for  $\bar{\lambda} < -0.75$ . Hence, by (6.2.73) and (6.2.74), for  $\bar{\lambda} > -0.75$ , or  $\bar{\lambda} < -0.75$  and  $F_0 > F_{B_0}$ , we get a supercritical Hopf bifurcation from which a unique limit cycle solution bifurcates in  $U < U_{HB}$  and for  $\bar{\lambda} < -0.75$  and  $F_0 < F_{B_0}$  we get a subcritical Hopf bifurcation from which a unique limit cycle solution bifurcates in  $U > U_{HB}$ .

Figures 6.22 and 6.23 show the typical bifurcation diagrams zoomed in around the supercritical and subcritical Hopf bifurcations, respectively, and Figure 6.24 shows examples of limit cycle solutions for these parameter sets. We can see that both result in very short regions in  $U$  for which limit cycle solutions exist, which end in homoclinic bifurcations with either  $H_1$  or  $H_3$ .

By using these periodic travelling wave solutions as the initial condition in the IVP (6.1.25) and (6.1.27) with periodic boundary conditions, as we did

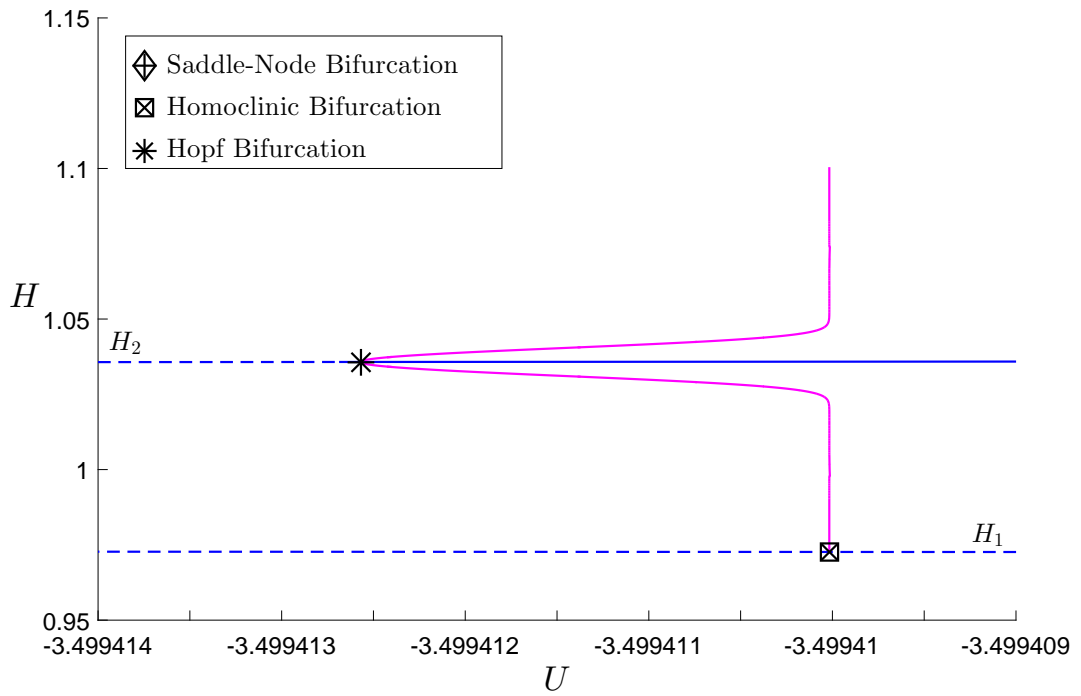
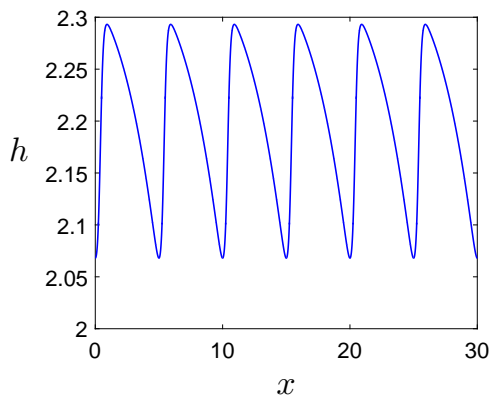
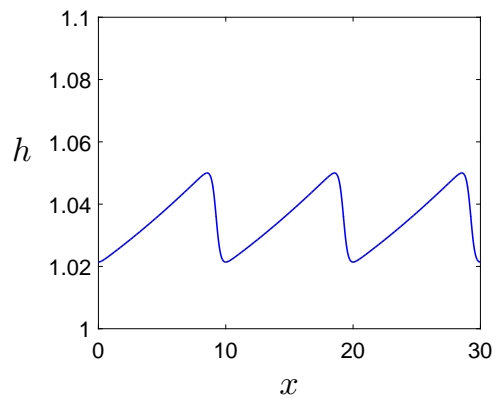


**Figure 6.23.:** The bifurcation diagram zoomed in around the Hopf bifurcation for  $B = 2.5$ ,  $\bar{\lambda} = -0.8$ ,  $F_0 = 0.4$ ,  $R_l = 50$  and  $\rho = 0.1$ .



**(a)**  $U = -2.491$ ,  $B = 2$ ,  $\bar{\lambda} = -0.2$ ,  
 $F_0 = 1.52$ ,  $R_l = 50$  and  $\rho = 0.1$ .



**(b)**  $U = -3.499$ ,  $B = 2.5$ ,  $\bar{\lambda} = -0.8$ ,  
 $F_0 = 0.4$ ,  $R_l = 50$  and  $\rho = 0.1$ .

**Figure 6.24.:** The limit cycle solutions for  $-1 < \bar{\lambda} < 0$  and  $B > 0$ .

in Section 5.2, we find these solutions produce unsteady periodic solutions which do not have a permanent form.

### 6.2.2.2 The case for $B < 0$

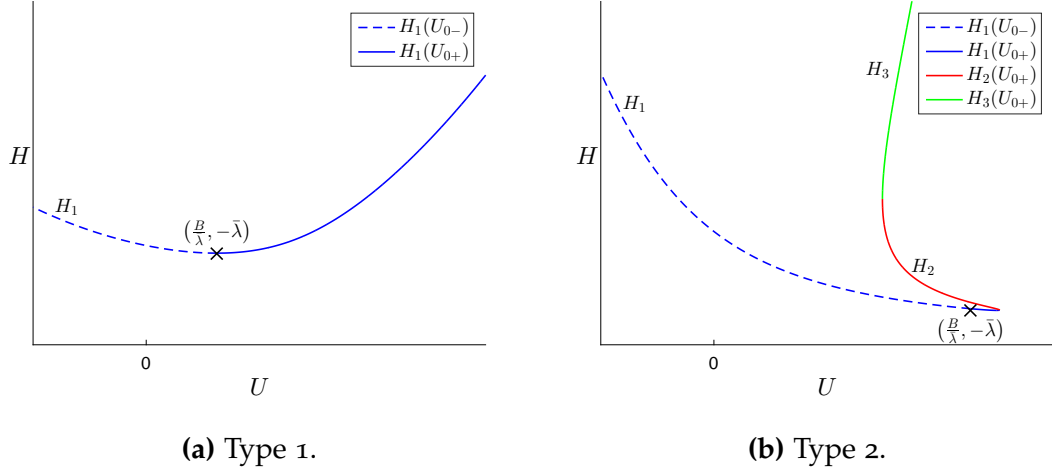


**Figure 6.25.:** The typical bifurcation diagrams for  $B < 0$  and  $-1 < \bar{\lambda} < 0$  with the dashed and solid lines corresponding to  $U_{0-}$  and  $U_{0+}$ , respectively.

For  $B < 0$ , from (6.2.15) we get no turning points on  $U_{0-}$ , hence  $U_{0-}$  gives one equilibrium point, which, by (6.2.22), is a node or spiral. Using (6.2.37) and (6.2.38) we find, as  $U_{0-}$  is monotone decreasing in  $H(\mu)$ ,  $aa'(0) < 0$  and  $\alpha(\mu < 0) > 0$ , hence the Hopf bifurcation theorem tells us  $(U_{\text{HB}}, h_{\text{HB}})$  is a subcritical Hopf bifurcation from which a unique limit cycle solution bifurcates in  $U > U_{\text{HB}}$ .

For  $U_{0+}$ , from (6.2.15) we see that there are turning points which, when substituted into (6.2.10), gives

$$U_{\text{SN}} = \sqrt{\frac{\bar{\lambda} + h_{\text{SN}}}{1 + \bar{\lambda}}} + \frac{h_{\text{SN}}}{2\sqrt{1 + \bar{\lambda}}\sqrt{\bar{\lambda} + h_{\text{SN}}}} > 0. \quad (6.2.77)$$

Similarly to our work in the previous subsection, from (6.2.58) onwards, we find

$$\left. \frac{d^2 U_{0+}}{dh_0^2} \right|_{h_0=h_{\text{SN}}} \begin{cases} < 0 & \text{for } h_{\text{SN}} < -\frac{4}{3}\bar{\lambda} \\ > 0 & \text{for } h_{\text{SN}} > -\frac{4}{3}\bar{\lambda} \end{cases}, \quad (6.2.78)$$

hence for  $h_{\text{SN}} < -\frac{4}{3}\bar{\lambda}$  we get a maximum and for  $h_{\text{SN}} > -\frac{4}{3}\bar{\lambda}$  we get a minimum, which only exist for  $B < -B_{\text{SNA}}$ , from (6.2.62).

For  $B > -B_{\text{SNA}}$  (as shown in Figure 6.25a), by using (6.2.62) in (6.2.22) we can find that

$$\left. \frac{df_3}{dh} \right|_{h=h_0, U=U_{0+}} < 0, \quad (6.2.79)$$

and that

$$\left. \frac{dH}{d\mu} \right|_{\mu=0} > \frac{3h_0^2\sqrt{-3\bar{\lambda}} - 16\bar{\lambda}^2\sqrt{\bar{\lambda}^2 + h_0}}{6\sqrt{1 + \bar{\lambda}}\sqrt{\bar{\lambda}} + h_0h_0^2\sqrt{-3\bar{\lambda}}} > 0, \quad (6.2.80)$$

hence we may simplify (6.2.37) and (6.2.38) to

$$\text{sign}(a\alpha'(0)) = \text{sign}\left(-2h_{\text{HB}}\sqrt{\frac{\bar{\lambda} + h_{\text{HB}}}{1 + \bar{\lambda}}} - B\right), \quad (6.2.81)$$

and

$$\alpha(\mu > 0) > 0. \quad (6.2.82)$$

Using (6.2.23) in (6.2.81) we find that we only get Hopf bifurcations for

$$F_0 > \frac{1}{2}\sqrt{1 - \rho}\sqrt{1 + \bar{\lambda}} \equiv F_{\text{Hmin}}, \quad (6.2.83)$$

where  $F_{\text{Hmin}} < F_c$  for  $\bar{\lambda} > -\frac{15}{16}$ . Using (6.2.39) we find that  $B_{0-} > -B_{\text{SNA}}$  only when  $F_0 > F_{B_0}$ , for which  $F_{B_0} > F_c$  for  $\bar{\lambda} < -0.75$ . Hence, by (6.2.81) and (6.2.82), for:

- $\bar{\lambda} < -0.75$  and  $B > B_{0-}$ ,
- $\bar{\lambda} > -0.75$  and  $F_0 < F_{B_0}$ , or

- $\bar{\lambda} > -0.75$ ,  $F_0 > F_{B_0}$  and  $B > B_{0-}$ ,

we get a subcritical Hopf bifurcation from which a unique limit cycle solution bifurcates in  $U < U_{\text{HB}}$ , and for:

- $\bar{\lambda} < -0.75$  and  $B < B_{0-}$ , or
- $\bar{\lambda} > -0.75$ ,  $F_0 > F_{B_0}$  and  $B < B_{0-}$ ,

we get a supercritical Hopf bifurcation from which a unique limit cycle solution bifurcates in  $U > U_{\text{HB}}$ . Figures 6.26 - 6.28 show typical bifurcation diagrams for varying  $B$ ,  $\bar{\lambda}$  and  $F_0$  and Figure 6.29 shows examples of limit cycle solutions for the parameter set used in Figure 6.26.

We see that the branch ceases to exist as  $h \rightarrow 0$  and the limit cycle solution amplitude tends to infinity. To understand the behaviour near  $h = 0$ , which is a line of singularities, we consider the transposed system of equations

$$H' = HW, \quad (6.2.84)$$

$$W' = W^2 - \frac{R_l}{B} \left[ \frac{(1-\rho)H^3}{F_0^2} - B^2 \right] W - \frac{R_l}{B} \left[ (B + UH)^2 - \frac{(\bar{\lambda} + H)H^2}{1 + \bar{\lambda}} \right]. \quad (6.2.85)$$

The equilibrium points and phase portrait of this system are the same as for (6.2.7) and (6.2.8), however we no longer have a line of singularities at  $h = 0$ . Equilibrium points of (6.2.84) and (6.2.85) satisfy

$$W = 0, \quad (B + UH_0)^2 - \frac{(\bar{\lambda} + H_0)H_0^2}{1 + \bar{\lambda}} = 0, \quad (6.2.86)$$

and

$$H = 0, \quad W_{0\pm} = \frac{1}{2} \left( -BR_l \pm \sqrt{B^2R_l^2 + 4BR_l} \right), \quad (6.2.87)$$

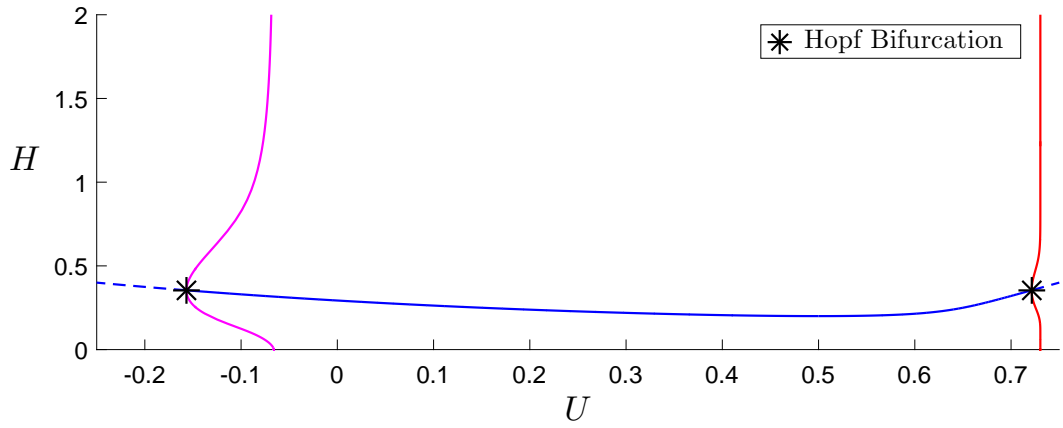


**Figure 6.26.:** The bifurcation diagram for  $B = -0.1$ ,  $\bar{\lambda} = -0.2$ ,  $F_0 = 2$ ,  $R_l = 50$  and  $\rho = 0.1$ .

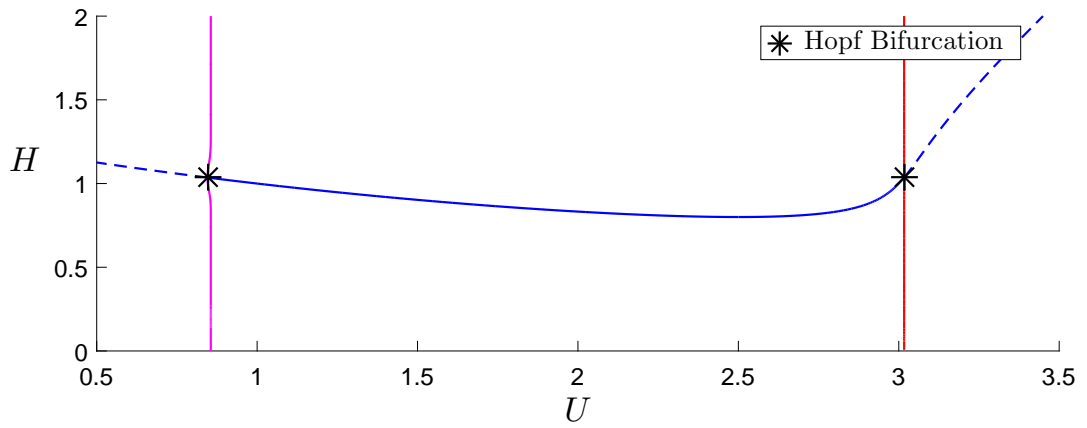


**Figure 6.27.:** The bifurcation diagram for  $B = -2$ ,  $\bar{\lambda} = -0.8$ ,  $F_0 = 0.5$ ,  $R_l = 50$  and  $\rho = 0.1$ .

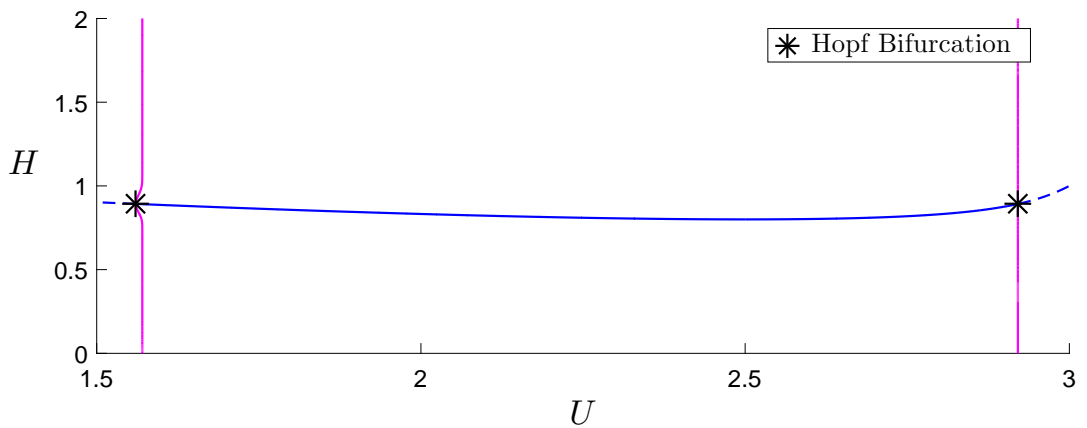


**Figure 6.28.:** The bifurcation diagram for  $B = -2$ ,  $\bar{\lambda} = -0.8$ ,  $F_0 = 0.4$ ,  $R_l = 50$  and  $\rho = 0.1$ .

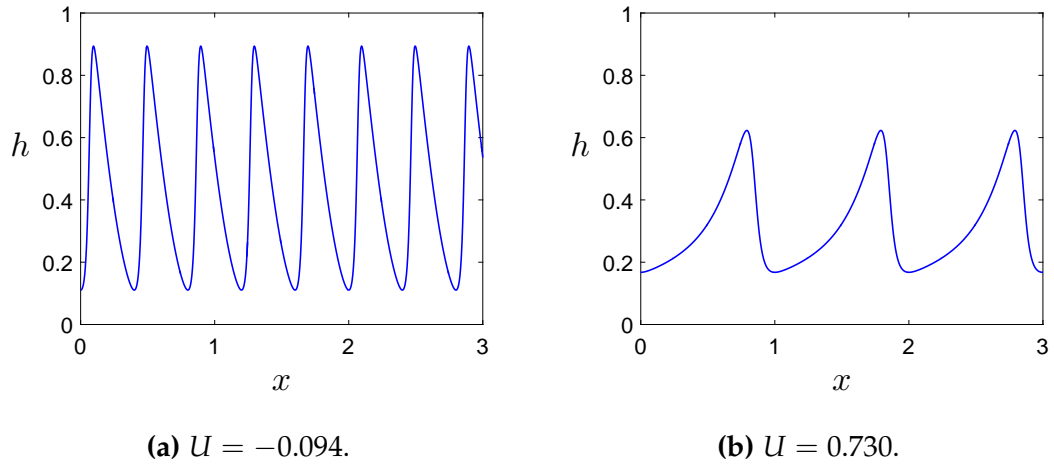


**Figure 6.29.:** The limit cycle solutions for  $B = -0.1$ ,  $\bar{\lambda} = -0.2$ ,  $F_0 = 2$ ,  
 $R_l = 50$  and  $\rho = 0.1$ .

where we find that  $W_{0-}$  is a saddle and  $W_{0+}$  is an unstable node and  $H_0$  is the same as those in the original system. We may also note that for  $H \gg 1$  (6.2.85), becomes

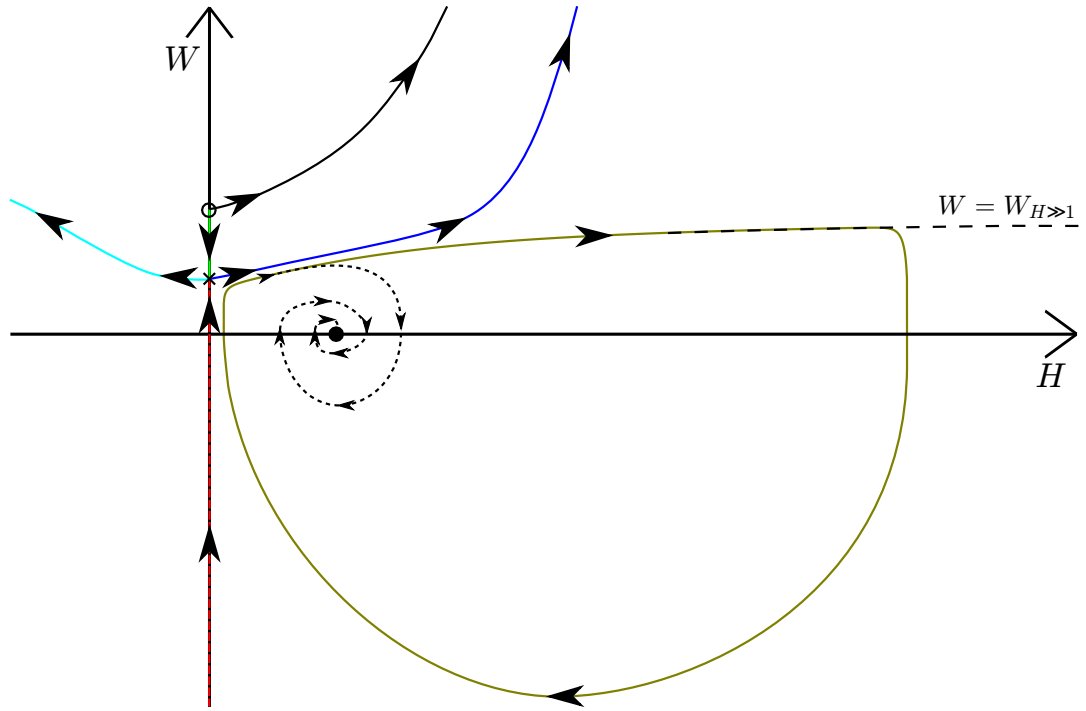
$$W' \approx -\frac{R_l}{B} \left( \frac{1-\rho}{F_0^2} W - \frac{1}{1+\bar{\lambda}} \right) H^3, \quad (6.2.88)$$

for which  $W' \approx 0$  when

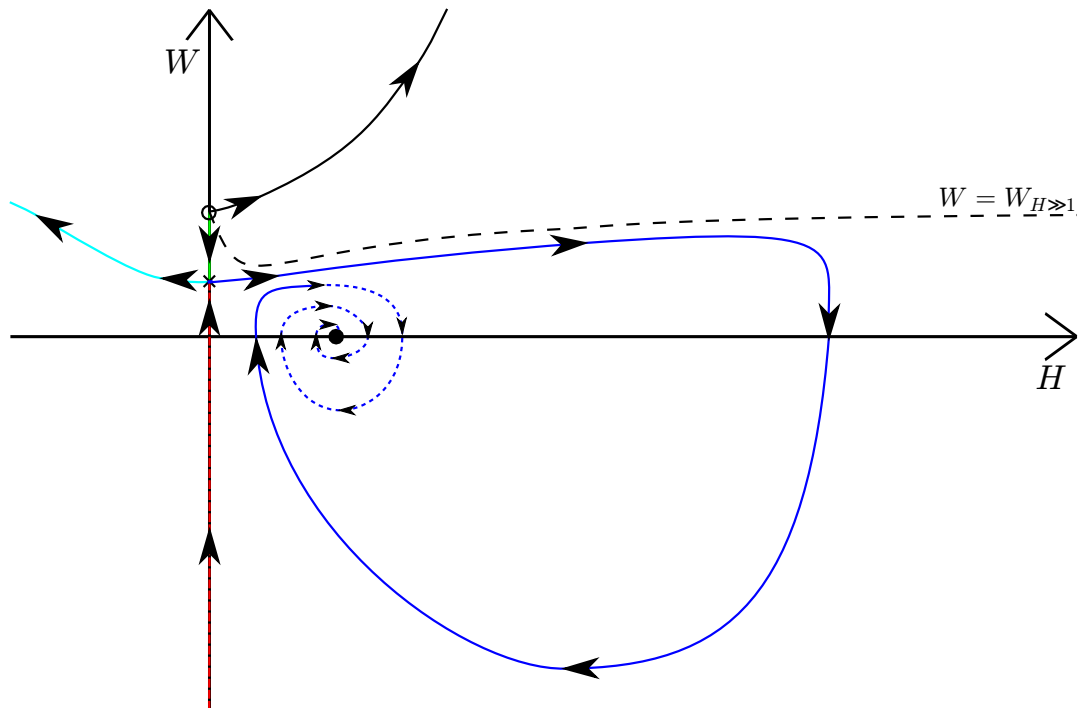
$$W = \frac{F_0^2}{(1-\rho)(1+\bar{\lambda})} \equiv W_{H \gg 1}. \quad (6.2.89)$$

By investigating the phase planes for the transposed system of equations we find that, before the limit cycles end, by tracking ( $H \gg 1, W' \approx W_{H \gg 1}$ ) backwards it originates from the limit cycle, as shown in Figure 6.30a, whereas after the limit cycle ends it originates from  $W_{0+}$ , as shown in Figure 6.30b. From this we may conclude that the limit cycle ends in a heteroclinic bifurcation with  $W_{0-}$  and a non-physical saddle point at infinity.

Figure 6.31 shows examples of the stable limit cycle solutions for the parameter set used in Figures 6.26 and 6.29 as we approach the heteroclinic bifurcation at  $U = U_{\text{het}}$ . Comparing Figures 6.29b and 6.31a we can see that, as we have approached the heteroclinic bifurcation, the limit cycle solution has increased in both length and height and the tail of the solution



(a) The phase plane before the heteroclinic bifurcation.



(b) The phase plane after the heteroclinic bifurcation.

**Figure 6.30.:** Phase planes for the limit cycle produced by the Hopf bifurcation on  $U_-$  for  $B = -0.1$ ,  $\bar{\lambda} = -0.2$ ,  $F_0 = 2$ ,  $R_l = 50$  and  $\rho = 0.1$ .

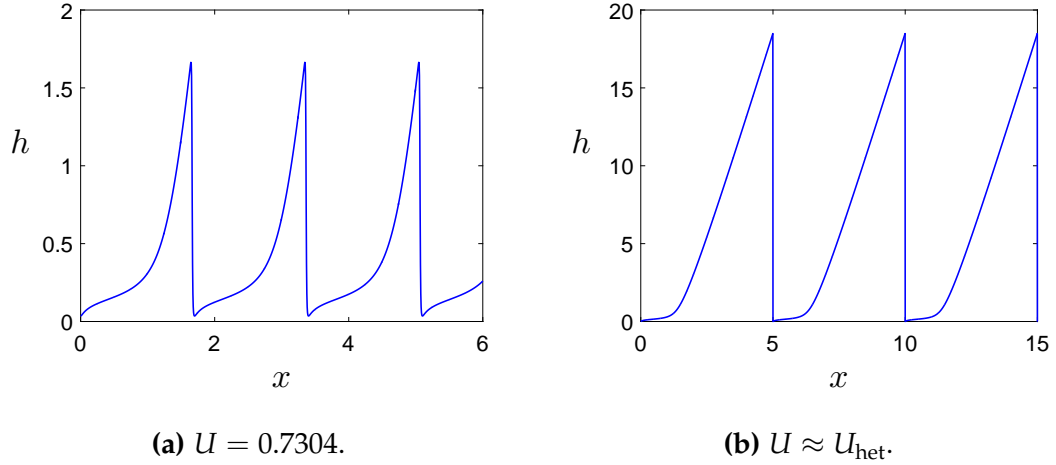


**Figure 6.31.:** The stable limit cycle solutions near the heteroclinic bifurcation for  $B = -0.1$ ,  $\bar{\lambda} = -0.2$ ,  $F_0 = 2$ ,  $R_l = 50$  and  $\rho = 0.1$ .

has begun to curl down towards  $h = 0$ . This corresponds to the phase plane now coming close to  $W_{0-}$ , as in Figure 6.30a. As  $U$  is increased further, as in Figure 6.31b, the limit cycle solution has grown further in length and height and continues to do so until the heteroclinic bifurcation, at which point the solution becomes infinite as it joins the physical saddle point,  $W_{0-}$ , with a non-physical saddle point at infinity.

For  $B < -B_{\text{SNA}}$  (as shown in Figure 6.25b), from (6.2.22) we can see that

$$\left. \frac{df_3}{dh} \right|_{h=h_0, U=U_{0+}} < 0 \quad \text{as} \quad h_0 \rightarrow -\bar{\lambda}^+, \quad (6.2.90)$$

and

$$\left. \frac{df_3}{dh} \right|_{h=h_0, U=U_{0+}} < 0 \quad \text{as} \quad h_0 \rightarrow +\infty, \quad (6.2.91)$$

hence  $U_{0+}(h_0 = H_1)$  and  $U_{0+}(h_0 = H_3)$  are nodes or spirals, hence  $U_{0+}(h_0 = H_2)$  must be a saddle.

We may simplify (6.2.37) and (6.2.38) by noting that, on  $U = U_{0+}$ ,

$$\left. \frac{dH}{d\mu} \right|_{\mu=0} > 0 \quad \text{as} \quad h_0 \rightarrow -\bar{\lambda}^+, \quad (6.2.92)$$

and

$$\left. \frac{dH}{d\mu} \right|_{\mu=0} > 0 \quad \text{as} \quad h_0 \rightarrow +\infty, \quad (6.2.93)$$

hence

$$\text{sign}(a\alpha'(0)) = \text{sign} \left( - \left[ B + 2h_{\text{HB}} \sqrt{\frac{\bar{\lambda} + h_{\text{HB}}}{1 + \bar{\lambda}}} \right] \right), \quad (6.2.94)$$

and

$$\alpha(\mu > 0) > 0, \quad (6.2.95)$$

on both  $U_{0+}(h_0 = H_1)$  and  $U_{0+}(h_0 = H_3)$ .

By (6.2.26), in order for  $h_{\text{HB}} < h_{\text{SN}-}$  or  $h_{\text{HB}} > h_{\text{SN}+}$ , if  $F_0 < F_{\text{HS}}$ , from (6.2.75), we must have  $B > B_{\text{HS}-}$ , whereas if  $F_0 > F_{\text{HS}}$ ,  $h_{\text{HB}} > h_{\text{SN}+}$  for all  $B < -B_{\text{SNA}}$ .

Hence, by (6.2.94) and (6.2.95), for  $\bar{\lambda} > -0.75$ ,  $F_0 < F_{B_0}$  and  $B > B_{0-}$ , we get a subcritical Hopf bifurcation on  $U_{0+}(h_0 = H_1)$  from which a unique limit cycle solution bifurcates in  $U < U_{\text{HB}}$ . Otherwise we get a supercritical Hopf bifurcation on  $U_{0+}(h_0 = H_3)$  from which a unique limit cycle solution bifurcates in  $U > U_{\text{HB}}$ .

Figures 6.32 - 6.34 show typical bifurcation diagrams for varying  $B$ ,  $\bar{\lambda}$  and  $F_0$  and Figure 6.35 shows examples of limit cycle solutions for these parameter sets. Again the limit cycles produced from the Hopf bifurcation on  $U_{0-}$  end in a heteroclinic bifurcation with  $W_{0-}$  and a saddle point at infinity. For the limit cycles produced from the Hopf bifurcation on  $U_{0+}$ , they may either end in a homoclinic bifurcation with  $H_2$  (Figures 6.32 and 6.34b), or a heteroclinic bifurcation (Figure 6.33) depending how close the Hopf bifurcation occurs to the saddle-node bifurcations.

By using the periodic travelling wave solutions for both  $B < -B_{\text{SNA}}$  and  $B > -B_{\text{SNA}}$  as the initial condition in the IVP (6.1.25) and (6.1.27) with periodic boundary conditions, as we did in Section 5.2, we find that solutions from the Hopf bifurcation on  $U_{0+}$  produce steady periodic solutions,

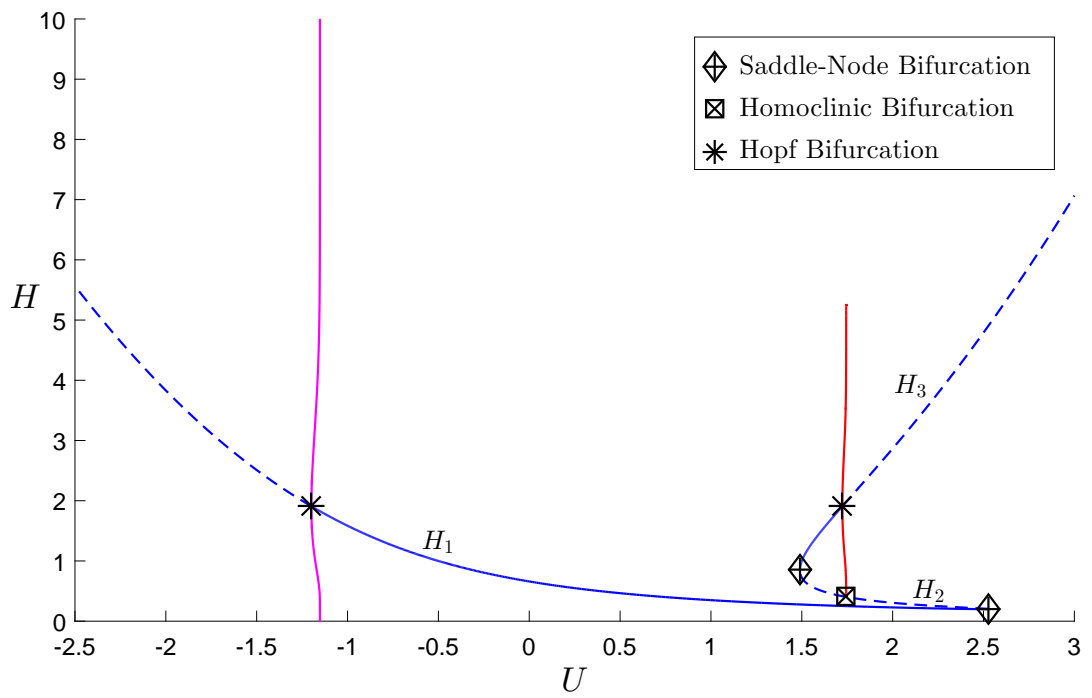


**Figure 6.32.:** The bifurcation diagram for  $B = -0.5$ ,  $\bar{\lambda} = -0.2$ ,  $F_0 = 5$ ,  $R_l = 50$  and  $\rho = 0.1$ .

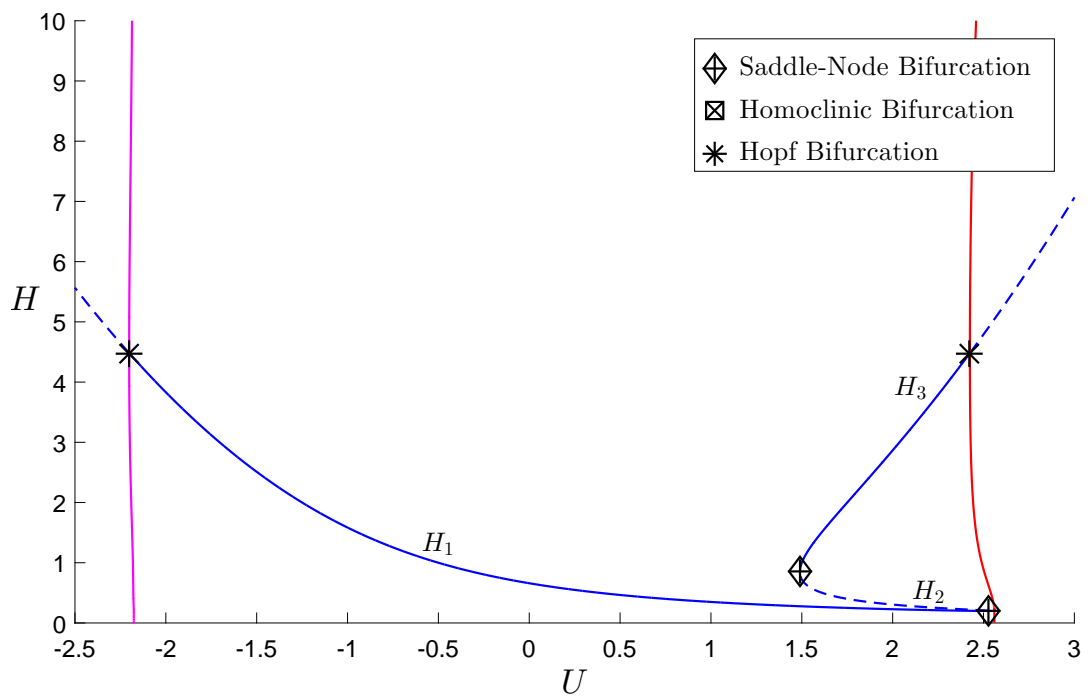
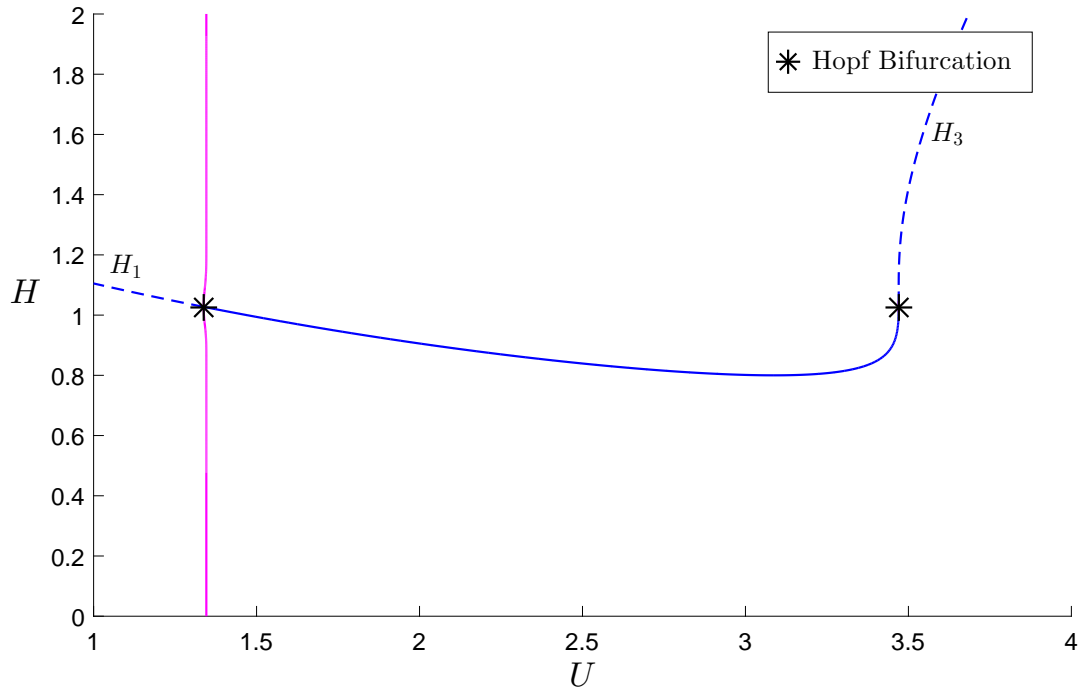
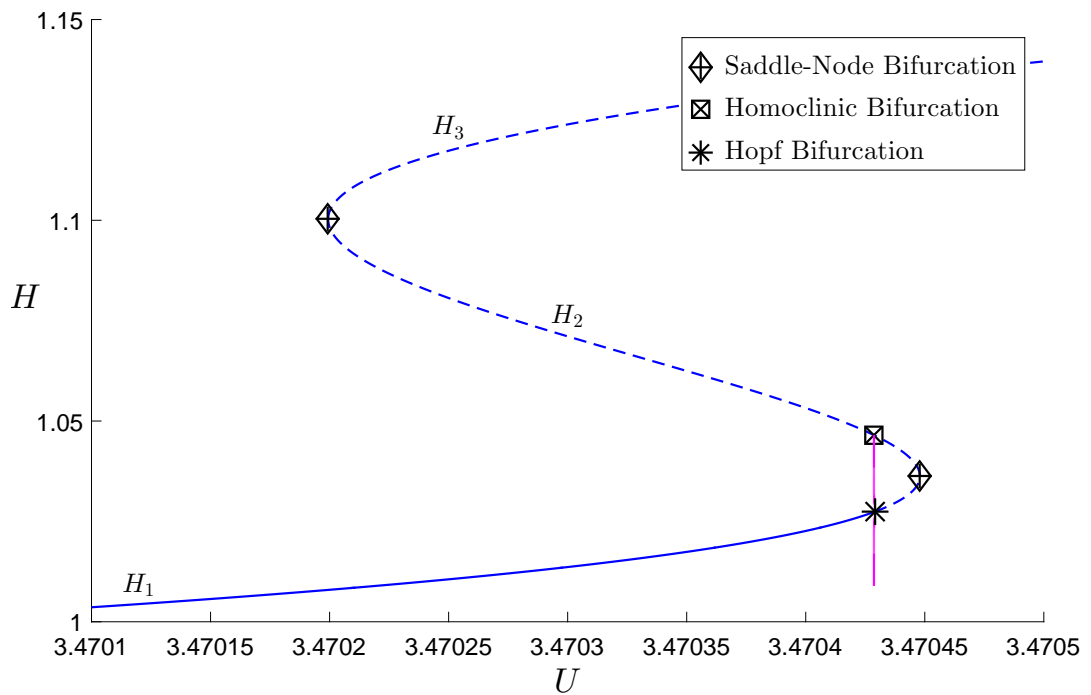


**Figure 6.33.:** The bifurcation diagram for  $B = -0.5$ ,  $\bar{\lambda} = -0.2$ ,  $F_0 = 18$ ,  $R_l = 50$  and  $\rho = 0.1$ .



(a) The complete bifurcation diagram.



(b) The bifurcation diagram zoomed in around the Hopf bifurcation on  $U_{0+}$ .

**Figure 6.34.:** The bifurcation diagram for  $B = -2.47$ ,  $\bar{\lambda} = -0.8$ ,  $F_0 = 0.4$ ,  $R_l = 50$  and  $\rho = 0.1$ .

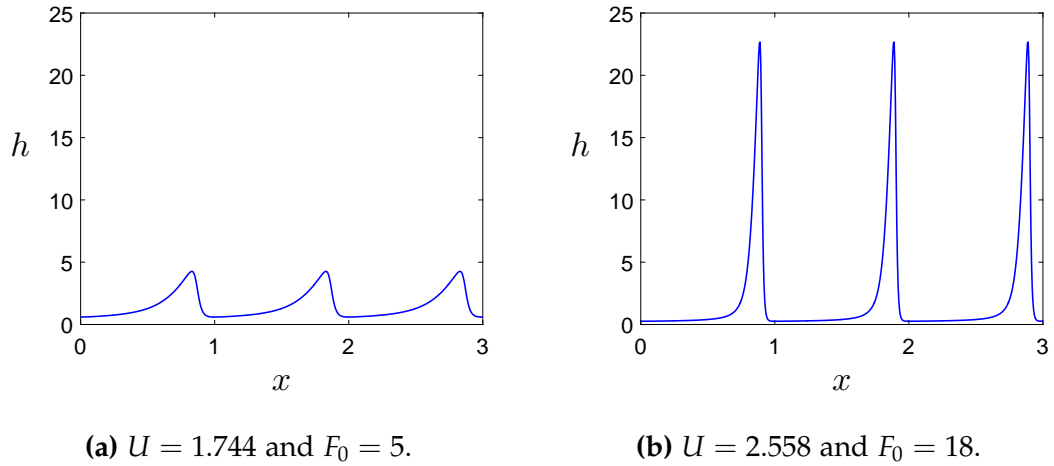


**Figure 6.35.:** The limit cycle solutions for  $B = -0.5$ ,  $\bar{\lambda} = -0.2$ ,  $R_l = 50$ ,  $\rho = 0.1$  and varying  $F_0$ .

while solutions from the Hopf bifurcation on  $U_{0-}$  produce unsteady periodic solutions which do not have a permanent form.

### 6.2.3 Summary of Periodic Travelling Wave Solutions

We have seen that for the  $\bar{\lambda} < -1$  (strongly uphill) and  $B < 0$  case, if  $B > B_{HS-}$  we generate subcritical Hopf bifurcations on  $H_1$  (in Figure 6.4) from which an unstable limit cycle solution bifurcates in  $U > U_{HB}$ . These limit cycle solutions grow in amplitude as  $U$  is increased until they end in a homoclinic bifurcation with  $H_2$ . When these periodic travelling wave solutions are used as the initial condition in the IVP with periodic boundary conditions, we find they produce unsteady periodic solutions which do not have a permanent form.

When we considered the case for  $\bar{\lambda} < -1$  (strongly uphill) and  $B > 0$ , we found the possibility of two Hopf bifurcations occurring concurrently. The first, Hopf<sub>1</sub>, is on  $H_2(U_{0-})$  (in Figure 6.7) and is either a supercritical Hopf bifurcation on  $H_2(U_{0-})$  from which a stable limit cycle solution bifurcates in  $U < U_{HB-}$ , or is a subcritical Hopf bifurcation from which an unstable limit cycle solution bifurcates in  $U > U_{HB-}$ . These limit cycle solutions end

in either a homoclinic bifurcation with  $H_1$ , or a periodic saddle-node bifurcation with an unstable limit cycle resulting from a homoclinic bifurcation on  $H_1$ , depending on the value of  $B$ .

The second Hopf bifurcation, Hopf2, exists for  $B > B_{HS+}$  on  $H_2(U_{0+})$  and is a subcritical Hopf bifurcation from which an unstable limit cycle solution bifurcates in  $U < U_{HB+}$ . These limit cycle solutions grow in amplitude as  $U$  is increased until they end in a homoclinic bifurcation with  $H_1$ . As  $B$  is increased, these two Hopf bifurcations and the corresponding homoclinic bifurcations move closer together until the homoclinic bifurcations points coalesce and the two regions of unstable limit cycle solutions join in a gluing bifurcation, creating one region, starting from and ending in a Hopf bifurcation. This region in  $U$  of unstable limit cycles decreases in size as the two Hopf bifurcations continue to move towards each other as  $B$  is increased until there is a Hopf-Hopf bifurcation for  $B = B_{max}$ . When these periodic travelling wave solutions are used as the initial condition in the IVP with periodic boundary conditions, we find that solutions from Hopf1 produce unsteady periodic solutions which do not have a permanent form, whereas those from Hopf2 produce steady periodic solutions.

For the case of  $-1 < \bar{\lambda} < 0$  (downhill) and  $B > 0$ , if  $B > B_{SNA}$  we find a Hopf bifurcation on  $H_2$  (in Figure 6.21b) which is either subcritical and from which an unstable limit cycle solution bifurcates in  $U > U_{HB}$ , or supercritical and from which a stable limit cycle solution bifurcates in  $U < U_{HB}$ . These limit cycle solutions grow in amplitude as  $U$  is increased until they end in a homoclinic bifurcation with either  $H_1$  or  $H_3$ . When these periodic travelling wave solutions are used as the initial condition in the IVP with periodic boundary conditions, we find they produce unsteady periodic solutions which do not have a permanent form.

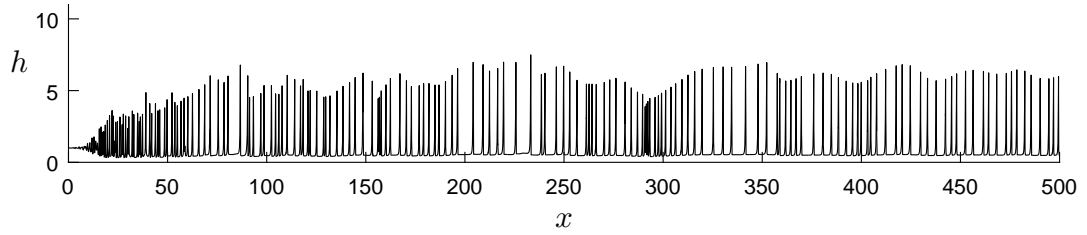
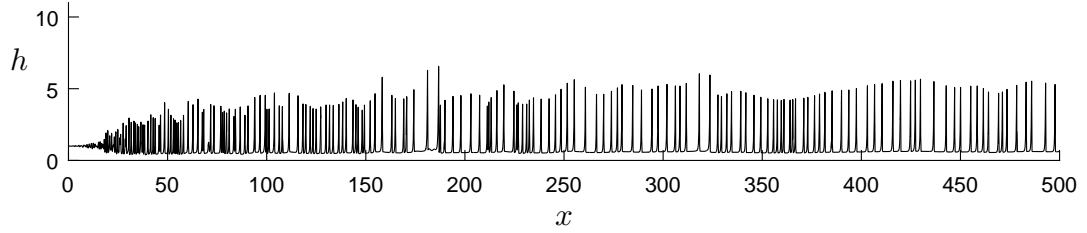
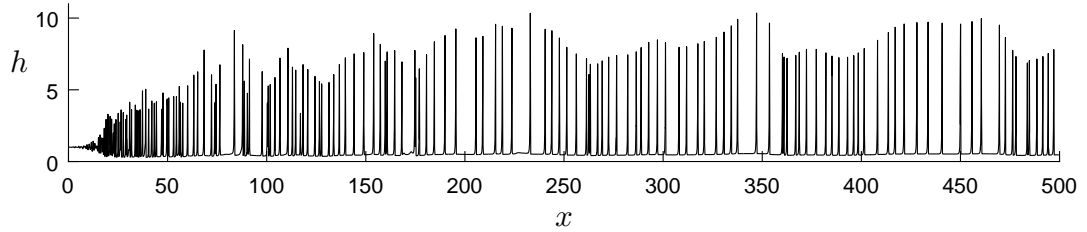
Finally, we consider the case for  $-1 < \bar{\lambda} < 0$  (downhill) and  $B < 0$  and found the possibility of two Hopf bifurcations occurring concurrently. The first is on  $H_1(U_{0-})$  (in Figure 6.25) and is a supercritical Hopf bifurcation from which an unstable limit cycle solution bifurcates in  $U > U_{HB-}$ . The

second Hopf bifurcation is on either  $H_1 (U_{0+})$  or  $H_3$  and is either a supercritical Hopf bifurcation from which a stable limit cycle solution bifurcates in  $U > U_{HB+}$ , or is a subcritical Hopf bifurcation from which an unstable limit cycle solution bifurcates in  $U < U_{HB+}$ . These limit cycle solutions end in either a homoclinic bifurcation with  $H_2$ , or a heteroclinic bifurcation with a saddle point at infinity. When these periodic travelling wave solutions are used as the initial condition in the IVP with periodic boundary conditions, we find that solutions from the Hopf bifurcations on  $U_{0-}$  produce unsteady periodic solutions which do not have a permanent form, whereas those from the Hopf bifurcations on  $U_{0+}$  produce steady periodic solutions.

### 6.3 CONSTANT $\bar{\theta}$ - INITIAL VALUE PROBLEM

Similarly to our work in Section 5.3, we will simulate the flow through the channel using some small random noise at the inlet and investigate for which parameter sets the flow develops into roll waves (as we have taken the thin film limit,  $\epsilon \rightarrow 0$ , we no longer have a top of the the channel at  $1/\epsilon$ , hence are unable to produce slugs). By using periodic boundary conditions and the uniform steady state with a small initial disturbance, Needham et al. [132] showed that for  $\bar{\lambda} > 0$  we are able to find large roll wave solutions in the IVP. We will now extend their work by investigating the  $\bar{\lambda} > 0$  case as well as  $\bar{\lambda} < 0$  in order to compare the effects of changing the angle of the channel to the horizontal case. We find that, as expected, lower values of  $\bar{\lambda}$  and larger values of  $F_0$  increase the size of the solutions, as shown in Figure 6.36. As we found in Section 5.3, the faster moving roll waves catch and absorb the slower ones and begin to grow. However, due to a lack of a top of the channel, they are now unable to maintain their size and revert back to smaller roll waves.

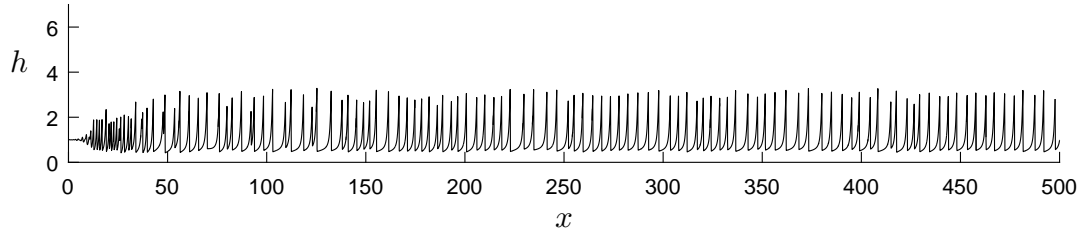
For the  $\bar{\theta} = 0$  case, as studied by Needham et al. [132], a smaller  $\bar{\lambda}$  is equivalent to less damping in the system and so would result in larger roll waves, as we have found. If we consider  $\lambda$  to be constant and consider

(a)  $\bar{\lambda} = 0.6$  and  $F_0 = 10$ .(b)  $\bar{\lambda} = 1$  and  $F_0 = 10$ .(c)  $\bar{\lambda} = 1$  and  $F_0 = 15$ .

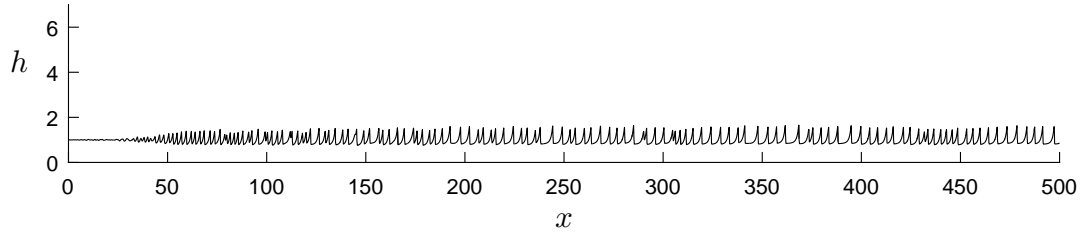
**Figure 6.36.:** The solutions at  $t = 1000$  for  $R_l = 50$  and  $\rho = 0.1$  and varying  $\bar{\lambda} > 0$  and  $F_0$ .

changes to  $\bar{\lambda}$  to be due to changing the value of  $\bar{\theta}$ , then in this example a smaller  $\bar{\lambda}$  is a result of a smaller value of  $\bar{\theta}$ . As a result of this, the liquid velocity will be higher due to the effects of gravity and hence results in larger roll waves.

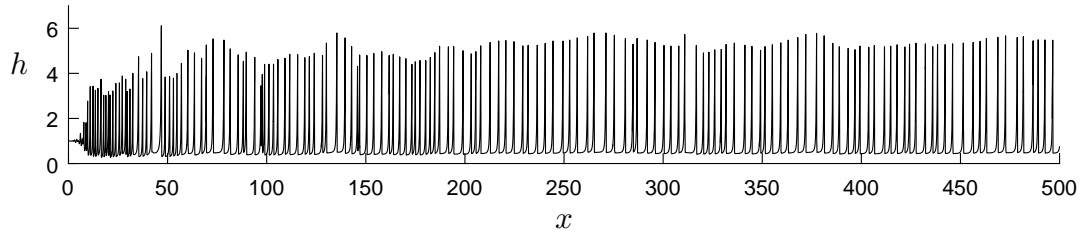
We may now consider the system for  $\bar{\lambda} < 0$ . We find that due to the method used for solving the IVP, when more extreme parameters are used in the system our code is unable to compute the solutions due to localised 'drying' (points for which  $h = 0$ ). For this work we will only include the results from parameters that we were able to compute fully and note that this is an area in which further research is needed.



(a)  $\bar{\lambda} = -0.5$  and  $F_0 = 2$ .



(b)  $\bar{\lambda} = -0.2$  and  $F_0 = 2$ .



(c)  $\bar{\lambda} = -0.2$  and  $F_0 = 5$ .

**Figure 6.37.:** The solutions at  $t = 1000$  for  $R_l = 50$  and  $\rho = 0.1$  and varying  $-1 < \bar{\lambda} < 0$  and  $F_0$ .

For  $-1 < \bar{\lambda} < 0$  (downhill) we again find that lower values of  $\bar{\lambda}$  and larger values of  $F_0$  increase the height of the roll waves, as shown in Figure 6.37. The main difference with the  $\bar{\lambda} > 0$  case is we are now able to find roll wave solutions for lower values of  $F_0$ , as  $F_c \rightarrow 0$  as  $\bar{\lambda} \rightarrow -1$ . By considering values of  $-1 < \bar{\lambda} < 0$  and  $\bar{\lambda} \geq 0$ , we find the effects of varying the parameters to be continuous in the parameter space  $\bar{\lambda} > -1$ , as shown in Figure 6.38.

We have calculated the 'Peak Height' parameter to be the average peak height of the roll waves in the last 20% of the channel. We find that for  $\bar{\lambda} < -0.6$  we are unable to compute solutions due to finding localised 'drying', similarly for larger values of  $F_0$  for  $\bar{\lambda} < 0$ , hence the incomplete left hand

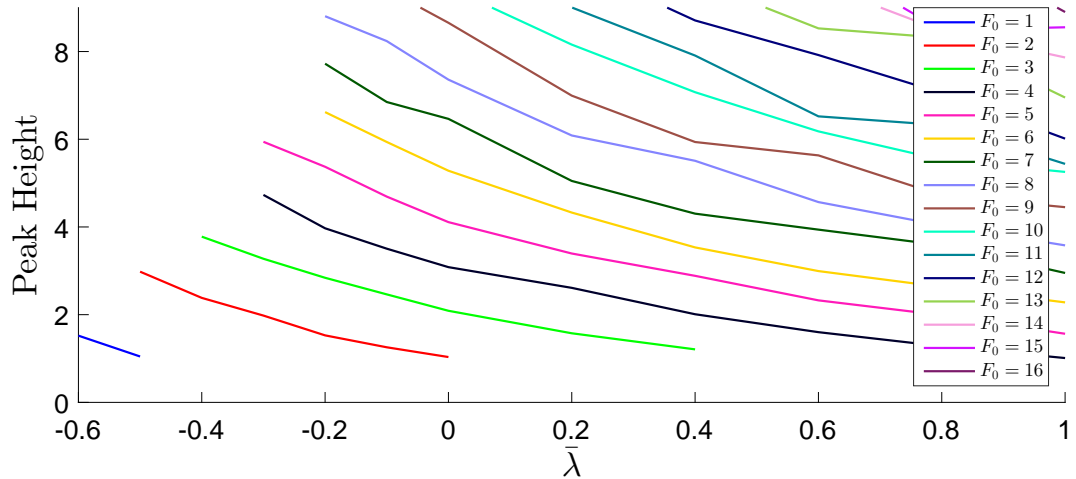


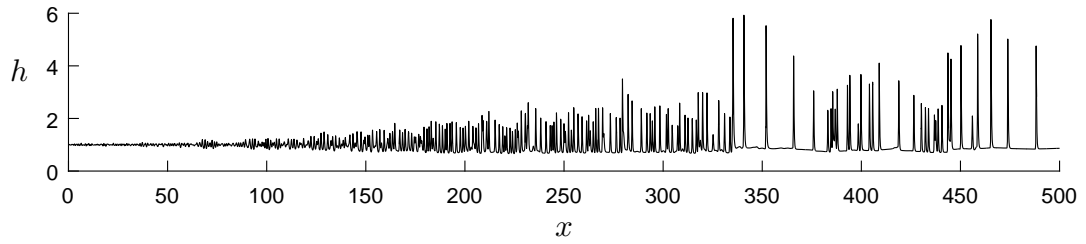
**Figure 6.38.:** The average peak height against  $\bar{\lambda} > -1$  for  $R_l = 50$  and  $\rho = 0.1$  and varying  $F_0$ .

side in Figure 6.38. However, we can see a clear correlation between  $\bar{\lambda}$ ,  $F_0$  and peak height and would expect this to continue for these parameter sets.

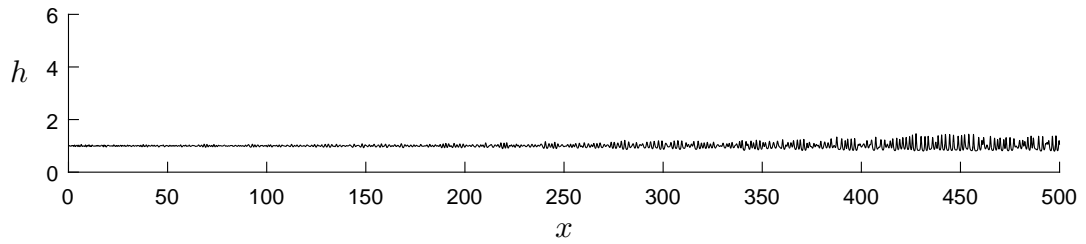
For  $\bar{\lambda} < -1$  (strongly uphill) we again find that larger values of  $F_0$  increase the size of the solutions, however lower values of  $\bar{\lambda}$  decrease the size of the solutions, as shown in Figure 6.39. This is due to the waves now propagating backwards relative to the flow, as we saw earlier, therefore a larger value of  $\bar{\lambda}$  (and so larger value of  $\bar{\theta}$ ) results in a more negative propagation speed and hence larger solutions. Figure 6.40 shows how the peak height varies with  $\bar{\lambda}$  and  $F_0$ , where we have been unable to compute solutions for  $\bar{\lambda} > -5$ .

From Figures 6.39b and 6.39c we can see that for  $\bar{\lambda} < -1$  we are able to find roll waves that are significantly larger than the average roll wave in the channel. As noted in Subsection 6.2.1.2, the roll waves are travelling backwards relative to the flow and their structure is opposite in  $x$  to those we have previously seen, i.e. they now have a sharp back and sloping front. As a result of this the way these larger roll waves form is also opposite to how we saw them form in Section 5.3.

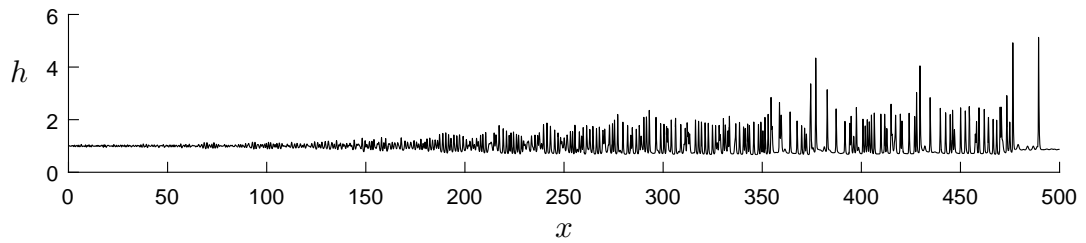
As in our work in Section 5.3, the larger roll waves begin as average roll waves, however they now propagate slightly slower than the roll waves



(a)  $\bar{\lambda} = -6$  and  $F_0 = 15$ .



(b)  $\bar{\lambda} = -7$  and  $F_0 = 15$ .



(c)  $\bar{\lambda} = -7$  and  $F_0 = 18$ .

**Figure 6.39.:** The solutions at  $t = 1000$  for  $R_l = 50$  and  $\rho = 0.1$  and varying  $\bar{\lambda} < -1$  and  $F_0$ .

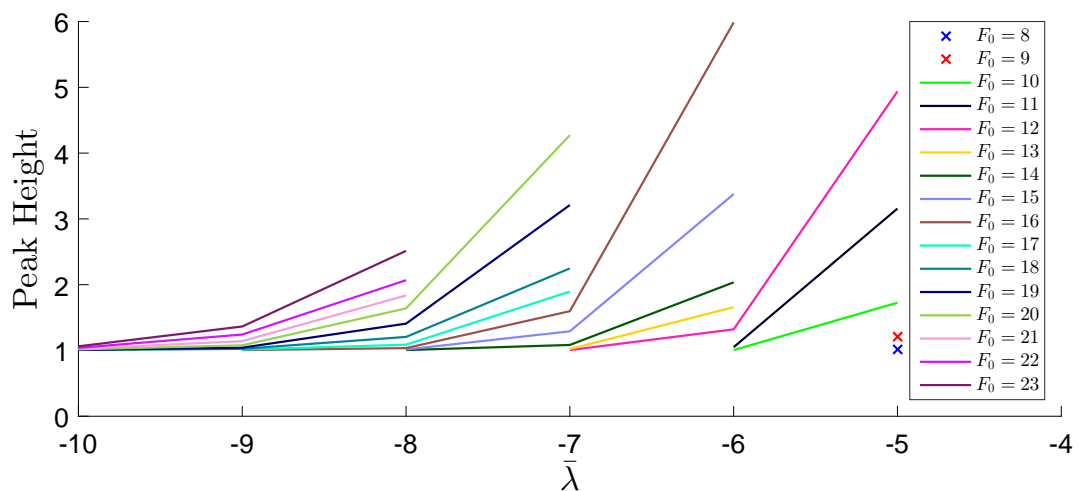


**Figure 6.40.:** The average peak height against  $\bar{\lambda} < -1$  for  $R_l = 50$  and  $\rho = 0.1$  and varying  $F_0$ .

around them. When a roll wave behind catches up to them they absorb it which increases their size. This process is then repeated by the larger roll waves, growing in size as they move down the channel as more roll waves catch up with them and are absorbed. Hence, in general, the larger roll waves further down the channel will be bigger than those further up the channel. This process is shown in Figure 6.42 where the roll wave of interest is shown in red. We can see in Figures 6.42a and 6.42b a roll wave catching up with the roll wave in front of it. Figure 6.42c then shows it absorbing the faster moving roll wave, after which, as shown in Figure 6.42d, it has formed into a larger roll wave. Also in Figure 6.42d we can see a small roll wave which is forming in front of the larger roll wave, which is highlighted in green. This is the discharge from the faster moving roll wave created as it is absorbed by the larger roll wave.

## 6.4 VARYING $\bar{\theta}$ - INITIAL VALUE PROBLEM

In order to solve the IVP for a non-constant  $\bar{\theta}$  we must use (6.1.26) and define a function for  $\bar{\theta}$ . We will begin by letting

$$\bar{\theta} = K(20 - x) \exp\left(-\frac{(20 - x)^2}{2}\right), \quad (6.4.1)$$

and use the inlet condition

$$h_1 = 1, \quad v_1 = 1, \quad (6.4.2)$$

and initial condition

$$h(t = 0) = 1, \quad v(t = 0) = 1. \quad (6.4.3)$$

This will allow us to see the effects of a small 'bump' in the channel (at  $x = 20$ ) on the uniform flow. Figure 6.43 shows the solution at  $t = 1000$  for  $F_0 = 10$ ,  $\lambda = 1$ ,  $R_l = 50$  and  $\rho = 0.1$ . We can see that the bump has caused a small disturbance to the flow which then grows into

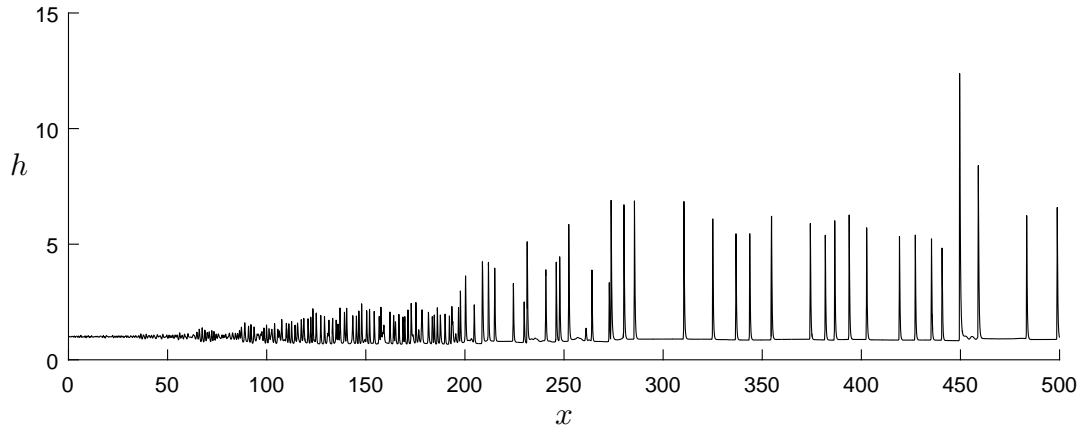
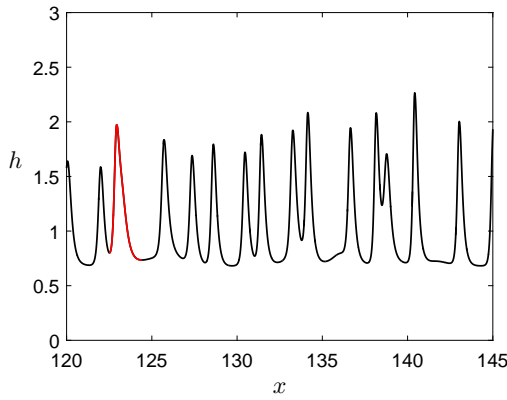
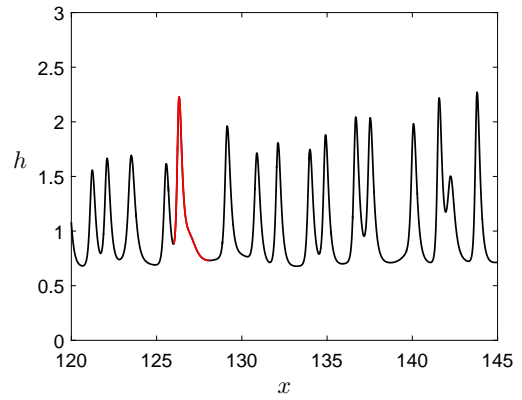


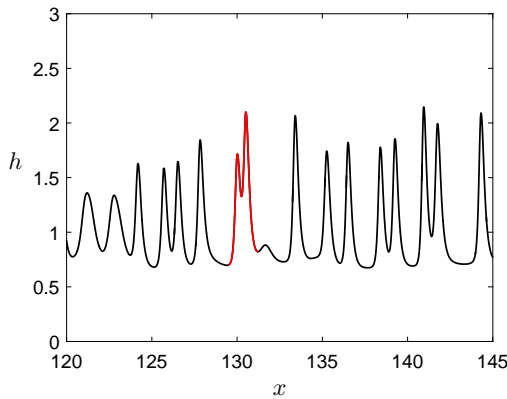
**Figure 6.41.:** The solution at  $t = 1000$  for  $\bar{\lambda} = -5$ ,  $R_l = 50$ ,  $\rho = 0.1$  and  $F_0 = 12$ .



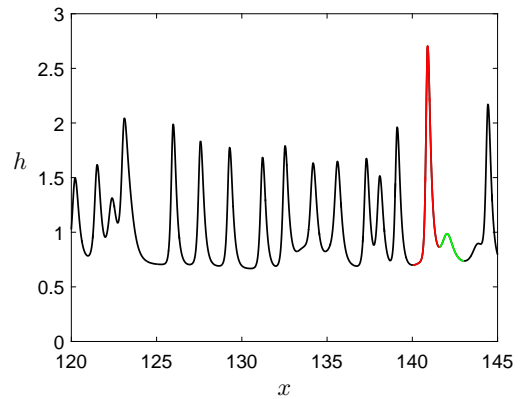
**(a)** The solution at  $t = 701$ .



**(b)** The solution at  $t = 703$ .



**(c)** The solution at  $t = 710$ .



**(d)** The solution at  $t = 723$ .

**Figure 6.42.:** The solutions as a larger roll wave is formed for  $\bar{\lambda} = -5$ ,  $R_l = 50$ ,  $\rho = 0.1$  and  $F_0 = 12$ .

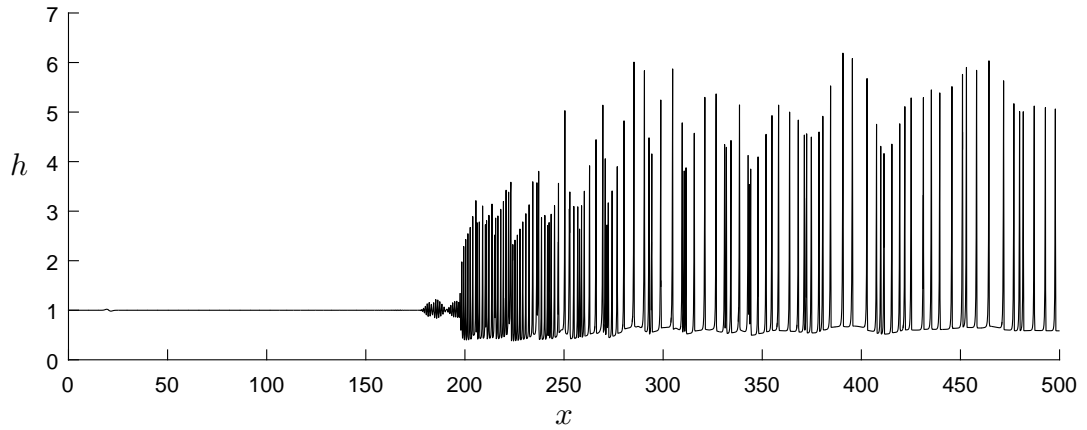


**Figure 6.43.:** The solution at  $t = 1000$  for a 'bump' in the channel at  $x = 20$  for  $F_0 = 10$ ,  $\lambda = 1$ ,  $R_l = 50$  and  $\rho = 0.1$ .

roll waves, similarly to the effects we found when applying a small random noise at the inlet. As the flow has not formed roll waves until it is further down the channel than when we apply a small random noise at the inlet, we will continue to use the small random noise in our simulations in order to minimise the time our simulations take to compute.

We will now investigate the effects of an undulating topography on the flow. In order to do this we will let

$$\bar{\theta} = K \frac{F_0^2}{1 - \rho} \sin \left( \frac{2\pi x}{CL} a + b\pi \right), \quad (6.4.4)$$

where  $a$  is the number of undulations,  $b$  can be set to choose whether we start by going uphill or downhill and  $K$  controls the maximum size of  $\bar{\theta}$ .

By varying the parameters we find, as we found previously, by increasing  $F_0$ , decreasing  $\lambda$  or making  $\bar{\theta}$  more negative we produce larger roll waves. When investigating  $\bar{\theta} > 0$  for smaller values of  $\bar{\theta}$  we find that increasing  $\bar{\theta}$  decreases the size of the roll waves. However, when  $\bar{\theta}$  is increased enough we begin to see the roll waves absorbing each other, as in the previous section for  $\bar{\lambda} < -1$  (strongly uphill), and increasing  $\bar{\theta}$  increases the size of these roll waves until we get localised 'drying' and our code is unable to continue to compute solutions.

Figure 6.44 shows the effects of varying  $a$  and  $b$  for  $F_0 = 10$ ,  $K = 0.4$ ,  $\lambda = 1$ ,  $R_l = 50$  and  $\rho = 0.1$ . We can see that as the channel goes uphill ( $\bar{\theta} > 0$ ) the roll waves decrease in size to a point where the flow has become stratified flow with a disturbance and as the flow goes downhill ( $\bar{\theta} < 0$ ) the roll waves significantly increase in size. We may also observe that the liquid builds up in the uphill regions, as shown in Figure 6.44c for  $0 < x < 150$  for which the liquid is highest for  $60 < x < 65$  which corresponds to the largest value of  $\bar{\theta}$ . As a result of this we can see in Figure 6.44 that we produce larger roll waves in a downhill region when it comes after an uphill region.

In order to understand why the liquid builds up as  $\bar{\theta}$  is increased, we must consider the steady state solution of our system of equations. By setting  $h_t = 0$  in (6.1.25) we find we must have

$$v = \frac{1}{h}, \quad (6.4.5)$$

which, along with  $v_t = 0$ , reduces (6.1.26) to

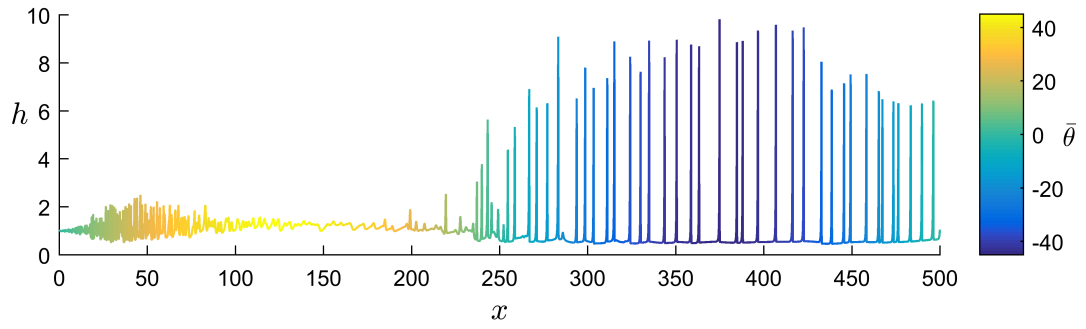
$$h_{xx} = R_l \left[ \left( \frac{1}{h} - \frac{1-\rho}{F_0^2} h^2 \right) h_x - \frac{1-\rho}{F_0^2} \bar{\theta} h^2 - \frac{1}{h} + \frac{h+\lambda}{1+\lambda} h + \frac{h_x^2}{R_l h} \right], \quad (6.4.6)$$

subject to

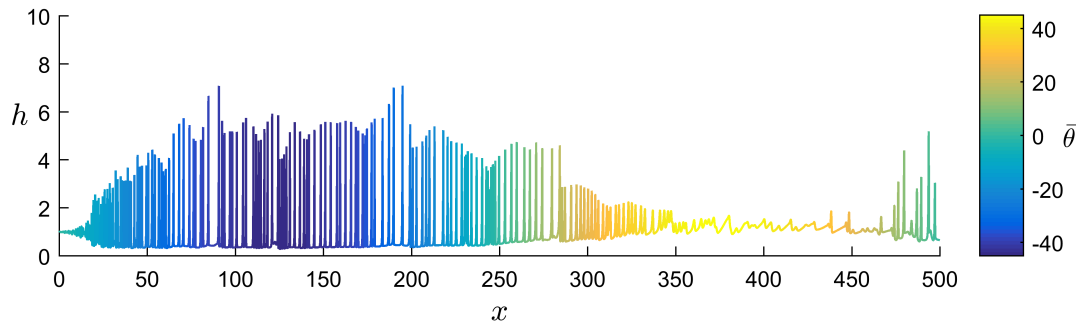
$$h(x=0) = h(x=CL) = 0, \quad \bar{\theta}(x=0) = \bar{\theta}(x=CL) = 0. \quad (6.4.7)$$

By solving (6.4.6) numerically in MATLAB using routine `bvp5c` we are able to find the steady state solution for a given set of parameters. Figure 6.45 shows the steady state solution for the parameters used in Figure 6.44c. We can see a clear positive correlation between  $h$  and  $\bar{\theta}$  for which, as  $v = 1/h$ , corresponds to the liquid velocity being lower the larger  $\bar{\theta}$  is, as we would expect. Hence, for uphill regions of the channel we get a build up of liquid, as seen in Figure 6.44c, which then results in there being more liquid in the following downhill regions and hence larger roll waves.

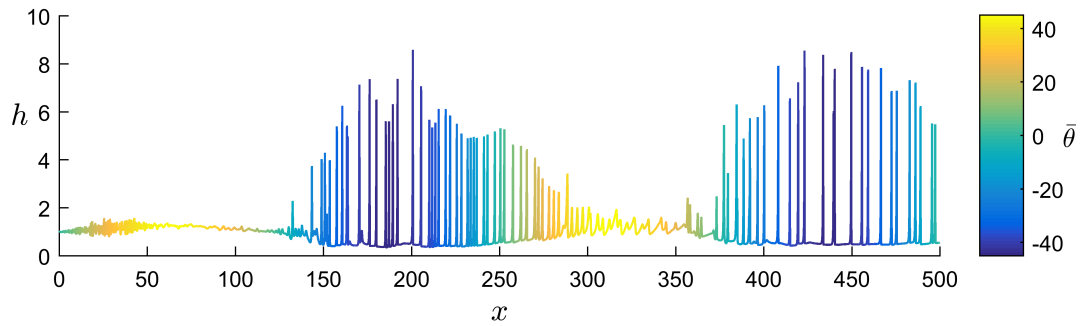
6.4 VARYING  $\bar{\theta}$  - INITIAL VALUE PROBLEM



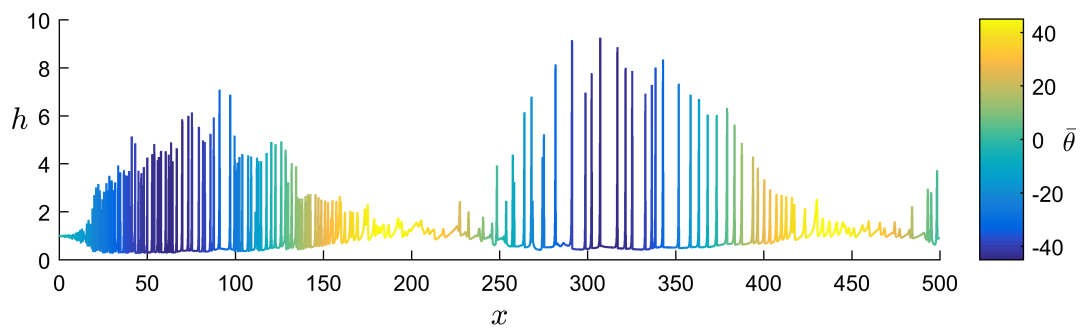
(a)  $a = 1$  and  $b = 0$ .



(b)  $a = 1$  and  $b = 1$ .



(c)  $a = 2$  and  $b = 0$ .



(d)  $a = 2$  and  $b = 1$ .

**Figure 6.44.:** The effects of varying  $a$  and  $b$  for  $F_0 = 10$ ,  $K = 0.4$ ,  $\lambda = 1$ ,  $R_l = 50$  and  $\rho = 0.1$ .

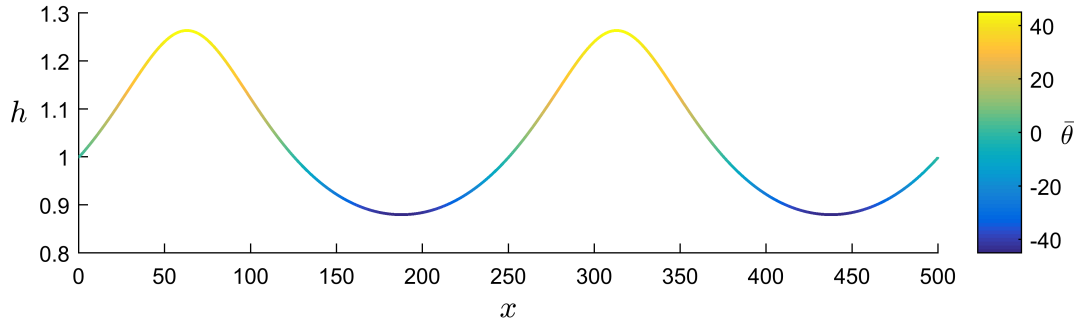


**Figure 6.45.:** The steady state solution for  $F_0 = 10$ ,  $K = 0.4$ ,  $a = 2$ ,  $b = 1$ ,  $\lambda = 1$ ,  $R_l = 50$  and  $\rho = 0.1$ .

We will now consider a channel which goes either uphill or downhill before levelling into a region where  $\bar{\theta} = 0$ , i.e. we let

$$\bar{\theta} = K \frac{F_0^2}{1 - \rho} \sin \left( 2\pi \min \left( \frac{x}{CL}, \frac{1}{2} \right) a + b\pi \right). \quad (6.4.8)$$

Figure 6.46 shows the effect of varying  $b$  for  $F_0 = 10$ ,  $K = 0.4$ ,  $\lambda = 1$ ,  $R_l = 50$  and  $\rho = 0.1$ . We can see that for  $b = 0$ , where we have an uphill region before the flat region, we have produced larger roll waves with greater separation.

## 6.5 CONCLUSION

By re-deriving our governing equations in a curvilinear coordinate system and assuming the angle of the channel bottom is  $\theta = O(c_l)$  and  $\theta' \ll 1/c_l$ , we found the governing equations were identical to those derived in Chapter 2 except for one extra term on the right hand side. We then considered the limit as  $\epsilon \rightarrow 0$  for constant  $\theta$  and by letting

$$\bar{\lambda} = \frac{F_0^2 + (1 - \rho)\bar{\theta}}{F_0^2 - (1 - \rho)\bar{\theta}\lambda} \lambda, \quad (6.5.1)$$

we were able to write the governing equations as found by Needham et al. [132], except with  $\lambda$  replaced by  $\bar{\lambda}$ .

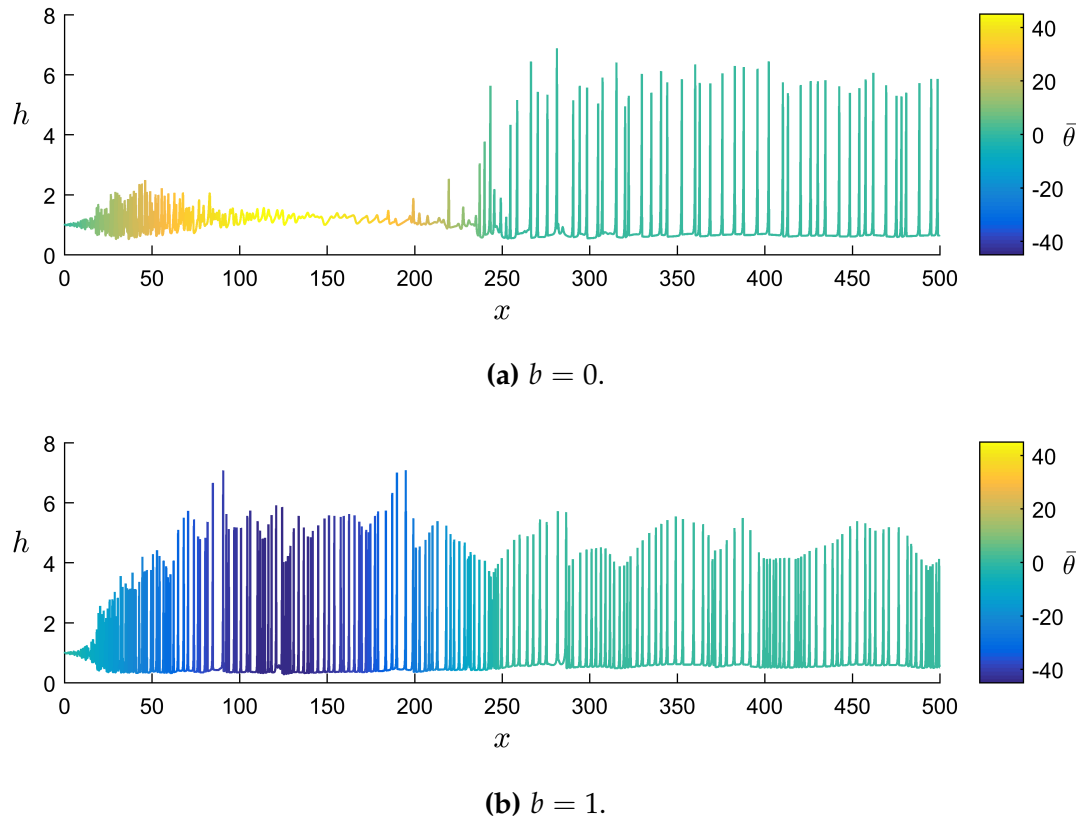


**Figure 6.46.:** The effect of varying  $b$  with a flat channel end for  $F_0 = 10$ ,  
 $K = 0.4$ ,  $\lambda = 1$ ,  $R_l = 50$  and  $\rho = 0.1$ .

We then investigated the existence of periodic travelling wave solutions and found that we may either get one, two or three equilibrium points which result in up to two Hopf bifurcations for both  $B > 0$  and  $B < 0$ . By investigating these Hopf Bifurcations and their resulting limit cycle solutions we found we have the possibility of:

- homoclinic bifurcations,
- heteroclinic bifurcations with a saddle point at infinity,
- saddle-node bifurcations,
- Hopf-Hopf bifurcations,
- gluing bifurcations, where two homoclinic bifurcations coalesce and

- periodic saddle-node bifurcations between stable and unstable limit cycles.

When these solutions were used as initial conditions in the IVP with periodic boundary conditions, we were able to find steady periodic solutions for  $\bar{\lambda} < -1$  and  $B > 0$ , for which the solutions travel backwards relative to the flow, and for  $-1 < \bar{\lambda} < 0$  and  $B < 0$ .

Similarly to our work in Section 5.3, we simulated the flow through the channel using some small random noise at the inlet and investigated the effects of varying the parameters. We found that for  $\bar{\lambda} > -1$ , increasing  $F_0$  or decreasing  $\bar{\lambda}$  increased the size of the roll waves and for  $-1 < \bar{\lambda} < 0$  (downhill) we were able to produce roll waves for smaller values of  $F_0$  than we were able to in the  $\bar{\lambda} > 0$  case. For  $\bar{\lambda} < -1$  (strongly uphill) we again found that larger values of  $F_0$  increased the size of the roll waves. However, due to the waves now propagating backwards relative to the flow, a larger value of  $\bar{\lambda}$  (hence greater incline of the channel) resulted in a more negative propagation speed and produced larger roll waves. In this case we were able to find roll waves that had grown significantly larger than the average roll wave in the channel due to their absorption of smaller roll waves. This process occurred in a similar process as we saw in Section 5.3, however it is the larger roll waves which propagate more slowly and hence the smaller roll waves catch them up and are absorbed.

Finally, we solved the IVP for a varying topography. We first considered a flat channel with a small 'bump' in it with inlet conditions  $h_1 = 1$  and  $v_1 = 1$  which created a small disturbance to the uniform flow. This disturbance then slowly grew into roll waves, similarly to the effects of using a small random noise at the inlet. We then considered the effects of an undulating topography and found the uphill sections had a dampening effect on the roll waves, whereas the downhill sections increased the size of the roll waves. By investigating the steady state solution of the system we found that we produced a larger layer of liquid as we increased the angle of the channel. As a result of this, when we investigated the effects of having either a downhill or uphill section of channel before a flat section, we produced

larger roll waves in the flat section when it followed an uphill section. This is of particular importance as the subsea natural gas pipelines must travel uphill as they leave the sea before travelling across land which may result in larger roll waves, and potentially slugs, forming.

---

## CONCLUSION

---

### 7.1 THESIS RESULTS

In this thesis, we have derived the governing equations of motion for two layer hydraulic flow through a semi-infinite channel. This was done using conservation of mass and conservation of momentum in both the gas and liquid phases and simplified using the long wavelength assumption, depth-averaged velocity and Chézy coefficients for the wall and interfacial shear. These equations were then combined and non-dimensionalised leaving a system of two equations governing the flow, which consisted of two variables that were functions of  $x$ , the horizontal distance from the inlet, and  $t$ , time, and seven parameters. We then discussed the typical values for the dimensional parameters in subsea natural gas pipelines and provided the corresponding values of our non-dimensional parameters.

In Chapter 3, we investigated how small-amplitude disturbances affected the uniform flow. Through this we determined a stability criterion,  $F_c$ , on the Froude number for which small-amplitude disturbances to the uniform flow would decay if  $F_0 < F_c$  and grow if  $F_0 > F_c$ . We also found a non-hyperbolic condition,  $F_{NH}$ , for which when  $F_0 > F_{NH}$  the IVP is ill-posed due to a short wavelength instability, hence the long wavelength assumption is invalid and suggests the flow regime would change to bubble flow. We then considered the solution for a single mode of spatial wave number in order

to investigate how fast different wavelengths grow. From this we found the neutral curve  $F_n$ , for which small disturbances will neither grow nor decay and a maximum growth rate curve  $F_m$ .

Once these disturbances begin to grow, they become dominated by non-linear effects and we expected them to form into roll waves, hence in Chapter 4 we investigated the existence of periodic travelling wave solutions. In order to do this we introduced the travelling co-ordinate  $z = x - Ut$ , where  $U$  is the wave propagation speed, which simplified our governing equations into one equation for one variable,  $h(z)$ , given by (4.0.7). We considered the equilibrium points of this equation and found two equilibrium points that vanish in the previously studied limit,  $\epsilon \rightarrow 0$ , ( $H_-$  and  $H_+$ ) which come into existence near the top of the channel for  $\delta U \approx 1$ . Through asymptotic analysis, we deduced that  $H_-$  is a saddle and  $H_+$  is a node or spiral where a Hopf bifurcation may occur.

We used MATLAB routines `ode45` and `bvp5c` to solve our equations numerically and found high amplitude periodic solutions. We investigated the phase portraits of these solutions for two sets of parameters while varying  $U$ . In one we found one Hopf bifurcation, two homoclinic bifurcations and a periodic saddle-node bifurcation which resulted in two separate regions in which periodic solutions can exist and which contained both stable and unstable limit cycle solutions which resulted in a stable-unstable limit cycle annihilation. In the other we found two Hopf bifurcations and five homoclinic bifurcations which resulted in four separate regions in which periodic solutions can exist. Although we were unable to establish a complete understanding of the phase portrait, our investigation of periodic travelling wave solutions gave us some insight into how the parameters affect the system and showed that slugs can exist.

In Chapter 5, we used a finite-difference method derived by Kurganov and Tadmor [114] which we combined with a second-order Runge-Kutta method to solve our governing equations as an initial value problem. We set the initial condition to be the uniform flow and used some small amplitude

random noise at the inlet and an outlet in order to simulate flow through a channel. We first used one of the parameter sets we had used in Section 4.3 in the initial value problem, which resulted in the channel being predominantly full of roll waves with a few slugs. By following these slugs as they travelled through the channel, we saw that they began as roll waves which propagated faster than the roll waves in front of them and as they caught the roll wave in front they absorbed it, increasing in size to form a slug. They continued this process as they travelled down the channel, increasing in size every time they absorbed a roll wave.

When we varied the parameters slightly we found that the data sets with the larger values of  $\delta$  produced the most slugs, whereas those with  $\delta \approx 0.5$  produced the widest slugs. This was because in the solutions which only produced a few slugs there were lots of roll waves for them to absorb as they travelled down the channel, so they were constantly growing in size. By varying  $\delta$  and  $\lambda$  we determined that  $\delta \approx 0.5$  is a critical limit which separated data sets which may lead to slugs and those which will not. It is at this ratio of liquid to homogeneous velocity that the liquid momentum is able to overcome the interfacial shear forces in order to grow into slugs.

Finally, in Chapter 6, we considered the effects of bottom topography in the thin layer limit. We first investigated the existence of periodic travelling wave solutions for constant channel inclination,  $\theta$ , and found that Hopf bifurcations can exist for  $B < 0$  and  $B > 0$ , whereas for the horizontal case it had only been possible for  $B < 0$ . By investigating these Hopf Bifurcations and their resulting limit cycle solutions we found, unlike in Chapter 4, that there is also the possibility of heteroclinic bifurcations with a saddle point at infinity and gluing bifurcations, where two homoclinic bifurcations coalesce. By solving this system as an initial value problem, we found that larger roll waves are generated in downhill channels than we had in the horizontal case. However, although the roll waves are smaller, it is in the strongly uphill case that we found roll waves absorbing smaller roll waves resulting in them growing in size, as occurs for horizontal channels. In this case, the

roll waves propagated backwards relative to the flow and the larger roll waves were the ones propagating slowest, resulting in them being caught up by smaller and faster roll waves which were then absorbed.

We then solved the governing equations as an initial value problem for an undulating topography. We found that the downhill sections resulted in larger roll waves and the uphill sections had a dampening effect on the roll waves. However, when we considered the steady state solution of the system, we found that the height of the layer of liquid increases with the angle of the channel. As a result of this, when we investigated the effects of having either a downhill or uphill section of channel before a flat section, larger roll waves were produced in the flat section when it followed an uphill section. This is of particular importance as subsea natural gas pipelines must travel uphill as they leave the sea before travelling across land which may result in larger roll waves and, potentially, slug formation.

## 7.2 FUTURE WORK

In Chapter 4, although we completed an in-depth analysis of the phase plane for several parameter sets, due to the number of parameters and the extremely complicated nature of the phase planes, an exhaustive catalogue of possibilities was not feasible. Part of the difficulty in deciphering the phase portrait is because of the number of separate regions, split by pairs of homoclinic bifurcations, in which the solutions exist. However, when we investigated the stability of these solutions in the initial value problem, we found that only the solutions from Region A (in Figures 5.4 and 5.5) are stable. Hence, concentrating on this region and tracking the bifurcations encompassing it would provide a more detailed insight into the solutions generated in the initial value problem.

In our simulations in Chapter 5 we found that faster propagating roll waves catch up with slower ones and may or may not absorb them. In order to determine conditions under which two roll waves will attract and form

one larger roll wave, or repel settling into their equilibrium roll wave state, interaction experiments could be performed. This could be done by using a short channel with periodic boundary conditions and two different roll waves as initial conditions. By varying the roll waves used, the parameters and the initial separation between the roll waves the conditions determining attraction or repulsion may be found.

It may be possible to analytically predict slug separation distances in channels long enough for the system to have settled into a solution dominated by a series of large slugs. By repeating the computations for a set of parameters a large number of times, we could then compute the distance,  $l$ , between slugs. By considering a histogram of the number of slugs separated by some distance,  $\Delta l$ , divided by the total number of slugs (the probability that the slugs are separated by a certain  $\Delta l$ ) we may find well-defined peaks. If this is the case, we must have self-organisation and it may be possible to develop an analytical model which predicts the slug separation and frequency. However, due to the length of channel needed combined with the need to repeat the simulations a large number of times, doing this will be very computationally expensive.

Due to the way the equations have been derived, it is not possible for the liquid to touch the top of the channel in our simulations as this results in denominators in our equations becoming zero. By re-writing our code and using a piecewise full-pipe solution as the initial condition, we would be able to investigate the effects of a slug touching the channel top. However, in order to simulate the generation of this type of slug, we would need to re-derive our governing equations taking into account the current behaviour as  $h \rightarrow 1/\epsilon$  (channel filling).

Similarly, in Chapter 6, we were unable to simulate flows which experienced localised drying due to  $h = 0$  causing denominators in our equations to become zero. There are several proposed methods for dealing with this

in the literature, such as that by Kurganov and Petrova [113]. This method proposes using

$$v = \frac{\sqrt{2}h(hv)}{\sqrt{h^4 + \max(h^4, \epsilon)}}, \quad (7.2.1)$$

where  $\epsilon$  is a small a-priori chosen positive number (for which they used  $\epsilon = (\Delta x)^4$ ). Although we tried this method with numerous values for  $\epsilon$ , it only slowed the 'drying'. A more thorough examination of the literature in this area is needed in order to find an appropriate numerical method.

In our work on the effects of bottom topography, we only investigated the case of a thin film layer ( $\epsilon \ll 1$ ). We have derived the governing equations for the non-thin film case, given by (6.1.20) and (6.1.24), which shows we need only add one extra term to our code from Chapter 5 in order to solve this case as an initial value problem. When we encountered 'drying' in the thin-film case, the peaks of the waves began to grow very large. Hence, we may find that the effects of a channel top bounding the maximum peak height may force liquid down and allow simulations for a wider range of parameters.

Finally, as our work is based on channel flow, a more accurate model for subsea natural gas pipelines could be developed by using a cylindrical pipe. In order to simplify the governing equations, they could be cross-sectionally averaged and width-averaged to give a one-dimensional model. Then all the topics in this thesis would need to be re-visited.

# A

---

## APPENDIX

---

### A.1 CHANNEL SIMULATIONS

The figures corresponding to the Data Sets given in Section 5.3 in Tables 5.4 - 5.6 on Pages 133 - 134. Figure A.1 show the plots of the solutions at  $t = 3000$  for  $CL = 1000$  and Figure A.2 shows the plots of width and peak height against location in the channel.

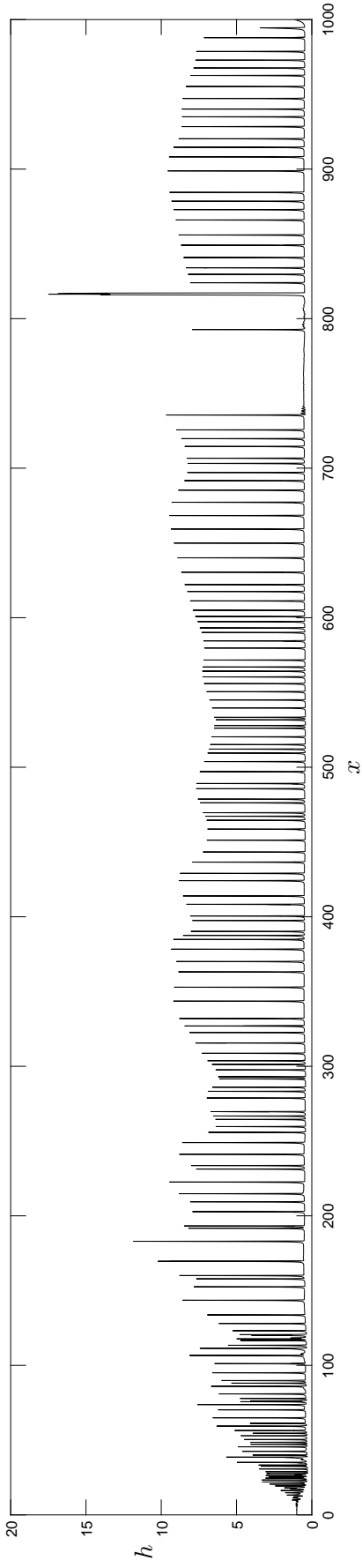


Figure A.1a.: The solution of Data Set 1 at  $t = 3000$ .

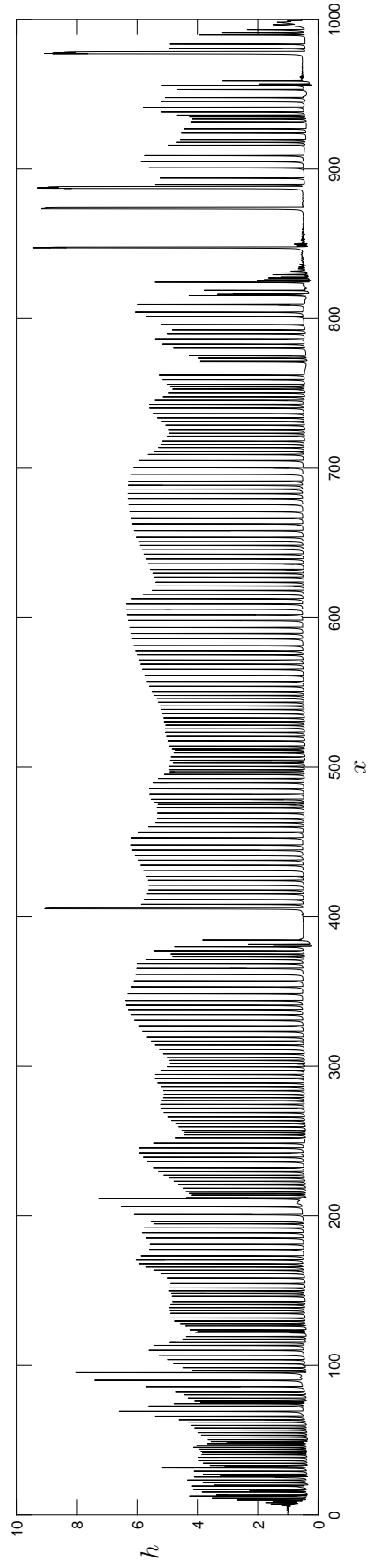


Figure A.1b.: The solution of Data Set 2 at  $t = 3000$ .

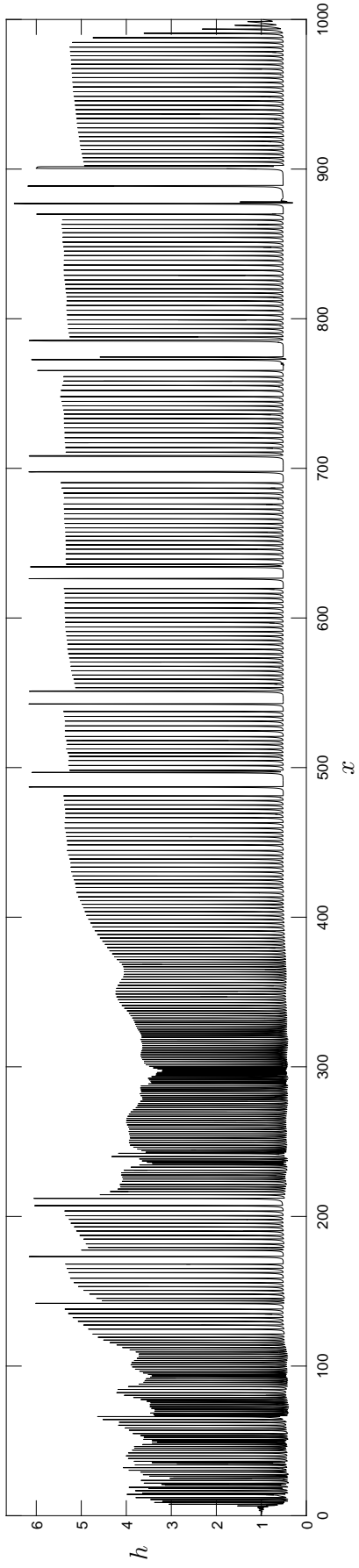


Figure A.1c.: The solution of Data Set 3 at  $t = 3000$ .

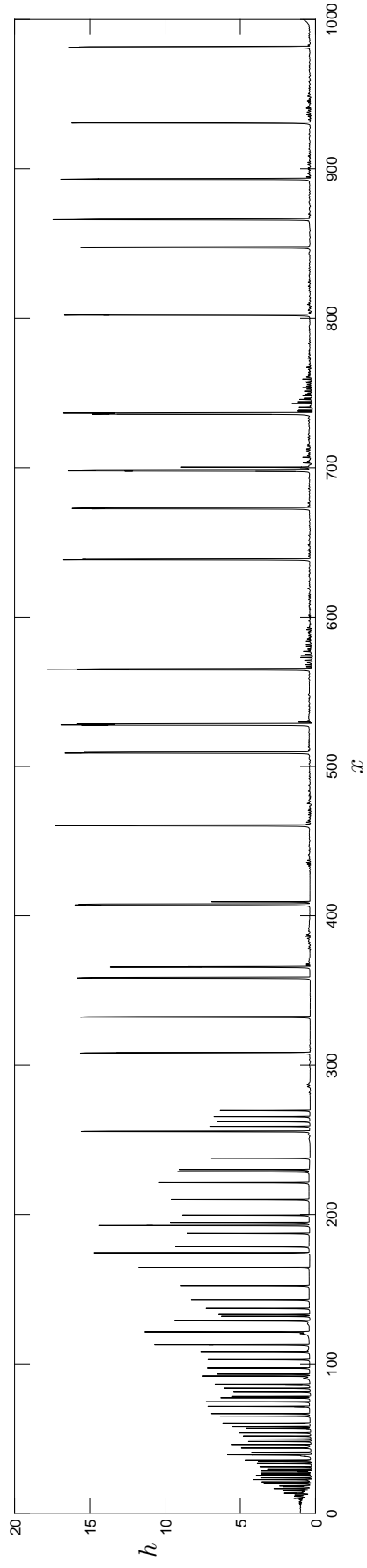


Figure A.1d.: The solution of Data Set 4 at  $t = 3000$ .

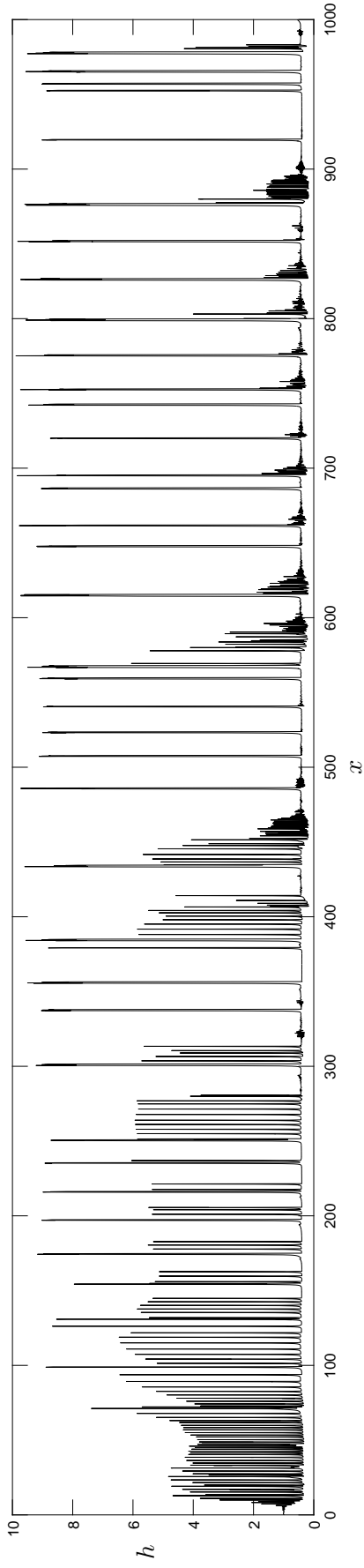


Figure A.1e.: The solution of Data Set 5 at  $t = 3000$ .

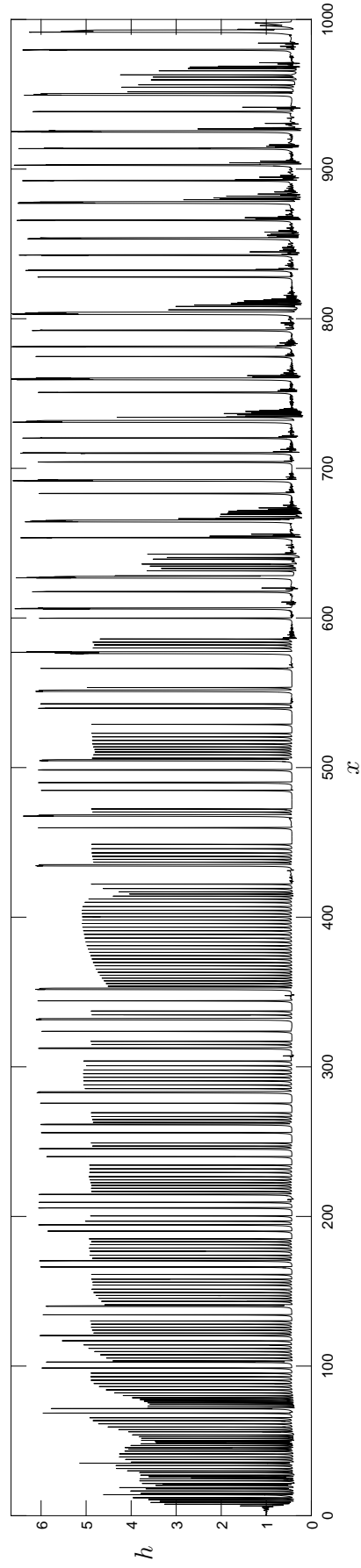


Figure A.1f.: The solution of Data Set 6 at  $t = 3000$ .

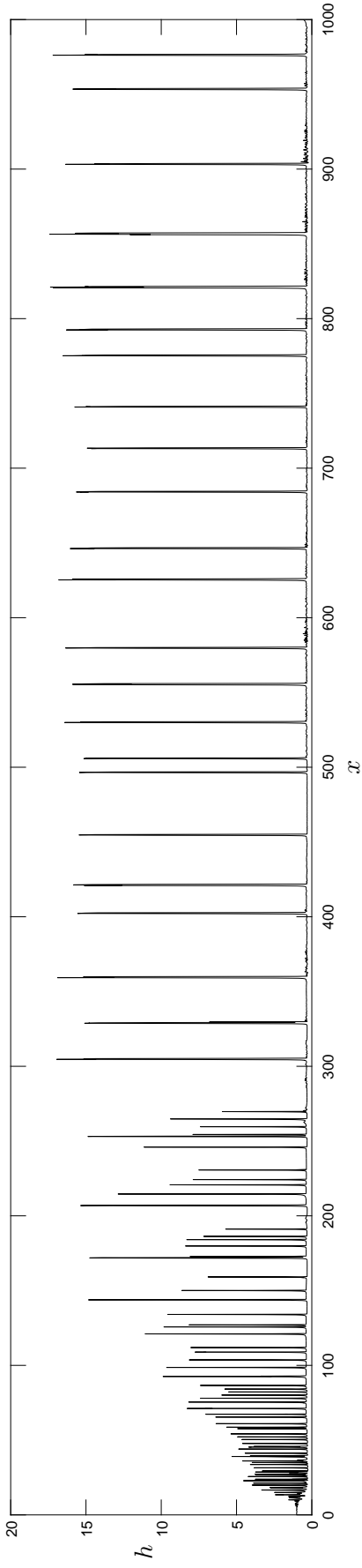


Figure A.1g.: The solution of Data Set 7 at  $t = 3000$ .

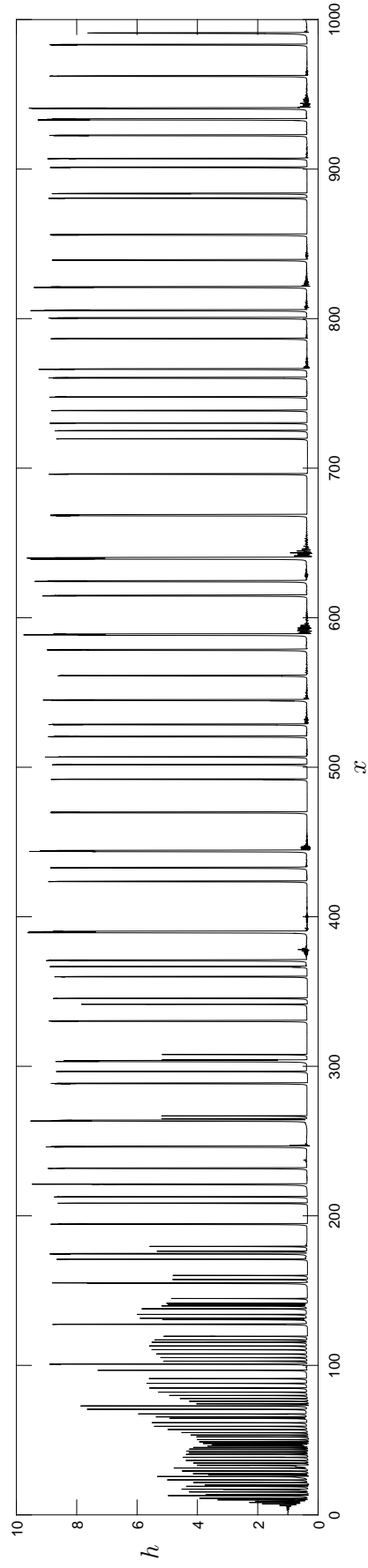


Figure A.1h.: The solution of Data Set 8 at  $t = 3000$ .

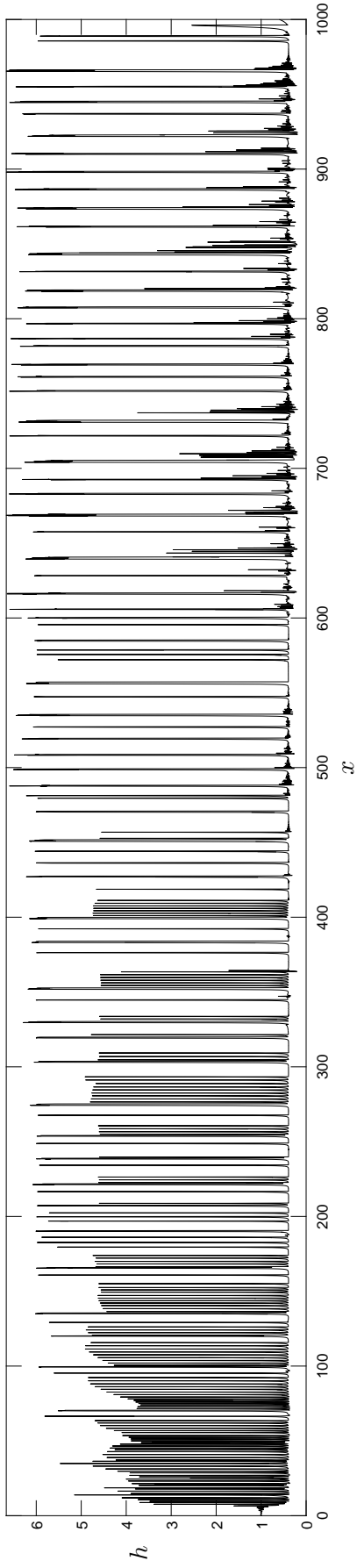


Figure A.1i.: The solution of Data Set 9 at  $t = 3000$ .

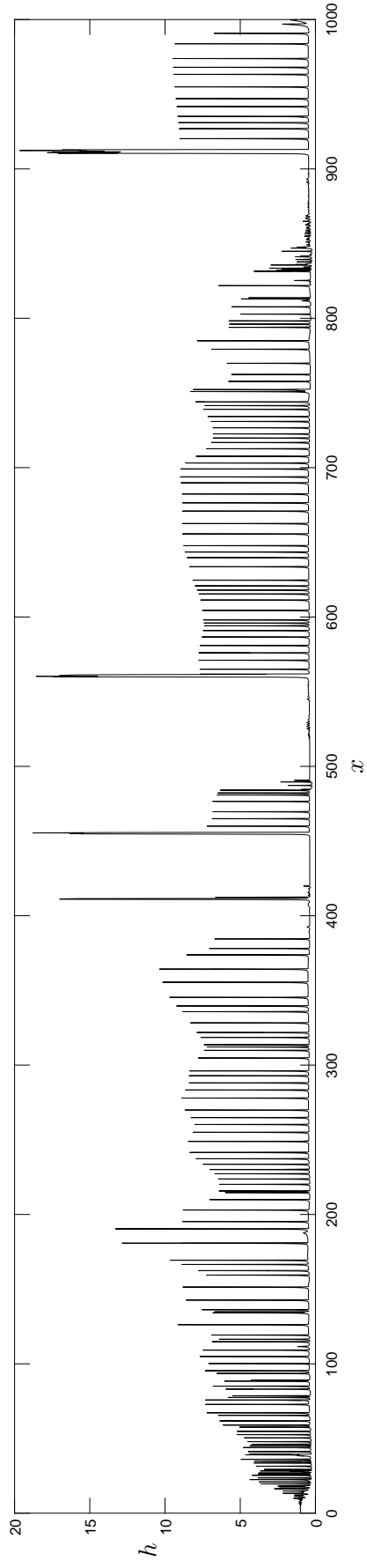


Figure A.1j.: The solution of Data Set 13 at  $t = 3000$ .

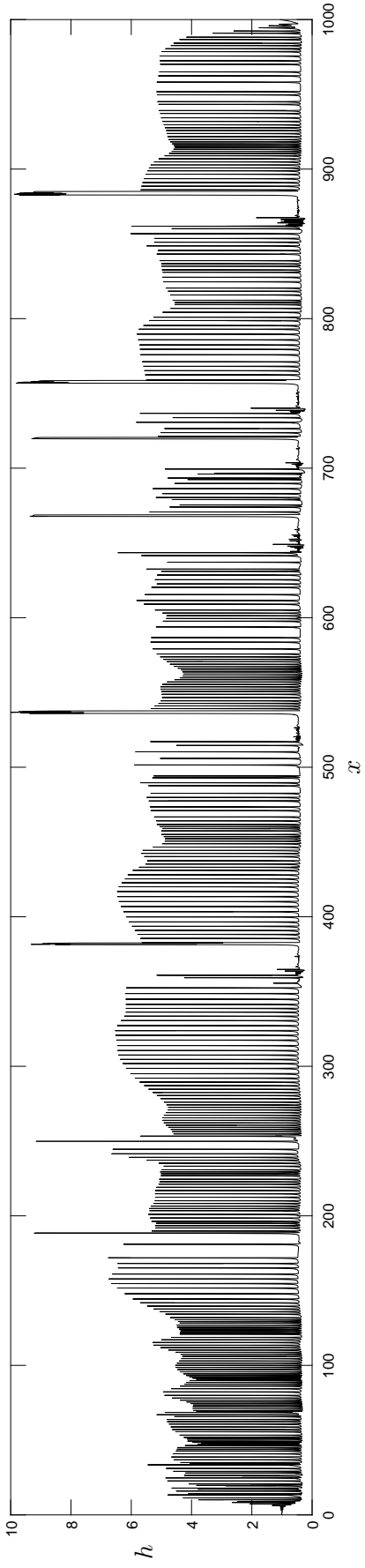


Figure A.1k.: The solution of Data Set 14 at  $t = 3000$ .

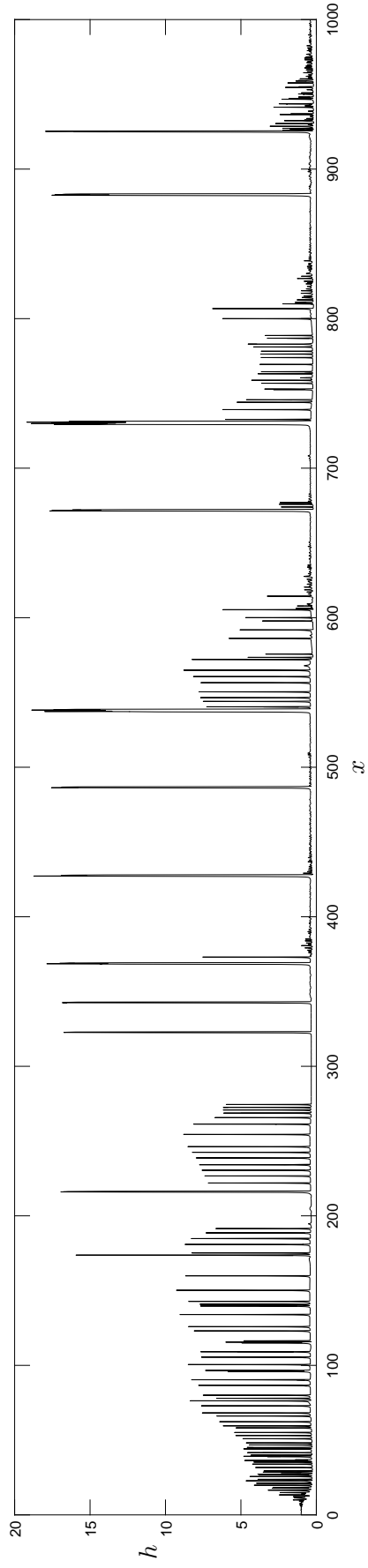


Figure A.1l.: The solution of Data Set 16 at  $t = 3000$ .

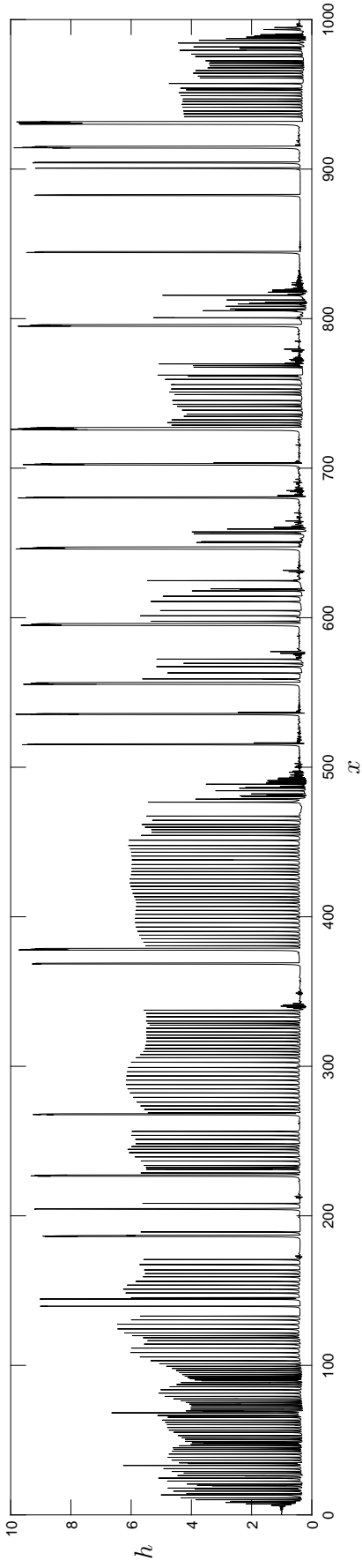


Figure A.1m.: The solution of Data Set 17 at  $t = 3000$ .

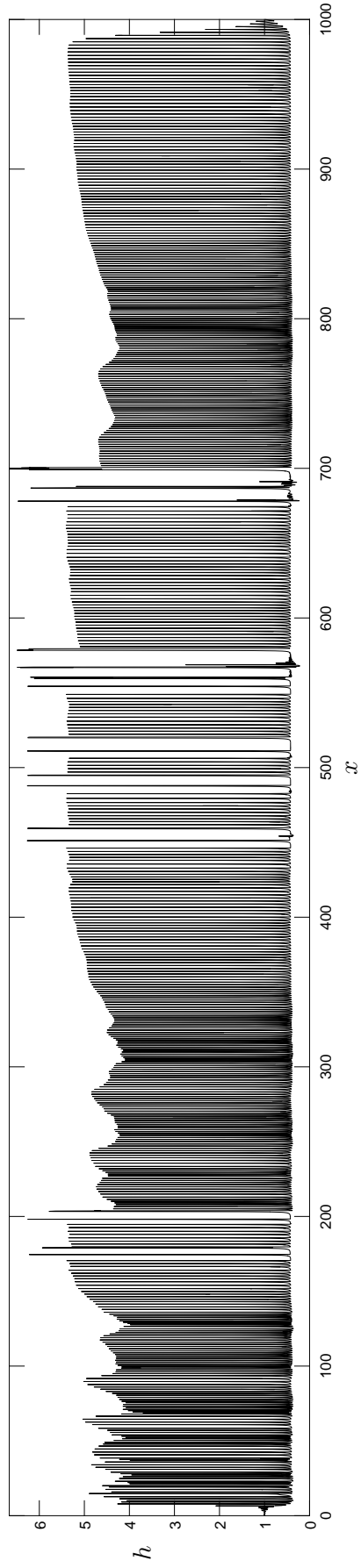


Figure A.1n.: The solution of Data Set 18 at  $t = 3000$ .

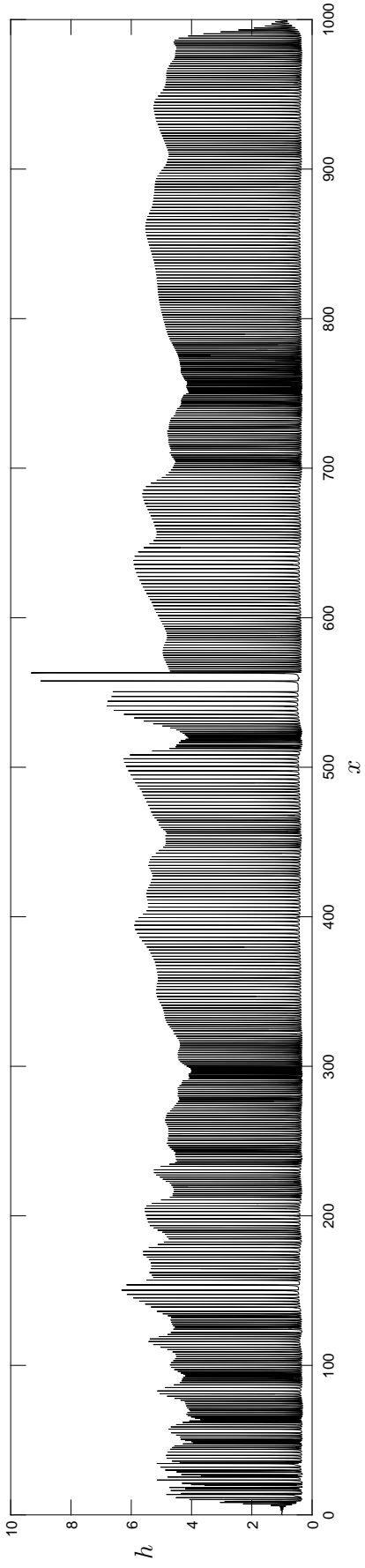


Figure A.10.: The solution of Data Set 23 at  $t = 3000$ .

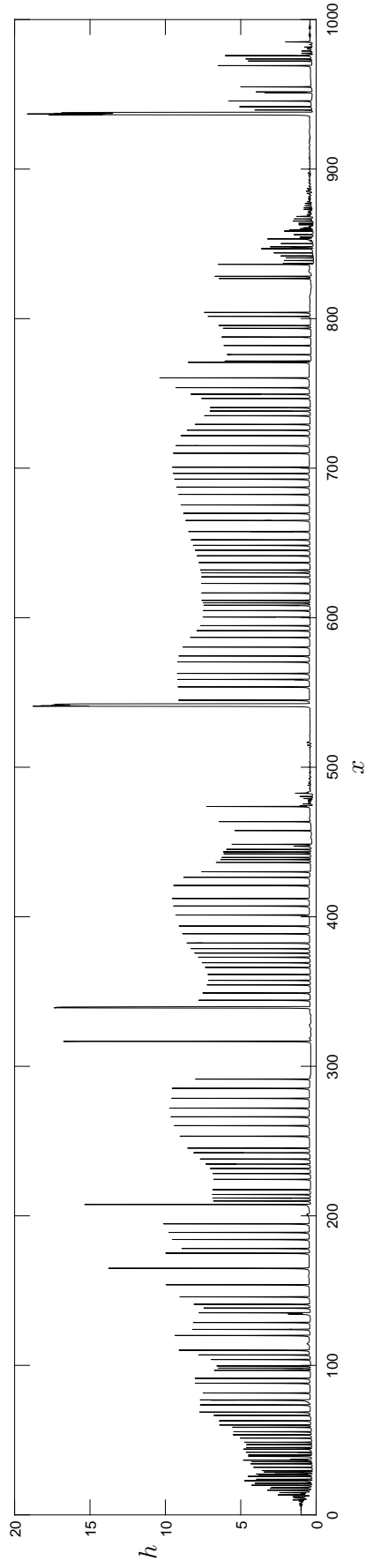


Figure A.11.: The solution of Data Set 25 at  $t = 3000$ .

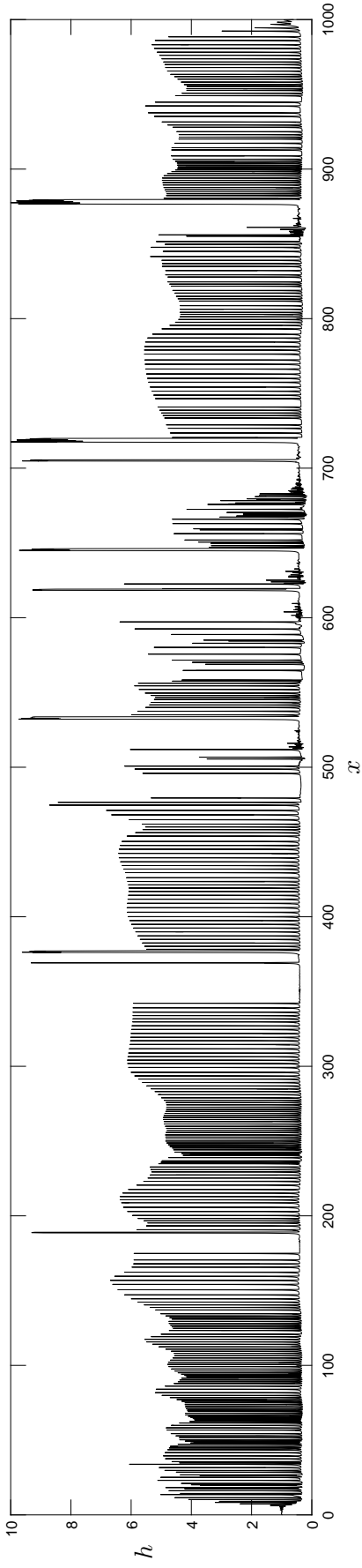


Figure A.1q.: The solution of Data Set 26 at  $t = 3000$ .

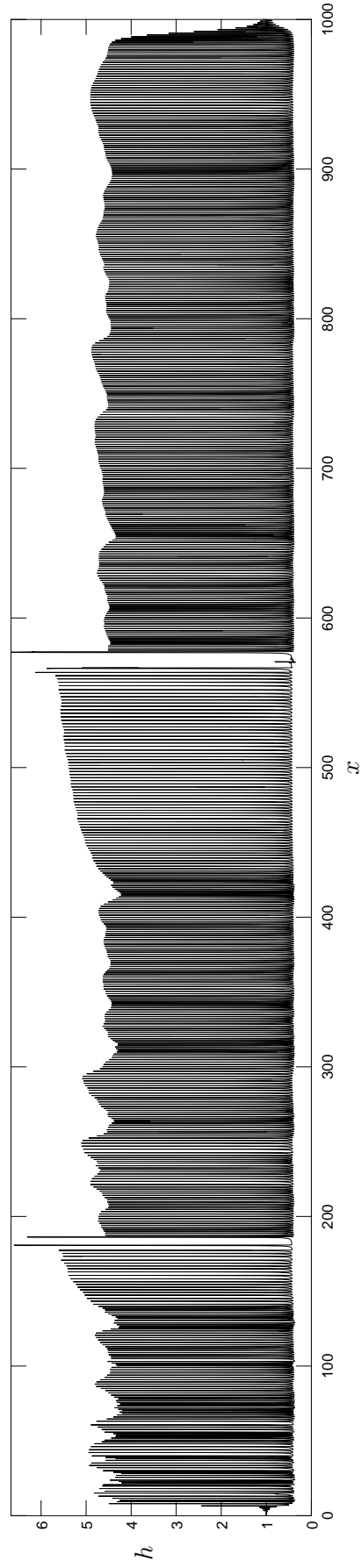
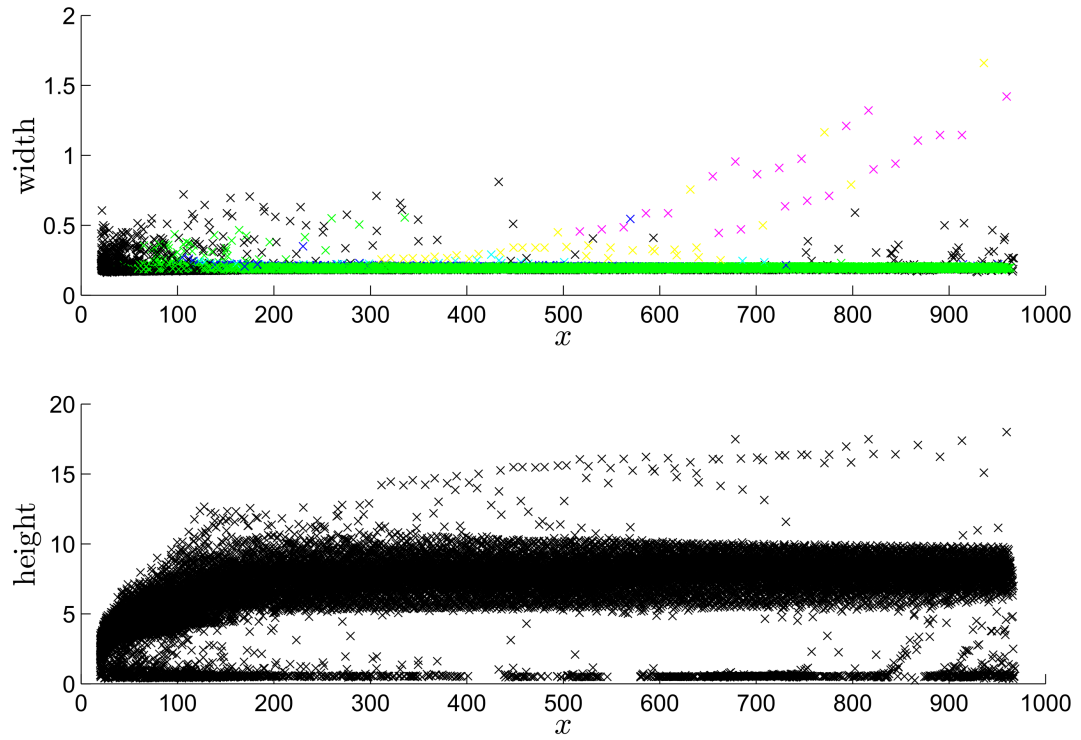
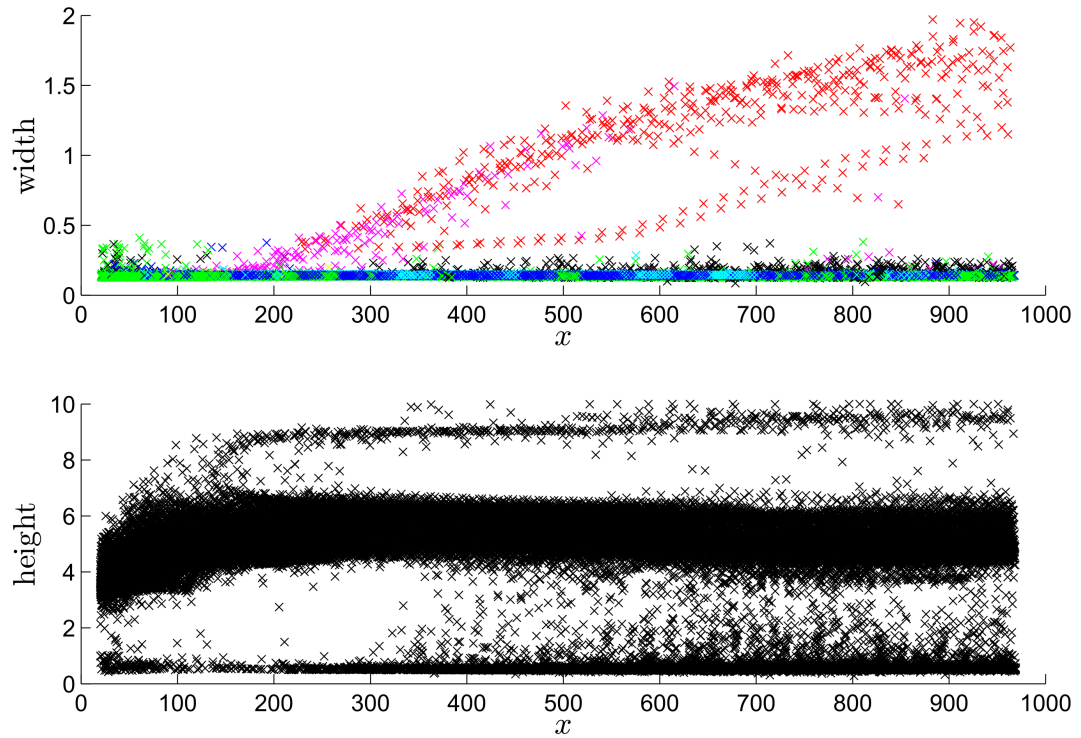


Figure A.1r.: The solution of Data Set 27 at  $t = 3000$ .

## A.1 CHANNEL SIMULATIONS



**Figure A.2a.:** The width and peak height against location in the channel of waves for Data Set 1.



**Figure A.2b.:** The width and peak height against location in the channel of waves for Data Set 2.

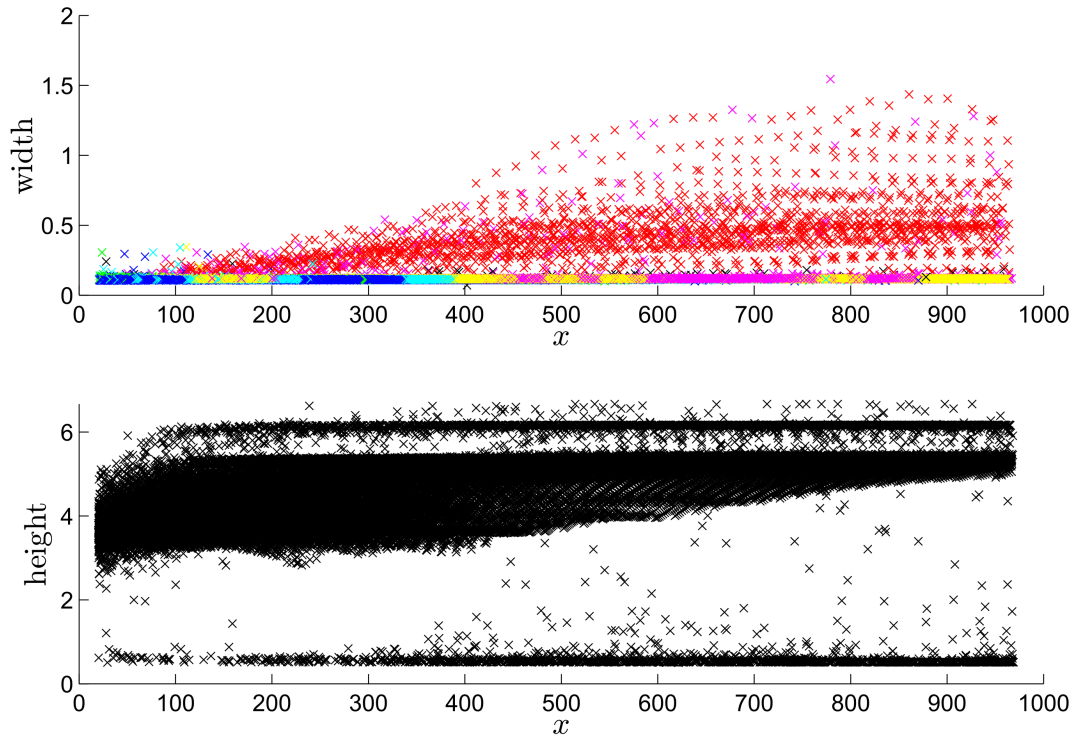


**Figure A.2c.:** The width and peak height against location in the channel of waves for Data Set 3.

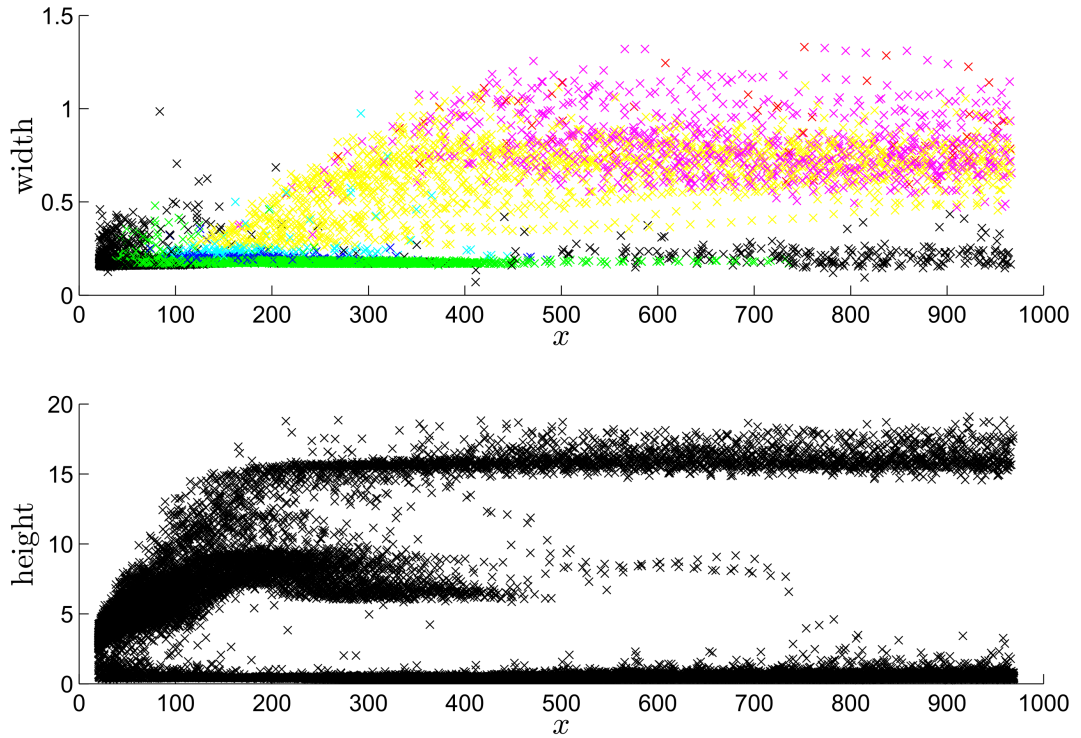


**Figure A.2d.:** The width and peak height against location in the channel of waves for Data Set 4.

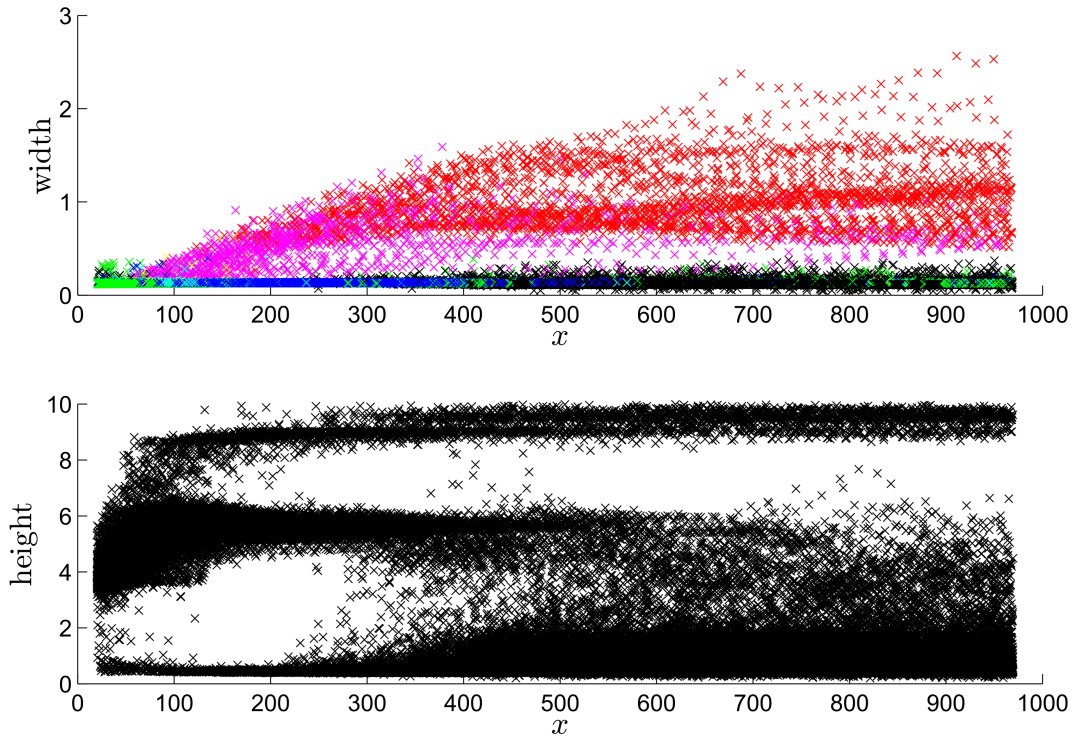


**Figure A.2e.:** The width and peak height against location in the channel of waves for Data Set 5.

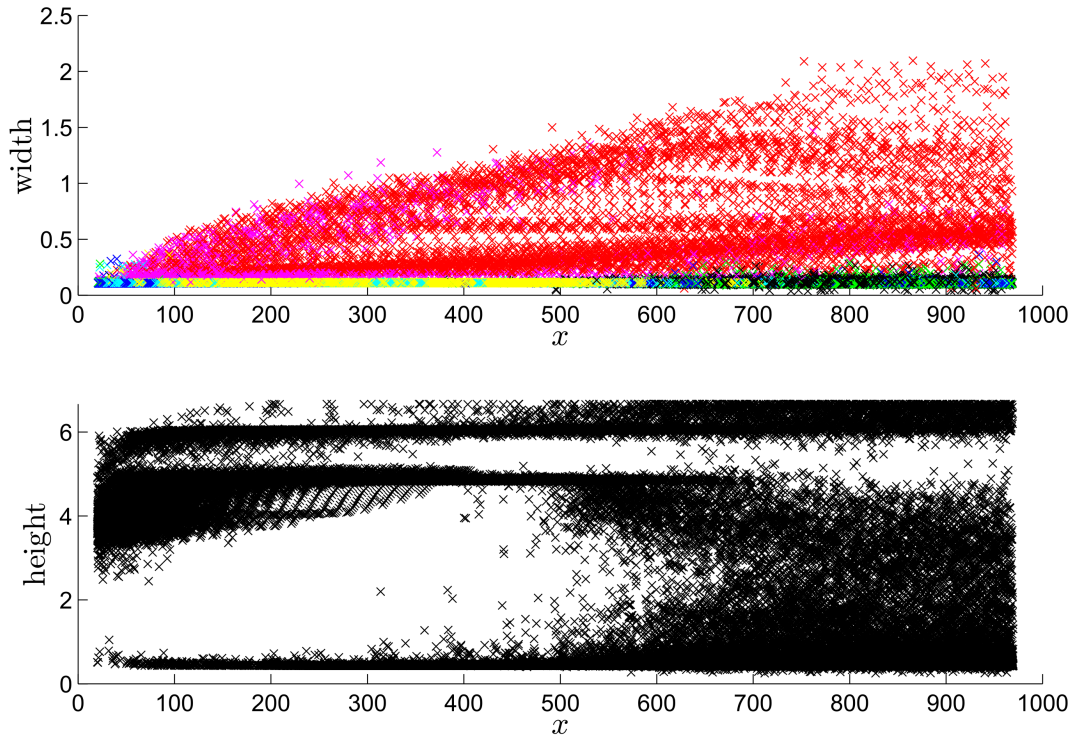


**Figure A.2f.:** The width and peak height against location in the channel of waves for Data Set 6.

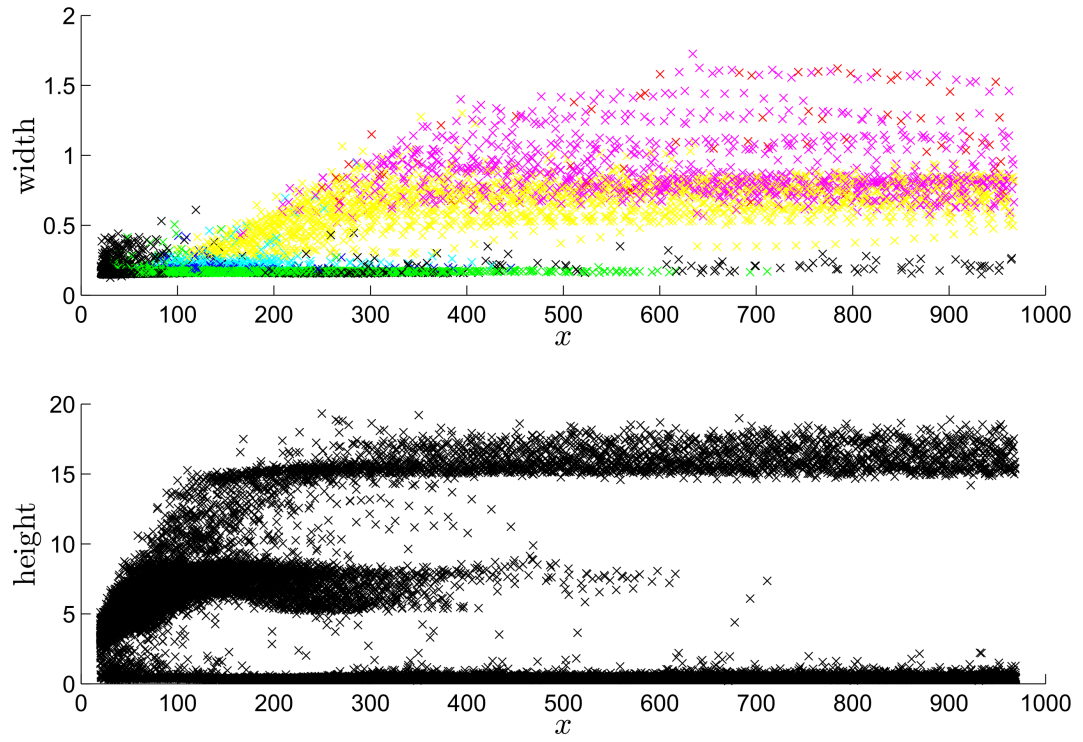


**Figure A.2g.:** The width and peak height against location in the channel of waves for Data Set 7.

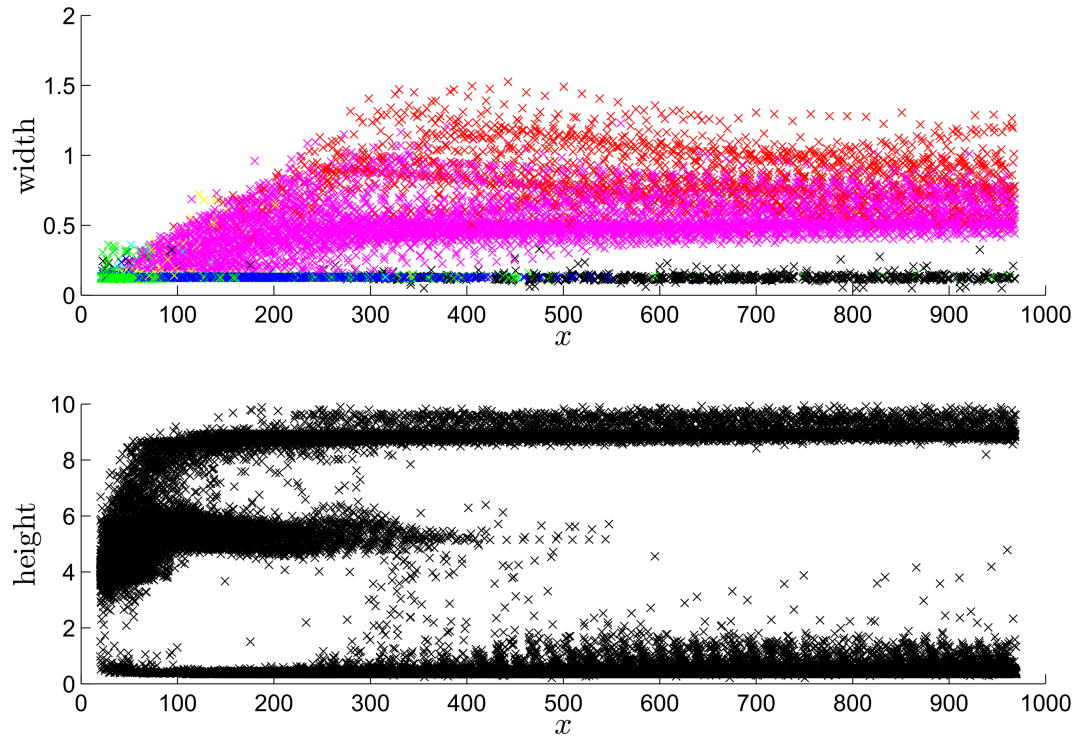


**Figure A.2h.:** The width and peak height against location in the channel of waves for Data Set 8.

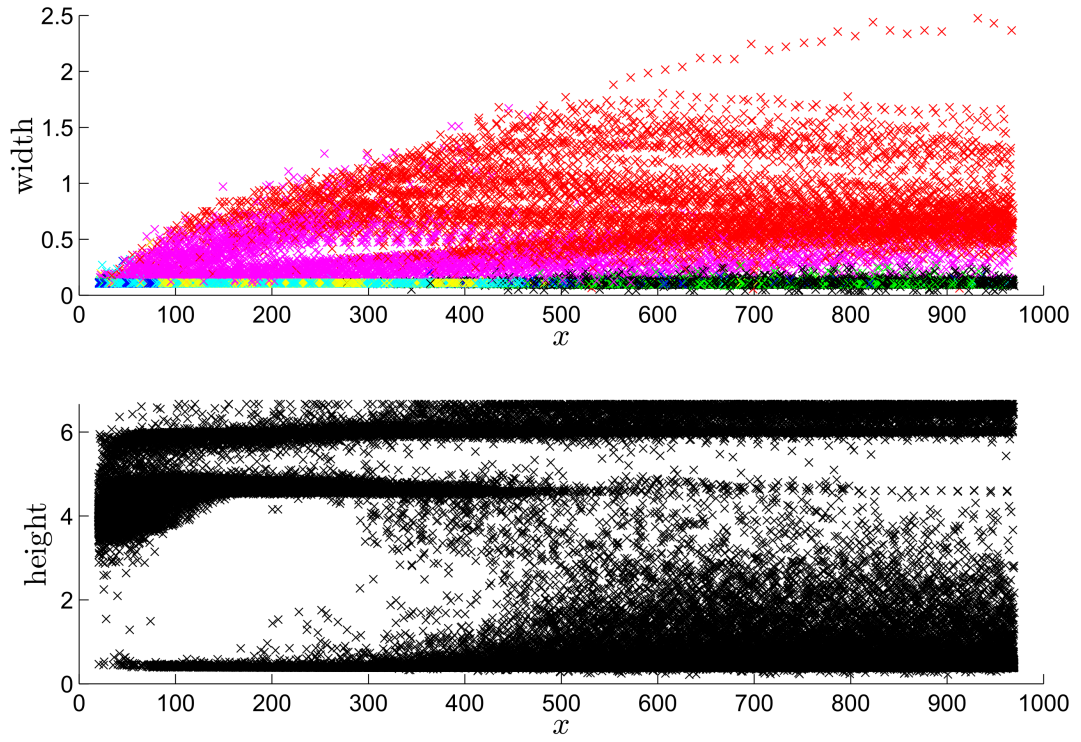


**Figure A.2i.:** The width and peak height against location in the channel of waves for Data Set 9.

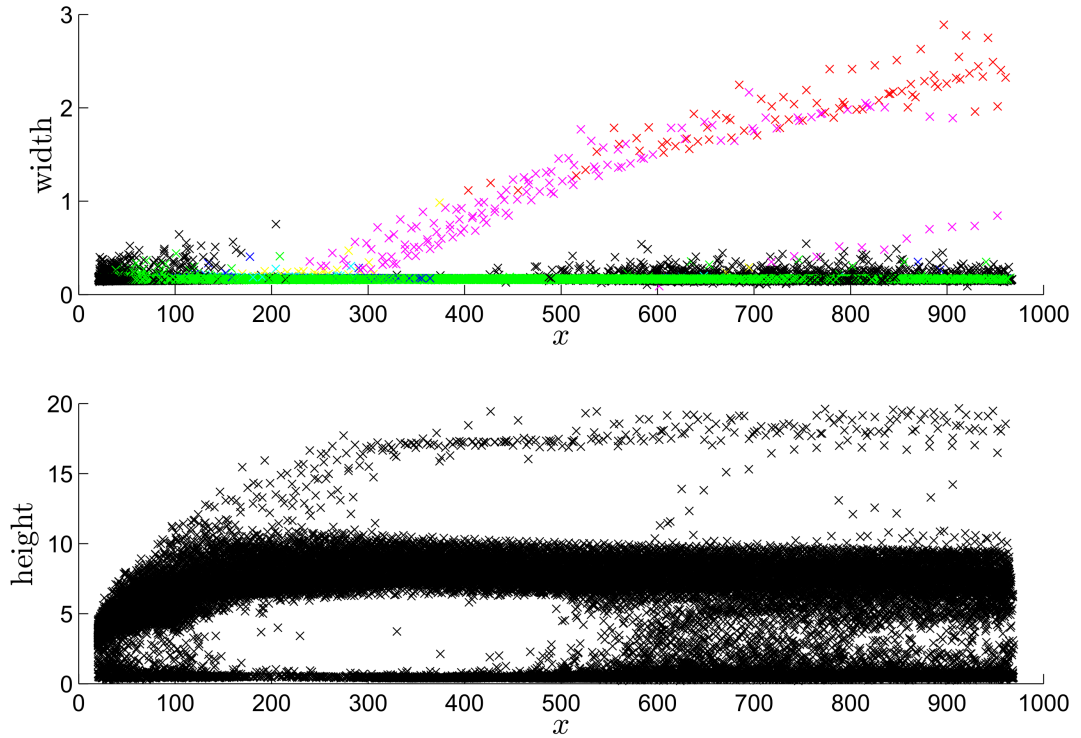


**Figure A.2j.:** The width and peak height against location in the channel of waves for Data Set 13.

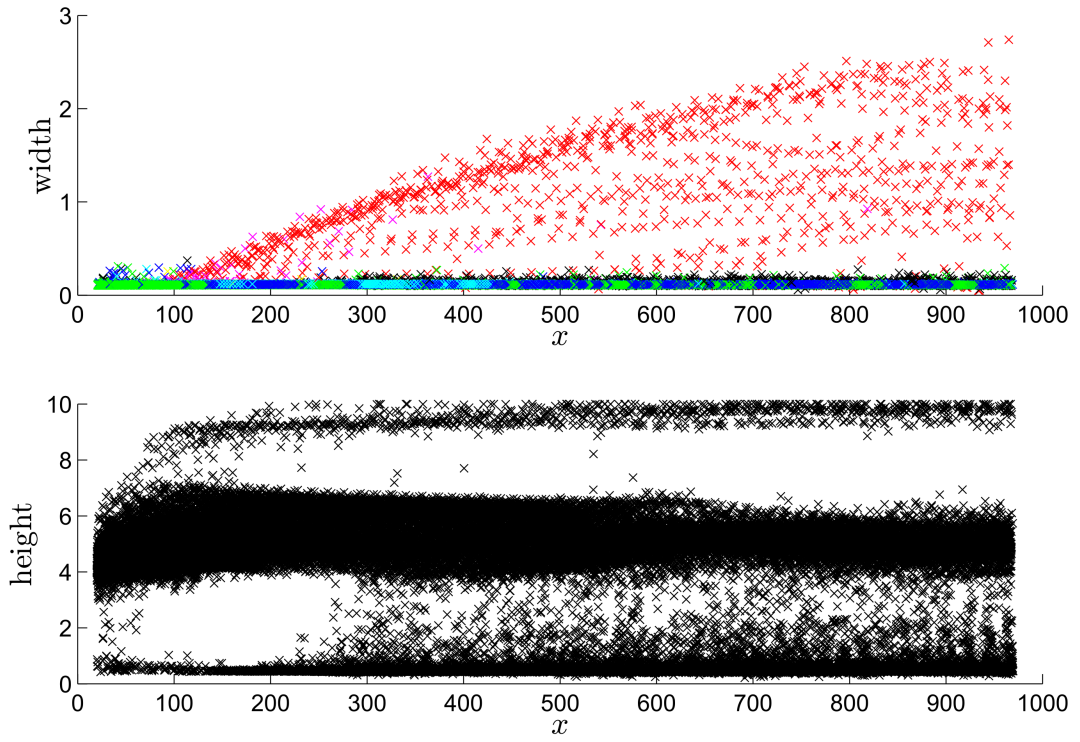


**Figure A.2k.:** The width and peak height against location in the channel of waves for Data Set 14.

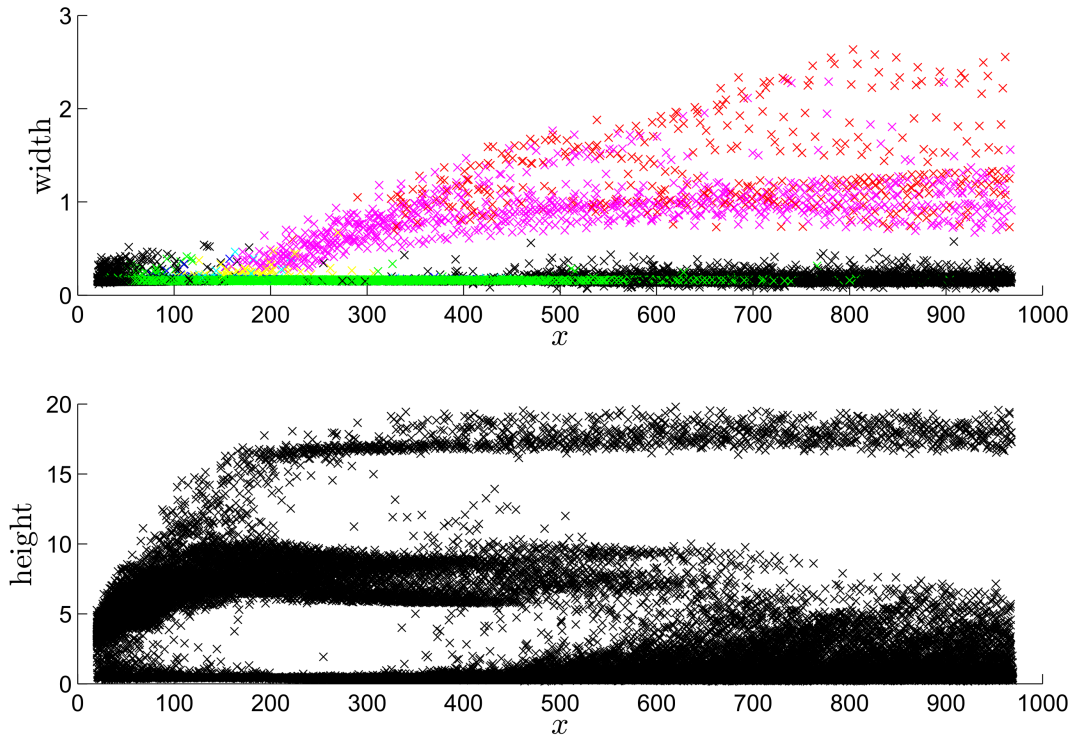


**Figure A.2l.:** The width and peak height against location in the channel of waves for Data Set 16.

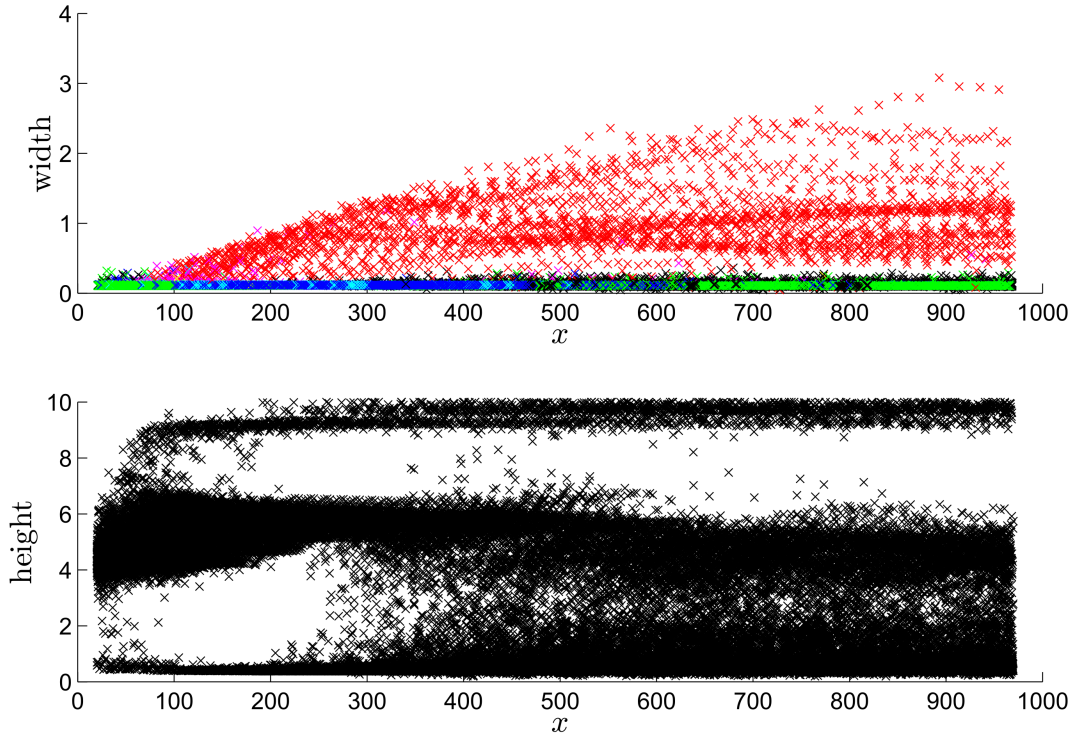


**Figure A.2m.:** The width and peak height against location in the channel of waves for Data Set 17

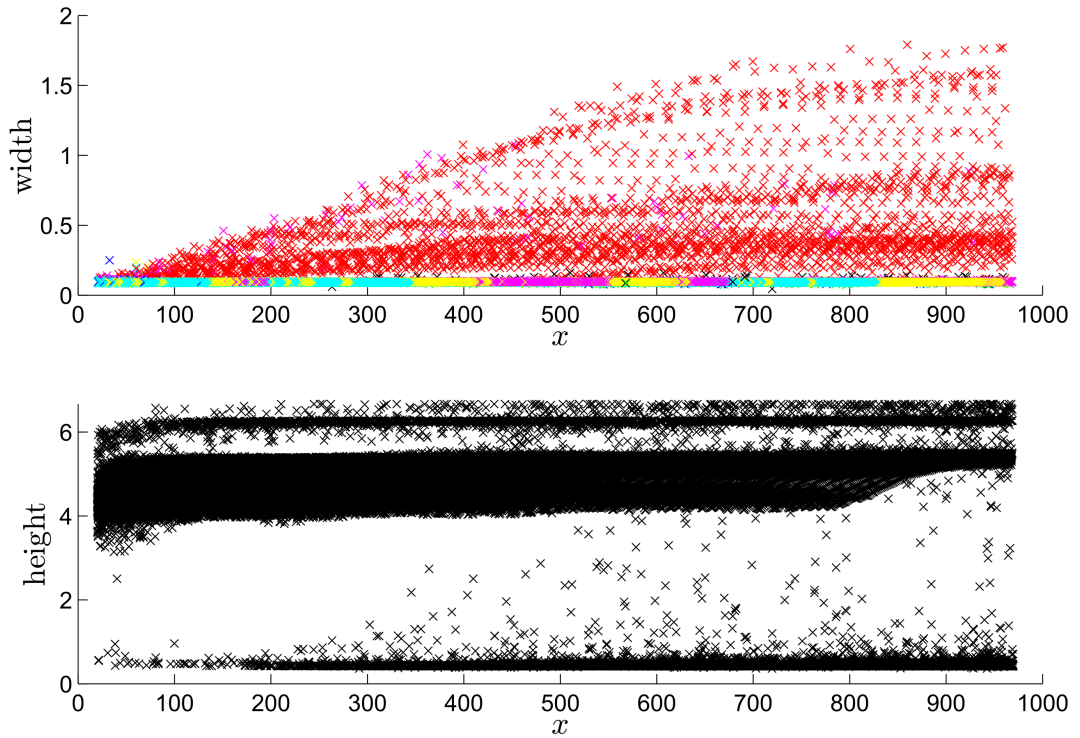


**Figure A.2n.:** The width and peak height against location in the channel of waves for Data Set 18.

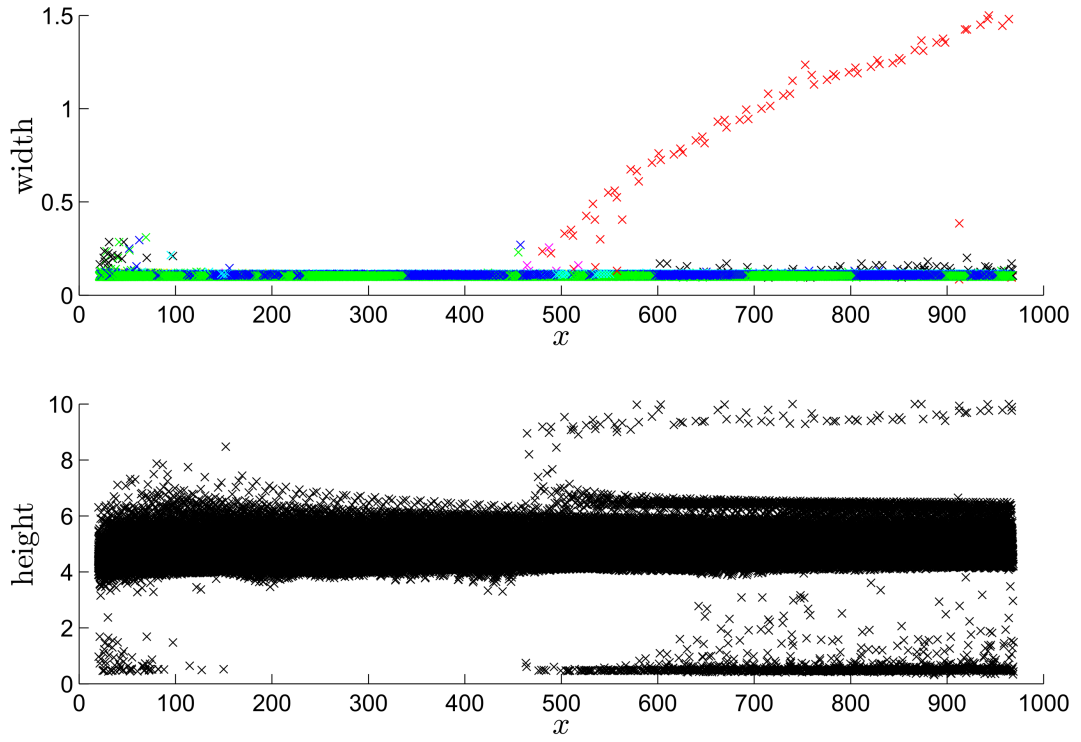


**Figure A.20.:** The width and peak height against location in the channel of waves for Data Set 23.

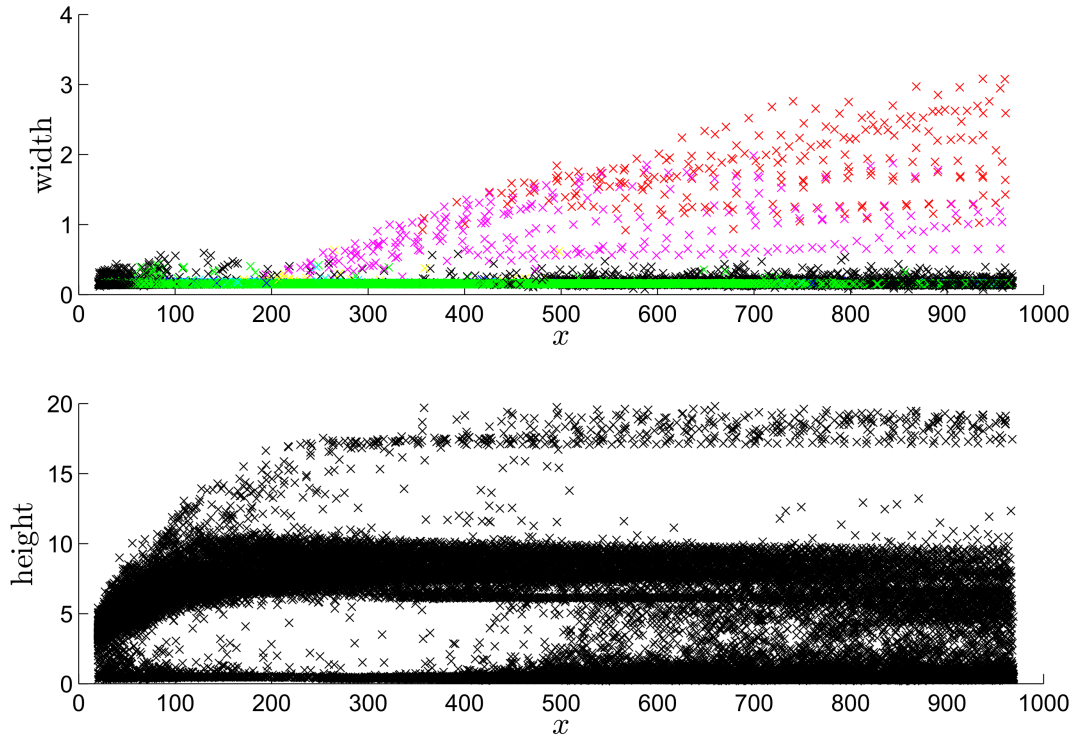


**Figure A.2p.:** The width and peak height against location in the channel of waves for Data Set 25.

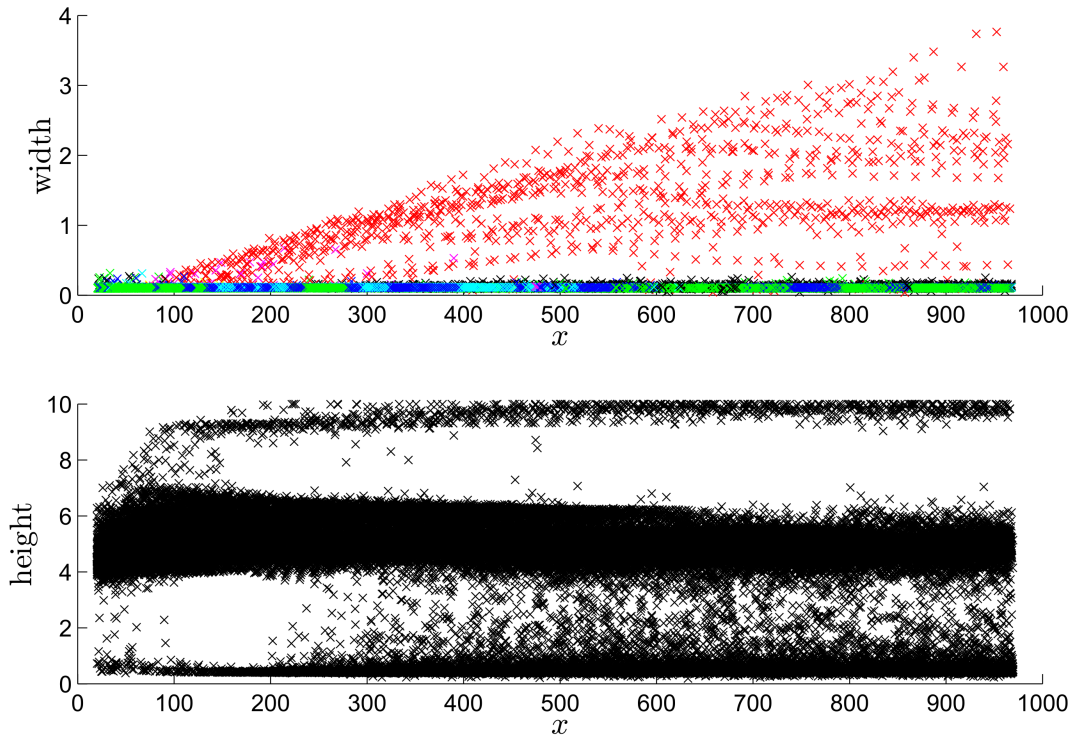


**Figure A.2q.:** The width and peak height against location in the channel of waves for Data Set 26.

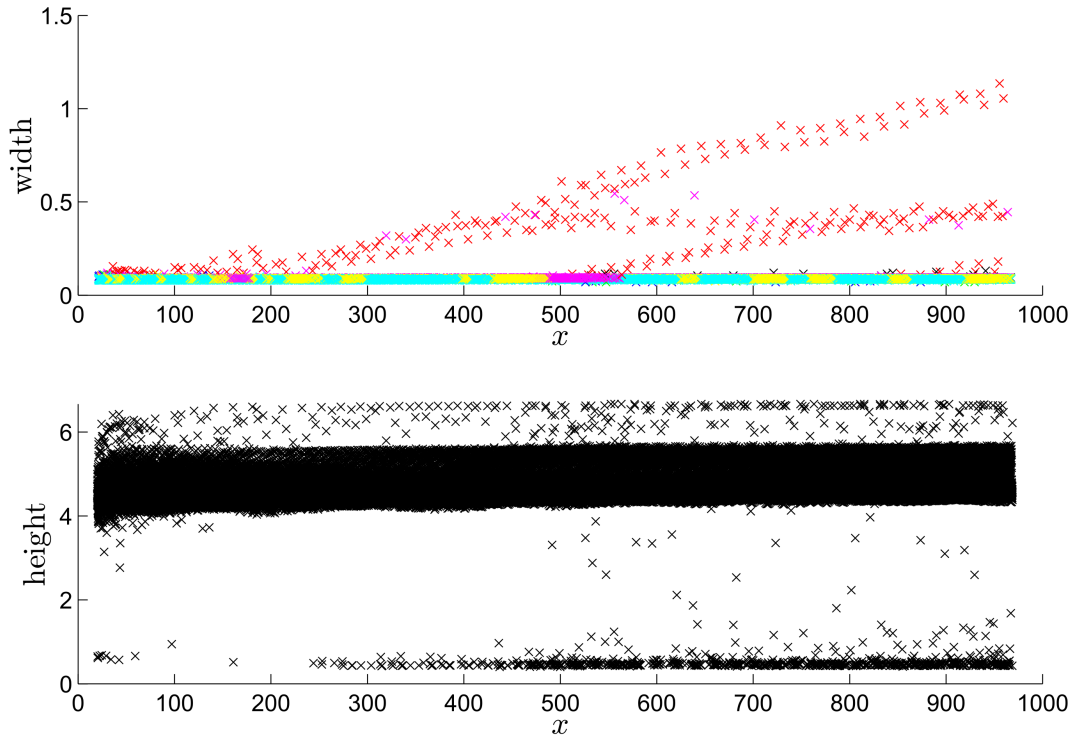


**Figure A.2r.:** The width and peak height against location in the channel of waves for Data Set 27.

**A.2 EFFECTS OF VARYING THE PARAMETERS**

The tables corresponding to all combinations of  $\delta = 0.45, 0.46, 0.47, 0.48, 0.49$  and  $0.5$ ,  $\lambda = 0.2, 0.4, 0.6, 0.8$  and  $1$  and  $F_0 = 5, 5.5, 6, 6.5, 7, 7.5,$  and  $8$  excluding values where  $F_0 > F_{NH}$  as discussed in Section 5.4 on Page 141. Table A.1 shows the Data Sets that produced slugs and Table A.2 shows the Data Sets that produced no slugs.

A.2 EFFECTS OF VARYING THE PARAMETERS

D.S.	$\delta$	$F_0$	$\lambda$	R.W. $h\%$	R.W. Width	Avg Slugs	Slug Width
11	0.47	6.000	0.2	51	0.114	0.451	0.661
12	0.47	6.500	0.2	49	0.104	0.294	0.875
13	0.47	7.000	0.2	55	0.100	1.118	1.172
16	0.48	6.000	0.2	54	0.118	0.569	0.750
17	0.48	6.500	0.2	54	0.110	1.314	1.192
18	0.48	7.000	0.2	54	0.103	2.647	1.415
19	0.48	7.500	0.2	54	0.098	4.471	1.633
22	0.49	6.000	0.2	56	0.123	0.451	0.558
23	0.49	6.500	0.2	55	0.113	1.745	1.231
24	0.49	7.000	0.2	52	0.105	4.137	1.406
25	0.49	7.500	0.2	51	0.100	6.294	1.444
28	0.5	6.000	0.2	58	0.127	0.784	0.667
29	0.5	6.500	0.2	50	0.117	4.314	1.053
30	0.5	7.000	0.2	51	0.109	6.510	1.256
31	0.5	7.500	0.2	49	0.104	7.882	1.184
32	0.5	8.000	0.2	45	0.100	9.176	1.640
45	0.47	7.000	0.4	53	0.101	0.529	1.317
49	0.48	6.500	0.4	52	0.111	0.608	0.734
50	0.48	7.000	0.4	53	0.104	1.824	1.296
51	0.48	7.500	0.4	54	0.100	2.902	1.757
55	0.49	6.500	0.4	55	0.115	1.078	1.056
56	0.49	7.000	0.4	54	0.108	3.157	1.352
57	0.49	7.500	0.4	48	0.102	5.255	1.478
60	0.5	6.000	0.4	54	0.129	0.078	0.400
61	0.5	6.500	0.4	57	0.119	2.392	1.136
62	0.5	7.000	0.4	51	0.113	4.902	1.192
63	0.5	7.500	0.4	46	0.105	8.039	1.455
64	0.5	8.000	0.4	45	0.099	8.667	1.545
81	0.48	6.500	0.6	51	0.112	0.490	0.710

A.2 EFFECTS OF VARYING THE PARAMETERS

---

82	0.48	7.000	0.6	53	0.106	0.804	1.202
83	0.48	7.500	0.6	55	0.102	2.353	1.626
87	0.49	6.500	0.6	52	0.117	0.431	1.113
88	0.49	7.000	0.6	53	0.110	2.157	1.140
89	0.49	7.500	0.6	51	0.104	3.863	1.508
93	0.5	6.500	0.6	57	0.124	0.627	0.828
94	0.5	7.000	0.6	52	0.113	3.451	1.370
95	0.5	7.500	0.6	49	0.108	6.020	1.349
96	0.5	8.000	0.6	47	0.104	7.902	1.390
113	0.48	6.500	0.8	48	0.113	0.196	0.430
114	0.48	7.000	0.8	51	0.106	0.412	0.884
115	0.48	7.500	0.8	54	0.102	1.118	1.243
119	0.49	6.500	0.8	52	0.119	0.098	0.700
120	0.49	7.000	0.8	54	0.111	0.608	1.206
121	0.49	7.500	0.8	54	0.106	2.863	1.588
125	0.5	6.500	0.8	53	0.123	0.020	0.290
126	0.5	7.000	0.8	57	0.117	1.902	1.268
127	0.5	7.500	0.8	49	0.112	4.549	1.348
128	0.5	8.000	0.8	52	0.103	6.647	1.393
146	0.48	7.000	1	49	0.107	0.255	1.000
147	0.48	7.500	1	54	0.103	0.392	0.910
152	0.49	7.000	1	51	0.111	0.314	1.018
153	0.49	7.500	1	53	0.106	2.255	1.355
158	0.5	7.000	1	54	0.118	0.333	1.175
159	0.5	7.500	1	52	0.110	2.804	1.553
160	0.5	8.000	1	47	0.106	5.569	1.620

---

**Table A.1.:** Data for which slugs form when varying  $\delta$ ,  $\lambda$  and  $F_0$ .

A.2 EFFECTS OF VARYING THE PARAMETERS

D.S.	$\delta$	$F_0$	$\lambda$	R.W. $h\%$	R.W. Width
1	0.45	5	0.2	48	0.130
2	0.45	5.5	0.2	44	0.113
3	0.45	6	0.2	46	0.103
4	0.45	6.5	0.2	49	0.097
5	0.46	5	0.2	47	0.135
6	0.46	5.5	0.2	49	0.120
7	0.46	6	0.2	46	0.107
8	0.46	6.5	0.2	49	0.101
9	0.47	5	0.2	48	0.140
10	0.47	5.5	0.2	52	0.126
14	0.48	5	0.2	45	0.142
15	0.48	5.5	0.2	52	0.130
20	0.49	5	0.2	46	0.147
21	0.49	5.5	0.2	52	0.134
26	0.5	5	0.2	47	0.152
27	0.5	5.5	0.2	52	0.137
33	0.45	5	0.4	46	0.132
34	0.45	5.5	0.4	45	0.116
35	0.45	6	0.4	44	0.104
36	0.45	6.5	0.4	48	0.098
37	0.46	5	0.4	45	0.138
38	0.46	5.5	0.4	49	0.123
39	0.46	6	0.4	48	0.111
40	0.46	6.5	0.4	48	0.102
41	0.47	5	0.4	45	0.142
42	0.47	5.5	0.4	48	0.127
43	0.47	6	0.4	48	0.115
44	0.47	6.5	0.4	50	0.106
46	0.48	5	0.4	43	0.146

A.2 EFFECTS OF VARYING THE PARAMETERS

---

47	0.48	5.5	0.4	49	0.132
48	0.48	6	0.4	50	0.120
52	0.49	5	0.4	44	0.151
53	0.49	5.5	0.4	50	0.136
54	0.49	6	0.4	52	0.125
58	0.5	5	0.4	44	0.156
59	0.5	5.5	0.4	50	0.140
65	0.45	5	0.6	43	0.134
66	0.45	5.5	0.6	45	0.118
67	0.45	6	0.6	46	0.107
68	0.45	6.5	0.6	47	0.099
69	0.46	5	0.6	43	0.140
70	0.46	5.5	0.6	45	0.125
71	0.46	6	0.6	47	0.112
72	0.46	6.5	0.6	48	0.103
73	0.47	5	0.6	42	0.145
74	0.47	5.5	0.6	49	0.130
75	0.47	6	0.6	48	0.117
76	0.47	6.5	0.6	50	0.108
77	0.47	7	0.6	51	0.102
78	0.48	5	0.6	42	0.150
79	0.48	5.5	0.6	46	0.133
80	0.48	6	0.6	50	0.122
84	0.49	5	0.6	42	0.155
85	0.49	5.5	0.6	47	0.138
86	0.49	6	0.6	52	0.127
90	0.5	5	0.6	42	0.159
91	0.5	5.5	0.6	46	0.142
92	0.5	6	0.6	54	0.131
97	0.45	5	0.8	42	0.137
98	0.45	5.5	0.8	44	0.120

A.2 EFFECTS OF VARYING THE PARAMETERS

---

99	0.45	6	0.8	45	0.108
100	0.45	6.5	0.8	47	0.100
101	0.46	5	0.8	41	0.143
102	0.46	5.5	0.8	45	0.126
103	0.46	6	0.8	46	0.113
104	0.46	6.5	0.8	49	0.105
105	0.47	5	0.8	41	0.148
106	0.47	5.5	0.8	46	0.131
107	0.47	6	0.8	48	0.119
108	0.47	6.5	0.8	48	0.109
109	0.47	7	0.8	50	0.102
110	0.48	5	0.8	41	0.154
111	0.48	5.5	0.8	45	0.136
112	0.48	6	0.8	47	0.123
116	0.49	5	0.8	40	0.158
117	0.49	5.5	0.8	45	0.141
118	0.49	6	0.8	49	0.128
122	0.5	5	0.8	40	0.163
123	0.5	5.5	0.8	44	0.144
124	0.5	6	0.8	50	0.132
129	0.45	5	1	41	0.140
130	0.45	5.5	1	45	0.122
131	0.45	6	1	45	0.109
132	0.45	6.5	1	46	0.100
133	0.46	5	1	40	0.146
134	0.46	5.5	1	44	0.127
135	0.46	6	1	45	0.114
136	0.46	6.5	1	47	0.105
137	0.47	5	1	40	0.152
138	0.47	5.5	1	45	0.133
139	0.47	6	1	47	0.120

A.2 EFFECTS OF VARYING THE PARAMETERS

---

140	0.47	6.5	1	48	0.110
141	0.47	7	1	50	0.103
142	0.48	5	1	39	0.157
143	0.48	5.5	1	44	0.138
144	0.48	6	1	47	0.125
145	0.48	6.5	1	48	0.115
148	0.49	5	1	39	0.162
149	0.49	5.5	1	43	0.143
150	0.49	6	1	48	0.129
151	0.49	6.5	1	51	0.120
154	0.5	5	1	39	0.167
155	0.5	5.5	1	43	0.147
156	0.5	6	1	49	0.134
157	0.5	6.5	1	51	0.124

---

**Table A.2.:** Data for which no slugs form when varying  $\delta$ ,  $\lambda$  and  $F_0$ .

---

## BIBLIOGRAPHY

---

- [1] S. S. Agrawal, G. A. Gregory, and G. W. Govier. An analysis of horizontal stratified two phase flow in pipes. *The Canadian Journal of Chemical Engineering*, 51(3):280–286, 1973.
- [2] A. H. Akselsen and O. J. Nydal. Applying multiple grids to a multi-field model—The resolution requirements of individual fields in the two-fluid model for 1D pipe flow. *Journal of Dispersion Science and Technology*, 36(10):1378–1387, 2015.
- [3] E. M. Al-Safran, Y. Taitel, and J. P. Brill. Prediction of slug length distribution along a hilly terrain pipeline using slug tracking model. *Journal of Energy Resources Technology*, 126(1):54–62, 2004.
- [4] V. Alavian. Behaviour of density currents on an incline. *Journal of Hydraulic Engineering*, 112(1):27–42, 1986.
- [5] P. Andreussi and L. N. Persen. Stratified gas-liquid flow in downwardly inclined pipes. *International Journal of Multiphase Flow*, 13(4):565–575, 1987.
- [6] P. Andreussi, J. C. Asali, and T. J. Hanratty. Initiation of roll waves in gas-liquid flows. *AIChE Journal*, 31(1):119–126, 1985.
- [7] N. Andritsos. *Effect of pipe diameter and liquid viscosity on horizontal stratified flow*. PhD thesis, University of Illinois, 1986.
- [8] N. Andritsos and T. J. Hanratty. Influence of interfacial waves in stratified gas-liquid flow. *AIChE Journal*, 33(3):444–454, 1987.

- [9] N. Andritsos and T. J. Hanratty. Interfacial instabilities for horizontal gas-liquid flows in pipelines. *International Journal of Multiphase Flow*, 13(5):583–603, 1987.
- [10] N. Andritsos, L. Williams, and T. J. Hanratty. Effect of liquid viscosity on the stratified-slug transition in horizontal pipe flow. *International Journal of Multiphase Flow*, 15(6):877–892, 1988.
- [11] M. R. Ansari and V. Shokri. Numerical modeling of slug flow initiation in a horizontal channels using a two-fluid model. *International Journal of Heat and Fluid Flow*, 32(1):145–155, 2011.
- [12] J. C. Asali. *Entrainment in vertical gas-liquid annular flows*. UMI, 1984.
- [13] J. C. Asali, T. J. Hanratty, and P. Andreussi. Interfacial drag and film height for vertical annular flow. *AIChE Journal*, 31(6):895–902, 1985.
- [14] O. Baker. Design of pipelines for the simultaneous flow of oil and gas. In *Fall Meeting of the Petroleum Branch of AIME*. Society of Petroleum Engineers, 1953.
- [15] N. J. Balmforth and S. Mandre. Dynamics of roll waves. *Journal of Fluid Mechanics*, 514:1–33, 2004.
- [16] D. Barnea. On the effect of viscosity on stability of stratified gas—liquid flow—application to flow pattern transition at various pipe inclinations. *Chemical Engineering Science*, 46(8):2123–2131, 1991.
- [17] D. Barnea and Y. Taitel. Kelvin-Helmholtz stability criterion for stratified flow; viscous versus non-viscous (inviscid) approaches. *International Journal of Multiphase Flow*, 19(4):639–649, 1993.
- [18] D. Barnea and Y. Taitel. A model for slug length distribution in gas-liquid slug flow. *International Journal of Multiphase Flow*, 19(5):829–838, 1993.

- [19] D. Barnea and Y. Taitel. Interfacial and structural stability of separated flow. *International Journal of Multiphase Flow*, 20:387–414, 1994.
- [20] D. H. Beggs and J. P. Brill. A study of two-phase flow in inclined pipes. *Journal of Petroleum Technology*, 25(05):607–617, 1973.
- [21] K. Bendiksen, I. Brandt, K. A. Jacobsen, and C. Pauchon. Dynamic simulation of multiphase transportation systems. In *Multiphase Technology and Consequences for Field Development Forum*, Stavanger, Norway, 1987.
- [22] K. Bendiksen, D. Malnes, T. Straume, and P. Hedne. A non-diffusive numerical model for transient simulation of oil-gas transportation systems. In *European Simulation Multiconference*, pages 508–515, Nüremberg, 1990.
- [23] K. H. Bendiksen. An experimental investigation of the motion of long bubbles in inclined tubes. *International Journal of Multiphase Flow*, 10(4):467–483, 1984.
- [24] K. H. Bendiksen, D. Maines, R. Moe, and S. Nuland. The dynamic two-fluid model OLGA: Theory and application. *SPE Production Engineering*, 6(02):171–180, 1991.
- [25] T. B. Benjamin. Wave formation in laminar flow down an inclined plane. *Journal of Fluid Mechanics*, 2(06):554–573, 1957.
- [26] D. J. Benney. Long waves on liquid films. *Journal of Mathematics and Physics*, 45(1):150–155, 1966.
- [27] H. Blasius. Das ähnlichkeitsgesetz bei reibungsvorgängen in flüssigkeiten. In *Mitteilungen über Forschungsarbeiten auf dem Gebiete des Ingenieurwesens*, pages 1–41. Springer, 1913.
- [28] M. Bonizzi, P. Andreussi, and S. Banerjee. Flow regime independent, high resolution multi-field modelling of near-horizontal gas-liquid

- flows in pipelines. *International Journal of Multiphase Flow*, 35(1):34–46, 2009.
- [29] R. H. Bonnecaze, W. Erskine, and E. J. Greskovich. Holdup and pressure drop for two-phase slug flow in inclined pipelines. *AIChE Journal*, 17(5):1109–1113, 1971.
- [30] N. Brauner and D. M. Maron. Characteristics of inclined thin films, waviness and the associated mass transfer. *International Journal of Heat and Mass Transfer*, 25(1):99–110, 1982.
- [31] R. R. Brock. *Development of roll waves in open channels*. PhD thesis, California Institute of Technology, 1967.
- [32] R. R. Brock. Roll-wave trains in open channels. *Journal of the Hydraulics Division*, 1969.
- [33] A. Cabal, J. Szumbariski, and J. M. Floryan. Stability of flow in a wavy channel. *Journal of Fluid Mechanics*, 457:191–212, 2002.
- [34] Z. Cao, P. Hu, K. Hu, G. Pender, and Q. Liu. Modelling roll waves with shallow water equations and turbulent closure. *Journal of Hydraulic Research*, 53(2):161–177, 2015.
- [35] J. Carr. *Applications of centre manifold theory*. Springer Science & Business Media, 1981.
- [36] C. Chang, H., E. A. Demekhin, and E. Kalaidin. Simulation of noise-driven wave dynamics on a falling film. *AIChE Journal*, 42:1553–1568, 1996.
- [37] C. Chang, H., E. A. Demekhin, and E. Kalaidin. Coherent structures, self-similarity, and universal roll wave coarsening dynamics. *Physics of Fluids*, 12(9):2268–2278, 2000.

- [38] H.-C. Chang. Traveling waves on fluid interfaces: normal form analysis of the Kuramoto–Sivashinsky equation. *Physics of Fluids*, 29(10):3142–3147, 1986.
- [39] N. P. Cheremisinoff and E. J. Davis. Stratified turbulent-turbulent gas-liquid flow. *AIChE Journal*, 25(1):48–56, 1979.
- [40] L. S. Cohen and T. J. Hanratty. Effect of waves at a gas–liquid interface on a turbulent air flow. *Journal of Fluid Mechanics*, 31(03):467–479, 1968.
- [41] C. F. Colebrook and C. M. White. Experiments with fluid friction in roughened pipes. *Proceedings of the Royal Society of London. Series A, Mathematical and Physical Sciences*, 161(906):367–381, 1937.
- [42] C. F. Colebrook, T. Blench, H. Chatley, E. H. Essex, J. R. Finnicome, G. Lacey, J. Williamson, and G. G. Macdonald. Correspondence. Turbulent flow in pipes, with particular reference to the transition region between the smooth and rough pipe laws. (Includes plates). *Journal of the Institution of Civil Engineers*, 12(8):393–422, 1939.
- [43] M. Cook and M. Behnia. Slug length prediction in near horizontal gas–liquid intermittent flow. *Chemical Engineering Science*, 55(11):2009–2018, 2000.
- [44] V. Cornish. *Ocean waves and kindred geophysical phenomena*. Cambridge University Press, 1934.
- [45] C. J. Crowley, G. B. Wallis, and J. J. Barry. Validation of a one-dimensional wave model for the stratified-to-slug flow regime transition, with consequences for wave growth and slug frequency. *International Journal of Multiphase Flow*, 18(2):249–271, 1992.
- [46] T. J. Danielson, K. M. Bansal, B. Djoric, D. Larrey, S. T. Johansen, A. De Leebeek, and J. Kjolaas. Simulation of slug flow in oil and

- gas pipelines using a new transient simulator. In *Offshore Technology Conference*. Offshore Technology Conference, 2012.
- [47] H. Darcy. *Recherches expérimentales relatives au mouvement de l'eau dans les tuyaux*. Mallet-Bachelier, 1857.
- [48] A. De Leebeek and O. J. Nydal. Simulation of large amplitude waves in a slug tracking scheme compared to roll wave experiments at high pressure. *International Journal of Multiphase Flow*, 36(1):40–50, 2010.
- [49] E. A. Demekhin, E. N. Kalaidin, and E. M. Shapar'. On the theory of roll waves in inclined channels. *Doklady Physics*, 50(4):220–222, 2005.
- [50] R. F. Dressler. Mathematical solutions of the problem of roll-waves in inclined channels. *Communications on Pure and Applied Mathematics*, 2(2-3):149–194, 1949.
- [51] R. F. Dressler. New nonlinear shallow-flow equations with curvature. *Journal of Hydraulic Research*, 16:205–222, 1978.
- [52] R. F. Dressler and F. V. Pohle. Resistance effects on hydraulic instability. *Communications on Pure and Applied Mathematics*, 6(1):93–96, 1953.
- [53] X. Du and O. J. Nydal. Flow models and numerical schemes for single/two-phase transient flow in one dimension. *Applied Mathematical Modelling*, 2016.
- [54] A. E. Dukler and M. G. Hubbard. A model for gas-liquid slug flow in horizontal and near horizontal tubes. *Industrial and Engineering Chemistry Fundamentals*, 14(4):337–347, 1975.
- [55] A. E. Dukler, M. Wicks, and R. G. Cleveland. Frictional pressure drop in two-phase flow: A. A comparison of existing correlations for pressure loss and holdup. *AIChE Journal*, 10(1):38–43, 1964.

- [56] A. E. Dukler, M. Wicks, and R. G. Cleveland. Frictional pressure drop in two-phase flow: B. An approach through similarity analysis. *AIChE Journal*, 10(1):44–51, 1964.
- [57] A. E. Dukler, D. M. Maron, and N. Brauner. A physical model for predicting the minimum stable slug length. *Chemical Engineering Science*, 40(8):1379–1385, 1985.
- [58] J. Fabre and A. Liné. Modeling of two-phase slug flow. *Annual Review of Fluid Mechanics*, 24(1):21–46, 1992.
- [59] J. Fabre, G. Ferschneider, and L. Masbernat. Intermittent gas-liquid flow modeling in horizontal or weakly inclined pipes. *NASA STI/Recon Technical Report N*, 85:31465, 1983.
- [60] J. Fabre, A. Liné, and L. Peresson. Two fluid/two flow pattern model for transient gas±liquid flow in pipes. In *Proceedings of the 4th International Conference on Multiphase Flow*, pages 269–284, Nice, France, 1989.
- [61] Z. Fan, F. Lusseyran, and T. J. Hanratty. Initiation of slugs in horizontal gas-liquid flows. *AIChE Journal*, 39(11):1741–1753, 1993.
- [62] H. Felizola and O. Shoham. A unified model for slug flow in upward inclined pipes. *Journal of Energy Resources Technology*, 117(1):7–12, 1995.
- [63] R. C. Fernandes, R. Semiat, and A. E. Dukler. Hydrodynamic model for gas-liquid slug flow in vertical tubes. *AIChE Journal*, 29(6):981–989, 1983.
- [64] G. Ferschneider. Ecoulements diphasiques gaz-liquide à poches et à bouchons en conduites. *Revue de l'Institut Français du Pétrole*, 38(2):153–182, 1983.
- [65] A. B. Figueiredo, R. M. Baptista, F. B. de Freitas Rachid, and G. C. R. Bodstein. Numerical simulation of stratified-pattern two-phase flow

- in gas pipelines using a two-fluid model. *International Journal of Multiphase Flow*, 88:30–49, 2017.
- [66] J. M. Floryan. Centrifugal instability of Couette flow over a wavy wall. *Physics of Fluids*, 14(1):312–322, 2002.
- [67] M. G. Foley and V. A. Vanoni. Pulsing flow in steep alluvial streams. *Journal of the Hydraulics Division*, 103(ASCE 13114 Proceeding), 1977.
- [68] L. B. Fore and A. E. Dukler. Droplet deposition and momentum transfer in annular flow. *AIChE Journal*, 41(9):2040–2046, 1995.
- [69] L. B. Fore, S. G. Beus, and R. C. Bauer. Interfacial friction in gas–liquid annular flow: analogies to full and transition roughness. *International Journal of Multiphase Flow*, 26(11):1755–1769, 2000.
- [70] T. Fukano and T. Furukawa. Prediction of the effects of liquid viscosity on interfacial shear stress and frictional pressure drop in vertical upward gas–liquid annular flow. *International Journal of Multiphase Flow*, 24(4):587–603, 1998.
- [71] T. Funada and D. D. Joseph. Viscous potential flow analysis of Kelvin-Helmholtz instability in a channel. *Journal of Fluid Mechanics*, 445:263–283, 2001.
- [72] L. E. Gomez, O. Shoham, Z. Schmidt, R. N. Chokshi, and T. Northug. Unified mechanistic model for steady-state two-phase flow: horizontal to vertical upward flow. *SPE Journal*, 5(03):339–350, 2000.
- [73] L. E. Gomez, O. Shoham, and Y. Taitel. Prediction of slug liquid holdup: horizontal to upward vertical flow. *International Journal of Multiphase Flow*, 26(3):517–521, 2000.
- [74] P. Griffith and K. S. Lee. The stability of an annulus of liquid in a tube. *Journal of Basic Engineering*, 86(4):666–668, 1964.

- [75] P. Griffith and G. B. Wallis. Two-phase slug flow. *Journal of Heat Transfer*, 83(3):307–318, 1961.
- [76] J. Guckenheimer and P. Holmes. *Nonlinear oscillations, dynamical systems, and bifurcations of vector fields*. Springer, 1983.
- [77] S. E. Haaland. Simple and explicit formulas for the friction factor in turbulent pipe flow. *Journal of Fluids Engineering*, 105(1):89–90, 1983.
- [78] M. Hanif Chaudhry. *Open-Channel Flow*. Springer, 2008.
- [79] T. J. Hanratty. Interfacial instabilities caused by air flow over a thin liquid layer. *Waves on Fluid Interfaces*, pages 221–259, 1983.
- [80] T. J. Hanratty and J. M. Engen. Interaction between a turbulent air stream and a moving water surface. *AIChE Journal*, 3(3):299–304, 1957.
- [81] T. J. Hanratty and A. Hershman. Initiation of roll waves. *AIChE Journal*, 7(3):488–497, 1961.
- [82] W. H. Henstock and T. J. Hanratty. The interfacial drag and the height of the wall layer in annular flows. *AIChE Journal*, 22(6):990–1000, 1976.
- [83] H. Holmås, T. Sira, M. Nordsveen, H. P. Langtangen, and R. Schulkes. Analysis of a 1D incompressible two-fluid model including artificial diffusion. *IMA Journal of Applied Mathematics*, 73(4):651–667, 2008.
- [84] P. Hu, Z. Cao, K. Hu, and G. Pender. Discussion of “modeling the spatial evolution of roll waves with diffusive saint venant equations” by Ziyi Huang and Jin-Jen Lee. *Journal of Hydraulic Engineering*, 142(9):07016007, 2016.
- [85] Z. Huang and J.-J. Lee. Modeling the spatial evolution of roll waves with diffusive Saint Venant equations. *Journal of Hydraulic Engineering*, 141(2):06014022, 2014.
- [86] S.-H. Hwang and H.-C. Chang. Turbulent and inertial roll waves in inclined film flow. *Physics of Fluids*, 30(5):1259–1268, 1987.

- [87] R. I. Issa and M. H. W. Kempf. Simulation of slug flow in horizontal and nearly horizontal pipes with the two-fluid model. *International Journal of Multiphase Flow*, 29(1):69–95, 2003.
- [88] R. I. Issa, M. Bonizzi, and S. Barbeau. Improved closure models for gas entrainment and interfacial shear for slug flow modelling in horizontal pipes. *International Journal of Multiphase Flow*, 32(10):1287–1293, 2006.
- [89] R. I. Issa, J. Castagna, and A. Sheikh. Accurate simulation of intermittent/slug flow in oil and gas pipelines. In *15th International Conference on Multiphase Production Technology*. BHR Group, 2011.
- [90] R. M. Iverson, M. Logan, R. G. LaHusen, and M. Berti. The perfect debris flow? Aggregated results from 28 large-scale experiments. *Journal of Geophysical Research: Earth Surface*, 115(F3), 2010.
- [91] H. Jeffreys. On the formation of water waves by wind. *Proceedings of the Royal Society of London. Series A, Containing Papers of a Mathematical and Physical Character*, 107(742):189–206, 1925.
- [92] H. Jeffreys. The flow of water in an inclined channel of rectangular section. *The London, Edinburgh, and Dublin Philosophical Magazine and Journal of Science*, 49(293):793–807, 1925.
- [93] H. Jeffreys. On the formation of water waves by wind (second paper). *Proceedings of the Royal Society of London. Series A, Containing Papers of a Mathematical and Physical Character*, 110(754):241–247, 1926.
- [94] S. T. Johansen, S. Mo, E. Meese, J. E. S. Oliveira, J. F. R. Reyes, and J. N. E. Carneiro. CFD simulations of multiphase flows containing large scale interfaces and dispersed phases with selected production technology applications. In *OTC Brasil. Offshore Technology Conference*, 2015.

- [95] D. D. Joseph and J.-C. Saut. Short-wave instabilities and ill-posed initial-value problems. *Theoretical and Computational Fluid Dynamics*, 1(4):191–227, 1990.
- [96] D. D. Joseph, J. Belanger, and G. S. Beavers. Breakup of a liquid drop suddenly exposed to a high-speed airstream. *International Journal of Multiphase Flow*, 25(6):1263–1303, 1999.
- [97] U. Kadri, R. F. Mudde, R. V. A. Oliemans, M. Bonizzi, and P. Andreussi. Prediction of the transition from stratified to slug flow or roll-waves in gas–liquid horizontal pipes. *International Journal of Multiphase Flow*, 35(11):1001–1010, 2009.
- [98] D. L. V. Katz and R. L. Lee. *Natural gas engineering: production and storage*. McGraw-Hill Economics Department, 1990.
- [99] T. Kawahara and S. Toh. Nonlinear dispersive periodic waves in the presence of instability and damping. *Physics of Fluids*, 28(6):1636–1638, 1985.
- [100] J. Kevorkian. *Partial Differential Equations: Analytical Solution Techniques*. Springer, 1990.
- [101] A. C. King, J. Billingham, and S. R. Otto. *Differential Equations - Linear, Nonlinear, Ordinary, Partial*. Cambridge University Press, 2003.
- [102] T. K. Kjeldby, R. A. W. M. Henkes, and O. J. Nydal. Lagrangian slug flow modeling and sensitivity on hydrodynamic slug initiation methods in a severe slugging case. *International Journal of Multiphase Flow*, 53:29–39, 2013.
- [103] J. Kjølås. *Plug propagation in multiphase pipelines: Modeling and small scale experiments*. PhD thesis, Norwegian University of Science and Technology, 2007.

- [104] J. Kjølaas and S. T. Johansen. Terrain slugging in a high-pressure pipeline-riser system - large scale experiments and predictions with LedaFlow. In *9th North American Conference on Multiphase Technology*. BHR Group, 2014.
- [105] J. Kjølaas, A. De Leebeek, and S. T. Johansen. Simulation of hydrodynamic slug flow using the LedaFlow slug capturing model. In *16th International Conference on Multiphase Production Technology*. BHR Group, 2013.
- [106] E. Kordyban. Some characteristics of high waves in closed channels approaching Kelvin-Helmholtz instability. *Journal of Fluids Engineering*, 9(2):339–346, 1977.
- [107] E. Kordyban. Some details of developing slugs in horizontal two-phase flow. *AIChE Journal*, 31(5):802–806, 1985.
- [108] E. Kordyban. Horizontal slug flow: a comparison of existing theories. *Journal of Fluids Engineering*, 112(1):74–83, 1990.
- [109] E. S. Kordyban. Some characteristics of aerodynamic pressure over high waves in closed channels. *ASME Paper*, (73-FE):6, 1973.
- [110] E. S. Kordyban and T. Ranov. Mechanism of slug formation in horizontal two-phase flow. *Journal of Basic Engineering*, 92(4):857–864, 1970.
- [111] J. E. Kowalski. Wall and interfacial shear stress in stratified flow in a horizontal pipe. *AIChE Journal*, 33(2):274–281, 1987.
- [112] C. Kranenburg. On the evolution of roll waves. *Journal of Fluid Mechanics*, 245:249–261, 1992.
- [113] A. Kurganov and G. Petrova. A second-order well-balanced positivity preserving central-upwind scheme for the Saint-Venant system. *Communications in Mathematical Sciences*, 5(1):133–160, 2007.

- [114] A. Kurganov and E. Tadmor. New high-resolution central schemes for nonlinear conservation laws and convection-diffusion equations. *Journal of Computational Physics*, 160(1):241–282, 2000.
- [115] P. Y. Lin and T. J. Hanratty. Prediction of the initiation of slugs with linear stability theory. *International Journal of Multiphase Flow*, 12:79–98, 1986.
- [116] S. P. Lin. Finite amplitude side-band stability of a viscous film. *Journal of Fluid Mechanics*, 63(03):417–429, 1974.
- [117] J. S. Lioumbas, S. V. Paras, and A. J. Karabelas. Co-current stratified gas–liquid downflow — Influence of the liquid flow field on interfacial structure. *International Journal of Multiphase Flow*, 31(8):869–896, 2005.
- [118] I. G. Manolis. *High pressure gas-liquid slug flow*. PhD thesis, Imperial College London, 1995.
- [119] I. G. Manolis, M. A. Mendes-Tatsis, and G. F. Hewitt. The effect of pressure on flow pattern transition and pressure gradient in two-phase horizontal slug. In *ICHEME Research Event*, pages 5–6, Edinburgh, UK, 1995.
- [120] I. G. Manolis, M. A. Mendes-Tatsis, and G. F. Hewitt. The effect of pressure on slug frequency on two-phase horizontal flow. In *2nd International Multiphase Flow Conference*, Kyoto, Japan, 1995.
- [121] B. S. Massey and J. Ward-Smith. *Mechanics of fluids*. Nelson Thornes, 7th edition, 1998.
- [122] C. Mata, E. Pereyra, J. L. Trallero, and D. D. Joseph. Stability of stratified gas-liquid flows. *International Journal of Multiphase Flow*, 28(8):1249–1268, 2002.

- [123] P. G. Mayer. Roll waves and slug flows in inclined open channels. *Transactions of the ASCE*, 126(1):505–535, 1961.
- [124] J. H. Merkin and D. J. Needham. An infinite period bifurcation arising in roll waves down an open inclined channel. In *Proceedings of the Royal Society of London Series A: Mathematical, Physical and Engineering Sciences*, volume 405, pages 103–116. The Royal Society of London, 1986.
- [125] J. H. Merkin and D. J. Needham. On infinite period bifurcations with an application to roll waves. *Acta Mechanica*, 60(1-2):1–16, 1986.
- [126] K. Mishima and M. Ishii. Theoretical prediction of horizontal slug flow. *Journal of Fluids Engineering*, 102:441–445, 1980.
- [127] S. Mo, A. Ashrafian, J.-C. Barbier, and S. T. Johansen. Quasi-3D modelling of two-phase slug flow in pipes. *The Journal of Computational Multiphase Flows*, 6(1):1–12, 2014.
- [128] S. Montes. *Hydraulics of open channel flow*. 1998.
- [129] L. F. Moody. Friction factors for pipe flow. *Transactions of the ASME*, 66(8):671–684, 1944.
- [130] C. Nakaya. Long waves on a thin fluid layer flowing down an inclined plane. *Physics of Fluids*, 18(11):1407–1412, 1975.
- [131] D. J. Needham and J. H. Merkin. On roll waves down an inclined channel. *Proceedings of the Royal Society of London Series A: Mathematical Physical and Engineering Sciences*, 394(1807):259–278, 1984.
- [132] D. J. Needham, J. Billingham, R. M. S. M. Schulkes, and A. C. King. The development of slugging in two-layer hydraulic flows. *IMA Journal of Applied Mathematics*, 73(1):274–322, 2008.

- [133] M. K. Nicholson, K. Aziz, and G. A. Gregory. Intermittent two phase flow in horizontal pipes: predictive models. *The Canadian Journal of Chemical Engineering*, 56(6):653–663, 1978.
- [134] D. J. Nicklin, J. O. Wilkes, and D. J. F. Two phase flow in vertical tubes. *Transactions of the Institution of Chemical Engineers*, 40(a):61–68, 1962.
- [135] A. O. Nieckele, J. N. E. Carneiro, R. C. Chucuya, and J. H. P. Azevedo. Initiation and statistical evolution of horizontal slug flow with a two-fluid model. *Journal of Fluids Engineering*, 135(12):121302, 2013.
- [136] J. Nikuradse. Gesetzmäßigkeiten der turbulenten strömung in glatten rohren. *Forschung im Ingenieurwesen*, 4(1):44–44, 1932.
- [137] J. Nikuradse. Strömungsgestze in rauhen rohren. 1933.
- [138] O. B. Novik. Model description of roll-waves. *Journal of Applied Mathematics and Mechanics*, 35(6):938–951, 1971.
- [139] S. Nuland, I. Malvik, A. Valle, and P. Hende. Gas fractions in slugs in dense-gas two-phase flow from horizontal to 60 degrees of inclination. In *ASME Fluids Engineering Division*.
- [140] O. J. Nydal and S. Banerjee. Object oriented dynamic simulation of slug flow. In *2nd International Conference on Multiphase Flow*, pages 3–7, Kyoto, Japan, 1995.
- [141] O. J. Nydal and S. Banerjee. Dynamic slug tracking simulations for gas-liquid flow in pipelines. *Chemical Engineering Communications*, 141(1):13–39, 1996.
- [142] O. J. Nydal, S. Pintus, and P. Andreussi. Statistical characterization of slug flow in horizontal pipes. *International Journal of Multiphase Flow*, 18(3):439–453, 1992.

- [143] A. Orell and R. Rembrand. A model for gas-liquid slug flow in a vertical tube. *Industrial & Engineering Chemistry Fundamentals*, 25(2): 196–206, 1986.
- [144] N. Petalas and K. Aziz. Development and testing of a new mechanistic model for multiphase flow in pipes. In *ASME Fluids Engineering Division*, pages 153–159, San Diego, CA, USA, 1996.
- [145] L. Prandtl. Neuere ergebnisse der turbulenzforschung. *VDI-Ztschr*, 77 (5):105, 1933.
- [146] T. Prokopiou, M. Cheng, and H.-C. Chang. Long waves on inclined films at high reynolds number. *Journal of Fluid Mechanics*, 222:665–691, 1991.
- [147] A. Pumir, P. Manneville, and Y. Pomeau. On solitary waves running down an inclined plane. *Journal of Fluid Mechanics*, 135:27–50, 1983.
- [148] S. Y. Razavi and M. M. Namin. Numerical model of slug development on horizontal two-phase flow. In *International Conference on Recent Trends in Transportation, Environmental and Civil Engineering*. Citeseer, 2011.
- [149] F. Renault. *A Lagrangian slug capturing scheme for gas-liquid flows in pipes*. PhD thesis, Norwegian University of Science and Technology, 2007.
- [150] G. L. Richard and S. L. Gavrilyuk. A new model of roll waves: comparison with Brock’s experiments. *Journal of Fluid Mechanics*, 698: 374–405, 2012.
- [151] E. S. Rosa, R. A. Mazza, R. E. Morales, H. T. Rodrigues, and C. Cozin. Analysis of slug tracking model for gas–liquid flows in a pipe. *Journal of the Brazilian Society of Mechanical Sciences and Engineering*, 37(6):1665–1686, 2015.

- [152] H. Rouse. *Fluid mechanics for hydraulic engineers*. Dover Publications Inc., 1938.
- [153] H. Rouse. Evaluation of boundary roughness. In *Proceedings of the Second Hydraulics Conference*, pages 105–116. University of Iowa Studies in Engineering, 1943.
- [154] A. Sanchis, G. W. Johnson, and A. Jensen. The formation of hydrodynamic slugs by the interaction of waves in gas–liquid two-phase pipe flow. *International Journal of Multiphase Flow*, 37(4):358–368, 2011.
- [155] H. Schlichting and K. Gersten. *Boundary-Layer Theory*. Springer, 8th edition, 2000.
- [156] Ž. Schmidt. *Experimental study of two-phase slug flow in a pipeline-riser pipe system*. PhD thesis, University of Tulsa, 1977.
- [157] Z. Schmidt, J. P. Brill, and H. D. Beggs. Experimental study of severe slugging in a two-phase-flow pipeline-riser pipe system. *Society of Petroleum Engineers Journal*, 20(05):407–414, 1980.
- [158] S. Selvarajan, E. G. Tulapurkara, and V. V. Ram. Stability characteristics of wavy walled channel flows. *Physics of Fluids*, 11(3):579–589, 1999.
- [159] J. Shi and G. Kocamustafaogullari. Interfacial measurements in horizontal stratified flow patterns. *Nuclear Engineering and Design*, 149(1):81–96, 1994.
- [160] E. F. Simões, J. N. E. Carneiro, and A. O. Nieckele. Numerical prediction of non-boiling heat transfer in horizontal stratified and slug flow by the two-fluid model. *International Journal of Heat and Fluid Flow*, 47:135–145, 2014.
- [161] G. I. Sivashinsky and D. M. Michelson. On irregular wavy flow of a liquid film down a vertical plane. *Progress of Theoretical Physics*, 63(6):2112–2114, 1980.

- [162] R. V. Smith, J. S. Miller, and J. W. Ferguson. Flow of natural gas through experimental pipe lines and transmission lines. Technical report, Bureau of Mines, Bartlesville, OK (USA), 1956.
- [163] A. Soleimani and T. J. Hanratty. Critical liquid flows for the transition from the pseudo-slug and stratified patterns to slug flow. *International Journal of Multiphase Flow*, 29(1):51–67, 2003.
- [164] P. L. Spedding and N. P. Hand. Prediction in stratified gas-liquid co-current flow in horizontal pipelines. *International Journal of Heat and Mass Transfer*, 40(8):1923–1935, 1997.
- [165] J. J. Stoker. *Water waves*. New York: Wiley InterScience, 1957.
- [166] T. Straume, M. Nordsveen, and K. Bendiksen. Numerical simulation of slugging in pipelines. In *Multiphase Flow in Wells and Pipelines*, volume 144, pages 103–112, Anaheim, California, USA, 1992. ASME.
- [167] M. Suo and P. Griffith. Two-phase flow in capillary tubes. *Journal of Basic Engineering*, 86(3):576–582, 1964.
- [168] P. K. Swanee and A. K. Jain. Explicit equations for pipeflow problems. *Journal of the Hydraulics Division*, 102(5), 1976.
- [169] N. D. Sylvester. A mechanistic model for two-phase vertical slug flow in pipes. *Journal of Energy Resources Technology*, 109(4):206–213, 1987.
- [170] Y. Taitel and D. Barnea. Two-phase slug flow. *Advances in Heat Transfer*, 20:83–132, 1990.
- [171] Y. Taitel and D. Barnea. Effect of gas compressibility on a slug tracking model. *Chemical Engineering Science*, 53(11):2089–2097, 1998.
- [172] Y. Taitel and A. E. Dukler. A model for predicting flow regime transitions in horizontal and near horizontal gas-liquid flow. *AIChE Journal*, 22(1):47–55, 1976.

- [173] Y. Taitel and A. E. Dukler. A theoretical approach to the Lockhart-Martinelli correlation for stratified flow. *International Journal of Multiphase Flow*, 2(5):591–595, 1976.
- [174] Y. Taitel, C. Sarica, and J. P. Brill. Slug flow modeling for downward inclined pipe flow: theoretical considerations. *International Journal of Multiphase Flow*, 26(5):833–844, 2000.
- [175] D. Tseluiko and S. Kalliadasis. Nonlinear waves in counter-current gas–liquid film flow. *Journal of Fluid Mechanics*, 673:19–59, 2011.
- [176] C. Tzotzi and N. Andritsos. Interfacial shear stress in wavy stratified gas–liquid flow in horizontal pipes. *International Journal of Multiphase Flow*, 54:43–54, 2013.
- [177] A. E. Uhl. Steady flow in gas pipelines. Technical Report 10, Institute of Gas Technology, 1965. American Gas Association.
- [178] P. M. Ujang, C. J. Lawrence, and G. F. Hewitt. Conservative incompressible slug tracking model for gas-liquid flow in a pipe. In *5th BHRG North American Conference on Multiphase Technology*, volume 31, Banff, Canada, 2006.
- [179] R. Van Hout, L. Shemer, and D. Barnea. Spatial distribution of void fraction within a liquid slug and some other related slug parameters. *International Journal of Multiphase Flow*, 18(6):831–845, 1992.
- [180] M. Vlachogiannis and V. Bontozoglou. Experiments on laminar film flow along a periodic wall. *Journal of Fluid Mechanics*, 457:133–156, 2002.
- [181] T. Von Kármán. Mechanische ähnlichkeit und turbulenz. In *Proceedings of the Third International Congress of Applied Mechanics*, pages 79–93, 1930.

- [182] G. B. Wallis. *One-dimensional two-phase flow*. McGraw-Hill Companies, 1969.
- [183] G. B. Wallis and J. E. Dobson. The onset of slugging in horizontal stratified air-water flow. *International Journal of Multiphase Flow*, 1(1): 173–193, 1973.
- [184] X. Wang, L. Guo, and X. Zhang. Development of liquid slug length in gas-liquid slug flow along horizontal pipeline: Experiment and simulation. *Chinese Journal of Chemical Engineering*, 14(5):626–633, 2006.
- [185] J. Weisbach. *Lehrbuch der Ingenieur- und Maschinen-Mechanik*, volume 1. Vieweg und Sohn, 1845.
- [186] F. M. White. *Fluid Mechanics*. McGraw-Hill, 7th edition, 2009.
- [187] G. B. Whitham. *Linear and Nonlinear Waves*. New York: Wiley Inter-Science, 1974.
- [188] B. D. Woods, E. T. Hurlburt, and T. J. Hanratty. Mechanism of slug formation in downwardly inclined pipes. *International Journal of Multiphase Flow*, 26(6):977–998, 2000.
- [189] H. L. Wu, B. F. M. Pots, J. F. Hollenberg, and R. Meerhoff. Flow pattern transitions in two-phase gas/condensate flow at high pressure in an 8-inch horizontal pipe. In *3rd International Conference on Multiphase Flow*, pages 13–21, The Hague, The Netherlands, 1987.
- [190] C.-S. Yih. Stability of liquid flow down an inclined plane. *Physics of Fluids*, 6(3):321, 1963.
- [191] J. Yu and J. Kevorkian. Nonlinear evolution of small disturbances into roll waves in an inclined open channel. *Journal of Fluid Mechanics*, 243: 575–594, 1992.
- [192] G. Zabarvas, A. E. Dukler, and D. Moalem-Maron. Vertical upward cocurrent gas-liquid annular flow. *AIChE Journal*, 32(5):829–843, 1986.

- [193] M. V. Zagarola and A. J. Smits. Mean-flow scaling of turbulent pipe flow. *Journal of Fluid Mechanics*, 373:33–79, 1998.
- [194] G. Zheng, J. P. Brill, and Y. Taitel. Slug flow behavior in a hilly terrain pipeline. *International Journal of Multiphase Flow*, 20(1):63–79, 1994.
- [195] G. H. Zheng. *Two-phase slug flow in hilly terrain pipelines*. PhD thesis, University of Tulsa, Oklahoma, USA, 1991.
- [196] G. H. Zheng, J. P. Brill, and O. Shoham. An experimental study of two-phase slug flow in hilly terrain pipelines. In *67th Annual Technical Conference and Exhibition*, Washington DC, USA, 1992. Society of Petroleum Engineers.